frontiers
RESEARCH TOPICS

MOTOR CORTEX MICROCIRCUITS (FRONTIERS IN BRAIN MICROCIRCUITS SERIES)

Topic Editors
Michael Brecht, Nicholas Hatsopoulos, Takehsi Kaneko and Gordon M. G. Shepherd

frontiers in
NEURAL CIRCUITS

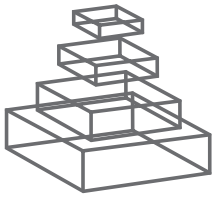

frontiers

Cover image provided by Ibbl sarl, Lausanne CH

ISSN 1664-8714
ISBN 978-2-88919-389-9
DOI 10.3389/978-2-88919-389-9

ABOUT FRONTIERS

Frontiers is more than just an open-access publisher of scholarly articles: it is a pioneering approach to the world of academia, radically improving the way scholarly research is managed. The grand vision of Frontiers is a world where all people have an equal opportunity to seek, share and generate knowledge. Frontiers provides immediate and permanent online open access to all its publications, but this alone is not enough to realize our grand goals.

FRONTIERS JOURNAL SERIES

The Frontiers Journal Series is a multi-tier and interdisciplinary set of open-access, online journals, promising a paradigm shift from the current review, selection and dissemination processes in academic publishing.
All Frontiers journals are driven by researchers for researchers; therefore, they constitute a service to the scholarly community. At the same time, the Frontiers Journal Series operates on a revolutionary invention, the tiered publishing system, initially addressing specific communities of scholars, and gradually climbing up to broader public understanding, thus serving the interests of the lay society, too.

DEDICATION TO QUALITY

Each Frontiers article is a landmark of the highest quality, thanks to genuinely collaborative interactions between authors and review editors, who include some of the world's best academicians. Research must be certified by peers before entering a stream of knowledge that may eventually reach the public - and shape society; therefore, Frontiers only applies the most rigorous and unbiased reviews.
Frontiers revolutionizes research publishing by freely delivering the most outstanding research, evaluated with no bias from both the academic and social point of view.
By applying the most advanced information technologies, Frontiers is catapulting scholarly publishing into a new generation.

WHAT ARE FRONTIERS RESEARCH TOPICS?

Frontiers Research Topics are very popular trademarks of the Frontiers Journals Series: they are collections of at least ten articles, all centered on a particular subject. With their unique mix of varied contributions from Original Research to Review Articles, Frontiers Research Topics unify the most influential researchers, the latest key findings and historical advances in a hot research area!
Find out more on how to host your own Frontiers Research Topic or contribute to one as an author by contacting the Frontiers Editorial Office: researchtopics@frontiersin.org

MOTOR CORTEX MICROCIRCUITS (FRONTIERS IN BRAIN MICROCIRCUITS SERIES)

Topic Editors:
Michael Brecht, Humboldt University Berlin, Germany
Nicholas Hatsopoulos, University of Chicago, USA
Takehsi Kaneko, Kyoto University, Japan
Gordon M. G. Shepherd, Northwestern University, USA

Table of Contents

frontiers in
NEURAL CIRCUITS

EDITORIAL
published: 12 December 2013
doi: 10.3389/fncir.2013.00196

Motor cortex microcircuits

Michael Brecht[1]*, Nicholas G. Hatsopoulos[2]*, Takeshi Kaneko[3]* and Gordon M. G. Shepherd[4]*

[1] *Bernstein Center for Computational Neuroscience, Humboldt University, and Cluster of Excellence NeuroCure, Charité-Universitätsmedizin, Berlin, Germany*
[2] *Department of Organismal Biology and Anatomy, Committees on Computational Neuroscience and Neurobiology, University of Chicago, Chicago, IL, USA*
[3] *Department of Morphological Brain Science, Graduate School of Medicine, Kyoto University, Kyoto, Japan*
[4] *Department of Physiology, Feinberg School of Medicine, Northwestern University, Chicago, IL, USA*
**Correspondence: michael.brecht@bccn-berlin.de; nicho@uchicago.edu; kaneko@mbs.med.kyoto-u.ac.jp; g-shepherd@northwestern.edu*

Edited by:
Idan Segev, The Hebrew University of Jerusalem, Israel

Keywords: motor cortex, motor control, intracortical connectivity, corticospinal neurons, directional tuning

The goal of this Research Topic was to bring together articles representing the spectrum of current research aimed at understanding the functional organization motor cortex at the level of microcircuits.

The original research articles in this collection address a wide range of aspects of motor cortex microcircuits. The monkey's motor cortex is an especially important model system because of the similarities to the human brain, and the ability to train monkeys to perform complex movements. However, information about the cellular composition of different primates has been limited; Young et al. (2013) now describe the cell densities in motor cortex across multiple primate species. Studying reaching and grasping is a powerful approach to understanding complex movements in monkeys. Riehle et al. (2013) describe the spatio-temporal structure of motor cortical local field potentials and spiking activities during reach-to-grasp movements. Dickey et al. (2013) report on the heterogeneity of signals detected as monkeys make corrective movements while reaching. Motor cortical influences on lower limb function are also crucial for many types of motor behavior, and Hudson et al. (2013) report new findings of differences in the cortical output to fast and slow muscles of the ankle. The rodent motor cortex offers a complementary model system providing more immediate access to identified cells and circuits using optogenetic and related tools. In rats, Tanaka et al. (2011) dissect the local connectivity of corticospinal neurons with different classes of interneurons. Smith and Alloway (2013) show that the whisker motor cortex has distinct sensory-input and motor-output sub-regions. Applying optogenetic tools in mice, Hira et al. (2013) characterize the synaptic connectivity between rostral and caudal sub-regions encoding the forelimb representation. Studying genetically labeled pyramidal neurons in layer 5, Yu et al. (2008) demonstrate cell-type-specific local circuits and firing patterns. Also examining firing patterns, Hedrick and Waters (2012) report on their high sensitivity to temperature.

The review-type articles provide new syntheses of current knowledge about different aspects of motor cortex function and dysfunction. Kaneko (2013) focuses on microcircuits of excitatory neurons in the rodent motor cortex, and develops novel concepts about the organization of thalamic innervation to motor cortex microcircuits. Tsubo et al. (2013) assess current knowledge about *in vivo* dynamic activity across motor cortical layers in relation to movement. Harrison and Murphy (2012) emphasize the significance of particular classes of projection neurons and how these may be investigated with optogenetic strategies to determine their roles in motor function. Capaday et al. (2013) address the functional organization of the motor cortex from the perspective of intracortical connectivity. Castro-Alamancos (2013) discusses how motor cortex operates as a dynamic, frequency-tuned, oscillating network. Mahan and Georgopoulos (2013) review directional tuning from the perspective of resonance and the role of inhibitory mechanisms. Di Lazzaro and Ziemann (2013) review evidence, gathered from transcranial magnetic stimulation studies, for the roles of different types of microcircuits in the functions of human motor cortex. Diseases of the motor cortex have devastating consequences for motor control; Estrada-Sanchez and Rebec (2013) review the state of research on motor cortical involvement in Huntington's disease.

We are impressed not only with the diversity of contributions included here, but even more so we were delighted that researchers from all walks of motor cortex investigation enthusiastically steered their research toward the microcircuit theme pursued in this volume. More than ever it seems clear that we all are working toward a common goal, i.e., describing motor cortical function in terms of the transactions in identified cellular circuits. We thank the authors for their contributions, and are additionally grateful to the many reviewers who contributed their efforts.

REFERENCES

Capaday, C., Ethier, C., Van Vreeswijk, C., and Darling, W. G. (2013). On the functional organization and operational principles of the motor cortex. *Front. Neural Circuits* 7:66. doi: 10.3389/fncir.2013.00066

Castro-Alamancos, M. A. (2013). The motor cortex: a network tuned to 7-14 Hz. *Front. Neural Circuits* 7:21. doi: 10.3389/fncir.2013.00021

Dickey, A. S., Amit, Y., and Hatsopoulos, N. G. (2013). Heterogeneous neural coding of corrective movements in motor cortex. *Front. Neural Circuits* 7:51. doi: 10.3389/fncir.2013.00051

Di Lazzaro, V., and Ziemann, U. (2013). The contribution of transcranial magnetic stimulation in the functional evaluation of microcircuits in human motor cortex. *Front. Neural Circuits* 7:18. doi: 10.3389/fncir.2013.00018

Estrada-Sanchez, A. M., and Rebec, G. V. (2013). Role of cerebral cortex in the neuropathology of Huntington's disease. *Front. Neural Circuits* 7:19. doi: 10.3389/fncir.2013.00019

Harrison, T. C., and Murphy, T. H. (2012). Towards a circuit mechanism for movement tuning in motor cortex. *Front. Neural Circuits* 6:127. doi: 10.3389/fncir.2012.00127

Hedrick, T., and Waters, J. (2012). Effect of temperature on spiking patterns of neocortical layer 2/3 and layer 6 pyramidal neurons. *Front. Neural Circuits* 6:28. doi: 10.3389/fncir.2012.00028

Hira, R., Ohkubo, F., Tanaka, Y. R., Masamizu, Y., Augustine, G. J., Kasai, H., et al. (2013). In vivo optogenetic tracing of functional corticocortical connections between motor forelimb areas. *Front. Neural Circuits* 7:55. doi: 10.3389/fncir.2013.00055

Hudson, H. M., Griffin, D. M., Belhaj-Saif, A., and Cheney, P. D. (2013). Cortical output to fast and slow muscles of the ankle in the rhesus macaque. *Front. Neural Circuits* 7:33. doi: 10.3389/fncir.2013.00033

Kaneko, T. (2013). Local connections of excitatory neurons in motor-associated cortical areas of the rat. *Front. Neural Circuits* 7:75. doi: 10.3389/fncir.2013.00075

Mahan, M. Y., and Georgopoulos, A. P. (2013). Motor directional tuning across brain areas: directional resonance and the role of inhibition for directional accuracy. *Front. Neural Circuits* 7:92. doi: 10.3389/fncir.2013.00092

Riehle, A., Wirtssohn, S., Grun, S., and Brochier, T. (2013). Mapping the spatio-temporal structure of motor cortical LFP and spiking activities during reach-to-grasp movements. *Front. Neural Circuits* 7:48. doi: 10.3389/fncir.2013.00048

Smith, J. B., and Alloway, K. D. (2013). Rat whisker motor cortex is subdivided into sensory-input and motor-output areas. *Front. Neural Circuits* 7:4. doi: 10.3389/fncir.2013.00004

Tanaka, Y. H., Tanaka, Y. R., Fujiyama, F., Furuta, T., Yanagawa, Y., and Kaneko, T. (2011). Local connections of layer 5 GABAergic interneurons to corticospinal neurons. *Front. Neural Circuits* 5:12. doi: 10.3389/fncir.2011.00012

Tsubo, Y., Isomura, Y., and Fukai, T. (2013). Neural dynamics and information representation in microcircuits of motor cortex. *Front. Neural Circuits* 7:85. doi: 10.3389/fncir.2013.00085

Young, N. A., Collins, C. E., and Kaas J. H. (2013). Cell and neuron densities in the primary motor cortex of primates. *Front. Neural Circuits* 7:30. doi: 10.3389/fncir.2013.00030

Yu, J., Anderson, C. T., Kiritani, T., Sheets, P. L., Wokosin, D. L., Wood, L., et al. (2008). Local-circuit phenotypes of layer 5 neurons in motor-frontal cortex of YFP-H mice. *Front. Neural Circuits* 2:6. doi: 10.3389/neuro.04.006.2008

Received: 21 September 2013; accepted: 26 November 2013; published online: 12 December 2013.

Citation: Brecht M, Hatsopoulos NG, Kaneko T and Shepherd GMG (2013) Motor cortex microcircuits. Front. Neural Circuits **7**:*196. doi: 10.3389/fncir.2013.00196*

This article was submitted to the journal Frontiers in Neural Circuits.

frontiers in
NEURAL CIRCUITS

REVIEW ARTICLE
published: 28 May 2013
doi: 10.3389/fncir.2013.00075

Local connections of excitatory neurons in motor-associated cortical areas of the rat

Takeshi Kaneko*

Department of Morphological Brain Science, Graduate School of Medicine, Kyoto University, Kyoto, Japan

Edited by:
Gordon M. G. Shepherd, Northwestern University, USA

Reviewed by:
Scott Hooper, Ohio University, USA
Alex M. Thomson, University of London, UK
Joshua C. Brumberg, Queens College, City University of New York, USA

***Correspondence:**
Takeshi Kaneko, Department of Morphological Brain Science, Graduate School of Medicine, Kyoto University, Yoshida-Konoe-Cho, Sakyo-Ku, Kyoto 606-8501, Japan. e-mail: kaneko@mbs.med.kyoto-u.ac.jp

In spite of recent progress in brain sciences, the local circuit of the cerebral neocortex, including motor areas, still remains elusive. Morphological works on excitatory cortical circuitry from thalamocortical (TC) afferents to corticospinal neurons (CSNs) in motor-associated areas are reviewed here. First, TC axons of motor thalamic nuclei have been re-examined by the single-neuron labeling method. There are middle layer (ML)-targeting and layer (L) 1-preferring TC axon types in motor-associated areas, being analogous to core and matrix types, respectively, of Jones (1998) in sensory areas. However, the arborization of core-like motor TC axons spreads widely and disregards the columnar structure that is the basis of information processing in sensory areas, suggesting that motor areas adopt a different information-processing framework such as area-wide laminar organization. Second, L5 CSNs receive local excitatory inputs not only from L2/3 pyramidal neurons but also from ML spiny neurons, the latter directly processing cerebellar information of core-like TC neurons (TCNs). In contrast, basal ganglia information is targeted to apical dendrites of L2/3 and L5 pyramidal neurons through matrix TCNs. Third, L6 corticothalamic neurons (CTNs) are most densely innervated by ML spiny neurons located just above CTNs. Since CTNs receive only weak connections from L2/3 and L5 pyramidal neurons, the TC recurrent circuit composed of TCNs, ML spiny neurons and CTNs appears relatively independent of the results of processing in L2/3 and L5. It is proposed that two circuits sharing the same TC projection and ML neurons are embedded in the neocortex: one includes L2/3 and L5 neurons, processes afferent information in a feedforward way and sends the processed information to other cortical areas and subcortical regions; and the other circuit participates in a dynamical system of the TC recurrent circuit and may serve as the basis of autonomous activity of the neocortex.

Keywords: local circuit, microcircuit, pyramidal neurons, excitatory connection, thalamocortical projection, corticothalamic projection neurons, corticospinal projection neurons, motor cortex

MOTOR-ASSOCIATED AREAS IN RODENTS

Motor-associated areas in the rodent cerebral cortex here include the primary motor (M1), secondary motor (M2), forelimb (FL), and hindlimb (HL) areas (Paxinos and Watson, 2007). Areas M1 and M2 correspond to lateral and medial agranular areas, respectively, of Donoghue and Wise (1982). Areas FL and HL have first been included in the primary somatosensory area (area S1; SmI neocortex of Welker, 1971), but later considered as mixed areas of motor and somatosensory information processing for the limbs. Although areas FL and HL are granular with developed layer (L) 4 and respond to somatosensory stimuli like area S1 for the face and trunk (Welker, 1971; Donoghue et al., 1979), area HL and the medial part of area FL have as low a threshold for intracortical microstimulation to evoke a motor response as area M1 (Hall and Lindholm, 1974; Donoghue and Wise, 1982; Sanderson et al., 1984; Neafsey et al., 1986; Tennant et al., 2011). A recent optogenetic stimulation technique with channelrhodopsin-2 expression in pyramidal neurons has supported the overlap of the M1 and somatosensory areas for the HL and FL (Ayling et al., 2009). Furthermore, when corticospinal projection neurons (CSNs) are labeled by injection of retrograde tracers into the corticospinal tract at the rat cervical spinal cord, many labeled neurons are continuously found in L5 from area M1 of the lateral agranular field to areas HL and FL of the lateral granular field (Wise and Jones, 1977; Leong, 1983; Miller, 1987; Killackey et al., 1989; Kaneko et al., 2000; Cho et al., 2004b; Tanaka et al., 2011a). Thus, area HL and the medial part of area FL are considered to have characteristics of motor areas, and, together with areas M1 and M2, treated as motor-associated areas in the present review.

Since areas M1 and M2 of rodents are called "agranular areas" as motor areas of higher mammals, these areas have generally been considered to lack L4. It is, however, often intriguing from the time of Krieg (1946) whether areas M1 and M2 in rodents have L4 or not. For example, Skoglund et al. (1997) reported the presence of L4 in area M1 by using the computerized analysis system based on their optical dissector method. Their conclusion was later supported by the presence of L4 in rat area M1 by using immunoreactivity for vesicular glutamate transporter 2 (VGluT2), which is a marker for thalamic afferents in the cerebral cortex (Fujiyama et al., 2001). The VGluT2-immunoreactive band in area M1 is continuous to that of area S1, and VGluT2

immunoreactivity in the band is as intense as that in L4 of area S1, although the band is thinner than L4 of area S1 (Cho et al., 2004a). However, in the present review, "the deepest part of L3 (L3d)" is conservatively used instead of "L4" in areas M1 and M2 to indicate the cortical layer receiving massive afferents from the thalamic nuclei, and "L2/3" is applied to superficial layers excluding this L3d to keep L2/3 of areas M1 and M2 homologous to L2/3 of areas HL and FL.

INTRODUCTION OF LOCAL CIRCUIT ANALYSIS IN THE MOTOR-ASSOCIATED AREAS

The local excitatory connection of the rodent neocortex has been initially examined by the combination of intracellular recording and focal electrical stimulation (Connors et al., 1982; Chagnac-Amitai and Connors, 1989; Sutor and Hablitz, 1989; Silva et al., 1991; Hwa and Avoli, 1992). However, the results of the focal electrical stimulation in the neocortex are difficult to interpret, because it is unclear which components in the tissue are stimulated. Researchers may like to activate neuronal cell bodies and their local axon collaterals in the focal stimulation site, but afferent axons from thalamic nuclei and other cortical areas can also be activated. This uncertainty has been removed by the combined technique of intracellular recording and spike-triggered averaging (Thomson et al., 1988), or by the paired intracellular or whole-cell recording technique with intracellular stimulation (Thomson and West, 1993; Markram and Tsodyks, 1996; Buhl et al., 1997; Ohana and Sakmann, 1998; Galarreta and Hestrin, 1999). In the rodent neocortex including motor-associated areas, the synaptic connection between excitatory neurons has been examined extensively (Thomson and West, 1993; Deuchars et al., 1994; Thomson, 1997; Thomson et al., 2002; Bannister and Thomson, 2007). The paired recording technique is useful for examining the electrophysiological and pharmacological properties of monosynaptic connections between the excitatory neurons, and a high connectivity rate between neuronal groups, such as L4-to-L2/3 and L2/3-to-L5 connectivity rates (Thomson and Bannister, 1998; Thomson et al., 2002; Bannister and Thomson, 2007), suggests strong connections between the groups. However, the technique is usually unsuitable for quantitatively estimating connectivity between excitatory neuron groups because of sample selection biases. To remove the biases, Lefort et al. (2009) have quantified connectivity maps between excitatory neurons within a barrel column of mouse area S1 by randomly sampling a large number (2550) of excitatory neurons and testing 8895 possible synaptic connections within the column. Although this multiple whole-cell recording technique with random sampling is effective in mapping the local excitatory connections of the neocortex, no similar studies have been reported in the motor-associated areas yet.

Recently, another method for investigating cortical local connections has been developed by a combination of the whole-cell clamp recording and scanning laser photostimulation with caged glutamate in cortical slices (Dalva and Katz, 1994; Katz and Dalva, 1994). This photo-uncaging technique is useful for the selective stimulation of neuronal cell bodies, and has been applied not only to sensory cortical slices but also to motor cortical ones. For instance, in the mouse motor–frontal areas or vibrissal region of area M1, the photostimulation of L2/3 frequently evokes excitatory postsynaptic currents (EPSCs) in L5 pyramidal neurons (Weiler et al., 2008; Yu et al., 2008; Hooks et al., 2011). In addition, it has been reported that upper L5b CSNs and lower L5a crossed corticostriatal neurons, the latter of which send axons to the contralateral striatum, receive excitatory inputs from L2/3 neurons, whereas lower L5b CSNs accept inputs mainly from L5b neurons (Anderson et al., 2010). Further recently, the subcellular channelrhodopsin-2-assisted circuit mapping has been introduced (Petreanu et al., 2009). This optogenetic technique has revealed that neurons in area M1 send excitatory connections onto the apical dendrites of L2/3 and L5b pyramidal neurons and onto the basal dendrites of L5b neurons in the primary somatosensory area. These scanning laser photo-uncaging and optogenetic techniques are helpful in analyzing local or remote inputs to single cortical neurons.

There are only a few quantitative morphological analyses of local excitatory connections in the rodent neocortex. Using the electron-microscopic technique, Somogyi (1978) reported that excitatory asymmetric synapses with the intracortical axon collaterals of L4 pyramidal neurons were evenly found on the dendritic shafts of presumed interneurons and on the dendritic spines of excitatory spiny neurons in L4 of rat primary visual area (area V1). A similar result was reported in mouse area S1 by White and Hersch (1981). In contrast, the local collaterals of area M1-projecting pyramidal neurons in L3 of mouse area S1 preferred dendritic spines (∼85%) within L3 and L5 of area S1 as their synaptic targets (Figures 3.1 and 7.1 in White, 1989). It is further interesting that most local axon collaterals (≥90%) of L5–L6 corticothalamic neurons (CTNs) in mouse area S1 terminated on the dendritic shafts of presumed interneurons within L4–L6 (White and Keller, 1987). Since only 37–46% of total asymmetric synapses were located on dendritic shafts in neuropil of L4–L5 of area S1 (Figure 7.1 in White, 1989), the local collaterals of CTNs clearly preferred the dendritic shafts of presumed interneurons as their targets. Although these electron-microscopic results suggest the presence of some specific connections in the intracortical circuitry of excitatory neurons, postsynaptic neuron groups are not fully identified except that they belong to spiny projection neurons or to non-spiny interneurons.

In our laboratory, several attempts have been made to find out a technique for breaking this limitation in the identification of postsynaptic neuron groups, and some results were obtained on the local circuit of the rat motor-associated areas. The method was basically composed of the specific retrograde or transgenic labeling approach and conventional intracellular staining technique: on one hand, the information-receiving sites (cell body and dendrites) of a functional group of cortical neurons were visualized by the Golgi stain-like retrograde labeling technique (Kaneko et al., 1996, 2000; Cho et al., 2004b; Tanaka et al., 2011a) or by the transgenic method for the expression of somatodendritic membrane-targeted green fluorescent protein (GFP; Tanaka et al., 2011b; Kameda et al., 2012); and, on the other hand, the local axonal arborization of single neurons was labeled by the sharp electrode intracellular (Kaneko et al., 2000; Cho et al., 2004b; Tanaka et al., 2011b) or whole-cell clamp recording technique (Tanaka et al., 2011a) with thick cortical slices. Subsequently, the local connection of single cortical neurons to the functional neuron group

was investigated morphologically and quantitatively. This technique for detecting "one-to-group" connection is considered to work as a complementary method for the scanning laser photouncaging and optogenetic experiments, where the inputs of a neuron group to one neuron are investigated. In the present review, the previous morphological findings obtained by the "one-to-group" connection analysis are introduced and discussed with a focus on the local excitatory connections of the motor-associated areas. In addition, since the thalamocortical (TC) afferents are the starting point of information processing in motor-associated areas, this review first describes the recent progress in the study of cortical projection of single TC neurons (TCNs) in the motor thalamic nuclei.

THALAMOCORTICAL INPUTS TO THE MOTOR-ASSOCIATED AREAS

The ventral anterior and ventral lateral thalamic nuclear complex (VA–VL) is the motor thalamic nuclei, receiving cerebellar and basal ganglia afferents and sending projections to motor-associated cortical areas. The VA–VL is divided into two portions (**Figures 1A–H**; Kuramoto et al., 2009, 2011): the rostroventrally located inhibitory input-dominant zone (IZ) and caudodorsally situated excitatory subcortical input-dominant zone (EZ). The IZ of the VA–VL contains large axon terminals immunoreactive for GABA-synthesizing enzyme (glutamic acid decarboxylase of 67 kDa, GAD67), whereas the EZ is filled with giant axon terminals with VGluT2 immunoreactivity. These GAD67- and

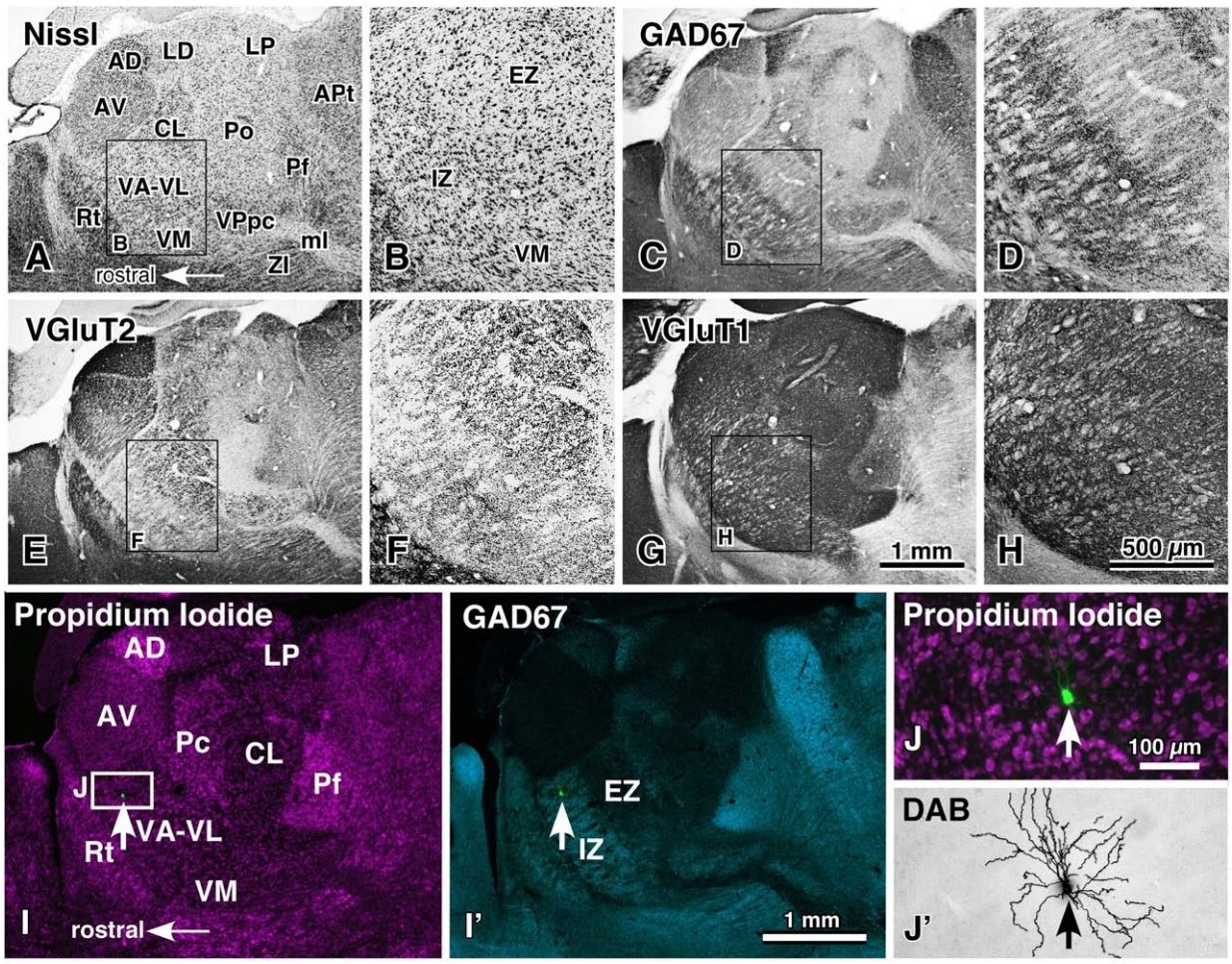

FIGURE 1 | Motor thalamic nuclei and single-neuron labeling with a viral vector expressing membrane-targeted GFP. The motor thalamic complex VA–VL of rats is divided into two portions, IZ and EZ **(A,B)**. The rostroventrally located IZ receives abundant basal ganglia inputs that are large varicosities immunoreactive for GAD67 **(C,D)**, whereas the caudodorsally situated EZ admits cerebellar inputs consisting of many giant VGluT2-immunoreactive terminals **(E,F)**. Thus, the two portions are called inhibitory input-dominant zone (IZ) and excitatory subcortical input-dominant zone (EZ), respectively. In contrast, fine cortically derived VGluT1-immunoreactive axon terminals are distributed rather homogeneously not only in the VA–VL, but also in the entire thalamic nuclei **(G,H)**. When an appropriately diluted solution of viral vectors expressing palGFP is injected into the VA–VL, single neurons are labeled green by chance (arrows in **I,I′,J**), and visualized up to the tip of the dendrites by the immunoperoxidase staining **(J′)**. AD, anterodorsal nucleus; APt, anterior pretectal area; AV, anteroventral nucleus; CL, central lateral nucleus; LD, lateral dorsal nucleus; LP, lateral posterior nucleus; ml, medial lemniscus; Pc, paracentral nucleus; Pf, parafascicular nucleus; Po, posterior nucleus; Rt, thalamic reticular nucleus; VM, ventral medial nucleus; VPpc, parvocellular part of the ventral posterior nucleus. Modified with permission from Figure 1 of Kuramoto et al. (2011) and Figure 2 of Kuramoto et al. (2009). Scale bar in **(H)** applies to **(A–H)**, that in **(I′)** to **(I,I′)**, and that in **(J)** to **(J,J′)**.

VGluT2-immunoreactive terminals have been extensively reduced by a large lesion in the substantia nigra and deep cerebellar nuclei, respectively (Kuramoto et al., 2011). This indicates that the IZ is principally innervated by the basal ganglia inhibitory afferents, whereas the EZ is mainly driven by the cerebellar excitatory afferents.

The whole axonal arborization of single IZ and EZ neurons was further investigated, using a viral vector expressing membrane-targeted GFP (palGFP). By injection of appropriately diluted solution of the viral vector into the VA–VL, single-neuron labeling of IZ or EZ neurons was obtained by chance (**Figures 1I–J′**). Because of the strong expression of palGFP in the infected neuron, the whole axonal arborization of single neurons was visualized up to the end of the axons (**Figures 2A–D**). When the axonal arborization was reconstructed, the following differences between IZ and EZ neurons were noticed (**Figures 2E–K**):

(1) The cortical axons of IZ neurons preferred L1 of motor-associated areas, 54.0 ± 7.3% of intracortical axon boutons being distributed in L1. In contrast, only 5.8 ± 5.1% of intracortical boutons of EZ neurons were found in L1, and mainly distributed in middle layers (MLs; L3–L4).

(2) Almost no EZ neurons sent axon collaterals to the striatum, whereas all IZ neurons projected a considerable amount of collaterals to the striatum.

(3) The cortical axonal arborization of IZ neurons was very wide in areas M1, M2, HL, FL and S1. The arborization of EZ neurons was also widespread, but narrower than that of IZ neurons.

(4) The dendritic arborization of EZ neurons was denser than that of IZ neurons.

These results are partly compatible with the concept of "core" and "matrix" projections of TCNs, proposed mainly in the sensory thalamic neurons by Jones (for review, see Jones, 1998, 2001). In the monkey and cat thalamic nuclei, core-type neurons are immunopositive for parvalbumin and mainly form spatially restrictive projection to cortical MLs with the size of a functional column, whereas the matrix-type neurons are positive for calbindin D28k and send their axons preferentially and widely to L1. In the concept of Jones, it is the most important point that matrix-type neurons are distributed throughout the thalamic nuclei. In addition to the L1-preferring wide arborization of IZ axons, the IZ was filled with calbindin-immunoreactive cell bodies (Kuramoto et al., 2009). Thus, IZ neurons are considered to fulfill the definition of matrix-type neurons. On the other hand, because no thalamic neurons are positive for parvalbumin in rodents, only the spatially restrictive, columnar projection to the middle cortical layers can be used to identify core-type neurons in rodent TCNs. Actually, this columnar projection of TCNs to the MLs has been reported in primary sensory areas of rats (Furuta et al., 2011) as observed in those of monkeys and cats. However, the cortical axons of EZ neurons were widely, though not evenly, distributed in the motor-associated areas (**Figures 3A,B**), although their main target layers were L3d in areas M1 and M2 and L4 in areas FL and HL as those of core-type somatosensory and visual relay neurons (**Figures 3C,D**). Thus, EZ neurons are tentatively named "core-like" neurons here. This difference in axonal arborization between sensory core-type and motor core-like TCNs suggests that motor-associated areas adopt a different information-processing framework from that of sensory areas. In other words, the motor-associated areas might apply "non-columnar," area-wide information processing for motor control. Furthermore, because the axonal arborizations of both EZ and IZ neurons were widely distributed, single pyramidal neurons with developed apical dendrites in the motor-associated areas are likely to receive and integrate two kinds of motor information: one from the basal ganglia to the apical dendrites of pyramidal neurons, and the other from the cerebellum to their basal dendrites.

LOCAL INPUTS TO CORTICOSPINAL NEURONS

In contrast to the previous section on thalamic inputs, output neurons of motor-associated areas are a main subject in this section. The group of CSNs can be retrogradely labeled up to the tip of the dendritic processes by injection of tetramethylrhodamine-dextran amine into the corticospinal tract with an acidic vehicle (**Figure 4A**; Kaneko et al., 1996). With this technique, more than 45% of L5 neurons were efficiently labeled (red stained neurons in **Figures 4B–H**; Kaneko et al., 2000; Cho et al., 2004b), and it was assumed that the vast majority of CSNs were visualized in motor-associated areas (see Discussion in Cho et al., 2004b). In 500-μm-thick cortical slices containing retrogradely labeled L5 CSNs, single pyramidal/spiny neurons that were located in each cortical layer were labeled intracellularly for the "one-to-group" connection analysis. The appositions formed between the local axon collaterals of the intracellularly labeled pyramidal neurons and the dendrites of CSNs were traced as shown in **Figure 5**. In a different set of experiments, about 60–77% of appositions were electron-microscopically confirmed to make axodendritic synaptic contacts of asymmetric type mainly on dendritic spines (**Figures 4I–K′** and **8O–R**; Cho et al., 2004b; Tanaka et al., 2011b), suggesting that the number of appositions could be applied as a quantitative indicator of synaptic connections.

As summarized in **Figure 6A**, L5 CSNs received local inputs from all the cortical layers with some differences in connectional weight (the number of appositions/presynaptic neuron). The pyramidal neurons in the upper half of L2/3 (upper L2/3) sent the least number of appositions to CSNs (neurons 1 and 2 in **Figure 5A**), but those in the lower half of L2/3 (lower L2/3) projected densely to CSNs (neurons 7, 10, and 12). This result is consistent with the previous observation in the cat motor cortex (Kaneko et al., 1994a,b); pyramidal neurons receiving monosynaptic inputs from area 2 were located mainly in lower L2/3, made two axon collateral bushes in L2/3 and L5, and projected densely to L5 pyramidal neurons including Betz cells, whereas pyramidal neurons accepting polysynaptic inputs alone were situated more superficially in L2/3, formed a single collateral bush in L2/3 and sent much fewer axons to L5 pyramidal neurons.

Furthermore, it was an unexpected and interesting result that L3d and L4 star-pyramidal neurons, which had an apical dendrite without tufts, were the most abundant source of inputs to CSNs among the pyramidal neurons examined (**Figures 5B** and **6A**). In L3d of area M1 and L4 of areas HL and FL, about 2/3 of spiny cells were star-pyramidal neurons, and the remaining 1/3 were pyramidal neurons (Cho et al., 2004a). The lack or poverty of apical tufts suggests that these star-pyramidal neurons would not receive

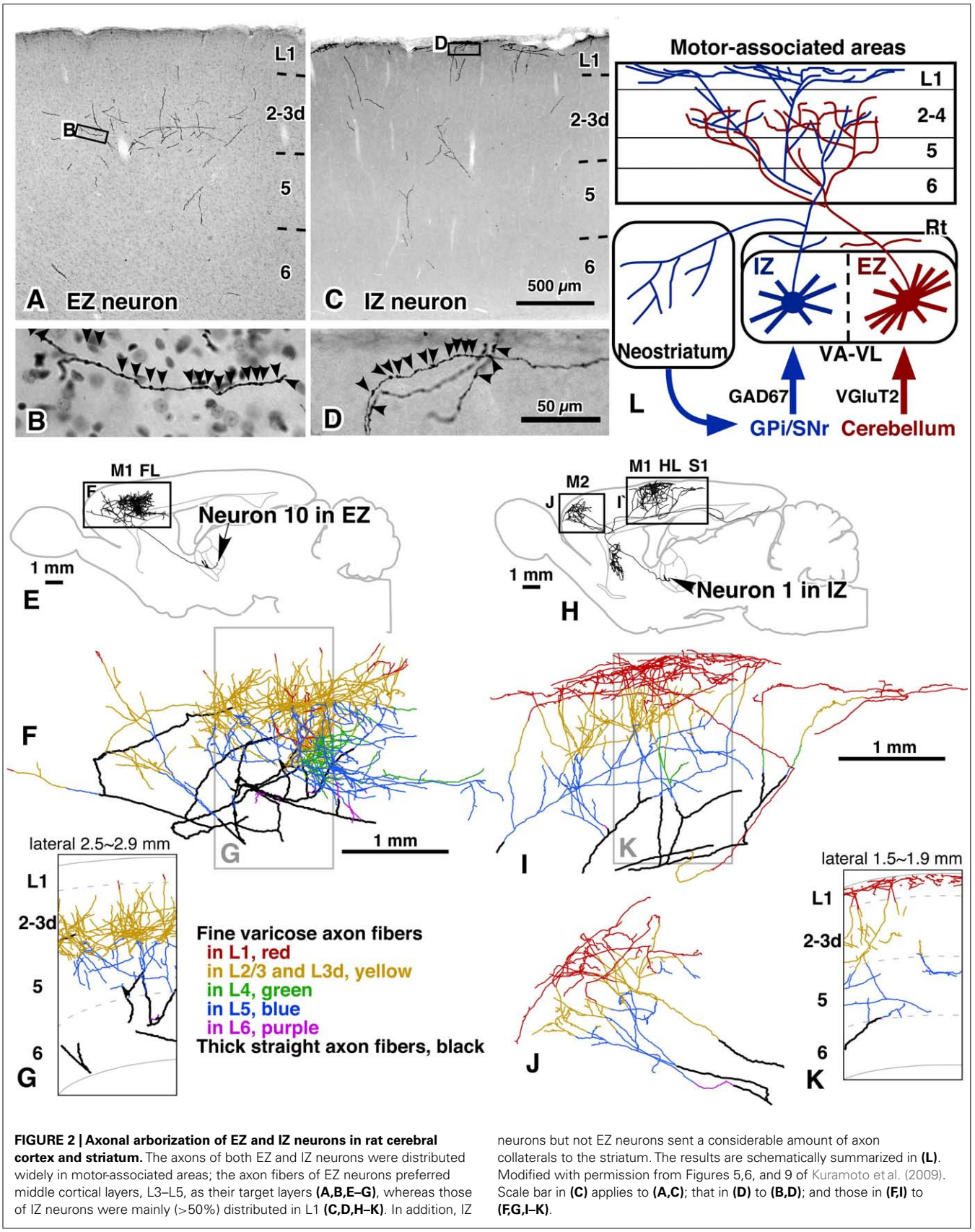

FIGURE 2 | Axonal arborization of EZ and IZ neurons in rat cerebral cortex and striatum. The axons of both EZ and IZ neurons were distributed widely in motor-associated areas; the axon fibers of EZ neurons preferred middle cortical layers, L3–L5, as their target layers **(A,B,E–G)**, whereas those of IZ neurons were mainly (>50%) distributed in L1 **(C,D,H–K)**. In addition, IZ neurons but not EZ neurons sent a considerable amount of axon collaterals to the striatum. The results are schematically summarized in **(L)**. Modified with permission from Figures 5,6, and 9 of Kuramoto et al. (2009). Scale bar in **(C)** applies to **(A,C)**; that in **(D)** to **(B,D)**; and those in **(F,I)** to **(F,G,I–K)**.

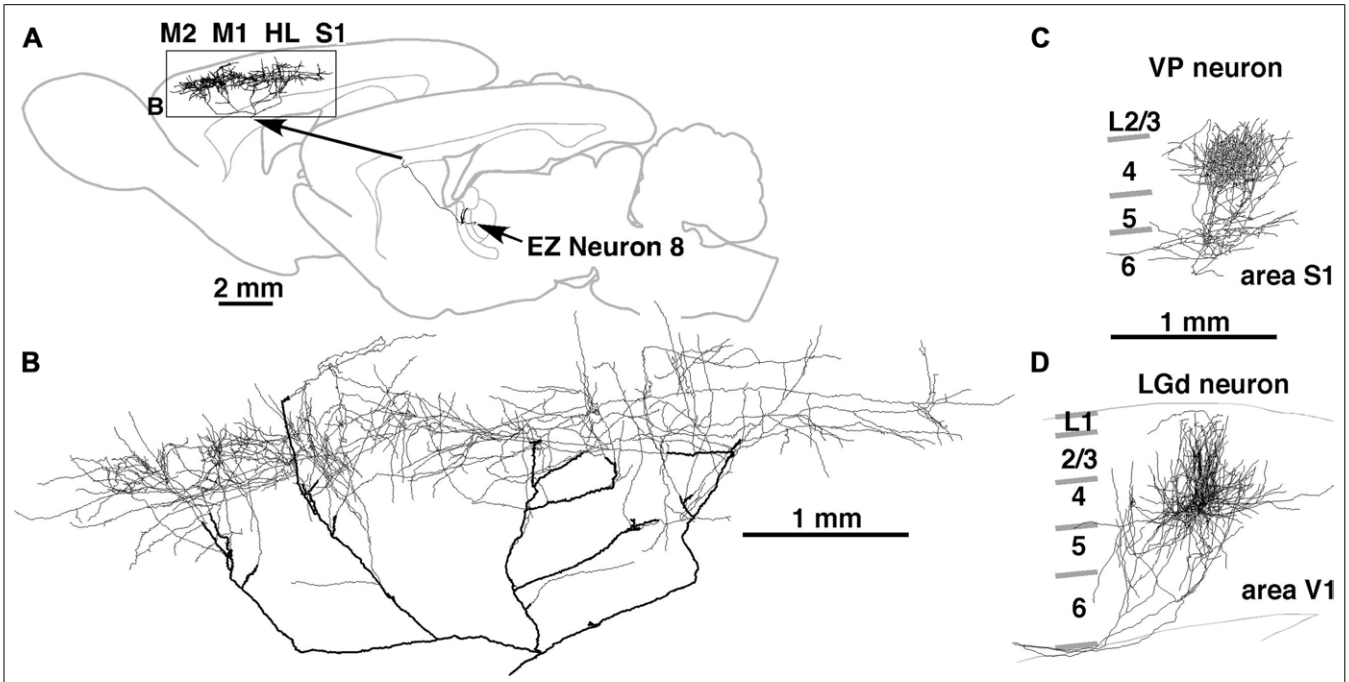

FIGURE 3 | Axonal arborization of an EZ neuron in comparison with that of primary sensory thalamic neurons in rats. The axons of EZ neurons were distributed very widely, often in the cortical area spanning more than 5 mm **(A,B)**. This distribution is in sharp contrast to those of sensory thalamic neurons, such as neurons in the VP and dorsal lateral geniculate nucleus (LGd). The axonal arborization of VP and LGd neurons was concentrated to the middle layers of a cortical region with the size of a single column **(C,D)**. Modified with permission from Figure 8 of Kuramoto et al. (2009) **(A,B)** and Figure 3 of Furuta et al. (2011) **(C)**. The axonal arborization of a single LGd neuron in area V1 **(D)** was labeled and illustrated with the same method as that in Kuramoto et al. (2009) by Nakamura and Kaneko.

the matrix-type IZ afferents that were discussed in the previous section to transmit the basal ganglia information preferentially to L1 (**Figure 6B**). It was further interesting that all these L3d and L4 star-pyramidal neurons showed regular-spiking responses with fast adaptation to current pulse injections (**Figure 5D**; Cho et al., 2004a). The phasic responses of L3d and L4 star-pyramidal neurons suggest that these neurons serve as a kind of high-pass/low-cut filter to the core-like EZ afferents, which mainly convey cerebellar information (**Figure 6B**). In contrast, L2/3 neurons consistently displayed regular-spiking responses with slow adaptation, which resulted in a tonic activity during current pulse injections (**Figure 5B**).

These results suggest the following local circuits in motor-associated areas (**Figure 6B**):

(1) Basal ganglia information directly enters the apical dendrites not only of L2/3 pyramidal neurons but also of L5 CSNs through IZ neurons of the VA–VL. Because L1-preferring TC afferents are associated with the cortical activity prior to the motor execution (for review, see Roland, 2002) and modulate the gain of pyramidal cell response (Larkum et al., 2004), the basal ganglia system may give motor preparatory information to CSNs through its disinhibitory mechanism on IZ neurons.

(2) L2/3 neurons in rodent area M1 further receive information from the other cortical areas such as the somatosensory cortex by corticocortical connection (Akers and Killackey, 1978; Welker et al., 1988; Hoffer et al., 2003) as well as cerebellar information *via* L3d and L4 neurons. Because movement-related potentials such as the readiness potential (Bereitschaftspotential; Kornhuber and Deecke, 1965), which is the cortical activity preceding the movement, are known to occur mainly in L2/3 (for review, see Colebatch, 2007), the tonic firing property of L2/3 pyramidal neurons may be helpful in developing a preparatory activity of CSNs. In addition, the tonic activity of L2/3 pyramidal neurons may be useful in maintaining the activity of CSNs during the motor execution through L2/3-to-L5 excitatory connection.

(3) On the other hand, cerebellar motor command is mainly transferred to L3d and L4 star-pyramidal neurons through EZ neurons of the VA–VL, and sent to L5 CSNs as well as to L2/3 neurons. Since L3d and L4 star-pyramidal neurons show the characteristics of a high-pass filter, timing information within the cerebellar command or "go" signal may be conveyed to CSNs *via* this connection. It is thus presumed that, when CSNs are prepared for a motion by the "ready" signal from the basal ganglia or other cortical areas, CSNs are easily activated in the exact timing by the cerebellar "go" signal and discharge a motor execution signal to the spinal cord (**Figure 6B**).

LOCAL INPUTS TO CORTICOTHALAMIC NEURONS

Corticothalamic neurons in motor-associated areas were mainly located in L6 and sent their axons massively to the VA–VL of the thalamus. In comparison to CSNs, CTNs received much less information from L2/3 pyramidal neurons (Kaneko et al.,

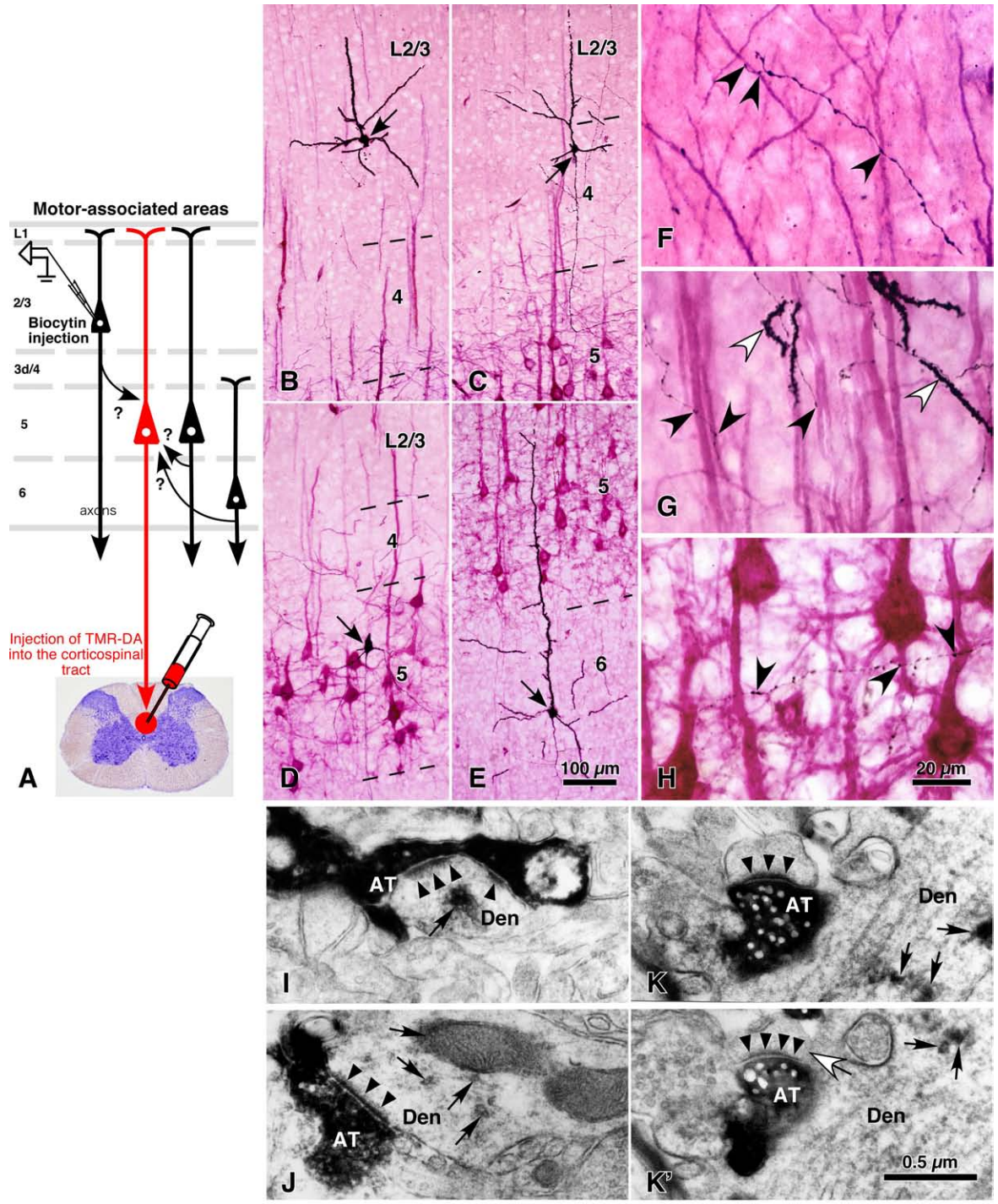

FIGURE 4 | Local excitatory inputs to CSNs in rat cerebral cortex. The dendrites of CSNs in the motor-associated areas were retrogradely labeled in a Golgi stain-like manner by the injection of tetramethylrhodamine-dextran amine (TMR-DA) into the corticospinal tract in the cervical cord with an acidic vehicle (**A**; Kaneko et al., 1996). In 500-μm-thick cortical slices containing labeled CSNs, pyramidal/spiny neurons were recorded and labeled intracellularly at each cortical layer (arrows in **B–E**). The axodendritic appositions between black-labeled axon varicosities and red-visualized dendrites (black arrowheads in **F–H**) were quantitatively analyzed. In some samples, the appositions were confirmed to make synaptic contacts in electron-microscopic images **(I–K′)**, where black arrowheads and arrows indicated the postsynaptic densities and immunoreaction products for TMR-DA, respectively. Figure **(K)** is the image next to **(K′)**, in which a white arrow points to the spine neck connecting the unlabeled spine to the TMR-DA-labeled dendrite. **(B–K′)** Modified with permission from Figures 1 and 8 of Cho et al. (2004b). AT, intracellularly labeled axon terminals; Den, TMR-DA-labeled dendritic profiles. Scale bar in **(E)** applies to **(B–E)**, that in **(H)** to **(F–H)**, and that in **(K′)** to **(I–K′)**.

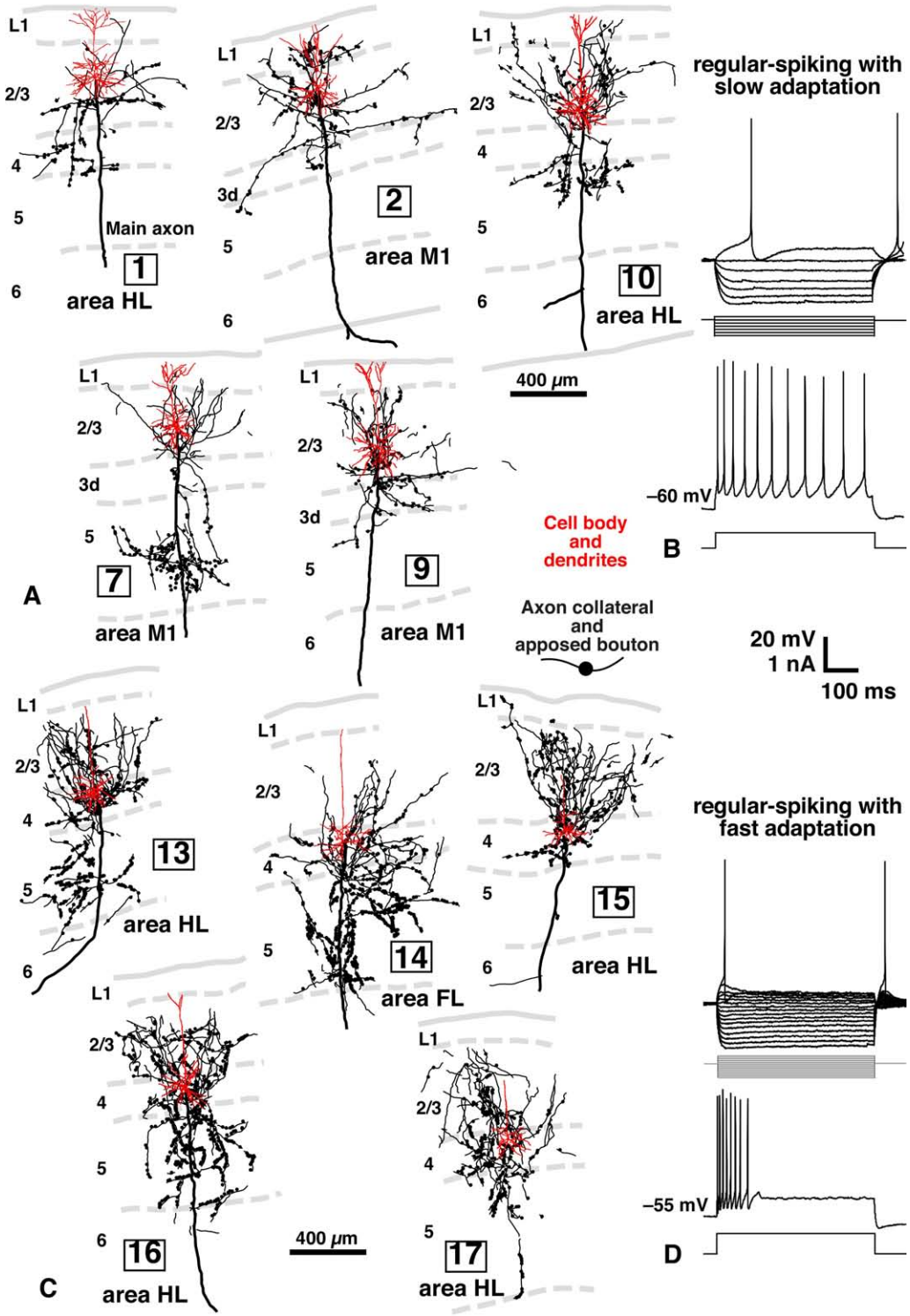

FIGURE 5 | Inputs of L2/3 pyramidal and L3d and L4 spiny neurons to CSNs, and electrical properties of L2/3 and L3d/L4 neurons in rat brain. Many axon boutons of L2/3 pyramidal neurons were in close apposition to the apical or basal dendrites of CTNs **(A)**. However, unexpectedly, the axons of L3d/L4 star-pyramidal neurons formed more appositions with the dendrites of CTNs **(C)** than those of L2/3 pyramidal neurons. The two groups of excitatory neurons were different in electrical properties: L2/3 pyramidal neurons showed regular-spiking responses with slow adaptation **(B)**, whereas L3d/L4 star-pyramidal neurons exhibited regular-spiking ones with fast adaptation **(D)**, when a long depolarizing current pulse was injected. Modified with permission from Figures 2–4 of Cho et al. (2004b) and Figures 4 and 5 of Cho et al. (2004a).

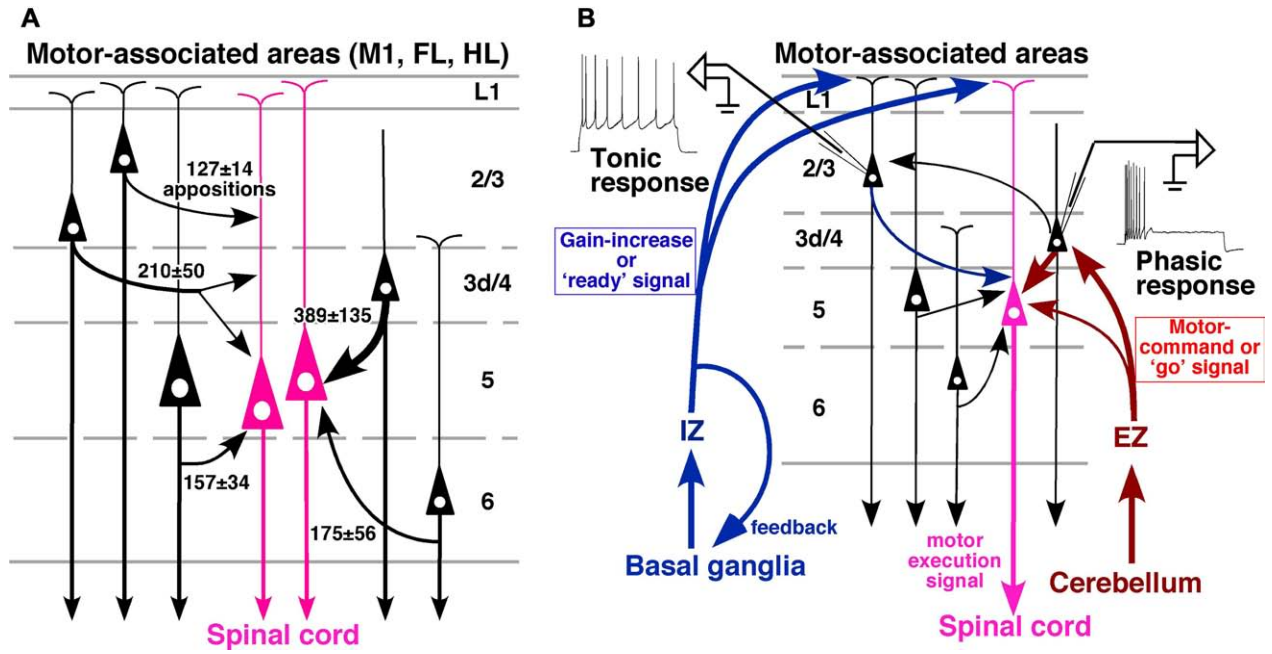

FIGURE 6 | Summary of local excitatory inputs to CSNs and hypothesized circuit for motor control. (A) Although lower L2/3 pyramidal neurons send a considerable number of apposed boutons to CSNs, the strongest inputs are derived from L3d/L4 star-pyramidal neurons. The thickness of a curved arrow indicates the relative intensity of the projection. **(B)** A conceivable cortical circuit for motor control, which is composed of thalamic afferents and local connections to CSNs. Modified with permission from Figure 9 of Cho et al. (2004b) and Figure 9 of Kuramoto et al. (2009).

2000). Actually, single L2/3 pyramidal neurons sent much fewer (∼1/4) axon varicosities to CTNs than to CSNs by the quantitative "one-to-group" connection analysis as described above (**Figures 7A,B**). This was confirmed electrophysiologically (Kaneko et al., 2000); the electrical stimulation in L2/3 of motor-associated areas produced excitatory postsynaptic potentials (EPSPs) with a short and constant latency in L5 pyramidal neurons (**Figures 7C,D**), suggesting a monosynaptic connection from L2/3 excitatory neurons to L5 pyramidal neurons. This result is supported by recent experiments of photo-uncaging stimulation, in which L5b pyramidal neurons or CSNs in the mouse motor area received excitatory monosynaptic inputs from L2/3 neurons (Anderson et al., 2010; Hooks et al., 2011). In contrast, EPSPs observed in L6 pyramidal neurons showed longer latencies, and higher stimulation currents were needed to evoke EPSPs (**Figures 7D,E**). These EPSPs often exhibited double-shock facilitation of onset latencies (**Figure 7C**), and were suppressed by blocking *N*-methyl-D-aspartate receptors (Kaneko et al., 2000), indicating the polysynaptic nature of the EPSPs. These morphological and electrophysiological results suggest that L6 CTNs in motor-associated areas are relatively independent of the information that is processed in L2/3.

Subsequently, a recent morphological analysis on the local excitatory inputs to CTNs is introduced here, although the analysis was performed in sensory areas (area S1, FL, and HL; Tanaka et al., 2011b). For the analysis, an adenoviral vector expressing somatodendritic membrane-targeted GFP (myrGFP-LDLRct; **Figure 8A**) was developed. After injection of a high-titer vector solution into the ventral posterior thalamic nuclei (VP) at a high-salt condition, CTNs were retrogradely infected (**Figures 8B–C**), and all their somatodendritic structures including thin portions and spines of the dendrites were visualized clearly (**Figures 8D–H**). About 60% of L6 neurons in the VP-projecting region of sensory areas were labeled with this technique, and the vast majority of CTNs were considered to be visualized in the region, because the labeling efficiency was saturated even by injection of a higher concentration of the vector (Tanaka et al., 2011b). For the "one-to-group" connection analysis of inputs to CTNs (**Figure 8I**), cortical slices containing many myrGFP-LDLRct-expressing CTNs were used; single pyramidal neurons in each cortical layer and their axon fibers were visualized black, and the dendrites of CTNs were stained brown (**Figures 8J–N**). The axon boutons of black axon fibers were frequently apposed to brown dendritic spines (**Figures 8O,P**), and most of them were revealed to make axospinous synaptic contacts under the electron-microscope (**Figures 8Q,R**).

The results of the local excitatory inputs to CTNs in sensory areas are summarized in **Figure 9**. **Figure 9A** exemplifies the distribution of boutons closely apposed to CTNs along the local axon collaterals of an L4 star-pyramidal neuron and a retrogradely labeled L6 CTN ($L6^+$ neuron; **Figure 8M′**). The local inputs of single excitatory neurons to the CTN group were in the following order (from the most abundant to the least): retrogradely unlabeled, presumably corticocortical L6 neurons ($L6^-$ neurons; **Figure 8N′**), mean ± SD of the number of apposed boutons/presynaptic neuron = 953 ± 500 (25% of total axon boutons); $L6^+$ pyramidal neurons, 612 ± 223 (35%); L5a pyramidal neurons, 529 ± 148 (10%); L5b pyramidal neurons, 374 ± 142 (22%); L4

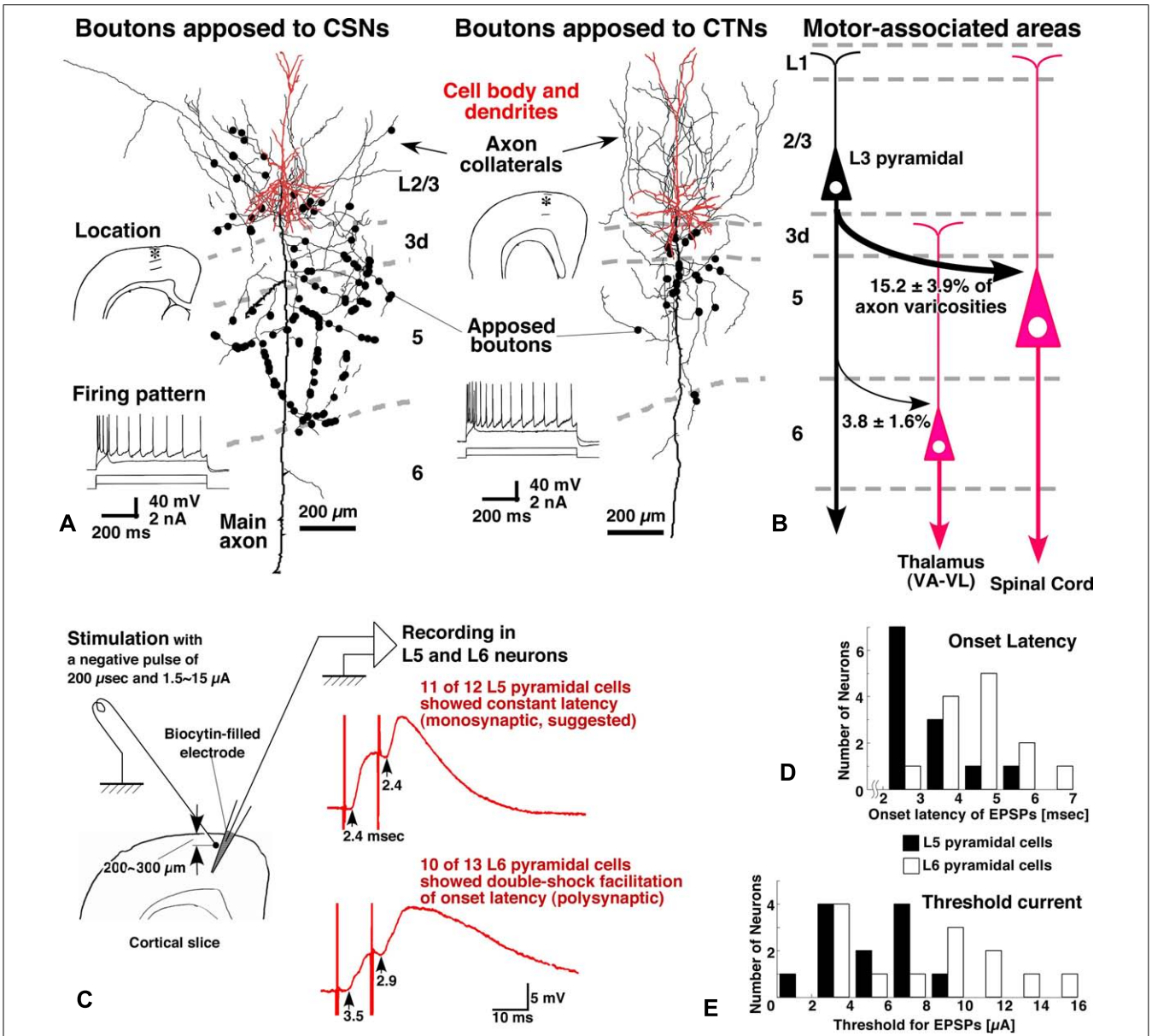

FIGURE 7 | Inputs of L3 pyramidal neurons to CSNs and CTNs in rat motor-associated areas. The morphological experiments were performed in a similar way to that illustrated in **Figure 4A**, except that the injection was made not only into the corticospinal tract but into the VA–VL. L3 pyramidal neurons preferentially sent apposed boutons to CSNs, but much fewer (about 1/4) to CTNs **(A,B)**. When the superficial layers of motor-associated areas were stimulated electrically (left figure in **C**), EPSPs were evoked with shorter latencies and lower thresholds in L5 pyramidal neurons than in L6 pyramidal neurons **(D,E)**. Furthermore, in double-shock stimulation experiments, EPSPs in 11 of 12 L5 pyramidal neurons showed a constant latency, being a sign of monosynaptic inputs, whereas those in L6 pyramidal neurons displayed double-shock facilitation of onset latencies, indicating that the connection was polysynaptic **(C)**. These morphological and electrophysiological findings suggest that L6 pyramidal neurons do not receive strong monosynaptic inputs from L3 pyramidal neurons. **(A,C–E)** Modified with permission from Figures 4, 6, and 7 of Kaneko et al. (2000).

spiny neurons, 327 ± 164 (6%); and L2/3 pyramidal neurons, 167 ± 115 (3%). The L2/3-to-CTN connection was thus weakest of the local excitatory connections to CTNs, being consistent with the previous results in motor-associated areas (Kaneko et al., 2000). Therefore, L5 pyramidal neurons and L4 spiny neurons, including spiny stellate, star-pyramidal and pyramidal neurons, were important sources of translaminar excitatory inputs to CTNs in terms of the number of apposed boutons/presynaptic neuron, although the local connection within L6 was most abundant. It is noticeable that single L6$^+$ CTNs sent 35% of axon boutons to the CTN group, because this result appears contradictory to the previous finding that the local axon collaterals of CTNs principally targeted interneurons in mouse area S1 (White and Keller, 1987). This inconsistency is unlikely to be due to a species difference, as recent paired recording studies showed that CTN-to-L6 pyramid connectivity rate (1/75) was much lower than CTN-to-L6

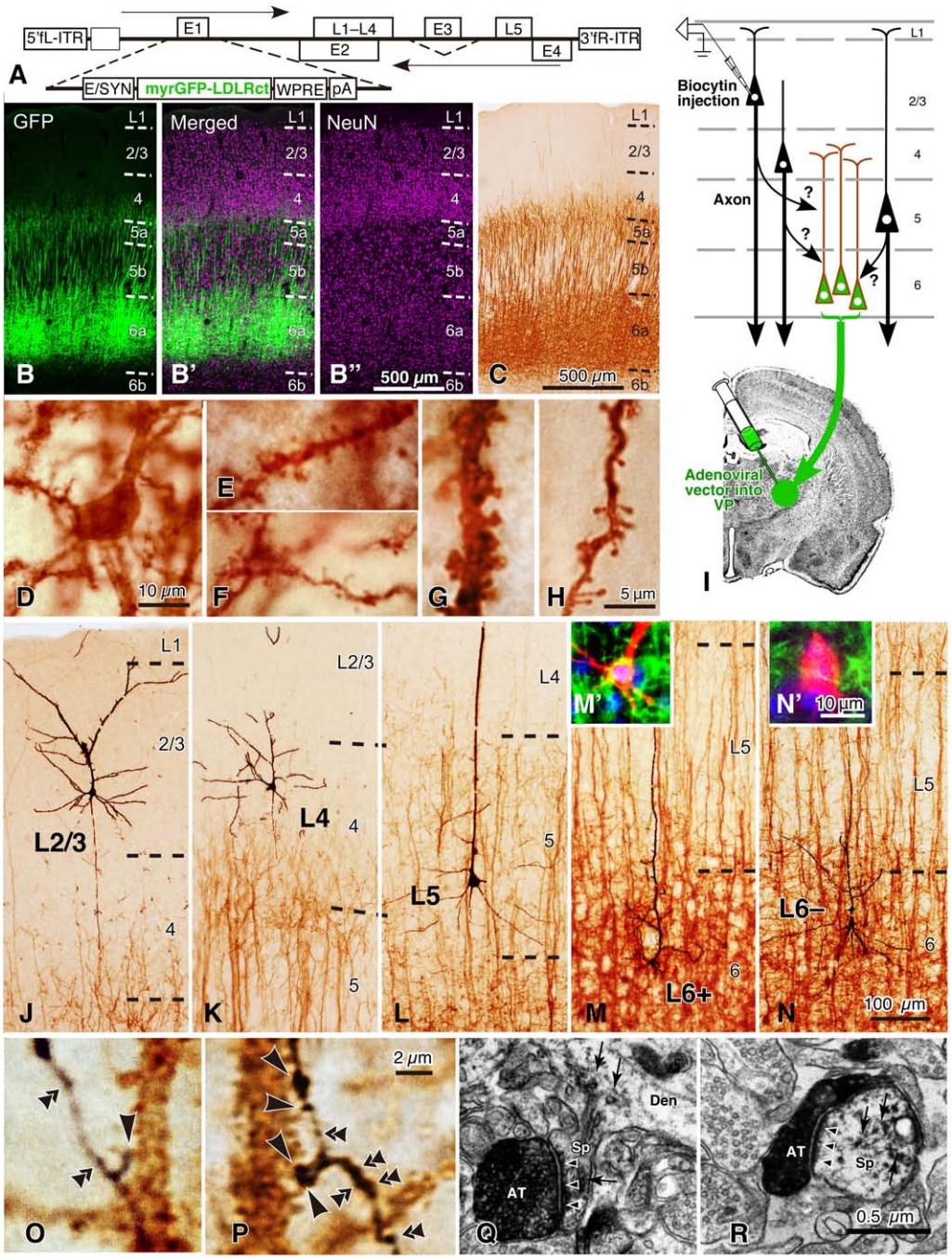

FIGURE 8 | Golgi stain-like labeling of CTNs with a viral vector and intracellular staining of pyramidal neurons in rat areas S1, FL, and HL. When high titers of adenoviral vectors expressing myrGFP-LDLRct (**A**; Kameda et al., 2008) were injected into the VP with 0.6 M NaCl, many L6 pyramidal neurons were retrogradely infected in the somatosensory motor area **(B–B″)**. After the brown immunoperoxidase staining with anti-GFP antibody and diaminobenzidine (DAB; **C**), the cell body **(D)**, basal dendrites **(E,F)**, and apical dendrites **(G,H)** of CTNs were fully visualized. Note that even fine spines were visualized effectively. In 500-μm-thick cortical slices, single spiny neurons were labeled intracellularly **(I)** and visualized black **(J–N)** by the peroxidase method with DAB and nickel. In L6, retrogradely labeled **(M′)** and unlabeled neurons **(N′)** were indicated by $L6^+$ and $L6^-$ pyramidal neurons, respectively. Most $L6^-$ neurons were considered to belong to corticocortical projection neurons, because their apical dendrites were short and the basal dendrites were abundant as reported previously (Zhang and Deschênes, 1997). In contrast, $L6^+$ CTNs were taller and more slender than $L6^-$ neurons. **(O,P)** It was examined whether each axon bouton of the intracortical collaterals was in close apposition to the retrogradely labeled CTN dendritic spines (large arrowheads) or not (double arrowheads). **(Q,R)** In addition, 77% of those appositions were electron-microscopically confirmed to form asymmetric synaptic contacts with the labeled spines (small arrowheads). The reaction products of retrograde labeling are indicated by small arrows. AT, labeled axon terminals; Den, dendritic profile; Sp, spine. Modified from Figures 1, 2, and 4 of Tanaka et al. (2011b). Scale bar in **(B″)** applies to **(B–B″)**, that in **(H)** to **(E–H)**, that in **(N)** to **(J–N)**, that in **(N′)** to **(M′,N′)**, that in **(P)** to **(O,P)**, and that in **(R)** to **(Q,R)**.

interneuron connectivity rate (1/4) in rat area S1 and area V1 (Mercer et al., 2005; West et al., 2006). On the other hand, recent scanning laser photostimulation studies revealed that L6 CTNs or presumed CTNs preferentially received excitatory inputs from surrounding L6 neurons in rat area V1 (Zarrinpar and Callaway, 2006) and in mouse primary auditory area (Llano and Sherman, 2009), partly supporting the results of Tanaka et al. (2011b). Regardless, the postsynaptic components of L6 CTN axon collaterals should be investigated further.

In **Figure 9B**, it is noticed that, when the horizontal spread of these local connections was examined, L4 and $L6^+$ neurons formed appositions with the CTN group in a narrower range than L2/3, L5, or $L6^-$ pyramidal neurons (Tanaka et al., 2011b), suggesting that the spatial organization is of crucial importance to the understanding of local inputs to CTNs. In addition, to compare these spatial data with the maps observed in previous scanning laser photostimulation studies on excitatory inputs to L6 pyramidal neurons (Zarrinpar and Callaway, 2006; Llano and Sherman, 2009; Hooks et al., 2011), we tried to constitute an input map to a CTN, actually CTN dendrites in a unit volume, using the spatial information of the experimental data. When the inputs to CTNs are reconstructed from the viewpoint of a CTN, the following assumptions are made: (1) the density of CTN dendrites is constant in the horizontal direction at a given cortical depth (y), (2) the distribution of cell bodies of various pyramidal/spiny neurons is also horizontally constant at given depth y, and (3) as a group, pyramidal/spiny neurons at given depth y deliver their apposed boutons to CTNs isotropically but as a function of horizontal distance x. From the original data of the experiments (**Figure 9B**), one can obtain an input intensity map $i(x, y)$, which is the density of boutons derived from presynaptic neurons within a cube located at horizontal distance x and normalized cortical depth y and closely apposed to the postsynaptic CTN dendrites within the green square prism (**Figures 9C,D**; for detail, see the legend of **Figure 9**). As a result, the two-dimensional map $i(x, y)$ in **Figure 9E** reveals that the highest $i(x, y)$ is located at L4 and the second highest is found at L6a. Thus, L4 and L6 pyramidal/spiny neurons are important local sources of inputs to CTNs, and at least a portion of L4 neurons have a strong impact on the CTNs that are located in a narrow region ($\leq$40 μm) underneath these L4 neurons. This result is relatively compatible with the results of scanning laser photostimulation studies; presumed CTNs in L6 or L6 pyramidal neurons received significant, if not strong, excitatory inputs from L4 in rat area V1 (Zarrinpar and Callaway, 2006) or in mouse area S1 (Hooks et al., 2011), respectively, although paired whole-cell recording experiments did not detect a high connectivity rate of L4-to-L6 connection (Lefort et al., 2009). Finally, this strong L4-to-CTN connection appears to be formed by the descending axon collaterals of L4 spiny neurons (**Figure 9A**, left).

LOCAL CIRCUITS IN MOTOR-ASSOCIATED AREAS AND DISCUSSION

A scheme shown in **Figure 10A** summarizes the main local excitatory connections in the cerebral cortex including motor-associated areas. When minor neuronal populations, such as L6 corticocortical neurons, and weak connections are omitted, the excitatory connections may be described in the following way:

(1) The cortex receives two kinds of TC afferents. The core-type or core-like TC projection mainly targets L3d and L4 spiny neurons and partially L6 pyramidal neurons. The latter may directly receive the TC projection because the apical dendritic tufts of CTNs are densely distributed in L4–L5a (**Figure 8C**) and partly because the core-type projection sends some axon collaterals to L6 (**Figure 3C**). In contrast, the matrix-type projection targets the apical dendritic tufts of L2/3 and L5 pyramidal neurons as discussed in Section "Thalamocortical Inputs to the Motor-associated Areas."

(2) L2/3 pyramidal neurons may receive dense inputs from L3d and L4 neurons, which send dense axonal arborization to L2/3 as shown in motor-associated areas (**Figure 5C**) as well as in sensory areas (Figure 3 of Tanaka et al., 2011b). The presence of this dense connection is supported in rat neocortex by the paired electrical recording experiments revealing a relatively high connectivity rate in the L4-to-L2/3 connection (Thomson et al., 2002; Bannister and Thomson, 2007). In addition, the dense L4-to-L2/3 connection is constantly shown by scanning laser photostimulation studies in rodent sensory areas (Shepherd and Svoboda, 2005; Shepherd et al., 2005; Hooks et al., 2011). A similar dense connection to L2/3 of the motor areas is originated from the border region between L3 and L5, which might contain L3d (Wood et al., 2009; Wood and Shepherd, 2010). After the local information processing, L2/3 pyramidal neurons are well known to project to other cortical areas (for review, see Jones, 1984).

(3) L5 pyramidal neurons including CSNs receive massive inputs from L3d and L4 spiny neurons and less massive inputs from L2/3 neurons (**Figure 6A**), and send axons to subcortical regions including the spinal cord. The latter L2/3-to-L5 connection is supported in motor areas by scanning laser photostimulation studies (Weiler et al., 2008; Anderson et al., 2010; Hooks et al., 2011) and paired electrical recording experiments (Thomson and Bannister, 1998; Thomson et al., 2002).

(4) Corticothalamic neurons collect dense inputs from L4 spiny neurons, but rarely receive input connections from L2/3 or L5 (**Figure 9E**). The key point of this local connection scheme (**Figure 10A**) is the relative independence of CTNs from the information processing performed by L2/3 and L5 neurons, which are indicated with blue color in the scheme. This observation is supported by the laser scanning photostimulation studies revealing that L6 neurons receive very few, if any, inputs from L2/3 and L5 not only in area S1 (Zarrinpar and Callaway, 2006; Llano and Sherman, 2009; Hooks et al., 2011) but also in area M1 (Hooks et al., 2011).

Although the scheme in **Figure 10A** is commonly applicable to many cortical areas, a large difference in TC afferents between sensory and motor areas has to be emphasized here. The core-type afferents to the primary sensory areas basically show columnar organization as well as laminar arrangement (**Figures 3C,D**), and the afferent information is processed within a functional column at least in its initial step. However, in the case of motor thalamic neurons (**Figures 2** and **3**), the information of a TCN is delivered to area-wide cortical regions. This area-wide distribution of core-like motor thalamic afferents may be relevant to the fact that the motor information is already processed in the cerebellar cortex, although the relationship of cerebellar information processing to

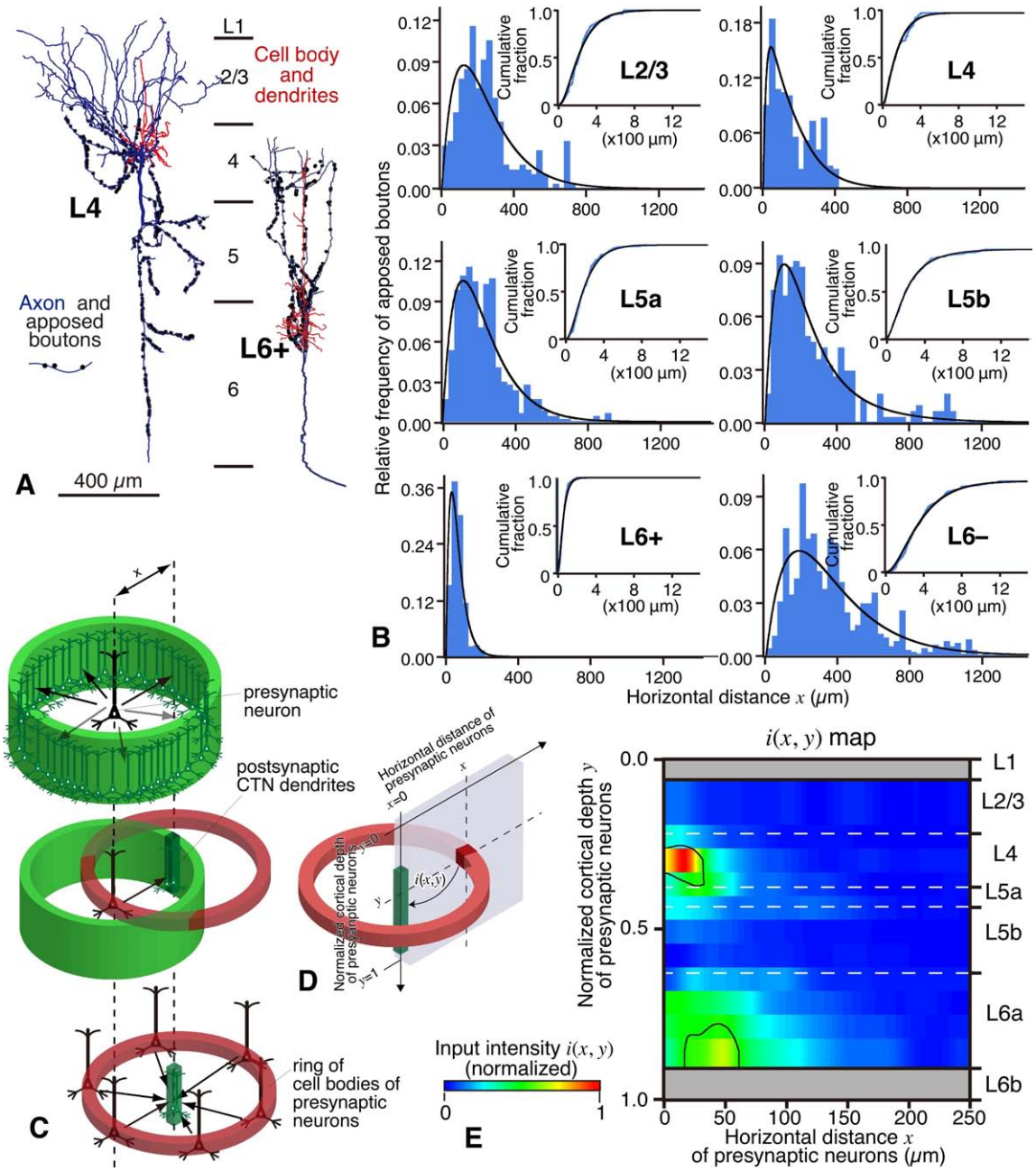

FIGURE 9 | Local excitatory inputs to VP-projecting CTNs in rat areas S1, HL, and FL. (A) Single L4 star-pyramidal and $L6^{+}$ pyramidal neurons sent many apposed boutons to CTNs. **(B)** The horizontal distribution (fitted with a gamma distribution) of the apposed boutons of representative neurons were different from layer to layer. L4 spiny and $L6^{+}$ pyramidal neurons sent apposed boutons to CTN dendrites that were located in a narrow range, whereas L5 and $L6^{-}$ neurons projected them to CTN dendrites that spread horizontally. **(C,D)** From the original data in **(B)**, the number of apposed boutons arising from an average presynaptic neuron as a function of horizontal distance x is obtained (**C**, top) under the assumption that cortical excitatory neurons sending axons to CTN dendrites are distributed homogeneously in horizontal directions at a given depth (y). When the presynaptic neuron sends a certain amount of apposed boutons to postsynaptic CTN dendrites in a given unit volume (slender dense green square prism in **C**, middle), the CTN dendrites are expected to receive the same amount of projections from each neuron located in all directions at the same distance from them (**C**, bottom). Therefore, as shown in **(D)**, a section can be cut out to make a two-dimensional input map; in other words, one can obtain input intensity map $i(x, y)$, which is the density of axon boutons derived from presynaptic neurons within a red cube located at horizontal distance x and normalized cortical depth y and closely apposed to the postsynaptic CTN dendrites within the green square prism. In this estimate, the number of neurons in the cube located at (x, y) is calculated from the density of presynaptic VGluT1 mRNA-expressing neurons at depth y. **(E)** Input intensity map $i(x, y)$. From the viewpoint of CTN dendrites in a unit prism, L4 spiny neurons are the most abundant source of local excitatory inputs. The regions encircled by black borders in **(E)** show significantly high $i(x, y)$ (> mean + 2SD). For more detail, see Tanaka et al. (2011b). Modified with permission from Figures 5–8 of Tanaka et al. (2011b).

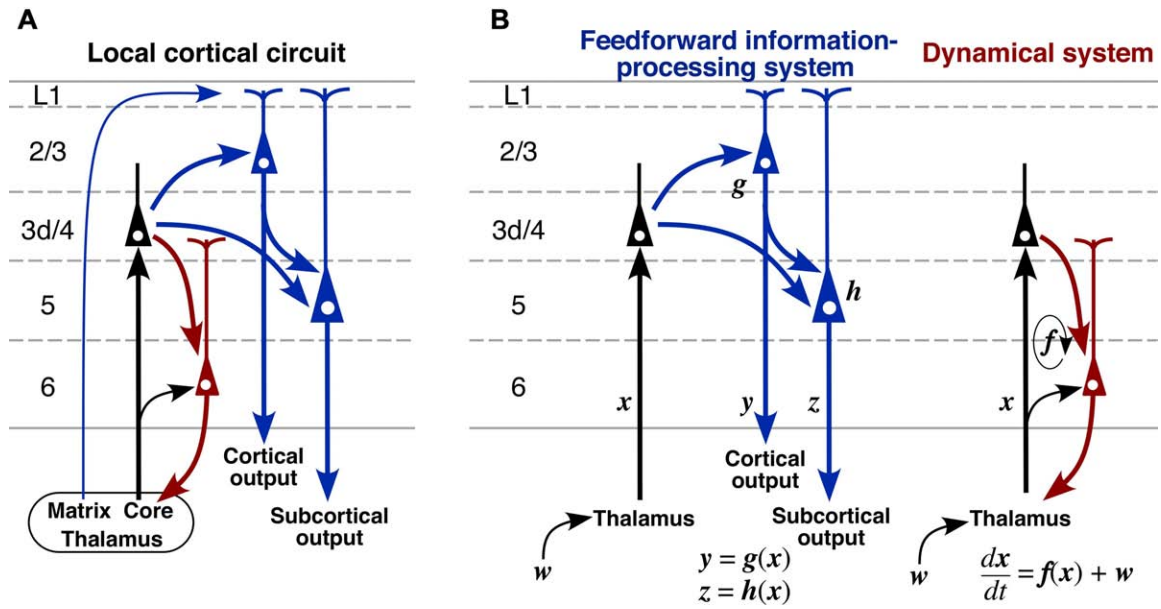

FIGURE 10 | A proposed model of cortical excitatory circuitry. (A) L3d and L4 spiny neurons receive abundant core-type or core-like thalamic inputs, whereas L2/3 and L5 pyramidal neurons accept matrix-type inputs on their apical tufts. L2/3 pyramidal and L3d/L4 spiny neurons send axons to L5 pyramidal neurons, and L2/3 and L5 pyramidal neurons project to other cortical areas and subcortical regions, respectively (blue circuit). In contrast, L6 CTNs receive thalamic inputs directly and indirectly *via* L3d/L4 neurons, and then send their activity back to the thalamic neurons (red circuit). **(B)** It is likely that these two circuits are embedded in the cortical microcircuit with relative independence. The blue circuit may behave like a feedforward information-processing system, whereas the red one may serve as a dynamical system because of its recurrent nature. ***w***, subcortical or cortical "driver" afferent vector; ***x***, state vector of thalamic neurons; ***y***, output vector of L2/3 pyramidal neurons; ***z***, output vector of L5 pyramidal neurons.

cerebral cortical processing is not yet fully understood. In addition, even in the sensory thalamic nuclei such as the posterior nucleus, the core-type cortical afferents of single TCNs show a wide distribution far exceeding the columnar size even in area S1, although the distribution is narrower than that of motor thalamic neurons (Ohno et al., 2012). These findings suggest that the dual, columnar and laminar, organization of TC afferents is limited to the primary sensory thalamic nuclei, but that the majority of TCNs use the laminar organization alone.

The summarized scheme in **Figure 10A** allows the following hypothesis on the local cortical circuitry to be proposed. The blue circuit is likely to serve as a feedforward information-processing system (**Figure 10B**, left). This is strongly supported by well known facts that L4 of area V1 almost exclusively contains simple cells, and contrastingly that L2/3 and L5 mainly comprise complex cells representing information of higher order (Hubel and Wiesel, 1962; Gilbert, 1977). The processed information is further sent to subcortical and/or other cortical regions *via* L2/3 and L5 neurons. Recently, L5 of the rodent motor/frontal cortex has been reported to contain at least two kinds of pyramidal neuron groups: subcerebral projection neurons, including CSNs and corticopontine neurons, and crossed corticostriatal neurons. The two neuron groups differ not only in major projection targets but also in local connections (Morishima et al., 2011; Kiritani et al., 2012). Moreover, L2/3 pyramidal neurons in motor-associated areas should be classified into two types as illustrated in **Figure 6A** (Kaneko et al., 1994b; Cho et al., 2004b); pyramidal neurons forming two axon collateral bushes in L2/3 and L5 are more frequently encountered in lower L2/3 than in upper L2/3, whereas those making only one bush in L2/3 are more numerous in upper L2/3 than in lower L2/3. These findings suggest that the information processing is more complicated than that illustrated with the blue circuit. However, the findings are not contradictory to the concept that the blue circuit is a feedforward information-processing system.

In contrast to the blue circuit in **Figure 10**, the red circuit sends the input information back to the input source site, i.e., the thalamic nuclei, with relative independence from the blue one (**Figure 10B**, right). The corticothalamic projection has generally been considered to work as a feedback circuit, because the thalamic nuclei are the sole input gate for corticopetal information flows, including sensory and motor/cerebellar flows (for review, cf. Alitto and Usrey, 2003), and the best site for feedback control. If CTNs work as a true "feedback" circuit like the circuit of a feedback control system in engineering, the output information of the system, i.e., the information presented by L2/3 and/or L5 pyramidal neurons, should be conveyed back to the input gate *via* CTNs. CTNs, however, receive only weak inputs from L2/3 or L5 neurons (**Figure 10A**). This finding is partly supported in area V1 by the *in vivo* electrophysiological observation that many L6 neurons show simple cell responses (Hubel and Wiesel, 1962; Gilbert, 1977; Martinez et al., 2005), indicating that L6 neurons do not effectively use the information expressed by L2/3 or L5 complex cells. It hence appears necessary to consider other functions for CTNs than the feedback control.

It has long been hypothesized that L6 CTNs, together with TCNs, constitute a recurrent circuit, because of well known phenomena suggesting TC reverberating activity, such as augmenting responses and repetitive discharges in sensory areas (Morison and Dempsey, 1943; Chang, 1950). Augmenting responses are also observed between the VA–VL and area M1 in the rat brain (Castro-Alamancos and Connors, 1996a,b). In addition, TCNs have been proposed to, with the help of thalamic reticular nucleus (Rt) neurons, serve as an oscillation generator in the corticothalamic loop (Buzsáki, 1991; Steriade et al., 1993). On the other hand, although the effect of CTN excitation on TCNs has long been elusive for lack of a CTN-selective stimulation method, recent progress in optogenetic techniques makes it feasible to stimulate CTN axons specifically, and the selective stimulation of CTNs has been shown to evoke clear EPSCs in TCNs and Rt neurons monosynaptically (Cruikshank et al., 2010). Since "modulator" afferents to thalamic relay neurons, the major population of which is L6 CTNs, are known to be far more numerous than subcortical and cortical "driver" afferents to relay neurons (for review, see Sherman and Guillery, 2006), the effect of L6 CTNs on TCNs is considered to be large as an assembly even if unitary EPSCs evoked by single CTN activation are small. Taken together, it is likely that the red circuit in **Figure 10B**, together with the black TC projection, constitutes a dynamical system, where the present state $\boldsymbol{x}(t)$ of TCNs has a large effect on the next state $\boldsymbol{x}(t + dt)$ through CTNs and Rt neurons, and thereby works as a mechanism producing autonomous, self-sustaining activity of the corticothalamic loop. Thus, it is plausible that the two blue and red circuits in **Figure 10** are embedded in the local circuit of the cerebral cortex as the parts of feedforward information-processing and autonomous dynamical systems, respectively.

REFERENCES

Akers, R. M., and Killackey, H. P. (1978). Organization of corticocortical connections in the parietal cortex of the rat. *J. Comp. Neurol.* 181, 513–537.

Alitto, H. J., and Usrey, W. M. (2003). Corticothalamic feedback and sensory processing. *Curr. Opin. Neurobiol.* 13, 440–445.

Anderson, C. T., Sheets, P. L., Kiritani, T., and Shepherd, G. M. (2010). Sublayer-specific microcircuits of corticospinal and corticostriatal neurons in motor cortex. *Nat. Neurosci.* 13, 739–744.

Ayling, O. G., Harrison, T. C., Boyd, J. D., Goroshkov, A., and Murphy, T. H. (2009). Automated light-based mapping of motor cortex by photoactivation of channelrhodopsin-2 transgenic mice. *Nat. Methods* 6, 219–224.

Bannister, A. P., and Thomson, A. M. (2007). Dynamic properties of excitatory synaptic connections involving layer 4 pyramidal cells in adult rat and cat neocortex. *Cereb. Cortex* 17, 2190–2203.

Buhl, E. H., Tamás, G., Szilágyi, T., Stricker, C., Paulsen, O., and Somogyi, P. (1997). Effect, number and location of synapses made by single pyramidal cells onto aspiny interneurones of cat visual cortex. *J. Physiol.* 500, 689–713.

Buzsáki, G. (1991). The thalamic clock: emergent network properties. *Neuroscience* 41, 351–364.

Castro-Alamancos, M. A., and Connors, B. W. (1996a). Spatiotemporal properties of short-term plasticity sensorimotor thalamocortical pathways of the rat. *J. Neurosci.* 16, 2767–2779.

Castro-Alamancos, M. A., and Connors, B. W. (1996b). Cellular mechanisms of the augmenting response: short-term plasticity in a thalamocortical pathway. *J. Neurosci.* 16, 7742–7756.

Chagnac-Amitai, Y., and Connors, B. W. (1989). Synchronized excitation and inhibition driven by intrinsically bursting neurons in neocortex. *J. Neurophysiol.* 62, 1149–6112.

Chang, H.-T. (1950). The repetitive discharges of corticothalamic reverberating circuit. *J. Neurophysiol.* 13, 235–257.

Cho, R.-H., Segawa, S., Mizuno, A., and Kaneko, T. (2004a). Intracellularly labeled pyramidal neurons in the cortical areas projecting to the spinal cord. I. Electrophysiological properties of pyramidal neurons. *Neurosci. Res.* 50, 381–394.

Cho, R.-H., Segawa, S., Okamoto, K., Mizuno, A., and Kaneko, T. (2004b). Intracellularly labeled pyramidal neurons in the cortical areas projecting to the spinal cord. II. Intra- and juxta-columnar projection of pyramidal neurons to corticospinal neurons. *Neurosci. Res.* 50, 395–410.

Colebatch, J. G. (2007). Bereitschaftspotential and movement-related potentials: origin, significance, and application in disorders of human movement. *Mov. Disord.* 22, 601–610.

Connors, B. W., Gutnick, M. J., and Prince, D. A. (1982). Electrophysiological properties of neocortical neurons in vitro. *J. Neurophysiol.* 48, 1302–1320.

Cruikshank, S. J., Urabe, H., Nurmikko, A. V., and Connors, B. W. (2010). Pathway-specific feedforward circuits between thalamus and neocortex revealed by selective optical stimulation of axons. *Neuron* 65, 230–245.

Dalva, M. B., and Katz, L. C. (1994). Rearrangements of synaptic connections in visual cortex revealed by laser photostimulation. *Science* 265, 255–258.

Deuchars, J., West, D. C., and Thomson, A. M. (1994). Relationships between morphology and physiology of pyramid–pyramid single axon connections in rat neocortex in vitro. *J. Physiol.* 478, 423–435.

Donoghue, J. P., Kerman, K. L., and Ebner, F. F. (1979). Evidence for two organizational plans within the somatic sensory-motor cortex of the rat. *J. Comp. Neurol.* 183, 647–664.

Donoghue, J. P., and Wise, S. P. (1982). The motor cortex of the rat: cytoarchitecture and microstimulation mapping. *J. Comp. Neurol.* 212, 76–88.

Fujiyama, F., Furuta, T., and Kaneko, T. (2001). Immunocytochemical localization of candidates for vesicular glutamate transporters in the rat cerebral cortex. *J. Comp. Neurol.* 435, 379–387.

Furuta, T., Deschênes, M., and Kaneko, T. (2011). Anisotropic distribution of thalamocortical boutons in barrels. *J. Neurosci.* 31, 6432–6439.

Galarreta, M., and Hestrin, S. (1999). A network of fast-spiking cells in the neocortex connected by electrical synapses. *Nature* 402, 72–75.

Gilbert, C. D. (1977). Laminar differences in receptive field properties of cells in cat primary visual cortex. *J. Physiol.* 268, 391–421.

Hall, R. D., and Lindholm, E. P. (1974). Organization of motor and somatosensory neocortex in the albino rat. *Brain. Res.* 6, 23–38.

Hoffer, Z. S., Hoover, J. E., and Alloway, K. D. (2003). Sensorimotor corticocortical projections from rat barrel cortex have an anisotropic organization that facilitates integration of inputs from whiskers in the same row. *J. Comp. Neurol.* 466, 525–544.

Hooks, B. M., Hires, S. A., Zhang, Y. X., Huber, D., Petreanu, L., Svoboda, K., et al. (2011). Laminar analysis of excitatory local circuits in vibrissal motor and sensory cortical areas. *PLoS Biol.* 9:e1000572. doi: 10.1371/journal.pbio.1000572

Hubel, D. H., and Wiesel, T. N. (1962). Receptive fields, binocular interaction and functional architecture in the cat's visual cortex. *J. Physiol.* 160, 106–154.

Hwa, G. G., and Avoli, M. (1992). Excitatory postsynaptic potentials recorded from regular-spiking cells in layers II/III of rat sensorimotor cortex. *J. Neurophysiol.* 67, 728–737.

Jones, E. G. (1984). "Laminar distribution of cortical efferent cells," in *Cerebral Cortex*, Vol. 1, *Cellular Components of the Cerebral Cortex*, eds. A. Peters and E. G. Jones (New York, NY: Plenum Press), 521–553.

Jones, E. G. (1998). Viewpoint: the core and matrix of thalamic organization. *Neuroscience* 85, 331–345.

Jones, E. G. (2001). The thalamic matrix and thalamocortical synchrony. *Trends Neurosci.* 24, 595–601.

Kameda, H., Furuta, T., Matsuda, W., Ohira, K., Nakamura, K., Hioki, H., et al. (2008). Targeting green fluorescent protein to dendritic membrane in central neurons. *Neurosci. Res.* 61, 79–91.

Kameda, H., Hioki, H., Tanaka, Y. H., Tanaka, T., Sohn, J., Sonomura, T., et al. (2012). Parvalbumin-producing cortical interneurons receive inhibitory inputs on proximal portions and cortical excitatory inputs on distal dendrites. *Eur. J. Neurosci.* 35, 834–854.

Kaneko, T., Caria, M. A., and Asanuma, H. (1994a). Information processing within the motor cortex. I. Responses of morphologically identified motor cortical cells to stimulation of the somatosensory cortex. *J. Comp. Neurol.* 345, 161–171.

Kaneko, T., Caria, M. A., and Asanuma, H. (1994b). Information processing within the motor cortex. II. Intracortical connections between neurons receiving somatosensory cortical input and motor output neurons of the cortex. *J. Comp. Neurol.* 345, 172–184.

Kaneko, T., Cho, R., Li, Y., Nomura, S., and Mizuno, N. (2000). Predominant information transfer from layer III pyramidal neurons to corticospinal neurons. *J. Comp. Neurol.* 423, 52–65.

Kaneko, T., Saeki, K., Lee, T., and Mizuno, N. (1996). Improved retrograde axonal transport and subsequent visualization of tetramethylrhodamine (TMR)-dextran amine by means of an acidic injection vehicle and antibodies against TMR. *J. Neurosci. Methods.* 65, 157–165.

Katz, L. C., and Dalva, M. B. (1994). Scanning laser photostimulation: a new approach for analyzing brain circuits. *J. Neurosci. Methods* 54, 205–218.

Killackey, H. P., Koralek, K. A., Chiaia, N. L., and Rhodes, R. W. (1989). Laminar and areal differences in the origin of the subcortical projection neurons of the rat somatosensory cortex. *J. Comp. Neurol.* 282, 428–445.

Kiritani, T., Wickersham, I. R., Seung, H. S., and Shepherd, G. M. (2012). Hierarchical connectivity and connection-specific dynamics in the corticospinal–corticostriatal microcircuit in mouse motor cortex. *J. Neurosci.* 32, 4992–5001.

Kornhuber, H. H., and Deecke, L. (1965). Hirnpotentialänderungen bei Willkürbewegungen und passiven Bewegungen des Menschen: Bereitschaftspotential und reafferente Potentiale. *Pflügers Arch.* 284, 1–17.

Krieg, W. J. (1946). Connections of the cerebral cortex. I. The albino rat. B. Structure of the cortical areas. *J. Comp. Neurol.* 84, 277–323.

Kuramoto, E., Fujiyama, F., Nakamura, K. C., Tanaka, Y., Hioki, H., and Kaneko, T. (2011). Complementary distribution of glutamatergic cerebellar and GABAergic basal ganglia afferents to the rat motor thalamic nuclei. *Eur. J. Neurosci.* 33, 95–109.

Kuramoto, E., Furuta, T., Nakamura, K. C., Unzai, T., Hioki, H., and Kaneko, T. (2009). Two types of thalamocortical projections from the motor thalamic nuclei of the rat: a single neuron-tracing study using viral vectors. *Cereb. Cortex* 19, 2065–2077.

Larkum, M. E., Senn, W., and Luscher, H. R. (2004). Top-down dendritic input increases the gain of layer 5 pyramidal neurons. *Cereb. Cortex.* 14, 1059–1070.

Lefort, S., Tomm, C., Floyd Sarria, J. C., and Petersen, C. C. (2009). The excitatory neuronal network of the C2 barrel column in mouse primary somatosensory cortex. *Neuron* 61, 301–316.

Leong, S. K. (1983). Localizing the corticospinal neurons in neonatal, developing and mature albino rat. *Brain Res.* 265, 1–9.

Llano, D. A., and Sherman, S. M. (2009). Differences in intrinsic properties and local network connectivity of identified layer 5 and layer 6 adult mouse auditory corticothalamic neurons support a dual corticothalamic projection hypothesis. *Cereb. Cortex* 19, 2810–2826.

Markram, H., and Tsodyks, M. (1996). Redistribution of synaptic efficacy between neocortical pyramidal neurons. *Nature* 382, 807–810.

Martinez, L. M., Wang, Q., Reid, R. C., Pillai, C., Alonso, J.-M., Sommer, R. T., and Hirsch, J. A. (2005). Receptive field structure varies with layer in the primary visual cortex. *Nat. Neurosci.* 8, 372–379.

Mercer, A., West, D. C., Morris, O. T., Kirchhecker, S., Kerkhoff, J. E., and Thomson, A. M. (2005). Excitatory connections made by presynaptic cortico-cortical pyramidal cells in layer 6 of the neocortex. *Cereb. Cortex* 15, 1485–1496.

Miller, M. W. (1987). The origin of corticospinal projection neurons in rat. *Exp. Brain. Res.* 67, 339–351.

Morishima, M., Morita, K., Kubota, Y., and Kawaguchi, Y. (2011). Highly differentiated projection-specific cortical subnetworks. *J. Neurosci.* 31, 10380–10391.

Morison, R. S., and Dempsey, E. W. (1943). Mechanism of thalamocortical augmentation and repetition. *Am. J. Physiol.* 138, 297–308.

Neafsey, E. J., Bold, E. L., Haas, G., Hurley-Gius, K. M., Quirk, G., Sievert, C. F., et al. (1986). The organization of the rat motor cortex: a microstimulation mapping study. *Brain Res. Rev.* 11, 77–96.

Ohana, O., and Sakmann, B. (1998). Transmitter release modulation in nerve terminals of rat neocortical pyramidal cells by intracellular calcium buffers. *J. Physiol.* 513, 135–148.

Ohno, S., Kuramoto, E., Furuta, T., Hioki, H., Tanaka, Y. R., Fujiyama, F., et al. (2012). Morphological analysis of thalamocortical axon fibers of rat posterior thalamic nuclei: a single neuron tracing study with viral vectors. *Cereb. Cortex* 22, 2840–2857.

Paxinos, G., and Watson, C. (2007). *The Rat Brain in Stereotaxic Coordinates*, 6th Edn. London: Academic Press.

Petreanu, L., Mao, T., Sternson, S. M., and Svoboda, K. (2009). The subcellular organization of neocortical excitatory connections. *Nature* 457, 1142–1145.

Roland, P. E. (2002). Dynamic depolarization fields in the cerebral cortex. *Trends Neurosci.* 25, 183–190.

Sanderson, K. J., Welker, W., and Shambes, G. M. (1984). Reevaluation of motor cortex and of sensorimotor overlap in cerebral cortex of albino rats. *Brain. Res.* 292, 251–260.

Shepherd, G. M., Stepanyants, A., Bureau, I., Chklovskii, D., and Svoboda, K. (2005). Geometric and functional organization of cortical circuits. *Nat. Neurosci.* 8, 782–790.

Shepherd, G. M., and Svoboda, K. (2005). Laminar and columnar organization of ascending excitatory projections to layer 2/3 pyramidal neurons in rat barrel cortex. *J. Neurosci.* 25, 5670–5679.

Sherman, S. M., and Guillery, R. G. (2006). *Exploring the Thalamus and its Role in Cortical Function.* Cambridge, MA: The MIT Press.

Silva, L. R., Gutnick, M. J., and Connors, B. W. (1991). Laminar distribution of neuronal membrane properties in neocortex of normal and reeler mouse. *J. Neurophysiol.* 66, 2034–2040.

Skoglund, T. S., Pascher, R., and Berthold, C. H. (1997). The existence of a layer IV in the rat motor cortex. *Cereb. Cortex* 7, 178–180.

Somogyi, P. (1978). The study of Golgi stained cells and of experimental degeneration under the electron microscope: a direct method for the identification in the visual cortex of three successive links in a neuron chain. *Neuroscience* 3, 167–180.

Steriade, M., McCormick, D. A., and Sejnowski, T. J. (1993). Thalamocortical oscillations in the sleeping and aroused brain. *Science* 262, 679–685.

Sutor, B., and Hablitz, J. J. (1989). EPSPs in rat neocortical neurons in vitro. I. Electrophysiological evidence for two distinct EPSPs. *J. Neurophysiol.* 61, 607–620.

Tanaka, Y. H., Tanaka, Y. R., Fujiyama, F., Furuta, T., Yanagawa, Y., and Kaneko, T. (2011a). Local connections of layer 5 GABAergic interneurons to corticospinal neurons. *Front. Neural Circuits* 5:12. doi: 10.3389/fncir.2011.00012

Tanaka, Y. R., Tanaka, Y. H., Konno, M., Fujiyama, F., Sonomura, T., Okamoto-Furuta, K., et al. (2011b). Local connections of excitatory neurons to corticothalamic neurons in the rat barrel cortex. *J. Neurosci.* 31, 18223–28236.

Tennant, K. A., Adkins, D. L., Donlan, N. A., Asay, A. L., Thomas, N., Kleim, J. A., et al. (2011). The organization of the forelimb representation of the C57BL/6 mouse motor cortex as defined by intracortical microstimulation and cytoarchitecture. *Cereb. Cortex* 21, 865–876.

Thomson, A. M. (1997). Activity-dependent properties of synaptic transmission at two classes of connections made by rat neocortical pyramidal axons in vitro. *J. Physiol.* 502, 131–147.

Thomson, A. M., and Bannister, A. P. (1998). Postsynaptic pyramidal target selection by descending layer III pyramidal axons: dual intracellular recordings and biocytin filling in slices of rat neocortex. *Neuroscience* 84, 669–683.

Thomson, A. M., Girdlestone, D., and West, D. C. (1988). Voltage-dependent currents prolong single-axon postsynaptic potentials in layer III pyramidal neurons in rat neocortical slices. *J. Neurophysiol.* 60, 1896–1907.

Thomson, A. M., and West, D. C. (1993). Fluctuations in pyramid–pyramid excitatory postsynaptic potentials modified by presynaptic firing pattern and postsynaptic membrane potential using paired intracellular recordings in rat neocortex. *Neuroscience* 54, 329–346.

Thomson, A. M., West, D. C., Wang, Y., and Bannister, A. P. (2002). Synaptic connections and small circuits involving excitatory and inhibitory neurons in layers 2–5 of adult rat and cat neocortex: triple intracellular recordings and biocytin labelling in vitro. *Cereb. Cortex* 12, 936–953.

Weiler, N., Wood, L., Yu, J., Solla, S. A., and Shepherd, G. M. (2008). Top-down laminar organization of the excitatory network in motor cortex. *Nat. Neurosci.* 11, 360–366.

Welker, C. (1971). Microelectrode delineation of fine grain somatotopic organization of SmI cerebral neocortex in albino rat. *Brain Res.* 26, 259–275.

Welker, E., Hoogland, P. V., and Van der Loos, H. (1988). Organization of feedback and feedforward projections of the barrel cortex: a PHA-L study in the mouse. *Exp. Brain Res.* 73, 411–435.

West, D. C., Mercer, A., Kirchhecker, S., Morris, O. T., and Thomson, A. M. (2006). Layer 6 cortico-thalamic pyramidal cells preferentially innervate interneurons and generate facilitating EPSPs. *Cereb. Cortex* 16, 200–211.

White, E. L. (1989). *Cortical Circuits: Synaptic Organization of the Cerebral Cortex – Structure, Function and Theory*. Boston, MA: Birkhäuser.

White, E. L., and Hersch, S. M. (1981). Thalamocortical synapses of pyramidal cells which project from SmI to MsI cortex in the mouse. *J. Comp. Neurol.* 198, 167–181.

White, E. L., and Keller, A. (1987). Intrinsic circuitry involving the local axon collaterals of corticothalamic projection cells in mouse SmI cortex. *J. Comp. Neurol.* 262, 13–26.

Wise, S. P., and Jones, E. G. (1977). Cells of origin and terminal distribution of descending projections of the rat somatic sensory cortex. *J. Comp. Neurol.* 175, 129–157.

Wood, L., Gray, N. W., Zhou, Z., Greenberg, M. E., and Shepherd, G. M. (2009). Synaptic circuit abnormalities of motor–frontal layer 2/3 pyramidal neurons in an RNA interference model of methyl-CpG-binding protein 2 deficiency. *J. Neurosci.* 29, 12440–12448.

Wood, L., and Shepherd, G. M. (2010). Synaptic circuit abnormalities of motor–frontal layer 2/3 pyramidal neurons in a mutant mouse model of Rett syndrome. *Neurobiol. Dis.* 38, 281–287.

Yu, J., Anderson, C. T., Kiritani, T., Sheets, P. L., Wokosin, D. L., Wood, L., et al. (2008). Local-circuit phenotypes of layer 5 neurons in motor–frontal cortex of YFP-H mice. *Front. Neural Circuits* 2:6. doi: 10.3389/neuro.04.006.2008

Zarrinpar, A., and Callaway, E. M. (2006). Local connections to specific types of layer 6 neurons in the rat visual cortex. *J. Neurophysiol.* 95, 1751–1761.

Zhang, Z. W., and Deschênes, M. (1997). Intracortical axonal projections of lamina VI cells of the primary somatosensory cortex in the rat: a single-cell labeling study. *J. Neurosci.* 17, 6365–6379.

Conflict of Interest Statement: The author declares that the research was conducted in the absence of any commercial or financial relationships that could be construed as a potential conflict of interest.

Received: 30 November 2012; accepted: 03 April 2013; published online: 28 May 2013.

Citation: Kaneko T (2013) Local connections of excitatory neurons in motor-associated cortical areas of the rat. Front. Neural Circuits ***7****:75. doi: 10.3389/fncir.2013.00075*

frontiers in
NEURAL CIRCUITS

HYPOTHESIS AND THEORY ARTICLE
published: 15 May 2013
doi: 10.3389/fncir.2013.00092

Motor directional tuning across brain areas: directional resonance and the role of inhibition for directional accuracy

Margaret Y. Mahan*[1] *and Apostolos P. Georgopoulos*[1,2]*

[1] *Graduate Program in Biomedical Informatics and Computational Biology, University of Minnesota, Minneapolis, MN, USA*
[2] *Department of Neuroscience, University of Minnesota Medical School, Minneapolis, MN, USA*

Edited by:
Nicholas Hatsopoulos, University of Chicago, USA

Reviewed by:
Hugo Merchant, Universidad Nacional Autónoma de México, Mexico
Gerald Edelman, The Neurosciences Institute, USA
Ziaul Hasan, University of Illinois, Chicago, USA

****Correspondence:***
Apostolos P. Georgopoulos, Brain Sciences Center (11B), University of Minnesota, One Veterans Drive, Minneapolis, MN 55417, USA.
e-mail: omega@umn.edu

Motor directional tuning (Georgopoulos et al., 1982) has been found in every brain area in which it has been sought for during the past 30-odd years. It is typically broad, with widely distributed preferred directions and a population signal that predicts accurately the direction of an upcoming reaching movement or isometric force pulse (Georgopoulos et al., 1992). What is the basis for such ubiquitous directional tuning? How does the tuning come about? What are the implications of directional tuning for understanding the brain mechanisms of movement in space? This review addresses these questions in the light of accumulated knowledge in various sub-fields of neuroscience and motor behavior. It is argued (a) that direction in space encompasses many aspects, from vision to muscles, (b) that there is a directional congruence among the central representations of these distributed "directions" arising from rough but orderly topographic connectivities among brain areas, (c) that broad directional tuning is the result of broad excitation limited by recurrent and non-recurrent (i.e., direct) inhibition within the preferred direction loci in brain areas, and (d) that the width of the directional tuning curve, modulated by local inhibitory mechanisms, is a parameter that determines the accuracy of the directional command.

Keywords: motor directional tuning, inhibitory mechanisms, movement direction, directional precision, motor resonance

INTRODUCTION

> Here, as in the thalamus and cortex, the conclusion is unavoidable: either there is an amazing degree of selectivity in the innervation of single neurons by afferent fibers or inhibitory and other synaptic mechanisms ensure that most inputs remain subthreshold
>
> (Jones, 2007, p. 164)

In the quote above, Ted Jones referred to the high density of innervation of dorsal column nuclei by fibers traveling along the medial lemniscus, in what he called "enormous morphological convergence at all levels of the ascending somatosensory pathways" (Jones, 2007, p. 164), between periphery and cortex. The quote summarizes in a succinct way the puzzling fact that, despite all of this convergence, a remarkable specificity in receptive field size is present, which could be accounted for by "an amazing degree of selectivity ... or inhibitory and other mechanisms" (Jones, 2007, p. 164). In 1984, Eb Fetz compared sensory and motor representations in the somatosensory and motor cortices, respectively, as follows: "... the receptive fields of sensory cortex cells represent the symmetric inverse of the muscle fields of CM (corticomotoneuronal) cells, insofar as cortical inputs are coded analogously to outputs. The symmetric representation of spatial fields of peripheral elements by cortical cells is clearly the result of convergent input connections to sensory cells and divergent output connections from precentral CM cells" (Fetz, 1984, p. 471). This comparison is misconstrued, for it does not make sense to equate *convergence* in the somatosensory cortex of peripheral inputs onto a single somatosensory cortical cell with *divergence* in the motor cortex from a single motor cortical CM cell to several motoneuronal pools. The comparison should refer to the same cortical feature, namely convergence or divergence for both cortices. In fact, the similarity between motor and somatosensory cortex holds at the same level of enquiry, namely the large convergence of thalamic and cortical inputs to both cortices (Darian Smith et al., 1990, 1993). The difference then lies in the content of information, which is manifested as a receptive field in the somatosensory cortex (Mountcastle et al., 1957) and as a directional tuning field in the motor cortex (Georgopoulos and Stefanis, 2007). In this sense, the somatosensory *tactile receptive field*, with (a) its central peak corresponding to that point in the skin where mechanical stimulation elicits the highest response, (b) the gradual reduction of activation as the stimulus is moved farther away from the "hot spot," (c) the surrounding inhibition (Mountcastle and Powell, 1959; Mountcastle, 2005, p. 283), and (d) the gradual shift of the location of the receptive field in the skin, is qualitatively similar to the *directional tuning field* (Georgopoulos and Stefanis, 2007) with (a) its central peak corresponding to the preferred direction of movement, (b) the gradual reduction of activation with movements in directions farther away from the preferred direction, (c) the surrounding inhibition (Stefanis and Jasper, 1964a,b; Merchant et al., 2008; Georgopoulos and Stefanis, 2010), and (d) the gradual shift of the preferred direction in 3-D space (Naselaris et al., 2006b; Georgopoulos and Stefanis, 2007; Georgopoulos et al., 2007). As is the case with receptive fields being interconnected across sensory areas, an approximate topographic

correspondence would interconnect directional tuning fields across various motor areas, which would account for the concurrent activation of these areas at the initiation and execution of a movement in a particular direction. In both sensory and motor systems, receptive field size and directional tuning width would be sharpened by recurrent and non-recurrent (i.e., direct) inhibitory mechanisms.

MOTOR DIRECTIONAL TUNING

A basic finding in motor neurophysiology has been the discovery of directional tuning in space (Georgopoulos et al., 1982), namely the orderly variation of single cell activity with the direction of arm movement, such that activity is highest for a particular movement direction (the cell's "preferred direction") and decreases progressively with movements farther and farther away from the preferred direction. Overall, the tuning is broad and is readily captured by a cosine tuning function. It is important that directional tuning exists for movements made in 2-D (Georgopoulos et al., 1982) as well as in 3-D space (Schwartz et al., 1988; Caminiti et al., 1990a). In fact, the 3-D tuning volume can be derived from a polar plot of a 2-D tuning curve by rotating the 2-D tuning curve around the axis of the preferred direction in 3-D space. In addition, directional tuning has been described for isometric force pulses (Georgopoulos et al., 1992; Taira et al., 1996) and for isometric ramp-and-hold forces (Sergio et al., 2005). In the latter study, the same motor cortical cells were studied under the isometric ramp-and-hold task and in a movement task: broad directional tuning was observed in both tasks but with varying degrees of congruence in the respective preferred directions.

The following also holds for directional tuning. (a) Given an ongoing tonic level of discharge in a given cell, directional tuning can occur due to graded increase in cell activity, combination of increase or decrease in activity, or graded decrease in activity. Although increase or decrease in cell activity cannot be assigned to changes in excitatory or inhibitory drive or a combination thereof, without intracellular recording, it is common to refer to the ongoing neural discharge as "net excitatory drive." (b) Directional tuning is stable across different movement amplitudes wherever tested, including motor cortex (Fu et al., 1993), premotor cortex (Fu et al., 1993), supplementary motor area (Lee and Quessy, 2003), external and internal segments of the globus pallidus (Turner and Anderson, 1997), cerebellar cortex (Fortier et al., 1989), and deep cerebellar nuclei (Fortier et al., 1989). (c) The earliest changes in cell activity are also directionally tuned (Georgopoulos et al., 1982). And (d) the latency of onset of change in cell activity is also directionally tuned (Georgopoulos et al., 1982). These properties underscore the robustness of directional tuning which has now been described in various areas using fMRI (Fabbri et al., 2010).

The key parameter of the directional tuning curve is its preferred direction, for four main reasons. First, it is the only unique value in the curve; second, it encompasses the whole directional space, since it is distributed widely in 3-D space (Schwartz et al., 1988; Naselaris et al., 2006a); third, it is the basis for computing the neuronal population vector, a good predictor of movement direction (Georgopoulos et al., 1983, 1986, 1988; Schwartz, 1994), as the vectorial average of preferred directions weighted by the change in cell activity; and fourth, preferred directions are mapped in an orderly fashion in the motor cortex (Georgopoulos et al., 2007). Based on this mapping, we proposed (Georgopoulos and Stefanis, 2007) that the directional tuning curve comes about as the result of local, tangential interactions in the motor cortical circuit, with inhibition playing a crucial role (Georgopoulos and Stefanis, 2010; see also Merchant et al., 2012). Although these considerations capture the greater picture of directional tuning in the motor cortex, the details of motor cortical circuitry remains to be elucidated. A major advance in this field is the ability to record simultaneously from identified motor cortical cells *in vivo* (Sheets and Shepherd, 2011; Apicella et al., 2012) and thus explore relations based on cell type (e.g., inhibitory interneuron) and its projections (e.g., corticospinal or corticostriatal). This approach has already yielded novel insights into the local, orderly organization of motor cortical circuitry. An ultimate goal would be the combination of such an approach with behavior to elucidate the intricate relations between motor cortical circuitry and directional tuning.

THE UBIQUITOUSNESS OF MOTOR DIRECTIONAL TUNING AND ITS IMPLICATIONS

Although first described in the motor cortex for arm movements in space (Georgopoulos et al., 1982), directional tuning has been found in practically all motor areas where it has been sought for, including premotor cortex (Caminiti et al., 1990b; Fu et al., 1993; Stevenson et al., 2012), human supplementary motor area (Tankus et al., 2009), parietal area 5 (Kalaska et al., 1983; Johnson et al., 1996), parietal area PEc (Battaglia-Mayer et al., 2001; Ferraina et al., 2001), area 7m of the medial wall (Ferraina et al., 1997), parieto-occipital area 6A (Battaglia-Mayer et al., 2000, 2001), external (GPe) and internal (GPi) segments of the globus pallidus (Turner and Anderson, 1997), motor thalamus (Inase et al., 1996), cerebellar cortex (Fortier et al., 1989), and deep cerebellar nuclei (Fortier et al., 1989). An important issue concerns how the directional tuning arises, i.e., what are the relevant synaptic interactions that underlie the shaping of single cell activity to a typically broad tuning function?

Remarkably, directional tuning curves are very similar in all areas and generally follow a cosine tuning function for 2-D space. In addition to the general shape of the tuning curve, all the other properties of directional tuning mentioned above are also observed in different areas. If we were to trace the sequence of events across brain areas following the onset of a visual stimulus instructing a movement in that direction, we would be impressed by the close temporal and directionally tuned engagement of the various areas, from the onset of the instructing stimulus to the onset of the movement. Although it is reasonable to assume a progression of directional information transmission from posterior (visual) to anterior (motor) areas, and, therefrom, bidirectionally to subcortical (thalamic, basal ganglia, and cerebellar) loops, it is remarkable that drastic changes in cell activity were observed, at the limit, as early as 40 ms following stimulus onset in a randomized movement direction

task in the motor cortex (see, e.g., Figure 4 in Georgopoulos et al., 1982). These observations point to a strong directionally tuned co-activation among motor areas; we call this *directional motor resonance*. It is reasonable to suppose that this functional resonance emanates from the underlying pervasive anatomical, topographically organized, connectivity among the various motor areas and leads to the initiation of movement in the intended direction, an essential aspect of motor control (Hasan and Karst, 1989; Karst and Hasan, 1991a,b; Gottlieb et al., 1997). The orderly topographic connectivity constitutes one fundamental aspect of CNS motor control by which various brain areas become *directionally aligned*, so to speak. This seems to be matched by a ubiquitous local network mechanism that ensures spatial sharpening of directionality in each area, namely surround inhibition.

SYNAPTIC MECHANISMS UNDERLYING MOTOR DIRECTIONAL TUNING

The locale of every area where directional tuning has been observed comprises both excitatory and inhibitory mechanisms. Although specifics differ widely (**Table 1**), there are certain common features that could account for the uniformity of directional tuning in various brain areas, as follows. First, excitatory and inhibitory mechanisms are both in play; second, both excitatory and inhibitory neurons receive inputs from local neurons as well as from external inputs; and third, the net effect of this interplay is transmitted further to other areas by outgoing projection cells. This net output is a directionally circumscribed motor signal that is transmitted to orderly, topographically connected recipient areas of a corresponding directional focus. The synaptic interactions within a specific area closely resemble those observed in the spinal cord when, e.g., a motor command arrives at a motoneuronal pool (Baldissera et al., 1981). The motor command typically impinges on (a) the targeted (anatomically) motoneurons, and, possibly, their agonists and synergists (depending on the context), (b) the Ia inhibitory interneurons to their antagonists, and (c) the Renshaw cells that provide recurrent inhibition (Renshaw, 1941; Baldissera et al., 1981; Windhorst, 1996). Now, this recurrent inhibition is distributed to (a) the alpha-motoneurons from which the Renshaw cells receive input, (b) the gamma-motoneurons of that pool, (c) the pools of the agonists and synergists, and (d) the Ia inhibitory interneurons to the antagonists (Baldissera et al., 1981). These actions have two major effects, namely (a) to limit the discharge of the motoneurons contacting the Renshaw cells, and (b) to sharpen the spatial extent of the excitatory motor command by exerting a flat inhibitory drive. In addition, Renshaw cells receive descending signals (Haase and van der Meulen, 1961; MacLean and Leffman, 1967; Fromm et al., 1977; Pierrot Deseilligny et al., 1977; Hultborn and Pierrot Deseilligny, 1979a,b; Hultborn et al., 1979a,b; Baldissera et al., 1981; Hultborn et al., 2004; Hultborn, 2006) that effectively can increase (if excitatory to Renshaw cells) or decrease (if inhibitory to Renshaw cells) the actions of the Renshaw cells on the various cell groups, as described above.

Interestingly, qualitatively similar arrangements are found in all motor areas of the central nervous system, including the cerebral cortex, thalamus, cerebellar cortex, deep cerebellar nuclei, and basal ganglia, in the sense that inhibitory mechanisms play a major role in shaping the local activation landscape. However, there are differences in the origin and distribution of the inhibitory drive, as follows. In the cerebral and cerebellar cortex, all inhibitory mechanisms are local; there is no direct inhibitory input from the outside. By contrast, in the globus pallidus, all inhibitory input is external, arriving from the striatum. And in the thalamus and DCN, the situation is mixed, in that there are both local inhibitory neurons but also external inhibitory inputs arriving from the globus pallidus and cerebellar cortex, respectively. Excitatory inputs arrive from several sources to all areas above, namely from (a) all external inputs to the cerebral cortex (thalamocortical, corticocortical), (b) mainly the subthalamic nucleus to the globus pallidus, (c) corticothalamic and deep cerebellar nuclei inputs to the thalamus, (d) mossy and climbing fibers to the cerebellar cortex, and similarly to the (e) deep cerebellar nuclei (Uusisaari and De Schutter, 2011). In spite of this diversity of excitatory-inhibitory mechanisms, cells in all areas above show broad directional tuning (see above). *Thus, a remarkable functional relation to movement direction is preserved across areas*. The most likely explanation lies in the pervasive, albeit rough, topographical correspondence in anatomical connectivity and in the parallel presence of seemingly non-specific (Fino and Yuste, 2011; Fino et al., 2012) inhibitory mechanisms. This arrangement preserves (a) a correspondence of concurrent activation of neurons with similar preferred directions across various brain areas, and (b) limits the spatial extent of activation, resulting in the directional tuning.

At this point, a consideration of the diverse types of inhibitory neurons and their possible functional impact is in order. This

Table 1 | Summary of synaptic inputs to areas with known motor directional tuning.

	Directional tuning	Local inhibition	Excitatory external inputs	Inhibitory external inputs
Cerebral cortex	Yes	Yes	Yes (from thalamus and cortex)	No
Motor thalamus	Yes	Yes	Yes (from cortex and deep cerebellar nuclei)	Yes (from globus pallidus)
Globus pallidus	Yes	No	Yes (from subthalamic nucleus and cortex)	Yes (from putamen)
Cerebellar cortex	Yes	Yes	Yes (from mossy and climbing fibers)	No
Deep cerebellar nuclei	Yes	Yes	Yes (from mossy and climbing fibers)	Yes (from cerebellar cortex)

diversity has been stressed as implying a correspondingly diverse specificity in inhibitory action (Burkhalter, 2008); in contrast, a different view has been advanced (Battaglia et al., 2013), namely that such diversity does not have to translate necessarily to functional specificity and that, instead, a *functional degeneracy* is in play, namely that different neuronal populations can contribute and/or cooperate to the same function, as is the case, for example, for neurovascular coupling which can be mediated by multiple vasoactive messengers produced by different cell types (see Battaglia et al., 2013 for a more detailed discussion). An appreciable diversity in biochemical and histochemical cell properties exists for the Renshaw cells and other inhibitory interneurons in the ventral horn of the spinal cord (Fyffe, 1991; Alvarez et al., 1997; Hellstrom et al., 1999; Carr et al., 2000, 2001; Geiman et al., 2002; Hughes et al., 2013), and, yet, the overall function of inhibition exerted by Renshaw cells or Ia interneurons is relatively well-understood. Therefore, we agree with Battaglia et al. (2013) in their summary that the cell type diversity most probably reflects functional degeneracy (Edelman, 1987), "defined as the ability of heterogeneous elements to perform the same function (in this case, inhibition). Beyond *redundancy*, occurring when a given function is achieved by replicating homogeneous elements, *degeneracy* confers higher robustness through adaptability. Indeed, heterogeneous elements can react differently in different contexts providing a considerable margin of safety over a wide spectrum of conditions" (Battaglia et al., 2013, p. 19). In summary, there could very well be a meaningful function of cell type diversity within a neural circuit but this may not be necessary reflected at the "bird's eye view" level of assessing excitatory-inhibitory interactions within the circuit. For example, the view of a forest in the middle of a valley, and their borders, are clear-cut from an overflying helicopter but this does not preclude the fact that the forest may be composed of a variety of trees and the valley of a variety of grass and bushes. The internal composition of the forest and the valley perhaps may well-serve specific purposes but, for other purposes, the forest-valley distinction is clear-cut and does not depend on the respective internal compositions.

Now, there are additional aspects of directional motor control, e.g., strength and accuracy of a movement. It is worth exploring how the considerations above would be brought to play on these issues. For that purpose, it is instructive to examine the case of Renshaw cells in more detail. As mentioned above, descending inputs impinge on Renshaw cells to excite or inhibit them (see above): in the former case, net excitation is stronger and more widespread at the motoneuronal level, whereas in the latter case it is weaker and more spatially limited. Now, it has been shown in humans that such effects are meaningfully in operation. For example, weak tonic muscle contractions were associated with increased recurrent inhibition, whereas strong contractions were associated with decreased inhibition (Hultborn and Pierrot Deseilligny, 1979a). Thus, central control of Renshaw cell activity has been linked to a role of recurrent inhibition in spatial sharpening of the motor command to the spinal cord and in adjusting the magnitude of its effect, depending on the task.

It should be noted that the task-related modulation of Renshaw cell activity should be exerted independently of the motor command itself (Koehler et al., 1978). A separate control of motoneuronal and Renshaw cell excitability is almost necessary to achieve, for example, the strong and extensive excitation of the motoneuronal pool and its agonists: if the same, strong motor command was also applied indiscriminately to the Renshaw cells, its strength on, and extent among, motoneuronal pools would be limited by the increased recurrent inhibition. And the same considerations apply for the opposite case, namely the development of weak motoneuronal activations coupled with high spatial sharpening. Indeed, an independent control of Renshaw cell activity by descending inputs has been well-documented (Koehler et al., 1978).

THE ROLE OF INHIBITION IN MOTOR DIRECTIONAL TUNING

It is tempting, then, to speculate on a possible correspondence between Renshaw inhibition in the spinal cord and inhibitory mechanisms in the cerebral cortex with respect to shaping the motor command. In the Renshaw cell case, the shaping of the motor command refers to the distribution and strength of activation of various motoneuronal pools involved, whereas in the case of cortical inhibition the shaping of the motor command refers to the directional tuning, in preparation of the upcoming movement. Of course, the two commands are intimately interrelated (see next section). (See also Georgopoulos and Grillner, 1989, for a general discussion of similarities between motor cortical and spinal mechanisms in motor control.) Now, there are two features that are similar in both inhibitory mechanisms: first, the distribution of inhibition is basically non-specific (Baldissera et al., 1981; Fino and Yuste, 2011; Fino et al., 2012), and second, inhibitory cells are subject to control independently of other neighboring cells, e.g., motoneurons in the spinal cord or pyramidal cells in the cortex. As mentioned above, the role of Renshaw cell inhibition in weaning out weak excitation and spatially delimiting activation, is well-established (Baldissera et al., 1981). Similarly, the central role of inhibition in directional tuning in the cortex is widely accepted (see Merchant et al., 2012 for a review). However, a task-related control of the inhibitory drive has not been brought up in discussions of cortical inhibition, although it has been established with respect to Renshaw inhibition (Hultborn and Pierrot Deseilligny, 1979a). We would like to propose the existence of such a task-related function for the cortical inhibitory drive, namely *to change the width of the directional tuning curve, dependent on the directional accuracy of movement required*. Specifically, we hypothesize that the tuning width will be adjusted to implement the initiation of directionally accurate movements: *the more directional accuracy is required, the more narrow the directional tuning curve will be*. We examined the relation between directional accuracy and directional tuning width in a simulation, as follows.

(a) We generated 2-D directional tuning curves using the "circular normal distribution" (Amirikian and Georgopoulos, 2000):

$$d = e^{\kappa \cos(\theta - \mu)} \quad (1)$$

where d is the discharge rate of a hypothetical cell for a movement in direction μ, θ is the cell's preferred direction, and κ

is the concentration parameter (similar to the inverse of the variance in the normal distribution).

(b) The value of d was standardized to the peak of the curve:

$$d' = \frac{d}{\max(d)} \quad (2)$$

(c) We generated 30 basic tuning curves, one for each κ taking systematically the values {1, 2, 3, . . . , 28, 29, 30}. These curves are shown in **Figure 1**. We also calculated the tuning curve midwidth, which varied from 145 (κ = 1) to 25° (κ = 30). The midwidth was a power function of κ (**Figure 2**).

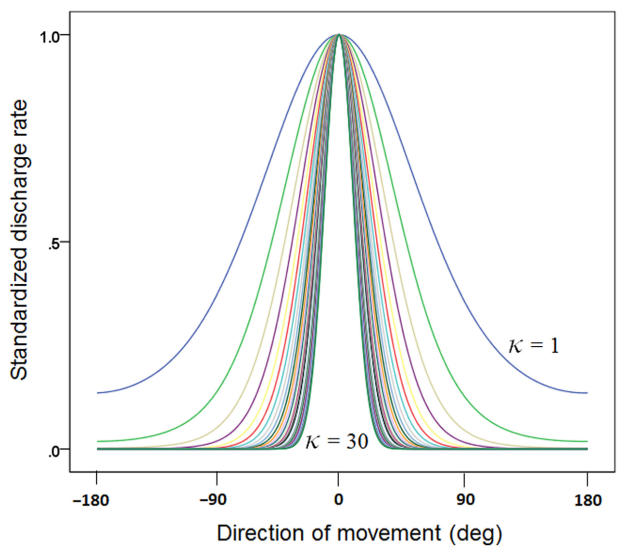

FIGURE 1 | Plot of 30 directional tuning curves generated using Equation 1 (see text), one for each one of 30 κ values {1, 2, 3, . . . , 28, 29, 30}. Each curve is standardized to its maximum.

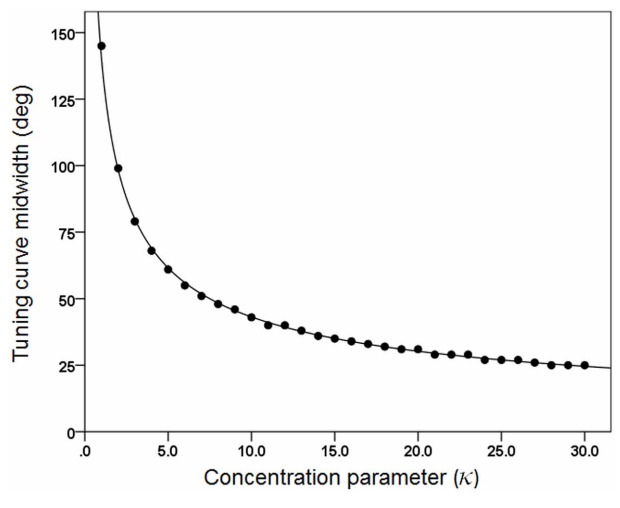

FIGURE 2 | The midwidth of the tuning curve is plotted against κ. The fitted line is a power function fit ($R^2 = 0.999$). $N = 30$.

(d) Next, we generated 10,000 tuning curves for each κ value, with θ chosen at random from a uniform distribution in the range of −180 to +180°, and with 1° resolution. (e) We fixed $\mu = 0$ and calculated 1000 population vectors using d' as a weight. (f) For each population vector, we calculated the angle ω between its direction and the direction of movement (at 0) and the resultant R which corresponds to the length of the population vector:

$$R = (\sin(\omega)^2 + \cos(\omega)^2)^{1/2} \quad (3)$$

The angle ω is signed (i.e., clockwise or counterclockwise). The average ω′ of the absolute value of the angle (over 1000 population vectors) is an estimate of the overall directional variability of the population vector ("variable error"):

$$\omega' = \frac{1}{1000} \sum |\omega| \quad (4)$$

whereas the average φ of the signed angle is a measure of directional bias of the population vector ("constant or signed error"):

$$S = \sum \sin(\omega) \quad (5)$$

$$C = \sum \cos(\omega) \quad (6)$$

$$\varphi = \text{atan}\left(\frac{S}{C}\right) \quad (7)$$

Figures 3, **4** plot the variable error ω′ of the population vector against the concentration parameter κ and midwidth of the tuning curve, respectively. It can be seen that the variable error of the population vector increases as a power function with decreasing κ (**Figure 3**) and as a quadratic function of tuning curve

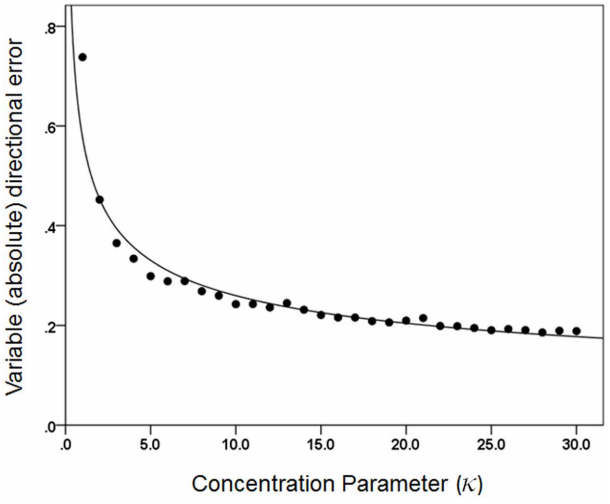

FIGURE 3 | The average directional variable error of the 1000 population vectors is plotted against κ. The fitted line is a power function fit ($R^2 = 0.957$). $N = 30$.

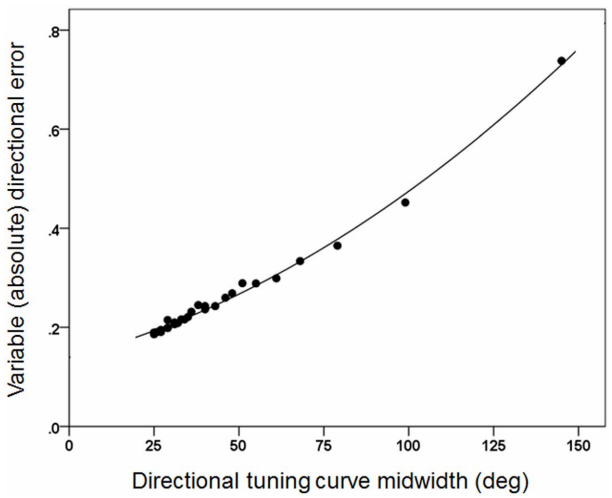

FIGURE 4 | The same variable error as in Figure 3 is plotted against the directional tuning curve midwidth. The fitted line is a quadratic fit ($R^2 = 0.995$).

midwidth (**Figure 4**). As expected, the constant, signed directional error of the population vector did not vary significantly from 0 for any κ (data not shown). These results demonstrate that, first of all, the width of the directional tuning curve is an important variable that can affect significantly and systematically the variation in direction of the population vector, a good predictor of the upcoming movement (Georgopoulos et al., 1983, 1984, 1986, 1988). Assuming that recurrent and non-recurrent (i.e., direct) inhibitory mechanisms are basic means by which the directional tuning width is manipulated, their control, in turn, provides a fundamental mechanism for initiating and controlling movement in space to desired specifications, according to a particular task. That way, the role, contribution and control of central inhibitory mechanisms is at last aligned with those known since long ago for the Renshaw inhibition in the spinal cord, since a fundamental aspect of both is their task- or context-dependent modulation.

Finally, the results above have additional implications for theoretical considerations and some findings in the literature. For example, it has been tacitly taken for granted that directional tuning is associated with a cosine function, since this function has fitted experimental data well. In the light of the results above, it is possible to attribute the wide presence of cosine tuning (i.e., a tuning midwidth of 90°) to the use of 8 movement directions (every 45°) used in those experiments (Georgopoulos et al., 1982, and all studies in other brain areas). Interestingly, when 20 directions were used (every 18°), the tuning midwidth was found to be ∼50° (Amirikian and Georgopoulos, 2000). This issue awaits further, systematic investigation.

Finally, our simulations above revealed another correspondence to the Renshaw cell regulation and to the motor field in general, namely the mechanisms underlying the speed-accuracy tradeoff. With respect to the Renshaw cell regulation, it was mentioned above that an increased supraspinal excitatory drive on the Renshaw cells results in two, combined effects, namely (a) spatially limiting the excitatory drive on the agonist motoneurons, and, therefore, (b) reducing the overall motor output, at the same time. This can be considered as the spinal neurophysiological basis for the well-known speed-accuracy tradeoff (Fitts, 1954) which states that movement time is a log function of movement amplitude and target width, as follows:

$$MT = a + b\log_2\left(\frac{2A}{W}\right) \tag{8}$$

where MT is the movement time, A is the amplitude of the movement, and W is the width of the target, and a and b are regression coefficients. MacKenzie (1992) derived a more accurate equation:

$$MT = a + b\log_2\left(1 + \frac{A}{W}\right) \tag{9}$$

For a movement of unit amplitude, Equation 9 becomes:

$$MT = a + b\log_2\left(1 + \frac{1}{W}\right) \tag{10}$$

Now, for a fixed movement of unit amplitude, the length of the population vector R (Equation 3) can be considered a velocity signal, such that:

$$MT' = \left(\frac{1}{R}\right) \tag{11}$$

Also, the variable directional error ω of the population vector can be considered as the target width. Substituting in Equation 10, we get:

$$MT' = \left(\frac{1}{R}\right) = a + b\log_2\left(1 + \frac{1}{\omega}\right) \tag{12}$$

We evaluated this model in the sample of 1000 population vectors generated by varying the width of the directional curves, as described above. There was a good fit ($r = 0.317$). In contrast, the fit for a linear model (i.e., without the log transformation in Equation 12) was poor ($r = 0.178$). These results demonstrate that the speed-accuracy tradeoff (Fitts' law) holds at the level of the population vector, which brings it into alignment with the Renshaw cell—motoneuronal output interactions discussed above. Specifically, in both cases, an increase in inhibitory drive will result in a more spatially (directionally) accurate but weaker (slower) motor output.

This idea of specifying the directional accuracy of the movement by modulating the inhibitory drive to the circuit is illustrated in **Figure 5**. An elementary cortical circuit consists of a pyramidal cell (P) and two inhibitory interneurons (I). There are three kinds of inputs to those cells: (a) afferents (A) which impinge on both pyramidal and inhibitory cells, (b) recurrent collateral (R) from the pyramidal cell on to the inhibitory interneuron, and (c) external inputs (E), private to inhibitory interneurons. Inputs A and R are standard in cortical microcircuitry literature (DeFelipe and Jones, 2010; Douglas and Martin,

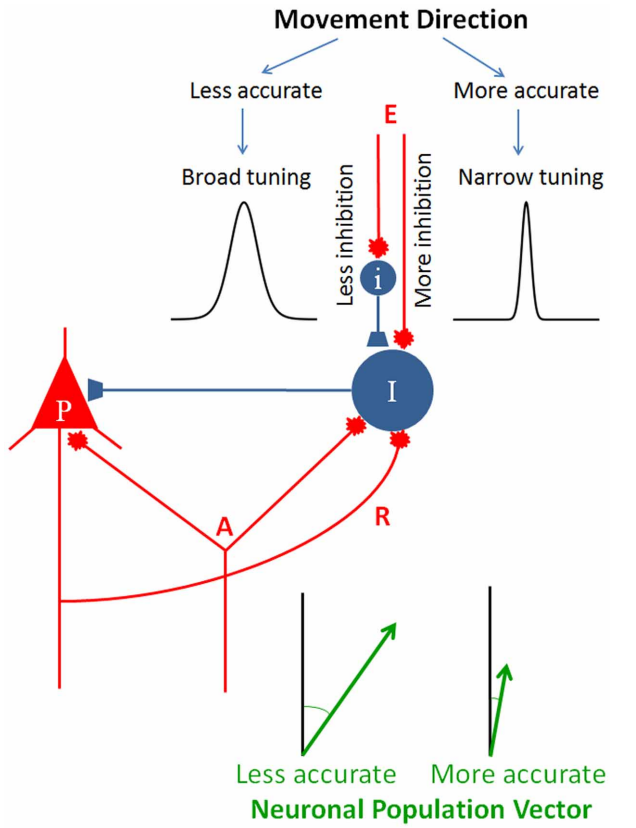

FIGURE 5 | Schematic diagram to illustrate the hypothesis of directional accuracy via a variably tuned circuit. Red and blue terminals indicate excitatory and inhibitory synapses, respectively. P, pyramidal cell; I and i, inhibitory interneurons; A, afferents impinging on both the pyramidal cell and inhibitory interneuron; R, recurrent collateral. The two tuning curves were chosen from those shown in **Figure 1** to illustrate two different tuning widths. The lengths of the two population vectors differ to illustrate the speed-accuracy tradeoff (see text for details).

2010; Georgopoulos and Stefanis, 2010; Markram, 2010) but input E is not. This kind of input is key to our hypothesis which posits a private modulation of the inhibitory drive for the control of tuning width, exemplified by the two tuning curves shown in **Figure 5**. To our knowledge, such an input has not been looked for. In fact, there has not been a systematic study of the inputs to inhibitory interneurons, beyond recurrent collaterals and common afferents. As Douglas and Martin (2009) succinctly pointed out, "While past research has focused almost exclusively on the output of the inhibitory neurons, one crucial aspect of future circuit analysis is to determine the source of the inputs to the inhibitory neurons and to then combine this with knowledge of the dynamics of spiking patterns and synaptic plasticity" (Douglas and Martin, 2009, p. R402). **Figure 5** illustrates two separate mechanisms controlling inhibitory drive of interneuron *I*, one purely excitatory and another inhibitory, exerted through interneuron *I*, although a continuous modulation of the excitatory input alone would be sufficient as well.

All of the discussion above was centered on directional control. The next question, therefore, is: why is movement direction such a pervasive motor parameter? We discuss this question next.

THE PERVASIVENESS OF MOTOR DIRECTION

The commonest use of the arm is to move the hand from one point to another to acquire objects of interest. The initial and final positions of the hand in extrapersonal space define a "visuomotor" vector. Motor directional tuning means that neural activity varies in an orderly fashion with the direction of this vector, relative to its origin. A neural population signal (neuronal population vector) calculated based on changes in cell activity from a set level predicts accurately the direction of the visuomotor vector above (Georgopoulos et al., 1983, 1984, 1986, 1988) in any area it has been calculated (Georgopoulos et al., 1988; Fortier et al., 1989; Kalaska et al., 1989; Caminiti et al., 1990a,b, 1991; Truccolo et al., 2008). In both cases, regarding either single cell activity or the population vector, the direction of movement is the central driving motor variable. The directional tuning was discovered at about the same time that emphasis was given to the movement trajectory (kinematics) as a key aspect of planning multijoint movements in space (Georgopoulos et al., 1981; Soechting and Lacquaniti, 1981; Abend et al., 1982; Viviani and Terzuolo, 1982), an idea that was further developed and amplified in several studies during the 1980's. Later on, the importance of the direction of movement within the muscles-and-torques domains became apparent. In a series of papers (Hasan and Karst, 1989; Karst and Hasan, 1991a,b). Zia Hasan and collaborators drew attention to the importance of direction for the initiation and control of multijoint arm movements by analyzing patterns of changes in electromyographic (EMG) activity in muscles engaged in such movements. Those studies identified the movement direction from the initial to the final position, relative to the forearm, as the key variable to which EMG sign, intensity, and muscle selection relates to. Two additional studies also identified movement direction as a key variable, from two very different perspectives. In one study (Gottlieb et al., 1997), subjects made reaching movements in the sagittal plane in different directions, from various starting positions and of various amplitudes. It was found that, for movements in almost every direction, the dynamic components of the muscle torques at both the elbow and shoulder were related almost linearly to each other, and that the relative scaling of the two joint torques varied continuously and regularly with movement direction, in spite of the complex non-linear dynamics of those multijoint movements (see also Shemmell et al., 2007). These findings underscore the importance of movement direction in multijoint torque coordination. The other study (Worringham and Beringer, 1989) discovered a fundamental relation between direction defined in visual field coordinates and direction of arm movement relative to the forearm. By testing subjects in postures that altered the relative positions of the head, trunk, and arm, it was found that subjects planned and executed movements much more rapidly when the direction of movement of the visual target was used to instruct the direction of arm movement relative to the forearm, rather than relative to the trunk or relative to the surroundings. The blending of visual, hand- and eye-related motor signals has been amply documented in neurophysiological

studies; in addition, there is a congruence in directional tuning between the two main effectors in eye-hand coordination, namely hand and eye movements (see Battaglia-Mayer and Caminiti, 2002 and Caminiti et al., 2010 for reviews). Remarkably, the interplay of these factors with respect to the direction of visually instructed eye or hand movements has been well-documented and delineated in a series of pioneer studies by Roberto Caminiti and collaborators, spanning an amazing range of cortical areas, from area 7 m to the premotor cortex (see Battaglia-Mayer and Caminiti, 2002). In fact, these investigators have proposed that degradation of the congruence in the directional tuning of neural activity to hand and eye movements ("global detuning") might be the neural mechanism underlying the clinical syndrome of optic ataxia, essentially a movement direction apraxia.

All of the studies above point to the direction of movement as a fundamental variable in arm motor control (Georgopoulos, 1996), both intrinsically and in a visuomotor setting. In fact, the fundamental role of motor direction extends beyond movement itself to isometric force control. In a series of experiments using a strictly isometric manipulandum (Massey et al., 1988), we found that visually instructed isometric force trajectories made by human subjects possessed all the known properties of multijoint movement trajectories, namely obeying the 2/3 power law and being piecewise planar (Massey et al., 1991a,b, 1992; Pellizzer et al., 1992). These findings point to the spatial aspects of the motor trajectory being at the heart of the matter, and not the coordination of moving limbs. This idea gained further support by the results of a neurophysiological experiment in which we recorded single cell activity in the motor cortex of monkeys while they produced force pulses in visually specified directions in the presence of static loads applied in various (steady) directions (Georgopoulos et al., 1992). We found that single cell activity was directionally tuned to the net force of the isometric pulse produced, and the neuronal population vector pointed in the direction of that net force. Steve Wise lucidly and succinctly discussed the implications of this finding for neural motor control (Wise, 1993). Finally, a broad directional tuning to isometric ramp-and-hold forces has also been described (Sergio et al., 2005). These investigators also recorded the activity of the same motor cortical cells in a movement task. A broad directional tuning was observed in that task as well but the preferred directions differed frequently, especially when calculated along different time bins. These results underscore the richness of the time-varying relations between motor cortical activity and motor parameters, depending on the task and its context.

In the context of this review, there are two points of interest. The first point emphasizes the importance of the spatial aspects of motor direction, in the absence of limb motion, as discussed above. The second point is more subtle but as important, namely that, during force pulse production, motor cortical activity related to the *change* in force, which was in the visually instructed direction. This result is relevant with respect to the findings above by Hasan and collaborators on the importance of the direction of arm movement *relative to the forearm* for specifying the pattern of muscle activation. Qualitatively, the static load against which the monkey was holding before the initiation of the force pulse could be compared to the maintenance of a fixed forearm posture before the initiation of movement. If so, motor cortical activity would indeed relate to the direction *relative to the static load*. In fact, the results of crucial neurophysiological experiments have addressed satisfactorily this issue. Specifically, when the neuronal population vector was calculated as a time-varying measure using as weights on single cell contributions the *difference* between their ongoing activity and the steady-state activity they had during the preceding control period (steady holding), the population vector direction was an unbiased estimate of the instantaneous direction of the movement trajectory (Georgopoulos et al., 1984, 1988; see also Georgopoulos, 1995). Even more interestingly, when the population vector was calculated under conditions of different initial arm positions, it was again an unbiased estimate of the direction of movement, even though the preferred direction of individual cells had shifted (Caminiti et al., 1990a,b, 1991).

CONCLUDING REMARKS

In summary, motor directional tuning is a fundamental aspect of brain control of movement. Beyond the scientific value of this finding, directional tuning is at the base of current neuroprosthetic applications (Velliste et al., 2008; Collinger et al., 2013; Hochberg et al., 2012). There are many different reasons why "direction" in space is so influential in driving cell activity in so many and diverse brain areas. There are three important points: first, various "directions" are quite congruous with each other, e.g., visually specified direction, direction of a saccadic eye movement, direction of reaching, direction of isometric force pulse; second, "direction" is fundamentally a spatial attribute, hence it cuts across specific instantiations above; and third, it so happens that the joint torques and EMG activity vary in an orderly fashion with movement direction. The net result of all of this is that "everywhere you look, there is direction," which means that cell activity in many different areas will vary with direction, but *not all of them for the same reason*. What saves the day is the pervasive *congruence* among the various "directions" and the covariation of multijoint limb kinetics and muscular activity with movement direction. This state of affairs enables a distributed *directional resonance* across diverse brain areas, each one of which is concerned with its own "direction" or directional blend(s) thereof. Of course, the directional congruence (and resulting resonance) comes from the rough anatomical/topographic correspondence in connectivity, which makes all of the areas involved to become concurrently active.

Another major question is why directional tuning is broad and so similar across diverse brain areas. We propose that this reflects two main factors, namely (a) the presence of recurrent and non-recurrent (i.e., direct) inhibition present in all these areas under different disguises, and (b) the accuracy demands of the specific task. Both of these factors have to do with the inhibitory drive which limits the spatial extent of activation. In addition, an independent excitatory or inhibitory control of local inhibitory mechanisms can modulate the width of directional tuning which, in turn, determines the variability of the direction of the motor command, as illustrated in **Figure 5**. Thus, movements of desired directional accuracy can be planned by varying

the degree of activation of the local inhibitory interneurons, a mechanism analogous to the known descending modulation of Renshaw cell inhibition in task-related contexts. The findings of our simulation studies presented above document and quantify this relation.

ACKNOWLEDGMENTS

Apostolos P. Georgopoulos dedicates this paper to the memory of Ted Jones, dear friend, shrewd neuroanatomist, and admirer of Greek culture. This work was supported by the University of Minnesota and the American Legion Brain Sciences Chair.

REFERENCES

Abend, W., Bizzi, E., and Morasso, P. (1982). Human arm trajectory formation. *Brain* 105, 331–348.

Alvarez, F. J., Dewey, D. E., Harrington, D. A., and Fyffe, R. E. (1997). Cell-type specific organization of glycine receptor clusters in the mammalian spinal cord. *J. Comp. Neurol.* 379, 150–170.

Amirikian, B., and Georgopoulos, A. P. (2000). Directional tuning profiles of motor cortical cells. *Neurosci. Res.* 36, 73–79.

Apicella, A. J., Wickersham, I. R., Seung, H. S., and Shepherd, G. M. (2012). Laminarly orthogonal excitation of fast-spiking and low-threshold-spiking interneurons in mouse motor cortex. *J. Neurosci.* 32, 7021–7033.

Baldissera, F., Hultborn, H., and Illert, M. (1981). "Integration in spinal neuronal systems," in *Handbook of Physiology, Section 1: The Nervous System, Volume II: Motor Control, Part 1,* eds J. M. Brookhart, V. B. Mountcastle, V. B. Brooks, and S. R. Geiger (Bethesda, MD: American Physiological Society), 509–595.

Battaglia, D., Karagiannis, A., Gallopin, T., Gutch, H. W., and Cauli, B. (2013). Beyond the frontiers of neuronal types. *Front. Neural Circuits* 7:13. doi: 10.3389/fncir.2013.00013

Battaglia-Mayer, A., and Caminiti, R. (2002). Optic ataxia as a result of the breakdown of the global tuning fields of parietal neurones. *Brain* 125, 225–237.

Battaglia-Mayer, A., Ferraina, S., Genovesio, A., Marconi, B., Squatrito, S., Molinari, M., et al. (2001). Eye hand coordination during reaching. II. An analysis of the relationships between visuomanual signals in parietal cortex and parieto frontal association projections. *Cereb. Cortex* 11, 528–544.

Battaglia-Mayer, A., Ferraina, S., Mitsuda, T., Marconi, B., Genovesio, A., Onorati, P., et al. (2000). Early coding of reaching in the parietooccipital cortex. *J. Neurophysiol.* 83, 2374–2391.

Burkhalter, A. (2008). Many specialists for suppressing cortical excitation. *Front. Neurosci.* 2:2. doi: 10.3389/neuro.01.026.2008

Caminiti, R., Chafee, M. V., Battaglia Mayer, A., Averbeck, B. B., Crowe, D. A., and Georgopoulos, A. P. (2010). Understanding the parietal lobe syndrome from a neurophysiological and evolutionary perspective. *Eur. J. Neurosci.* 31, 2320–2340.

Caminiti, R., Johnson, P. B., and Urbano, A. (1990a). Making arm movements within different parts of space: dynamic aspects in the primate motor cortex. *J. Neurosci.* 10, 2039–2058.

Caminiti, R., Johnson, P. B., Burnod, Y., Galli, C., and Ferraina, S. (1990b). Shift of preferred directions of premotor cortical cells with arm movements performed across the workspace. *Exp. Brain Res.* 83, 228–232.

Caminiti, R., Johnson, P. B., Galli, C., Ferraina, S., and Burnod, Y. (1991). Making arm movements within different parts of space: the premotor and motor cortical representation of a coordinate system for reaching to visual targets. *J. Neurosci.* 11, 1182–1197.

Carr, P. A., Liu, M., and Zaruba, R. A. (2001). Enzyme histochemical profile of immunohistochemically identified Renshaw cells in rat lumbar spinal cord. *Brain Res. Bull.* 54, 669–674.

Carr, P. A., Roller, M. J., and Zaruba, R. A. (2000). Peptidergic input to immunohistochemically-identified Renshaw cells. *Brain Res.* 887, 194–198.

Collinger, J. L., Wodlinger, B., Downey, J. E., Wang, W., Tyler-Kabara, E. C., Weber, D. J., et al. (2013). High-performance neuroprosthetic control by an individual with tetraplegia. *Lancet* 381, 557–564.

Darian Smith, C., Darian Smith, I., Burman, K., and Ratcliffe, N. (1993). Ipsilateral cortical projections to areas 3a, 3b, and 4 in the macaque monkey. *J. Comp. Neurol.* 335, 200–213.

Darian Smith, C., Darian Smith, I., and Cheema, S. S. (1990). Thalamic projections to sensorimotor cortex in the macaque monkey: use of multiple retrograde fluorescent tracers. *J. Comp. Neurol.* 299, 17–46.

DeFelipe, J., and Jones, E. G. (2010). "Neocortical microcircuits," in *Brain Microcircuits*, eds G. Shepherd and S. Grillner (New York, NY: Oxford), 5–14.

Douglas, R. J., and Martin, K. A. (2009). Inhibition in cortical circuits. *Curr. Biol.* 19, R398–R402.

Douglas, R. J., and Martin, K. A. (2010). "Canonical cortical circuits," in *Brain Microcircuits*, eds G. Shepherd and S. Grillner (New York, NY: Oxford), 15–21.

Edelman, G. M. (1987). *Neural Darwinism: The Theory of Neuronal Group Selection*. New York, NY: Basic Books.

Fabbri, S., Caramazza, A., and Lingnau, A. (2010). Tuning curves for movement direction in the human visuomotor system. *J. Neurosci.* 30, 13488–13498.

Ferraina, S., Battaglia Mayer, A., Genovesio, A., Marconi, B., Onorati, P., and Caminiti, R. (2001). Early coding of visuomanual coordination during reaching in parietal area PEc. *J. Neurophysiol.* 85, 462–467.

Ferraina, S., Garasto, M. R., Battaglia-Mayer, A., Ferraresi, P., Johnson, P. B., Lacquaniti, F., et al. (1997). Visual control of hand-reaching movement: activity in parietal area 7m. *Eur. J. Neurosci.* 9, 1090–1095.

Fetz, E. (1984). "The representation of movement direction in the motor cortex: single cell and population studies," in *Dynamic Aspects of Neocortical Function*, eds G. M. Edelman, W. M. Cowan, and W. E. Gall (New York, NY: Wiley), 453–473.

Fino, E., and Yuste, R. (2011). Dense inhibitory connectivity in neocortex. *Neuron* 69, 1188–1203.

Fino, E., Packer, A. M., and Yuste, R. (2012). The logic of inhibitory connectivity in the neocortex. *Neuroscientist.* doi: 10.1177/1073858412456743. [Epub ahead of print].

Fitts, P. M. (1954). The information capacity of the human motor system in controlling the amplitude of movement. *J. Exp. Psychol.* 47, 381–391.

Fortier, P. A., Kalaska, J. F., and Smith, A. M. (1989). Cerebellar neuronal activity related to whole arm reaching movements in the monkey. *J. Neurophysiol.* 62, 198–211.

Fromm, C., Haase, J., and Wolf, E. (1977). Depression of the recurrent inhibition of extensor motoneurons by the action of group II afferents. *Brain Res.* 120, 459–468.

Fu, Q. G., Suarez, J. I., and Ebner, T. J. (1993). Neuronal specification of direction and distance during reaching movements in the superior precentral premotor area and primary motor cortex of monkeys. *J. Neurophysiol.* 70, 2097–2116.

Fyffe, R. E. (1991). Glycine-like immunoreactivity in synaptic boutons of identified inhibitory interneurons in the mammalian spinal cord. *Brain Res.* 547, 175–179.

Geiman, E. J., Zheng, W., Fritschy, J. M., and Alvarez, F. J. (2002). Glycine and GABA(A) receptor subunits on Renshaw cells: relationship with presynaptic neurotransmitters and postsynaptic gephyrin clusters. *J. Comp. Neurol.* 444, 275–289.

Georgopoulos, A. P. (1995). Current issues in directional motor control. *Trends Neurosci.* 18, 506–510.

Georgopoulos, A. P. (1996). On the translation of directional motor cortical commands to activation of muscles via spinal interneuronal systems. *Brain Res. Cogn. Brain Res.* 3, 151–155.

Georgopoulos, A. P., Ashe, J., Smyrnis, N., and Taira, M. (1992). The motor cortex and the coding of force. *Science* 256, 1692–1695.

Georgopoulos, A. P., Caminiti, R., Kalaska, J. F., and Massey, J. T. (1983). Spatial coding of movement: a hypothesis concerning the coding of movement direction by motor cortical populations. *Exp. Brain Res. Suppl.* 7, 327–336.

Georgopoulos, A. P., and Grillner, S. (1989). Visuomotor coordination in reaching and locomotion. *Science* 245, 1209–1210.

Georgopoulos, A. P., Kalaska, J. F., Caminiti, R., and Massey, J. T. (1982). On the relations between the direction of two dimensional arm movements and cell discharge in primate motor cortex. *J. Neurosci.* 2, 1527–1537.

Georgopoulos, A. P., Kalaska, J. F., Crutcher, M. D., Caminiti, R., and Massey, J. T. (1984). "The representation of movement direction in the motor cortex: single cell and population studies," in *Dynamic Aspects of Neocortical Function*, eds G. M. Edelman, W. M. Cowan, and W.

E. Gall (New York, NY: Wiley), 501–524.

Georgopoulos, A. P., Kalaska, J. F., and Massey, J. T. (1981). Spatial trajectories and reaction times of aimed movements: effects of practice, uncertainty, and change in target location. *J. Neurophysiol.* 46, 725–743.

Georgopoulos, A. P., Kettner, R. E., and Schwartz, A. B. (1988). Primate motor cortex and free arm movements to visual targets in three dimensional space. II. Coding of the direction of movement by a neuronal population. *J. Neurosci.* 8, 2928–2937.

Georgopoulos, A. P., Merchant, H., Naselaris, T., and Amirikian, B. (2007). Mapping of the preferred direction in the motor cortex. *Proc. Natl. Acad. Sci. U.S.A.* 104, 11068–11072.

Georgopoulos, A. P., Schwartz, A. B., and Kettner, R. E. (1986). Neuronal population coding of movement direction. *Science* 233, 1416–1419.

Georgopoulos, A. P., and Stefanis, C. N. (2007). Local shaping of function in the motor cortex: motor contrast, directional tuning. *Brain Res. Rev.* 55, 383–389.

Georgopoulos, A. P., and Stefanis, C. (2010). "The motor cortical circuit," in *Brain Microcircuits*, eds G. Shepherd and S. Grillner (New York, NY: Oxford), 39–45.

Gottlieb, G. L., Song, Q., Almeida, G. L., Hong, D. A., and Corcos, D. (1997). Directional control of planar human arm movement. *J. Neurophysiol.* 78, 2985–2998.

Haase, J., and van der Meulen, J. (1961). Effects of supraspinal stimulation on Renshaw cells belonging to extensor motoneurones. *J. Neurophysiol.* 24, 510–520.

Hasan, Z., and Karst, G. M. (1989). Muscle activity for initiation of planar, two joint arm movements in different directions. *Exp. Brain Res.* 76, 651–655.

Hellstrom, J., Arvidsson, U., Elde, R., Cullheim, S., and Meister, B. (1999). Differential expression of nerve terminal protein isoforms in VAChT-containing varicosities of the spinal cord ventral horn. *J. Comp. Neurol.* 411, 578–590.

Hughes, D. I., Boyle, K. A., Kinnon, C. M., Bilsland, C., Quayle, J. A., Callister, R. J., et al. (2013). HCN4 subunit expression in fast-spiking interneurons of the rat spinal cord and hippocampus. *Neuroscience* 237, 7–18.

Hochberg, L. R., Bacher, D., Jarosiewicz, B., Masse, N. Y., Simeral, J. D., Vogel, J., et al. (2012). Reach and grasp by people with tetraplegia using a neurally controlled robotic arm. *Nature* 485, 372–375.

Hultborn, H. (2006). Spinal reflexes, mechanisms and concepts: from Eccles to Lundberg and beyond. *Prog. Neurobiol.* 78, 215–232.

Hultborn, H., Brownstone, R. B., Toth, T. I., and Gossard, J. P. (2004). Key mechanisms for setting the input output gain across the motoneuron pool. *Prog. Brain Res.* 143, 77–95.

Hultborn, H., Lindstrom, S., and Wigstrom, H. (1979a). On the function of recurrent inhibition in the spinal cord. *Exp. Brain Res.* 37, 399–403.

Hultborn, H., Pierrot Deseilligny, E., and Wigstrom, H. (1979b). Recurrent inhibition and after-hyperpolarization following motoneuronal discharge in the cat. *J. Physiol.* 297, 253–266.

Hultborn, H., and Pierrot Deseilligny, E. (1979a). Changes in recurrent inhibition during voluntary soleus contractions in man studied by an H reflex technique. *J. Physiol.* 297, 229–251.

Hultborn, H., and Pierrot Deseilligny, E. (1979b). Input output relations in the pathway of recurrent inhibition to motoneurones in the cat. *J. Physiol.* 297, 267–287.

Inase, M., Buford, J. A., and Anderson, M. E. (1996). Changes in the control of arm position, movement, and thalamic discharge during local inactivation in the globus pallidus of the monkey. *J. Neurophysiol.* 75, 1087–1104.

Johnson, P. B., Ferraina, S., Bianchi, L., and Caminiti, R. (1996). Cortical networks for visual reaching: physiological and anatomical organization of frontal and parietal lobe arm regions. *Cereb. Cortex* 6, 102–119.

Jones, E. G. (2007). *The Thalamus*. 2nd Edn. New York, NY: Cambridge.

Kalaska, J. F., Caminiti, R., and Georgopoulos, A. P. (1983). Cortical mechanisms related to the direction of two dimensional arm movements: relations in parietal area 5 and comparison with motor cortex. *Exp. Brain Res.* 51, 247–260.

Kalaska, J. F., Cohen, D. A., Hyde, M. L., and Prud'homme, M. (1989). A comparison of movement direction-related versus load direction-related activity in primate motor cortex, using a two-dimensional reaching task. *J. Neurosci.* 9, 2080–2102.

Karst, G. M., and Hasan, Z. (1991a). Initiation rules for planar, two joint arm movements: agonist selection for movements throughout the work space. *J. Neurophysiol.* 66, 1579–1593.

Karst, G. M., and Hasan, Z. (1991b). Timing and magnitude of electromyographic activity for two joint arm movements in different directions. *J. Neurophysiol.* 66, 1594–1604.

Koehler, W., Windhorst, U., Schmidt, J., Meyer Lohmann, J., and Henatsch, H. D. (1978). Diverging influences on Renshaw cell responses and monosynaptic reflexes from stimulation of capsula interna. *Neurosci. Lett.* 8, 35–39.

Lee, D., and Quessy, H. (2003). Activity in the supplementary motor area related to learning and performance during a sequential visuomotor task. *J. Neurophysiol.* 89, 1039–1056.

MacKenzie, S. I. (1992). Fitts' law as a research and design tool in human–computer interaction. *Hum. Comput. Interact.* 7, 91–139.

MacLean, J. B., and Leffman, H. (1967). Supraspinal control of Renshaw cells. *Exp. Neurol.* 18, 94–104.

Markram, H. (2010). "Microcircuitry of the neocortex," in *Brain Microcircuits,* eds G. Shepherd and S. Grillner (New York, NY: Oxford), 22–30.

Massey, J. T., Drake, R. A., and Georgopoulos, A. P. (1991a). Cognitive spatial motor processes. 5. Specification of the direction of visually guided isometric forces in two dimensional space: time course of information transmitted and effect of constant force bias. *Exp. Brain Res.* 83, 446–452.

Massey, J. T., Drake, R. A., Lurito, J. T., and Georgopoulos, A. P. (1991b). Cognitive spatial motor processes. 4. Specification of the direction of visually guided isometric forces in two dimensional space: information transmitted and effects of visual force feedback. *Exp. Brain Res.* 83, 439–445.

Massey, J. T., Hovey, G. W., Schneider, W., Chubbuck, J. G., and Georgopoulos, A. P. (1988). A method for studying the control of three dimensional isometric forces using dynamic stereogram. *J. Neurosci. Methods* 26, 123–127.

Massey, J. T., Lurito, J. T., Pellizzer, G., and Georgopoulos, A. P. (1992). Three dimensional drawings in isometric conditions: relation between geometry and kinematics. *Exp. Brain Res.* 88, 685–690.

Merchant, H., de Lafuente, V., Pena Ortega, F., and Larriva Sahd, J. (2012). Functional impact of interneuronal inhibition in the cerebral cortex of behaving animals. *Prog. Neurobiol.* 99, 163–178.

Merchant, H., Naselaris, T., and Georgopoulos, A. P. (2008). Dynamic sculpting of directional tuning in the primate motor cortex during three dimensional reaching. *J. Neurosci.* 28, 9164–9172.

Mountcastle, V. B. (2005). *The Sensory Hand*. Cambridge, MA: Harvard.

Mountcastle, V. B., Davies, P. W., and Berman, A. L. (1957). Response properties of neurons of cat's somatic sensory cortex to peripheral stimuli. *J. Neurophysiol.* 20, 374–407.

Mountcastle, V. B., and Powell, T. P. (1959). Neural mechanisms subserving cutaneous sensibility, with special reference to the role of afferent inhibition in sensory perception and discrimination. *Bull. Johns Hopkins Hosp.* 105, 201–232.

Naselaris, N., Merchant, H., Amirikian, B., and Georgopoulos, A. P. (2006a). Large-scale organization of preferred directions in the motor cortex. I. Motor cortical hyperacuity for forward reaching. *J. Neurophysiol.* 96, 3231–3236.

Naselaris, T., Merchant, H., Amirikian, B., and Georgopoulos, A. P. (2006b). Large scale organization of preferred directions in the motor cortex. II. Analysis of local distributions. *J. Neurophysiol.* 96, 3237–3247.

Pellizzer, G., Massey, J. T., Lurito, J. T., and Georgopoulos, A. P. (1992). Three dimensional drawings in isometric conditions: planar segmentation of force trajectory. *Exp. Brain Res.* 92, 326–337.

Pierrot Deseilligny, E., Morin, C., Katz, R., and Bussel, B. (1977). Influence of voluntary movement and posture on recurrent inhibition in human subjects. *Brain Res.* 124, 427–436.

Renshaw, B. (1941). Influence of discharge of motoneurons upon excitation of neighboring motoneurons. *J. Neurophysiol.* 4, 167–183.

Schwartz, A. B. (1994). Direct cortical representation of drawing. *Science* 265, 540–542.

Schwartz, A. B., Kettner, R. E., and Georgopoulos, A. P. (1988). Primate motor cortex and free arm movements to visual targets in three dimensional space. I. Relations between single cell discharge and direction of movement. *J. Neurosci.* 8, 2913–2927.

Sergio, L. E., Hamel-Paquet, C., and Kalaska, J. F. (2005). Motor cortex neural correlates of output kinematics and kinetics during isometric-force and arm-reaching tasks. *J. Neurophysiol.* 94, 2353–2378.

Sheets, P. L., and Shepherd, G. M. (2011). Cortical circuits for motor control. *Neuropsychopharmacology* 36, 365–366.

Shemmell, J., Hasan, Z., Gottlieb, G. L., and Corcos, D. M. (2007). The effect of movement direction on joint torque covariation. *Exp. Brain Res.* 176, 150–158.

Soechting, J. F., and Lacquaniti, F. (1981). Invariant characteristics of a pointing movement in man. *J. Neurosci.* 1, 710–720.

Stefanis, C., and Jasper, H. (1964a). Intracellular microelectrode studies of antidromic responses in cortical pyramidal tract neurons. *J. Neurophysiol.* 27, 828–854.

Stefanis, C., and Jasper, H. (1964b). Recurrent collateral inhibition in pyramidal tract neurons. *J. Neurophysiol.* 27, 855–877.

Stevenson, I. H., London, B. M., Oby, E. R., Sachs, N. A., Reimer, J., Englitz, B., et al. (2012). Functional connectivity and tuning curves in populations of simultaneously recorded neurons. *PLoS Comput. Biol.* 8:e1002775. doi: 10.1371/journal.pcbi.1002775

Taira, M., Boline, J., Smyrnis, N., Georgopoulos, A. P., and Ashe, J. (1996). On the relations between single cell activity in the motor cortex and the direction and magnitude of three dimensional static isometric force. *Exp. Brain Res.* 109, 367–376.

Tankus, A., Yeshurun, Y., Flash, T., and Fried, I. (2009). Encoding of speed and direction of movement in the human supplementary motor area. *J. Neurosurg.* 110, 1304–1316.

Truccolo, W., Friehs, G. M., Donoghue, J. P., and Hochberg, L. R. (2008). Primary motor cortex tuning to intended movement kinematics in humans with tetraplegia. *J. Neurosci.* 28, 1163–1178.

Turner, R. S., and Anderson, M. E. (1997). Pallidal discharge related to the kinematics of reaching movements in two dimensions. *J. Neurophysiol.* 77, 1051–1074.

Uusisaari, M., and De Schutter, E. (2011). The mysterious microcircuitry of the cerebellar nuclei. *J. Physiol.* 589, 3441–3457.

Velliste, M., Perel, S., Spalding, M. C., Whitford, A. S., and Schwartz, A. B. (2008). Cortical control of a prosthetic arm for self-feeding. *Nature* 453, 1098–1101.

Viviani, P., and Terzuolo, C. (1982). Trajectory determines movement dynamics. *Neuroscience* 7, 431–437.

Windhorst, U. (1996). On the role of recurrent inhibitory feedback in motor control. *Prog. Neurobiol.* 49, 517–587.

Wise, S. P. (1993). Monkey motor cortex: movements, muscles, motoneurons and metrics. *Trends Neurosci.* 16, 46–49.

Worringham, C. J., and Beringer, D. B. (1989). Operator orientation and compatibility in visual motor task performance. *Ergonomics* 32, 387–399.

Conflict of Interest Statement: The authors declare that the research was conducted in the absence of any commercial or financial relationships that could be construed as a potential conflict of interest.

Received: 07 January 2013; paper pending published: 26 March 2013; accepted: 26 April 2013; published online: 15 May 2013.

Citation: Mahan MY and Georgopoulos AP (2013) Motor directional tuning across brain areas: directional resonance and the role of inhibition for directional accuracy. Front. Neural Circuits 7:92. doi: 10.3389/fncir.2013.00092

frontiers in
NEURAL CIRCUITS

REVIEW ARTICLE
published: 03 May 2013
doi: 10.3389/fncir.2013.00085

Neural dynamics and information representation in microcircuits of motor cortex

Yasuhiro Tsubo*[1], *Yoshikazu Isomura*[2,3] *and Tomoki Fukai*[1,3]

[1] *Laboratory for Neural Circuit Theory, RIKEN Brain Science Institute, Wako, Saitama, Japan*
[2] *Brain Science Institute, Tamagawa University, Machida, Tokyo, Japan*
[3] *Core Research for Evolutional Science and Technology, Japan Science and Technology Agency, Sanbancho, Chiyoda-ku, Tokyo, Japan*

Edited by:
Takehsi Kaneko, Kyoto University, Japan

Reviewed by:
Yoshiyuki Kubota, National Institute for Physiological Sciences, Japan
Fumitaka Kimura, Osaka University Medical School, Japan
Yuji Ikegaya, The University of Tokyo, Japan

***Correspondence:**
Tomoki Fukai, Laboratory for Neural Circuit Theory, RIKEN Brain Science Institute, 2-1 Hirosawa, Wako, Saitama 351-0198, Japan.
e-mail: tfukai@riken.jp

The brain has to analyze and respond to external events that can change rapidly from time to time, suggesting that information processing by the brain may be essentially dynamic rather than static. The dynamical features of neural computation are of significant importance in motor cortex that governs the process of movement generation and learning. In this paper, we discuss these features based primarily on our recent findings on neural dynamics and information coding in the microcircuit of rat motor cortex. In fact, cortical neurons show a variety of dynamical behavior from rhythmic activity in various frequency bands to highly irregular spike firing. Of particular interest are the similarity and dissimilarity of the neuronal response properties in different layers of motor cortex. By conducting electrophysiological recordings in slice preparation, we report the phase response curves (PRCs) of neurons in different cortical layers to demonstrate their layer-dependent synchronization properties. We then study how motor cortex recruits task-related neurons in different layers for voluntary arm movements by simultaneous juxtacellular and multiunit recordings from behaving rats. The results suggest an interesting difference in the spectrum of functional activity between the superficial and deep layers. Furthermore, the task-related activities recorded from various layers exhibited power law distributions of inter-spike intervals (ISIs), in contrast to a general belief that ISIs obey Poisson or Gamma distributions in cortical neurons. We present a theoretical argument that this power law of *in vivo* neurons may represent the maximization of the entropy of firing rate with limited energy consumption of spike generation. Though further studies are required to fully clarify the functional implications of this coding principle, it may shed new light on information representations by neurons and circuits in motor cortex.

Keywords: synchronization, gamma oscillation, juxtacellular, multiunit, neural code, irregular firing, cortical layer, local circuit

Neocortical microcircuits have a stereotyped structure, comprising a six-layered network of excitatory pyramidal neurons and inhibitory interneurons. This structure is preserved across many neocortical regions (an exception is agranular areas lacking layer 4: Shepherd, 2009), and is often considered to represent the functional module of cortical information processing. Uncovering how neurons in the different layers process information is a key to understand the principles of cortical computations. Several recent studies have begun to uncover how the dynamics of neural populations underlie motor behavior (Churchland and Shenoy, 2007; Hatsopoulos and Suminski, 2011; Churchland et al., 2012). Unlike the classical view of direction-tuned neurons during reaching (Georgopoulos et al., 1986), direction tuning curves scale with the velocity of arm movement only in a minority of these neurons in primate motor cortex (Churchland and Shenoy, 2007; Hatsopoulos and Suminski, 2011). The results suggest that the relationship between the activity of motor cortex neurons and motor behavior is more divergent and heterogeneous than previously thought. Few studies, however, have evaluated the role of the layered structure of motor cortex in such dynamics. In this paper, we will review the results of our *in vitro* and *in vivo* recording studies that attempt to clarify the characteristic features of neuronal dynamics and information processing in different layers of rat motor cortex.

The first part is devoted to slice recordings of the phase response curves (PRCs) from motor cortex neurons in different layers. The PRC shows the responses of single neurons to a perturbative input and provides a useful mathematical tool for characterizing synchronization properties of a weakly coupled network of arbitrary oscillators (Reyes and Fetz, 1993a,b; Ermentrout, 1996; Ermentrout et al., 2001; Gutkin et al., 2005; Netoff et al., 2005b; Goldberg et al., 2007). Various experimental studies have shown that the local field potential (LFP) or unit activity of the primary motor cortex exhibits gamma-band (30–80 Hz) oscillations during behavior (Sanes and Donoghue, 1993; Murthy and Fetz, 1996; Donoghue et al., 1998; Farmer, 1998). Though these results are mainly from the primate, we also found strong gamma oscillatory components of the LFP and neuronal firing in the

motor cortex of behaving rats (Igarashi et al., unpublished observation). Therefore, it is of particular interest to clarify whether the tendency of synchronized oscillatory firing is layer-dependent in motor cortex. Our electrophysiological recordings from a slice preparation of rat motor cortex revealed that the preference to synchronization is layer- and frequency-dependent in rat motor cortex.

In the second part, we explore the relationship between neuronal activity in different cortical layers and motor behavior by conducting simultaneous multiunit recordings and juxtacellular recordings from the motor cortex of rats performing spontaneous voluntary movement (Isomura et al., 2009). The recordings were made in the forelimb area of the rat motor cortex (Donoghue and Wise, 1982; Rouiller et al., 1993; Brecht et al., 2004), where layer 2/3 pyramidal cells principally project to other cortical areas, layer 5 pyramidal cells to subcortical structures such as the spinal cord and the striatum, and layer 6 pyramidal cells to thalamic nuclei. These excitatory pyramidal cells, along with the star-like pyramidal cells in layer 4 of this area, also innervate local cortico-spinal pyramidal cells in layer 5 via axon collaterals (Cho et al., 2004a,b). An *in vitro* study of excitatory laminar connectivity predicted that motor information would flow primarily from layer 2/3 to layer 5 in the primary motor cortex (Weiler et al., 2008). However, the flow of information in the microcircuit of motor cortex requires clarification by recordings from behaving animals. The role of inhibition in motor cortex also needs to be tested by experiment. For instance, the traditional view suggests that inhibitory interneurons inhibit excitatory neurons encoding antagonistic movements (i.e., lateral inhibition). We addressed these issues by combining juxtacellular and multiunit recordings, where the former technique provides accurate spike events and morphological features for recorded neurons (Pinault, 1996; Klausberger et al., 2003; Lee et al., 2004; Mallet et al., 2006; de Kock et al., 2007) and the latter technique enables a simultaneous access to spike events of many neurons (Harris et al., 2000; Isomura et al., 2006; Merchant et al., 2008). Our approach uncovered the functional diversity of pyramidal cells and functional uniformity of fast-spiking (FS) interneurons across all cortical layers in the expression of voluntary movement.

In the third part, we interpret information coding by highly irregular firing of a single motor cortex neuron in terms of a variational principle. While the population signal such as LFP often exhibits oscillatory behavior in the motor cortex (and other cortical areas), activity of single neurons is generally highly irregular in various cortical areas including the primary motor cortex. Why local cortical circuits simultaneously exhibit rhythmic oscillatory activity and stochastic irregular firing remains unclear. However, findings on the biological machinery for irregular firing, namely a balanced excitatory and inhibitory synaptic input (Destexhe et al., 2003; Shu et al., 2003), suggest that the stochastic nature of local cortical circuits is essential for information processing by the brain (Rao et al., 2002; Ma et al., 2006; Berkes et al., 2011; Buesing et al., 2011; Teramae et al., 2012). We closely inspect the statistical properties of the irregular spike generation by cortical neurons. Based on our observations, we propose the constrained maximization of firing-rate entropy (CMFE) as a hypothesis for the neural code.

PHASE RESPONSE CURVES: MOTOR CORTEX NEURONS

Neurons firing periodically can be regarded as an oscillator. The PRC describes the response of an oscillator to a weak perturbation given at a certain phase of oscillation $\theta = 2\pi t/T$, where t and T denote the time from the previous spike and the period of repetitive firing, respectively (Kuramoto, 1984; Smeal et al., 2010). Depending on the stimulus time, the subsequent spike will be generated at an earlier or a later time. If a small perturbed current injected to a neuron advances the time of spike firing in the subsequent oscillatory cycle, the corresponding PRC takes a positive value at the phase angle. If the current delays the next spike, the value of PRC is negative. The PRC of a neuron can be classified into type 1 or type 2 (Hansel et al., 1995), depending on whether the curve almost always takes positive values (type 1) or takes both positive and negative values (type 2).

The PRC is of interest from a viewpoint of the network dynamics since it has crucial information about rhythmic synchronization (Kuramoto, 1984; Hansel et al., 1995; Ermentrout, 1996; Ermentrout et al., 2001; Nomura et al., 2003; Galan et al., 2005; Gutkin et al., 2005; Netoff et al., 2005a,b; Takekawa et al., 2007; Tsubo et al., 2007b), and several methods have been proposed for computing the PRC from model and experimental data (Torben-Nielsen et al., 2010). In general, neurons with a type-2 PRC can easily be synchronized when they are mutually coupled via fast excitatory synaptic connections, while those with a type-1 PRC may not perfectly be synchronized (Hansel et al., 1995). However, the stable phase difference calculated with the type-1 PRC can be close to zero at low firing rates (Tsubo et al., 2007a). Therefore, the relationship between the PRC types and the synchronization properties is not strict. Experimentally, pyramidal neurons in layer 5 of the cat motor cortex exhibited a type-1 PRC (Reyes and Fetz, 1993a,b), whereas glutamatergic stellate cells in layer 2 of the rat entorhinal cortex (Netoff et al., 2005b), pyramidal neurons in rat hippocampal CA3 (Lengyel et al., 2005) and fast spiking interneurons in somatosensory cortex (Tateno et al., 2007) displayed a predominantly type-2 PRC. In mouse visual cortex, the PRC of pyramidal neurons in layer 2/3 were switched from type 2 to type 1 by cholinergic action (Stiefel et al., 2008). Thus, neuromodulators can change the PRC type.

To obtain the PRC, we performed intracellular and whole-cell patch-clamp recordings at the soma of layer 2/3 and layer 5 pyramidal neurons of the rat motor cortex (Tsubo et al., 2007a) (**Figure 1**). Although cortical neurons showed a variety of responses to a step current injection, we only examined those neurons that displayed near-periodic firing patterns. We tested the PRC of pyramidal neurons in theta (4–8 Hz), alpha (8–13 Hz), beta (13–20 Hz), and gamma (20–45 Hz) frequency ranges. The PRC depended on the range of firing rates and the cortical layers to which neurons belong. In the theta, alpha and gamma frequency ranges, layer 2/3 or layer 5 pyramidal neurons tend to possess type-2 or type-1 PRCs, respectively. In the beta frequency ranges, the PRCs display type-1 properties in both layer 2/3 and layer 5 pyramidal neurons. However, simulations of coupled oscillators showed that the stable phase difference almost

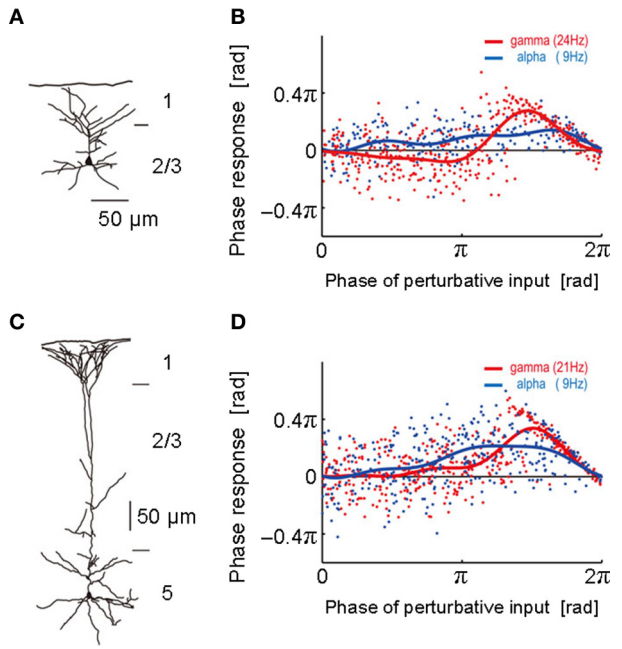

FIGURE 1 | Phase response curves obtained from different layers. **(A)** The morphological structure of a layer 2/3 pyramidal neuron was reconstructed. **(B)** Phase response curves obtained in the alpha (blue; 9 Hz) and gamma (red; 24 Hz) frequency ranges of the neuron described in **(A)**. The abscissa represents the phase at which the neuron was stimulated by a perturbative input and the ordinate the phase response to it. Each dot represents a noisy phase response to a stimulus. Blue and red solid curves display the average PRC obtained by the least-mean-square method. **(C,D)** The morphological structure of a layer 5 pyramidal neuron and its phase response curves obtained in the alpha (blue; 9 Hz) and gamma (red; 21 Hz) frequency ranges. [Modified from Tsubo et al. (2007a)].

vanishes at such low frequencies even if the PRC belongs to type 1 (**Figure 2**).

The implications of the above results for oscillatory synchronization are as follows. In the gamma frequency range, which is of particular cognitive importance (Ward, 2003; Herrmann et al., 2004), recurrent AMPA synaptic connections possibly promote synchronous neuronal firing of layer 2/3 pyramidal neurons, but not that of layer 5 pyramidal neurons. Compared to the gamma frequency range, the differences in the PRC type will not be crucial for synchronous firing in the theta, alpha and beta frequency ranges owing to the long time scales of the oscillation period relative to the decay constant of the AMPA receptor-mediated synaptic current.

In summary, the PRCs of the population of layer 5 pyramidal neurons displayed no significantly negative phase in all frequency ranges, suggesting that the PRC type of these neurons is primarily type 1. In contrast, the phase responses recorded from layer 2/3 pyramidal neurons constitutes a heterogeneous mixture of the two types. In the superficial layer, the type 2 is dominant phase response type in the gamma frequency range and seems to be dominant also in the theta frequency range. Both type 1 and type 2 appear equally often in the alpha and beta frequency ranges. In 46% of the layer 2/3 neurons and 30% of the layer 5 neurons, the PRC types were different in the different frequency ranges. Implications of the heterogeneous mixture of the PRC types for the dynamics of neuronal synchronization are found in Tsubo et al. (2007b).

MOTOR CORTEX ACTIVITY DURING VOLUNTARY MOVEMENTS

As described above, we found that the potential ability of single neurons for synchronization is different between superficial and deep layers of the rat motor cortex *in vitro*. Then, how do

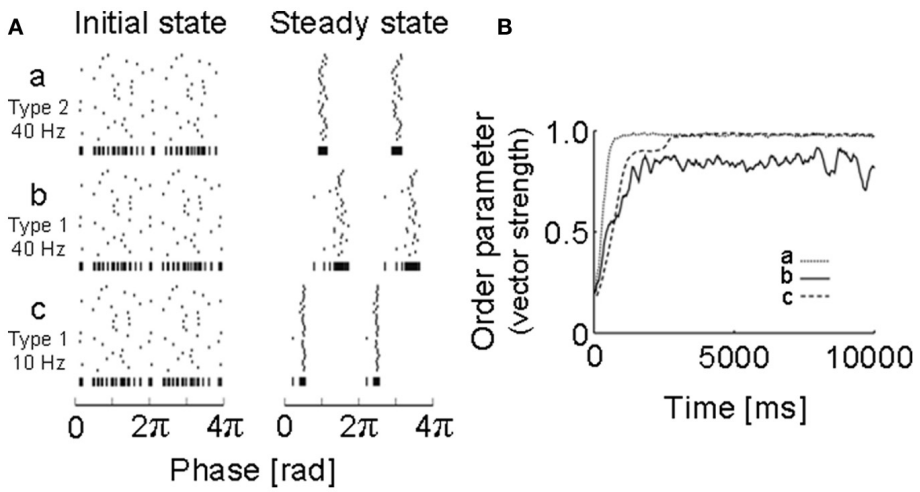

FIGURE 2 | Simulations of neural oscillators coupled with a PRC obtained for a motor cortex neuron. **(A)** Initial states and steady states were obtained by numerical simulations of 30 neuronal oscillators coupled mutually via fast AMPA synapses: a, 40 Hz (type 2); b, 40 Hz (type 1); c, 10 Hz (type 1). Vertical bars at the bottom of each raster plot represent all spikes of the 30 neurons in one sequence to visualize the degree of synchrony. **(B)** How the degree of synchrony evolved in the 30-neuron networks shown in **(A)** was presented using the phase order parameters, which are equal to unity when all oscillators are entrained into perfect in-phase synchronization, while it is zero when they exhibit asynchronous oscillations. [Modified from Tsubo et al. (2007a)].

the motor cortex neurons work cooperatively in order to execute a certain voluntary movement *in vivo*? For example, it is possible that superficial layer neurons of motor cortex may participate in preparation for the movement while deep layer neurons participate in execution of it. It is also possible that excitatory pyramidal cells of motor cortex may drive the movement while inhibitory interneurons simply suppress it. However, it has been technically difficult to morphologically identify an electrophysiologically recorded neuron, or even to distinguish excitatory (pyramidal cells) and inhibitory (interneurons), in awake animals, especially in those performing an operant behavioral task. To address this issue, we first developed an efficient task-training system in which several rats simultaneously and independently learned a behavioral task (e.g., an operant learning of lever manipulation with forelimb) in a head-fixed condition (Isomura et al., 2009; see also Kimura et al., 2012). This enabled us to test a sufficient number of behaving animals for morphological and electrophysiological experiments. We thus combined the behavioral task system with a juxtacellular recording, which is a unique electrophysiological technique to record spiking activity of a single neuron accurately and stably, and later to visualize its morphological structure (Pinault, 1996).

Our juxtacellular recordings from the forelimb area of motor cortex during forelimb movements revealed that identified pyramidal cells increased their spiking activity at a variety of timing around the onset of lever pull movement (Isomura et al., 2009). Some of them showed sustained or slowly changing activation in a lever hold period before the movement onset (**Figure 3A**; namely, hold-related activity), which might be involved in motor preparation or suppression, and others showed phasic activation during the movement (**Figure 3B**; movement-related activity), which might be involved in motor execution or sensory feedback. Thus, the pyramidal cells of motor cortex participate in several different functions for a voluntary movement. Importantly, we revealed the pyramidal cells with hold-related activity were not restricted to a specific layer, but in all the layers of motor cortex except for layer 1. The pyramidal cells with movement-related activity were also present in layers 2 through 6 of motor cortex. Though recent work in primate motor cortex suggests that relationships between neuronal activity and motor behavior are generally complex (Churchland et al., 2012), the execution and preparation phases of movement likely represent distinct task demands and may be treated separately, as in the present task. It is noteworthy that Weiler et al. (2008) indicated that an excitatory connection from superficial (2/3) layers to deep (5) layer is the strongest pathway between distinct layers of the motor cortex. Thus, the movement-related pyramidal cells in the layer 2/3 may send their motor information to those in the layer 5 to execute the movement.

Now we turn to the functional activity of a major subclass of neocortical GABAergic interneurons, i.e., FS interneurons including the basket cells and chandelier cells morphologically, and often expressing the calcium-binding protein parvalbumin as an FS neuron-specific marker (Markram et al., 2004). We obtained juxtacellular recordings from the FS interneurons of motor cortex during the voluntary movement. In contrast to the functional diversity of pyramidal cells, most of the FS neurons dominantly exhibited the phasic movement-related activity in relation to the voluntary movement (**Figure 3C**; Isomura et al., 2009). It is therefore unlikely that the FS neurons simply suppress actual

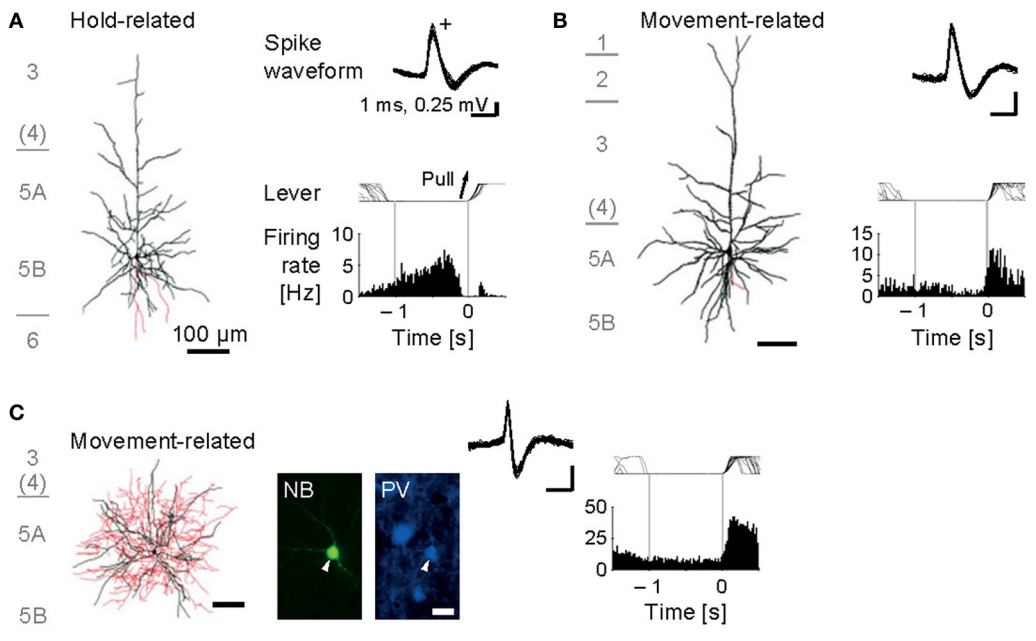

FIGURE 3 | Functional activity in identified motor cortex neurons. **(A)** Juxtacellularly identified layer 5 pyramidal cell that exhibited hold-related activity. Left, visualized soma and dendrites (black) and axons (red). Right, recorded spike waveforms (top) and functional spike activity histogram aligned with the onset of lever pull movement (0 s). **(B)** Layer 5 pyramidal cell with movement-related activity. **(C)** Layer 5 fast-spiking (FS) basket cell with movement-related activity. Bottom, fluorescent images for Neurobiotin (NB) and parvalbumin (PV). [Modified from Isomura et al. (2009)].

muscular movements through inhibitory synaptic transmissions. One may consider two possibilities to account for their phasic activation during voluntary movements. One possibility is "balanced inhibition" (feedforward inhibition), in which inhibitory FS neurons shape a motor command together with excitatory pyramidal cells. This hypothetical function is similar to balanced inhibition observed in the auditory cortex (Wehr and Zador, 2003) and somatosensory cortex (Okun and Lampl, 2008). The other is "recurrent inhibition" (feedback inhibition), in which excitatory pyramidal cells for a specific movement selectively inactivate nearby neurons coding unnecessary movements via collateral activation of inhibitory neurons (Georgopoulos and Stefanis, 2007). In any case, the FS neurons do not extinguish a voluntary movement, but actively elaborate it in cooperation with the pyramidal cells.

Furthermore, we analyzed multiunit activity in the motor cortex to examine functional interactions among putative excitatory and inhibitory cortical neurons during voluntary movements (Isomura et al., 2009). In the multiunit analysis, spikes were automatically isolated and clustered by our spike-sorting software (Takekawa et al., 2010, 2012), and then we classified the spike clusters into regular-spiking (RS) and FS neurons by the difference in spike width. The RS neurons in the neocortex appear to be mainly excitatory pyramidal cells, but also likely include inhibitory non-FS interneurons. Conversely, some pyramidal cells were recently shown to discharge thin spikes and may be misclassified as interneurons (Suter et al., 2012). **Figure 4** shows that an example pair of one RS neuron and one FS neuron with movement-related activity increased the probability of their synchronous spiking within several milliseconds, which is represented by a single short-latency peak in their cross-correlogram. The RS neuron displayed similar synchronous spiking with another RS neuron with hold-related activity, too. Thus, motor cortex neurons discharged synchronously with functionally similar or different neurons, which happened in about 2% of possible neuron pairs. Such synchronous spiking between two neurons can be driven directly by monosynaptic excitation (Barthó et al., 2004) or indirectly by common excitatory inputs from the third neuron. In both cases, the highly effective synaptic excitation may be clarified by exceptional large-amplitude synaptic transmissions (Lefort et al., 2009; Morishima et al., 2011).

IRREGULAR NEURONAL FIRING IN MOTOR CORTEX

In the former section, we showed the dynamical behavior of neuronal networks in the primary motor cortex of rats performing a simple lever movement behavior. The results of *in vivo* electrophysiological recordings demonstrated that motor cortical neurons exhibit diverse functional neuronal subtypes in different layers and each neuronal subtype is activated concurrently, rather than sequentially, in the multiple layers. In this section, we turn to yet another question about the implications of irregular firing of a single motor cortex neuron for information coding. Namely, we propose that firing of cortical neurons distribute their firing rates to maximize the amount of total information represented by the distributed firing rates under some constraints, which we may call "the CMFE" hypothesis.

We first explain key observations to the CMFE about the statistical property of irregular spike sequences in the motor cortex of behaving rats. For given statistics of input spike trains, distributions of inter-spike intervals (ISIs) represent a basic property of the responses of neurons. Poisson distributions or gamma distributions are generally considered to well represent the ISI distributions of cortical neurons. However, we recently found that the ISI distributions of the majority of motor cortex neurons show a power-law decaying long tail in behaving rats (**Figure 5**) (Tsubo et al., 2012). The power law of ISI distributions was found in more than half of the motor cortex neurons we recorded irrespective of their laminar locations and functional subtypes. Thus, a question was raised about whether the power-law ISI distributions have any implication for the information representation of cortical

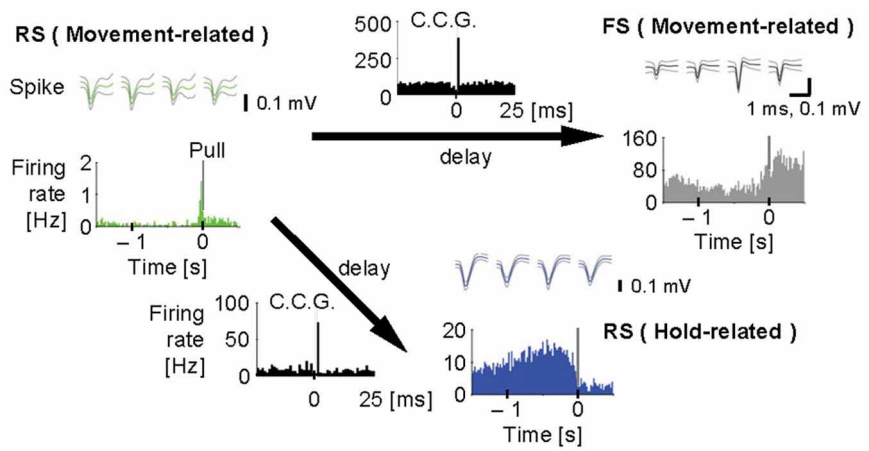

FIGURE 4 | Synchronous spiking among motor cortex neurons. Cross-correlograms (black, C.C.G.; 1 ms bins) among a regular-spiking (RS) neuron with movement-related activity (green), an FS neuron with movement-related activity (gray), and another RS neuron with hold-related activity (blue). **Top**, spike waveforms [scale bars, 1 ms (the same for all spike traces) and 0.1 mV]. **Bottom**, pull-aligned (0 s) functional spike activity histogram (colored; 20 ms bins) in each neuron. Vertical bars indicate the onset of lever-pull. Each arrow means the direction of delay suggested by the peak in C.C.G. Y-axes indicate firing rate (Hz) in all the histograms. [Modified from Isomura et al. (2009)].

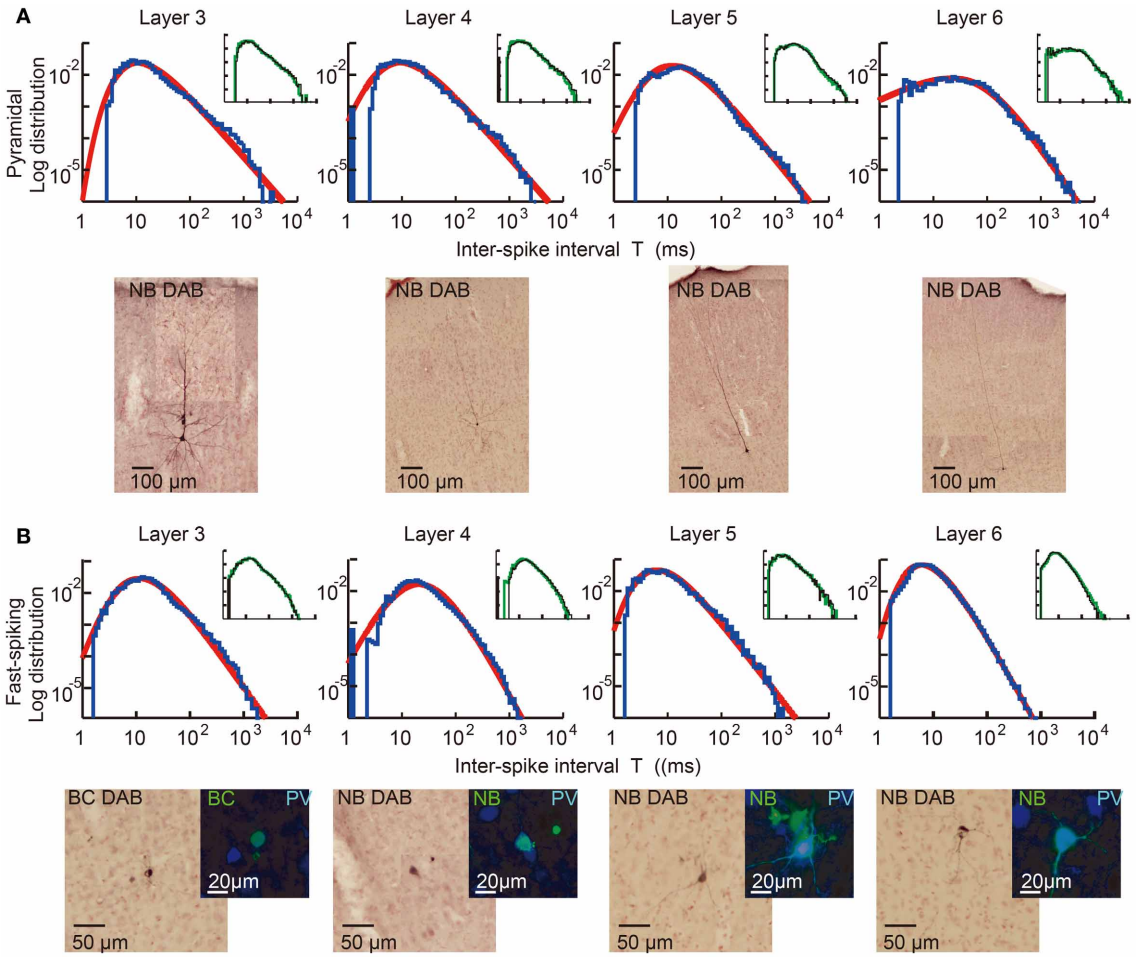

FIGURE 5 | Power-law ISI distributions of *in vivo* motor cortex neurons in different layers. Juxta-cellular visualization and double-logarithmic plots of the ISI histograms (blue curves) of pyramidal neurons **(A)** and fast-spiking interneurons **(B)** recorded in layers 3, 4, 5, and 6 of rat motor cortex. The plots were fitted by neuron-dependent beta-2 distributions (red), and light micrographs display the morphological reconstruction of the eight neurons obtained by DAB (3,3′-diaminodbenzidine)-Nickel staining. The four neurons in **(B)** expressed parvalbumin (PV), a fast-spiking interneuron specific marker (blue: PV, green: biocytin or Neurobiotin). Inset of each panel represents the ISI distributions constructed from the 1st (black) and 2nd (green) halves of the same spike train. They prove the stationarity of the ISI distributions during the recordings. [Modified from Tsubo et al. (2012)].

neurons. What message should we read out about cortical computation from such ISI distributions?

To answer this question, we employ the following double stochastic gamma (DSG) model and describe the ISI distributions of *in vivo* motor cortex neurons as:

$$P_{\text{vivo}}(T) = \int_0^\infty q(T|r)P_{\text{vivo}}(r)dr, \qquad (1)$$

where T stands for ISI. This equation regards a neuron as a translator of its internal state into an irregular output spike train of firing rate r, when irregular input spike trains set the neuron in the specific internal state. Note that here the firing rate r is regarded as a parameter that specifies neuron's internal state. For the consistency of the framework, the rate parameter should coincide with the firing rate of the neuron for stationary synaptic input. However, the value of r may vary dynamically and fluctuate in time for non-stationary synaptic input. Then, $P_{\text{vivo}}(r)$ is regarded as the probability that input to the neuron sets the value of the rate parameter equal to r, and $q(T|r)$ refers to the ISI distribution at given rate r and represents an intrinsic property of the neuron in spike generation.

We may determine the expression of $q(T|r)$ by measuring spike sequences of pharmacologically isolated neurons responding to a fluctuating input current that mimics balanced excitatory and inhibitory synaptic input. We indeed performed such recordings from a slice preparation of motor cortex and found that $q(T|r)$ is given as a gamma distribution for the mean rate r (Miura et al., 2007). Then, Equation 1 implies that the ISI distribution of an *in vivo* cortical neuron is given as the convolution of the ISI distribution of *in vitro* neurons and the distribution of the instantaneous values of the rate parameter. This is a good approximation if the rate parameter changes its value only slowly compared to the cell's instantaneous rate of spike generation. If we

use the fact that $P_{\text{vivo}}(T)$ is well expressed by a class of power-law distributions called "generalized beta-2 distribution":

$$P_{\text{vivo}}(T) \sim P_{\beta 2}(T) = \frac{\tau^{\alpha}\Gamma(\alpha+\kappa)}{\Gamma(\alpha)\Gamma(\kappa)} \frac{T^{\kappa-1}}{(T+\tau)^{\alpha+\kappa}}, \quad (2)$$

we can analytically show that $P_{\text{vivo}}(r)$ is well described as the gamma distribution with the mean $R = \alpha/\kappa\tau$: $P_{\text{vivo}}(r) = [(\alpha/R)^{\alpha}/\Gamma(\alpha)]r^{\alpha-1}e^{-\alpha r/R}$.

Now, an intriguing question arises. Why does $P_{\text{vivo}}(r)$ assume a form of the gamma distribution in the majority of motor cortex neurons? Does it happen to be so or is there any profound reason for that? In the next section, we show some evidence supporting for the latter.

CMFE: A VARIATIONAL PRINCIPLE

Fundamental principles in physics and biology are often written in terms of variational principles in mathematics. For instance, in statistical physics the equilibrium state of a stochastic system is represented as a solution that minimizes the free energy, which is a function of the temperature and the microscopic variables describing the dynamical system. This view was also argued for the nonlinear dynamics of neural networks (Friston, 2010). In the present case, we consider the problem of minimizing the following objective function:

$$J = -H[R] + \lambda_r\left(\bar{R} - R_{\max}\right) + \lambda_e\left(H[T|R] - H_{\max}\right) + \lambda_0\left(\int_0^{\infty} P_s(r)dr - 1\right). \quad (3)$$

Below, we explain the meaning of each term in the right-hand side of the above functional J.

The first term in Equation 3 expresses the negative entropy of the time-varying firing rate of the neuron as a functional of the stationary distribution of firing rate $P_s(r)$:

$$H[R] = -\int_0^{\infty} P_s(r)\ln P_s(r)dr. \quad (4)$$

We note that minimizing J essentially implies the maximization of the firing-rate entropy $H(R)$. If this entropy is larger, the neuron is considered to use a wider variety of firing rates in its output spike train. The second term involves the average firing rate of the neuron

$$\bar{R} = \int_0^{\infty} rP_s(r)dr, \quad (5)$$

and represents a constraint on the maximum value of the average firing rate. Since neuronal firing will require more energy at a higher frequency, this term imposes a limitation on the energy consumption of cell firing. The third term involves the conditional response entropy:

$$H[T|R] = -\int_0^{\infty} P_s(r)\int_0^{\infty} q(T|r)\log q(T|r)\,dTdr, \quad (6)$$

which represents the average uncertainty of sequence of the ISIs generated by the neuron. The above quantity was also called "neuronal noise" (Borst and Theunissen, 1999). In this view, the function $q(T|r)$ describes the degree of irregularity in the spike generation of the neuron at given firing rate r. Thus, the smaller the conditional response entropy is, the more reliable the spike generation is (Stevens and Zador, 1998). The last term in Equation 3 imposes the normalization condition on the probability density function $P_s(r)$.

To obtain the stationary firing-rate distribution $P_s(r)$ in CMFE, we have to find out such a $P_s(r)$ that minimizes J with Lagrange multipliers satisfying $-\infty < \lambda_0 < \infty$ and $\lambda_r, \lambda_e \geq 0$. This minimization problem implies the maximization of the entropy of the firing-rate distribution $H[R]$ under the constraints on the energy consumption (the maximum of average firing rate) and the maximum conditional entropy $H[T|R]$. For a scale-invariant ISI distribution $q(T|r)dT = f(Tr)rdT$, we can analytically solve the above maximization problem to find $P_s(r)$. Especially for the gamma ISI distribution $q(T|r) = [(\kappa r)^{\kappa}/\Gamma(\kappa)]T^{\kappa-1}e^{-\kappa rT}$ (Miura et al., 2007), $P_s(r)$ is also given as a gamma distribution (Kuhn and Tucker, 1951): $P_s(r) \propto r^{\lambda_e}e^{-\lambda_r r}$. Thus, $P_s(r)$ coincides with $P_{\text{vivo}}(r)$ after appropriate redefinition of the parameters.

IMPLICATIONS OF CMFE FOR NEURAL INFORMATION TRANSMISSIONS

The hypothesis of CMFE describes a solution to solve the cost-information trade-off in irregular neuronal firing. The CMFE hypothesis is an extension of the "maximum entropy of firing rate" with additional constraints on the conditional response entropy, where the firing-rate entropy means the variety of firing rates available for neuronal communication. The average energy consumed by a neuron may increase proportionally with firing rate. However, the conditional entropy will be increased for output spike trains if neurons use lower firing rate more frequently. Thus, our results imply that the firing rate values of motor cortex neurons are distributed so as to balance the tradeoff between the average uncertainty of output spike sequences and the energy consumption in spike generation.

The CMFE hypothesis is different from the so-called mutual information maximization (MIM). Mutual information between two probability variables represents the amount of information obtained for a variable by measuring the other. A widely adopted hypothesis is that neurons maximize mutual information between input and output (MacKay and McCulloch, 1952; Stein, 1967; Linsker, 1986; Bell and Sejnowski, 1995). According to MIM, noisy spiking neurons can maximize mutual information at given average firing rate only when it takes discrete values (Chan et al., 2005; Ikeda and Manton, 2009). However, such a discrete representation with firing rate does not seem to be consistent with our observations in rat motor cortex, and the CMFE hypothesis better accounts for the spike statistics of *in vivo* neurons in all layers of motor cortex.

DISCUSSION

We reviewed the PRCs of RS pyramidal neurons in layers 2/3 and 5 recorded from slice preparations of the rat motor cortex. The PRC is of particular interest since it gives some information on whether neurons may be synchronized or desynchronized with given

synaptic input. We have found that the intrinsic response property of pyramidal neurons in oscillatory synchronization depends on the range of firing rates and the cortical layers they belong to. Interesting differences between cortical layers are observed in the PRCs in gamma band. Namely, in the frequency range from 20 to 80 Hz, layer 2/3 or layer 5 pyramidal neurons tend to possess type-2 or type-1 PRCs, respectively. These results imply that recurrent AMPA synaptic connections possibly promote synchronous neuronal firing of layer 2/3 pyramidal neurons in gamma band, but not that of layer 5 pyramidal neurons. The PRC type was also different in the theta frequency range. However, numerical simulations of a network model showed that the stable phase difference is close to 0 at low frequencies of 8–13 Hz even if the PRC belongs to type 1 (Tsubo et al., 2007a). Therefore, the layer-dependence of the PRC type may play an active role in synchronous firing at gamma frequencies, but not in other frequency ranges in rat motor cortex.

We may speculate possible implications of the above findings on PRCs for layer-specific cortical computations. The major portion of excitatory synapses on layer 2/3 pyramidal neurons originates from the surrounding layer 2/3 pyramidal neurons (Thomson and Bannister, 2003; Binzegger et al., 2004). Then, the layer 2/3 pyramidal neurons might serve as "resonant oscillators" (Izhikevich, 2000, 2004) through the synergistic effects of the rich recurrent synapses and the type-2 PRC. By contrast, layer 5 pyramidal neurons might operate as "integrators" since the type-1 neuron exhibits a continuous spectrum of firing rate from very low to high frequencies (Hodgkin, 1948; Tateno et al., 2004). These views seem to be consistent with the significant differences in firing rate between the superficial and deep layers of motor cortex in behaving rats.

Our observations in the microcircuit of motor cortex in behaving rats undoubtedly excludes the "layer-by-layer activation" hypothesis in which each layer of motor cortex has its own function for the movement phases, e.g., layers 2/3 for motor preparation and layer 5 for motor execution; instead, it supports "multi-layer activation" hypothesis that all the cortical layers cooperatively participate in every phase of the voluntary movement. Nevertheless, it is quite likely that a superficial layer circuit and a deep layer circuit may process the same information by different circuitry algorithms or for different functional purposes, since the spiking activity of deep layer neurons is generally much higher than that of superficial layer neurons in the neocortex. In fact, our preliminary data suggest that hold-related activity neurons are not distributed uniformly along the motor cortex layers (Igarashi et al., unpublished observation). Besides layer differences, it remains elusive whether the motor information simply flows in a one-way direction from superficial to deeper layers intracortically or reverberates for signal amplification or development through cortico-cortical and cortico-subcortical loops [cf., Weiler et al. (2008) and Anderson et al. (2010) for layer-specific connectivity in motor cortex]. In addition, we recently found that most motor cortex neurons were phase-locked to gamma oscillations of LFP (Igarashi et al., unpublished observation). It suggests that these neurons may communicate in a microcircuit through spike synchronization on a specific phase of the gamma oscillations. As neocortical gamma oscillations are widely influenced by the hippocampal theta activity (Sirota et al., 2008), synchronous spiking during gamma oscillations may be a common mechanism underlying neuronal communications in the neocortex and hippocampus.

Finally, we have proposed CMFE to account for the power-law statistics of irregular firing of motor cortex neurons. The hypothesis of CMFE yields a novel view of the way neurons translate information on firing rate into irregular spike trains. A significant advantage of the brain over modern supercomputers is the very low power consumption. While the storage and transmission of information should be very accurate in electric computers, the CMFE does not require a very high accuracy. Artificial information machines require the precision at the expense of the amount of representable information, i.e., the entropy, whereas the brain likely possesses a variety of communication windows at the expense of the transfer information. The CMFE suggests a mathematical principle for neural information coding alternative to the maximization of mutual information.

Our results explained in this article have revealed some key features of the layer-specific information processing in the microcircuit of motor cortex. However, the basic circuit design for this information processing still remains largely unknown. In particular, we predict a link between the CMFE hypothesis for irregular spiking and the multi-band oscillations observed in motor cortex. In this respect, it is intriguing to examine whether the CMFE hypothesis is valid for sensory cortices, which often display significant gamma oscillations. What aspect of motor information is processed in each layer? How does such information flow between different layers? How does each layer of motor cortex communicate with other cortical and subcortical regions? All these questions should be answered more clearly in future studies.

ACKNOWLEDGMENTS

This work was partly supported by Grants-in-Aid for Scientific Research on Innovative Areas (no. 22115013) to Tomoki Fukai and Grants-in-Aid for Young Scientists (B) (22700323) to Yasuhiro Tsubo.

REFERENCES

Anderson, C. T., Sheets, P. L., Kiritani, T., and Shepherd, G. M. (2010). Sublayer–specific microcircuits of corticospinal and corticostriatal neurons in motor cortex. *Nat. Neurosci.* 13, 739–744.

Barthó, P., Hirase, H., Monconduit, L., Zugaro, M., Harris, K. D., and Buzsáki, G. (2004). Characterization of neocortical principal cells and interneurons by network interactions and extracellular features. *J. Neurophysiol.* 92, 600–608.

Bell, A. J., and Sejnowski, T. J. (1995). An information–maximization approach to blind separation and blind deconvolution. *Neural Compt.* 7, 1129–1159.

Berkes, P., Orbán, G., Lengyel, M., and Fiser, J. (2011). Spontaneous cortical activity reveals hallmarks of an optimal internal model of the environment. *Science* 331, 83–87.

Binzegger, T., Douglas, R. J., and Martin, K. A. (2004). A quantitative map of the circuit of cat primary visual cortex. *J. Neurosci.* 24, 8441–8453.

Borst, A., and Theunissen, F. E. (1999). Information theory and neural coding. *Nat. Neurosci.* 2, 947–957.

Brecht, M., Krauss, A., Muhammad, S., Sinai–Esfahani, L., Bellanca, S., and Margrie, T. W. (2004). Organization of rat vibrissa motor cortex and adjacent areas according to cytoarchitectonics, microstimulation and

intracellular stimulation of identified cells. *J. Comp. Neurol.* 479, 360–373.

Buesing, L., Bill, J., Nessler, B., and Maass, W. (2011). Neural dynamics as sampling: a model for stochastic computation in recurrent networks of spiking neurons. *PLoS Comput. Biol.* 7:e1002211. doi: 10.1371/journal.pcbi.1002211

Chan, T. H., Hranilovic, S., and Kschischang, F. R. (2005). Capacity–achieving probability measure for conditionally Gaussian channels with bounded inputs. *IEEE Trans. Inf. Theory* 51, 2073–2088.

Cho, R. H., Segawa, S., Mizuno, A., and Kaneko, T. (2004a). Intracellularly labeled pyramidal neurons in the cortical areas projecting to the spinal cord. I. Electrophysiological properties of pyramidal neurons. *Neurosci. Res.* 50, 381–394.

Cho, R. H., Segawa, S., Okamoto, K., Mizuno, A., and Kaneko, T. (2004b). Intracellularly labeled pyramidal neurons in the cortical areas projecting to the spinal cord. II. Intra– and juxta–columnar projection of pyramidal neurons to corticospinal neurons. *Neurosci. Res.* 50, 395–410.

Churchland, M. M., Cunningham, J. P., Kaufman, M. T., Foster, J. D., Nuyujukian, P., Ryu, S., et al. (2012). Neural population dynamics during reaching. *Nature* 487, 51–56.

Churchland, M. M., and Shenoy, K. V. (2007). Temporal complexity and heterogeneity of single-neuron activity in premotor and motor cortex. *J. Neurophysiol.* 97, 4235–4257.

de Kock, C. P. J., Bruno, R. M., Spors, H., and Sakmann, B. (2007). Layer– and cell type–specific suprathreshold stimulus representation in rat primary somatosensory cortex. *J. Physiol. (Lond.)* 581, 139–154.

Destexhe, A., Rudolph, M., and Paré, D. (2003). The high-conductance state of neocortical neurons *in vivo*. *Nat. Rev. Neurosci.* 4, 739–751.

Donoghue, J. P., Sanes, J. N., Hatsopoulos, N. G., and Gaál, G. (1998). Neural discharge and local field potential oscillations in primate motor cortex during voluntary movements. *J. Neurophysiol.* 79, 159–173.

Donoghue, J. P., and Wise, S. P. (1982). The motor cortex of the rat: cytoarchitecture and microstimulation mapping. *J. Comp. Neurol.* 212, 76–88.

Ermentrout, B. (1996). Type I membranes, phase resetting curves, and synchrony. *Neural Comput.* 8, 979–1001.

Ermentrout, B., Pascal, M., and Gutkin, B. (2001). The effects of spike frequency adaptation and negative feedback on the synchronization of neural oscillators. *Neural Comput.* 13, 1285–1310.

Farmer, S. F. (1998). Rhythmicity, synchronization and binding in human and primate motor systems. *J. Physiol.* 509, 3–14.

Friston, K. (2010). The free–energy principle: a unified brain theory? *Nat. Rev. Neurosci.* 11, 127–138.

Galan, R. F., Ermentrout, G. B., and Urban, N. N. (2005). Efficient estimation of phase–resetting curves in real neurons and its significance for neural–network modeling. *Phys. Rev. Lett.* 94, 158101.

Georgopoulos, A. P., Schwartz, A. B., and Kettner, R. E. (1986). Neuronal population coding of movement direction. *Science* 233, 1416–1419.

Georgopoulos, A. P., and Stefanis, C. N. (2007). Local shaping of function in the motor cortex: motor contrast, directional tuning. *Brain Res. Rev.* 55, 383–389.

Goldberg, J. A., Deister, C. A., and Wilson, C. J. (2007). Response properties and synchronization of rhythmically–firing dendritic neurons. *J. Neurophysiol.* 97, 208–219.

Gutkin, B. S., Ermentrout, G. B., and Reyes, A. D. (2005). Phase–response curves give the responses of neurons to transient inputs. *J. Neurophysiol.* 94, 1623–1635.

Hansel, D., Mato, G., and Meunier, C. (1995). Synchrony in excitatory neural networks. *Neural Comput.* 7, 307–337.

Harris, K. D., Henze, D. A., Csicsvari, J., Hirase, H., and Buzsáki, G. (2000). Accuracy of tetrode spike separation as determined by simultaneous intracellular and extracellular measurements. *J. Neurophysiol.* 84, 401–414.

Hatsopoulos, N. G., and Suminski, A. J. (2011). Sensing with the motor cortex. *Neuron* 72, 477–487.

Herrmann, C. S., Munk, M. H., and Engel, A. K. (2004). Cognitive functions of gamma–band activity: memory match and utilization. *Trends Cogn. Sci.* 8, 347–355.

Hodgkin, A. L. (1948). The local electric changes associated with repetitive action in a non–medullated axon. *J. Physiol.* 107, 165–181.

Ikeda, S., and Manton, J. H. (2009). Capacity of a single spiking neuron channel. *Neural Compt.* 21, 1714–1748.

Isomura, Y., Harukuni, R., Takekawa, T., Aizawa, H., and Fukai, T. (2009). Microcircuitry coordination of cortical motor information in self–initiation of voluntary movements. *Nat. Neurosci.* 12, 1586–1593.

Isomura, Y., Sirota, A., Ozen, S., Montgomery, S., Mizuseki, K., Henze, D. A., et al. (2006). Integration and segregation of activity in entorhinal–hippocampal subregions by neocortical slow oscillations. *Neuron* 52, 871–882.

Izhikevich, E. M. (2000). Neural excitability, spiking, and bursting. *Int. J. Bifurc. Chaos* 10, 1171–1266.

Izhikevich, E. M. (2004). Which model to use for cortical spiking neurons? *IEEE Trans. Neural Netw.* 15, 1063–1070.

Kimura, R., Saiki, A., Fujiwara–Tsukamoto, Y., Ohkubo, F., Kitamura, K., Matsuzaki, M., et al. (2012). Reinforcing operandum: rapid and reliable learning of skilled forelimb movements by head–fixed rodents. *J. Neurophysiol.* 108, 1781–1792.

Klausberger, T., Magill, P. J., Márton, L. F., Roberts, J. D., Cobden, P. M., Buzsáki, G., et al. (2003). Brain state– and cell type–specific firing of hippocampal interneurons *in vivo*. *Nature* 421, 844–848.

Kuhn, H. W., and Tucker, A. W. (1951). "Nonlinear programming," in *Proceedings of the Second Berkeley Symposium on Mathematical Statistics and Probability* (Berkeley, CA), 481–492.

Kuramoto, Y. (1984). *Chemical Oscillations, Waves, and Turbulence*. Berlin: Springer–Verlag.

Lee, M. G., Manns, I. D., Alonso, A., and Jones, B. E. (2004). Sleep–wake related discharge properties of basal forebrain neurons recorded with micropipettes in head–fixed rats. *J. Neurophysiol.* 92, 1182–1198.

Lefort, S., Tomm, C., Floyd Sarria, J. C., and Petersen, C. C. (2009). The excitatory neuronal network of the C2 barrel column in mouse primary somatosensory cortex. *Neuron* 61, 301–316.

Lengyel, M., Kwag, J., Paulsen, O., and Dayan, P. (2005). Matching storage and recall: hippocampal spike timing-dependent plasticity and phase response curves. *Nat. Neurosci.* 8, 1677–1683.

Linsker, R. (1986). From basic network principles to neural architecture: emergence of orientation-selective cells. *Proc. Natl. Acad. Sci. U.S.A.* 83, 8390–8394.

Ma, W. J., Beck, J. M., Latham, P. E., and Pouget, A. (2006). Bayesian inference with probabilistic population codes. *Nat. Neurosci.* 9, 1432–1438.

MacKay, D. M., and McCulloch, W. S. (1952). The limiting information capacity of a neuronal link. *Bull. Math. Biophys.* 14, 127–135.

Mallet, N., Ballion, B., Le Moine, C., and Gonon, F. (2006). Cortical inputs and GABA interneurons imbalance projection neurons in the striatum of parkinsonian rats. *J. Neurosci.* 26, 3875–3884.

Markram, H., Toledo–Rodriguez, M., Wang, Y., Gupta, A., Silberberg, G., and Wu, C. (2004). Interneurons of the neocortical inhibitory system. *Nat. Rev. Neurosci.* 5, 793–807.

Merchant, H., Naselaris, T., and Georgopoulos, A. P. (2008). Dynamic sculpting of directional tuning in the primate motor cortex during three–dimensional reaching. *J. Neurosci.* 28, 9164–9172.

Miura, K., Tsubo, Y., Okada, M., and Fukai, T. (2007). Balanced excitatory and inhibitory inputs to cortical neurons decouple firing irregularity from rate modulations. *J. Neurosci.* 27, 13802–13812.

Morishima, M., Morita, K., Kubota, Y., and Kawaguchi, Y. (2011). Highly differentiated projection–specific cortical subnetworks. *J. Neurosci.* 31, 10380–10391.

Murthy, V. N., and Fetz, E. E. (1996). Oscillatory activity in sensorimotor cortex of awake monkeys: synchronization of local field potentials and relation to behavior. *J. Neurophysiol.* 76, 3949–3967.

Netoff, T. I., Acker, C. D., Bettencourt, J. C., and White, J. A. (2005a). Beyond two–cell networks: experimental measurement of neuronal responses to multiple synaptic inputs. *J. Comput. Neurosci.* 18, 287–295.

Netoff, T. I., Banks, M. I., Dorval, A. D., Acker, C. D., Haas, J. S., Kopell, N., et al. (2005b). Synchronization in hybrid neuronal networks of the hippocampal formation. *J. Neurophysiol.* 93, 1197–1208.

Nomura, M., Fukai, T., and Aoyagi, T. (2003). Synchrony of fast–spiking interneurons interconnected by GABAergic and electrical synapses. *Neural Comput.* 15, 2179–2198.

Okun, M., and Lampl, I. (2008). Instantaneous correlation of excitation and inhibition during ongoing and sensory-evoked activities. *Nat. Neurosci.* 11, 535–537.

Pinault, D. (1996). A novel single–cell staining procedure performed *in vivo* under electrophysiological control: morpho–functional features of juxtacellularly labeled thalamic cells and other central neurons with biocytin or Neurobiotin. *J. Neurosci. Methods* 65, 113–136.

Rao, R. P. N., Olshausen, B. A., and Lewicki, M. S. (2002). *Probabilistic Models of the Brain*. Cambridge, MA: MIT Press.

Reyes, A. D., and Fetz, E. E. (1993a). Two modes of interspike interval shortening by brief transient depolarizations in cat neocortical neurons. *J. Neurophysiol.* 69, 1661–1672.

Reyes, A. D., and Fetz, E. E. (1993b). Effects of transient depolarizing potentials on the firing rate of cat neocortical neurons. *J. Neurophysiol.* 69, 1673–1683.

Rouiller, E. M., Moret, V., and Liang, F. (1993). Comparison of the connectional properties of the two forelimb areas of the rat sensorimotor cortex: support for the presence of a premotor or supplementary motor cortical area. *Somatosens. Mot. Res.* 10, 269–289.

Sanes, J. N., and Donoghue, J. P. (1993). Oscillations in local field potentials of the primate motor cortex. *Proc. Natl. Acad. Sci. U.S.A.* 90, 4470–4474.

Shepherd, G. M. G. (2009). Intracortical cartography in an agranular area. *Front. Neurosci.* 3:3. doi: 10.3389/neuro.01.030.2009

Shu, Y., Hasenstaub, A., and McCormick, D. A. (2003). Turning on and off recurrent balanced cortical activity. *Nature* 423, 288–293.

Sirota, A., Montgomery, S., Fujisawa, S., Isomura, Y., Zugaro, M., and Buzsáki, G. (2008). Entrainment of neocortical neurons and gamma oscillations by the hippocampal theta rhythm. *Neuron* 60, 683–697.

Smeal, R. M., Ermentrout, G. B., and White, J. A. (2010). Phase-response curves and synchronized neural networks. *Philos. Trans. R. Soc. Lond. B Biol. Sci.* 365, 2407–2422.

Stein, R. B. (1967). The information capacity of nerve cells using a frequency code. *Biophys. J.* 7, 797–826.

Stevens, C. F., and Zador, A. M. (1998). Input synchrony and the irregular firing of cortical neurons. *Nat. Neurosci.* 1, 210–217.

Stiefel, K. M., Gutkin, B. S., and Sejnowski, B. S. (2008). Cholinergic neuromodulation changes phase response curve shape and type in cortical pyramidal neurons. *PLoS ONE* 3:e3947. doi: 10.1371/journal.pone.0003947

Suter, B. A., Migliore, M., and Shepherd, G. M. (2012). Intrinsic electrophysiology of mouse corticospinal neurons: a class-specific triad of spike-related properties. *Cereb. Cortex*, doi: 10.1093/cercor/bhs184. [Epub ahead of print].

Takekawa, T., Aoyagi, T., and Fukai, T. (2007). Synchronous and asynchronous bursting states: role of intrinsic neural dynamics. *J. Comput. Neurosci.* 23, 189–200.

Takekawa, T., Isomura, Y., and Fukai, T. (2010). Accurate spike–sorting for multiunit recordings based on wavelet transform and robust variational Bayes. *Eur. J. Neurosci.* 31, 263–272.

Takekawa, T., Isomura, Y., and Fukai, T. (2012). Spike sorting of heterogeneous neuron types by multimodality–weighted PCA and explicit robust variational Bayes. *Front. Neuroinform.* 6:5. doi: 10.3389/fninf.2012.00005

Tateno, T., Harsch, A., and Robinson, H. P. (2004). Threshold firing frequency–current relationships of neurons in rat somatosensory cortex: type 1 and type 2 dynamics. *J. Neurophysiol.* 92, 2283–2294.

Tateno, T., Harsch, A., and Robinson, H. P. (2007). Phase resetting curves and oscillatory stability in interneurons of rat somatosensory cortex. *Biophys. J.* 92, 683–695.

Teramae, J. N., Tsubo, Y., and Fukai, T. (2012). Optimal spike-based communication in excitable networks with strong-sparse and weak-dense links. *Sci. Rep.* 2:485. doi: 10.1038/srep00485

Thomson, A. M., and Bannister, A. P. (2003). Interlaminar connections in the neocortex. *Cereb. Cortex.* 13, 5–14.

Torben-Nielsen, B., Uusisaari, M., and Stiefel, K. M. (2010). A comparison of methods to determine neuronal phase-response curves. *Front. Neuroinform.* 4:6. doi: 10.3389/fninf.2010.00006

Tsubo, Y., Isomura, Y., and Fukai, T. (2012). Power–law inter–spike interval distributions infer a conditional maximization of entropy in cortical neurons. *PLoS Comput. Biol.* 8:e1002461. doi: 10.1371/journal.pcbi.1002461

Tsubo, Y., Takada, M., Reyes, A. D., and Fukai, T. (2007a). Layer and frequency dependencies of phase response properties of pyramidal neurons in rat motor cortex. *Eur. J. Neurosci.* 25, 3429–3441.

Tsubo, Y., Teramae, J. N., and Fukai, T. (2007b). Synchronization of excitatory neurons with strongly heterogeneous phase responses. *Phys. Rev. Lett.* 99:228101. doi: 10.1103/PhysRevLett.99.228101

Ward, L. M. (2003). Synchronous neural oscillations and cognitive processes. *Trends Cogn. Sci.* 7, 553–559.

Weiler, N., Wood, L., Yu, J., Solla, S. A., and Shepherd, G. M. (2008). Top–down laminar organization of the excitatory network in motor cortex. *Nat. Neurosci.* 11, 360–366.

Wehr, M., and Zador, A. M. (2003). Balanced inhibition underlies tuning and sharpens spike timing in auditory cortex. *Nature* 426, 442–446.

Conflict of Interest Statement: The authors declare that the research was conducted in the absence of any commercial or financial relationships that could be construed as a potential conflict of interest.

Received: 07 December 2012; accepted: 16 April 2013; published online: 03 May 2013.

Citation: Tsubo Y, Isomura Y and Fukai T (2013) Neural dynamics and information representation in microcircuits of motor cortex. Front. Neural Circuits 7:85. doi: 10.3389/fncir.2013.00085

frontiers in
NEURAL CIRCUITS

REVIEW ARTICLE
published: 18 April 2013
doi: 10.3389/fncir.2013.00066

On the functional organization and operational principles of the motor cortex

Charles Capaday[1,2]*, Christian Ethier[3], Carl Van Vreeswijk[2] and Warren G. Darling[4]

[1] Brain and Movement Laboratory, Section of Biomedical Engineering, Department of Electrical Engineering, Danish Technical University, Lyngby, Denmark
[2] Laboratoire de Neurophysique et Physiologie du Systeme Moteur, CNRS UMR 8119, Université Paris-Descartes, Paris, France
[3] Department of Physiology, Northwestern University, Chicago, IL, USA
[4] Department of Health and Human Physiology, University of Iowa, Iowa City, IA, USA

Edited by:
Gordon M. G. Shepherd, Northwestern University, USA

Reviewed by:
Jon H. Kaas, Vanderbilt University, USA
Paul D. Cheney, University of Kansas Medical Center, USA

***Correspondence:**
Charles Capaday, Brain and Movement Laboratory, Section of Biomedical Engineering, Department of Electrical Engineering, Danish Technical University, Ørsteds Plads, Building 349, 2800 Kgs. Lyngby, Denmark.
e-mail: charles.capaday@ccapcable.com

Recent studies on the functional organization and operational principles of the motor cortex (MCx), taken together, strongly support the notion that the MCx controls the muscle synergies subserving movements in an integrated manner. For example, during pointing the shoulder, elbow and wrist muscles appear to be controlled as a coupled functional system, rather than singly and separately. The recurrent pattern of intrinsic synaptic connections between motor cortical points is likely part of the explanation for this operational principle. So too is the reduplicated, non-contiguous and intermingled representation of muscles in the MCx. A key question addressed in this article is whether the selection of movement related muscle synergies is a dynamic process involving the moment to moment functional linking of a variety of motor cortical points, or rather the selection of fixed patterns embedded in the MCx circuitry. It will be suggested that both operational principles are probably involved. We also discuss the neural mechanisms by which cortical points may be dynamically linked to synthesize movement related muscle synergies. Separate corticospinal outputs sum linearly and lead to a blending of the movements evoked by activation of each point on its own. This operational principle may simplify the synthesis of motor commands. We will discuss two possible mechanisms that may explain linear summation of outputs. We have observed that the final posture of the arm when pointing to a given spatial location is relatively independent of its starting posture. From this observation and the recurrent nature of the MCx intrinsic connectivity we hypothesize that the basic mode of operation of the MCx is to associate spatial location to final arm posture. We explain how the recurrent network connectivity operates to generate the muscle activation patterns (synergies) required to move the arm and hold it in its final position.

Keywords: motor cortex, cortical circuits, motor map, cortical connectivity, microstimulation, neural mechanisms of cortical activity spread, multi-unit recording arrays, balanced neural networks

INTRODUCTION

What the motor cortex (MCx) does and how it does it are major scientific questions that remain unresolved. These issues are important because they are at the core of understanding cortical function. The MCx is, to paraphrase Sherrington, the final common cortical area where willful intention is translated into observable action. Its activation is the result of massive neural integration in a large number of cortical and subcortical areas (e.g., see Rizzolatti and Kalaska, 2013). Consequently, the MCx cannot be fully understood in isolation. Nonetheless, because of its vantage point, studying the MCx can further our understanding of what is being integrated and how. Here we propose that the MCx integrates kinematics and kinetics. Specifically, we hypothesize that the MCx associates the spatial location to which the limb is commanded to move with the respective muscle synergies required to move it and hold it in place, as required. Our hypothesis on this basic mode of operation of the MCx is developed in the final section of the article. On the way there we review and discuss several key issues concerning the functional organization of the motor output map, the nature of the connectivity between the different map loci, the mode of operation of the motor cortical circuitry and how they are all related.

TOPOGRAPHY OF MUSCLE REPRESENTATIONS IN HUMANS AND ANIMALS

Mapping experiments based on electrical microstimulation of MCx in animals have demonstrated that a given muscle is represented at a multitude of non-contiguous loci and in various combinations with other muscles (e.g., Armstrong and Drew, 1985; Donoghue et al., 1992; Schneider et al., 2001). Schneider et al. (2001) showed unequivocally that such observations are not due to spread of stimulus current, or the result of conduction along intracortical axonal branches, to a single focus of representation (see also, Capaday, 2004). Subsequently, Rathelot and Strick (2006) used retrograde trans-neuronal transport of rabies virus injected in single digit muscles of macaques to study the distribution of corticospinal cells projecting to the respective motoneuron pool. This enabled them to identify

cortico-motoneuronal (CM) cells that make monosynaptic connections with the motoneurons of the injected muscle. They found that the CM cells of a single digit muscles are spatially widespread and fill the entire mediolateral extent of the arm area. Further, they emphasized that CM cells for digit muscles are found in regions of MCx that are known to contain the shoulder representation. The cortical territories occupied by CM cells for different muscles overlapped extensively. No evidence for a single focal representation of muscles in MCx was found. They concluded that the "*overlap and intermingling among the different populations of CM cells may be the neural substrate to create a wide variety of muscle synergies*," as had been previously demonstrated (Schneider et al., 2001) and emphasized (Phillips, 1975; Capaday, 2004).

Is the human MCx similarly organized? A detailed mapping study using transcranial magnetic stimulation (TMS) showed the essential likeness of human and animal motor cortical maps (Devanne et al., 2006). They found that areal representations of commonly used proximal and distal muscles overlap considerably, despite differences in the location of their optimal points. What was new in that study was their demonstration that, as with the animal studies, the observed overlap was not due to current spread (**Figure 1**). Furthermore and contrary to often encountered descriptions of human motor cortical maps, the areal representations of commonly used proximal and distal muscles—anterior deltoid (AD), extensor carpi radialis (ECR), and first dorsal interosseus (1DI)—are similar in size. The comparable areal representation of the single muscles AD, ECR, and 1DI does not imply, however, that the total areal representation of the shoulder, wrist and hand are of similar size. There are about 22 muscles in the arm; nine muscles move the shoulder and five the wrist (Alexander, 1992). By contrast, about 29 intrinsic and extrinsic muscles move the hand (Alexander, 1992). It is therefore not surprising that the hand area may occupy a larger motor cortical territory than that of the shoulder or wrist (Penfield and Rasmussen, 1950). What the results of Devanne et al. (2006) demonstrate is that commonly used shoulder, wrist and intrinsic hand muscles, taken singly, are represented in areas of similar size. The relatively large AD representation seems relevant to explaining the accuracy of human pointing and reaching movements (Lacquaniti and Soechting, 1982). An angular positioning error at the shoulder leads to a larger error between hand and target than a comparable angular positioning error at an index finger joint. The large representation of the AD would suggest that the finesse of motor cortical control of the AD may be comparable to that of finger muscles. More importantly, the shoulder is involved either as a base of postural support for movements of the forearm and hand, or in their transport. The large representation of the AD and its overlap with forearm and hand muscles is a likely neural substrate of such motor coordinations. Perusal of simian motor cortical maps obtained by microstimulation shows a large number of zones in which wrist, elbow, and shoulder representations are intermingled (e.g., Gould et al., 1986; Donoghue et al., 1992). The number of motor cortical sites from which shoulder muscles were activated was nearly equal to those from which wrist muscles were activated (Donoghue et al., 1992). Park et al. (2001) demonstrated in rhesus monkeys a specific motor cortical region containing neurons that represent functional synergies of distal and proximal muscles. The results obtained in human subjects are in fact rather similar to those obtained in animals. Despite considerable overlap of representations found in the human MCx by Devanne et al. (2006) and others (e.g., Wassermann et al., 1992; Krings et al., 1998), the optimal point of the AD is on average more medially situated along the motor strip than those of the more distal muscles ECR and 1DI. Thus, the classic notion that proximal muscles are represented more medially along the motor strip than distal muscles is not without merit, but the overlap of representations must be emphasized. It is also important to consider that experiments using spike-triggered averaging of rectified EMG activity in monkeys (McKiernan et al., 1998) showed that over 45% of recorded CM cells facilitated at least one proximal muscle (elbow or shoulder) and at least one distal muscle (wrist, digit, and intrinsic hand muscles). On the assumption that this is also the case in humans, it is difficult to see how discrete non-overlapping representations can be obtained.

The results presented here are consistent with the Jackson–Walshe perspective on the functional organization of the MCx, viz. that the MCx represents complex patterns of overlapping and graded movement/muscle representations (see Walshe, 1943; Capaday, 2004, for a historical account and Phillips, 1975, for a discussion doing away with the muscles vs. movements controversy). The muscles of the arm are not controlled singly and separately, a point that was made right at the genesis of research on the MCx (Jackson, 1882[1]). For one, individuated control does not make sense biomechanically, as torques generated at one joint produce motion at other joints. Additionally, a large number of muscles cross more than one joint and thus produce movements at all spanned joints (e.g., the effect of long finger flexors on the wrist). While individuated movements at single joints are possible, they do not represent the plurality of movements ordinarily executed. Such movements often involve activation of multiple muscles to stabilize other joints so as to counteract actions of multi-joint muscles and segmental interaction torques. Furthermore, this ability does not imply that the MCx controls the musculature singly and separately, as will be discussed further on. The intermingled and re-duplicated muscle representation pattern is consistent with and provides a basis for the idea that the upper limb is controlled in an integrated manner (Capaday, 2004). Still, taken by itself, this organizational feature can be interpreted as a piano keyboard type of arrangement (see Graziano, 2006, for a historical account). However, cortical points are not isolated from each other, they are interconnected by long range intrinsic collaterals (Huntley and Jones, 1991; Keller, 1993; Lund et al., 1993; Capaday et al., 2009). Thus, in the cat, no two cortical points are fully independent, over distances spanning up to 6–7 mm (**Figure 2**). The nature of this connectivity and its implications for the mode of operation of the MCx are considered next.

[1]Note the original cited references to Hughlings-Jackson may be found in the two volumes set "Selected writings" published in 1931. An excellent summary of his ideas on the organization and function of the motor cortex is in the paper titled "Some implications of dissolution of the nervous system" ("Selected writings" vol. II, p. 29).

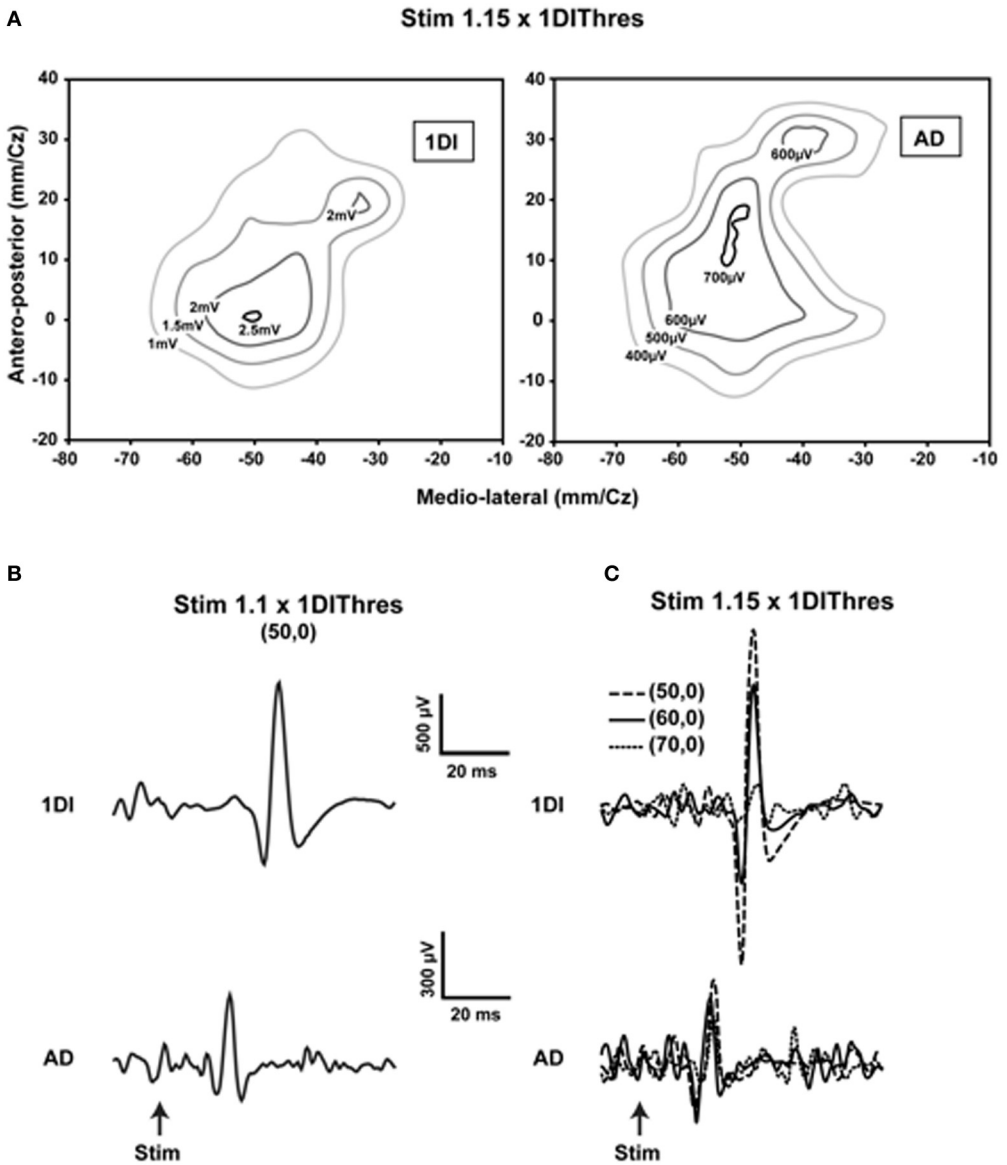

FIGURE 1 | Evidence showing that current spread does not explain the overlap of representations. (A) Contour plots of the first dorsal interosseus (1DI) and anterior deltoid (AD) in a single subject obtained at 1.15 times the active motor (AMT) threshold of the 1DI. Note the slightly larger representation of the AD and the considerable overlap of the two representations. Note also that the optimal points are within 10 mm of each other in the antero-posterior direction and essentially coincident in the medio-lateral direction. **(B)** When the stimulus is reduced to 1.1 × AMT of the of the 1DI and the stimulus applied at the 1DI optimal point, MEPs are elicited in both the 1DI and AD. Note that in this case the stimulus is at the AD threshold. **(C)** Movement of the coil laterally in steps of 10 mm, starting at coordinate (50, 0), reduces the 1DI MEPs significantly, whereas the AD MEPs are relatively more constant despite the fact that the coil was moved further away from its optimal point than it was from that of the 1DI. This demonstrates that the measured overlap of the AD and 1DI representations is not due to current spread [reproduced with permission from Devanne et al. (2006)].

ON THE NATURE OF THE INTRINSIC CONNECTIVITY OF THE MCx

Neuroanatomical studies in monkeys and cats have unambiguously demonstrated strong intrinsic connectivity between widespread areas of the MCx (Huntley and Jones, 1991; Keller, 1993; Lund et al., 1993; Capaday et al., 1998, 2009). Indeed, numerous electrophysiological studies have demonstrated lateral interactions between neurons of the MCx (Matsumura et al., 1996; Baker et al., 2001; Jackson et al., 2003; Smith and Fetz, 2009). Here we limit the discussion to the anatomical aspects. An example of the widespread intracortical connectivity of the cat MCx is shown in **Figure 2**. The axon collaterals are studded with synaptic boutons all along their course (Capaday et al., 2009), which may be inferred from their beaded appearance in **Figure 2**. The intrinsic connections of a cortical area outnumber its feedforward (inputs) and feedback (top-down) connections (e.g., White, 1989; Dayan and Abbott, 2001). Understanding the function of intrinsic connections is therefore fundamental to understanding

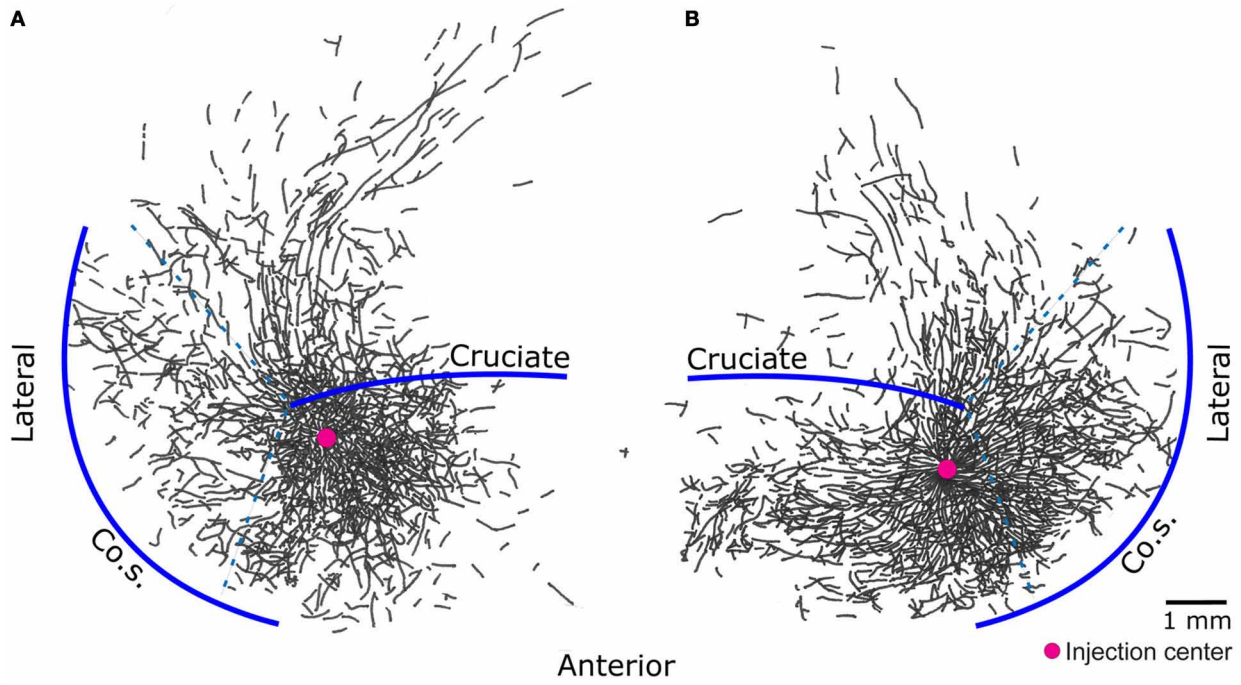

FIGURE 2 | Pyramidal cells of the cat motor cortex give rise to an extensive network of horizontal axon collaterals. The motor cortex is bounded laterally by the coronal sulcus (Co.S.), the location of the coronal gyrus is demarcated by the dashed lines - - -. The areas anterior and posterior to the cruciate sulcus, along with the coronal gyrus, constitute the cat primary motor cortex. Biocytin, an anterograde tracer, was injected in points marked by a red circle. Threshold level microstimulation at that point evoked activity in the brachialis muscle in **(A)** and the extensor carpi radialis in **(B)**. Note how the axon collaterals of pyramidal cells from both deep and superficial layers of a small cortical locus spread to cover nearly all of the forelimb representation area [figure modified from Capaday et al. (2009)].

the neural processing that occurs within a cortical area. Predicated on this idea, Capaday et al. (2009) linked anatomy and physiology in finer detail than previous studies. Motor output was measured by intramuscular EMG recordings from up to 10 muscles making for a detailed output map. Axonal collaterals were traced from origin to termination with special care to identify the synaptic boutons along their course using correlative light and electron microscopy. Superposition of the synaptic bouton distribution map and the motor output map revealed that motor cortical neurons do not make point-to-point connections, but rather bind together the representations of a variety of muscles within a large neighborhood (**Figure 3**). Spiking activity at a cortical point may thus potentially influence any other cortical point within its innervation territory. This would allow for synergistic interactions between arbitrary cortical points giving rise to a rich repertoire of possible movements. The Jackson–Walshe perspective of overlapping and graded movement representations finds credence in the relation between the intrinsic connectivity and motor output maps.

Two other features of the maps shown in **Figure 3** stand out. The dense core of bouton connectivity surrounding the injection point and the obvious intermingling of muscle representations. The dense core of connectivity has an area of about 3 mm^2. Note also in **Figure 3** that as the stimulus intensity is increased, responses from more muscles may appear and that their identity is not readily predictable from the responses of nearby points obtained at lower intensity. Such observations strongly argue against the idea that stimulus spread explains the recruitment of additional muscles with increasing stimulus strength. The more sensible conclusion is that the activation thresholds are different for the varied muscles that may be represented at a given cortical point. Capaday et al. (2009) also reported that excitatory and inhibitory neurons in the innervation territory of a cortical point receive synaptic inputs. This is nicely consistent with White's (1989) first canonical cortical circuit principle, viz. that "*every neuron in the target region of a projection receives input from the projection*" and, importantly, its corollary which states that "*axon terminals from any extrinsic or intrinsic source synapse onto every morphological or physiological neuronal type within their terminal projection field* …" This feature of the cortical circuitry is consistent with a balanced neural network as proposed by Van Vreeswijk and Sompolinsky (1996). A key property of balanced networks is that the population output is a linear function of the input, despite non-linear unit properties. We will take up this issue again in section "A Hypothesis on the Basic Mode of Operation of the MCx" when discussing the neural mechanisms underlying the linear summation of MCx outputs and their functional significance. The third feature that may be inferred from the connectivity pattern is its recurrent nature. Cortical points, within the limits of axon collateral lengths, are reciprocally connected. Recurrent networks have a property which appears relevant to MCx function as we see it, they can function as hetero-associative

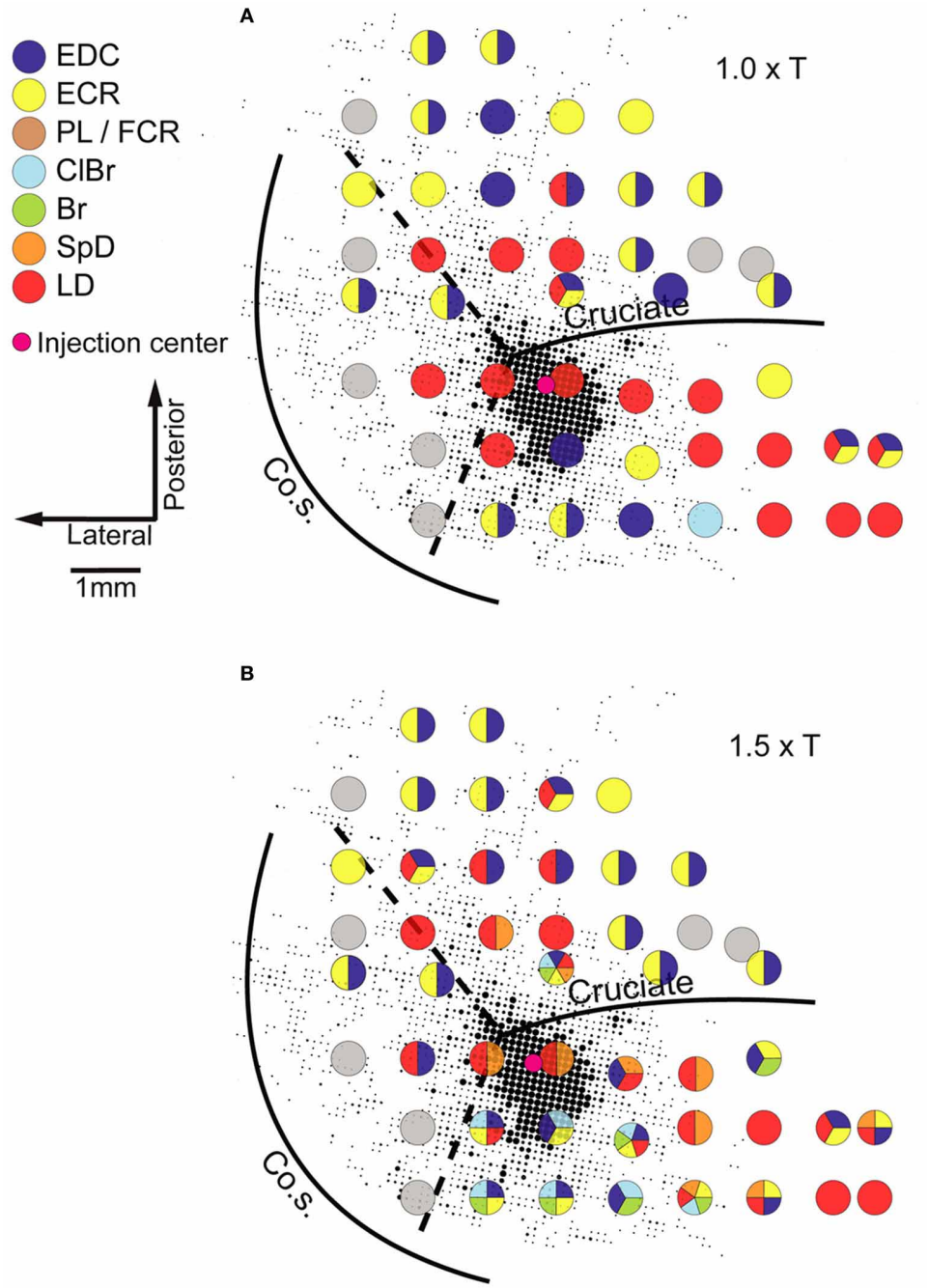

FIGURE 3 | Example of a superposition of the bouton density map on the microstimulation derived muscle map obtained in the same animal. The size of each dot is proportional to the number of boutons in a grid element of 83 × 83 mm, quantitative details may be found in Capaday et al. (2009). Evoked muscle responses at each point at which microstimulation was applied are represented by the color code of the legend (left). Gray circles represent points at which no response was obtained (NR). Note that at many cortical points more than one muscle was recruited. **(A)** The microstimulation derived muscle map at 1.0× threshold. **(B)** The muscle map obtained at 1.5× threshold. Muscle abbreviations: EDC, extensor digitorium communis; ECR, extensor carpi radialis; PL, palmarus longus; FDP, flexor digitorium profundus; ClBr, clavo brachialis; Br, brachialis; SpD, spino deltoid; LD, latissimus dorsi. Reproduced from Capaday et al. (2009).

systems (e.g., see Dayan and Abbott, 2001; Trappenberg, 2002). Our hypothesis on the basic mode of operation of the MCx is that it associates the spatial location to which the limb is commanded to move with the respective muscle synergies required to move it there and hold it in place, as required. The details will be presented in the final section of this article.

Why does the recurrent network pattern of the intracortical connectivity change the picture of how the MCx may function?

The answer, as we have already stated, is that activity at a cortical point can spread and activate nearby cortical points where different muscle groups are represented. But how far does neural activity actually spread? In the cat MCx, neural activity generated at a cortical point about 400 mm in radius spreads at a velocity of 0.1–0.24 m/s to recruit a cortical area of some 7.22 mm^2 (Capaday et al., 2011). The physiologically recruited cortical area is smaller than the area covered by the anatomical connections, but larger than the dense core of connectivity (**Figure 4**). From the aforesaid, we can infer that neural activity spreads over a radial distance of about 1.5 mm, when the balance between synaptic excitation and inhibition is not upset. However, cortical points up to 6–7 mm apart can be functionally coupled by reducing the strength of inhibition at one of the points (Schneider et al., 2002). This observation has led to the suggestion that motor commands may be synthesized by coupling cortical points through selected excitation and release of inhibition (Schneider et al., 2002; Capaday, 2004). It is clear therefore that an input to MCx will activate a cortical area whose size will depend on the intensity of the input and the level of inhibition at cortical points with which it is connected. We can use the connectivity map to understand individuated movements, such as index finger flexion and extension, as well as the more common natural movements requiring coordination between joints, such as reaching for an object. Imagine that a small focalized input to MCx will produce motion at the index finger. But this is only possible if nearby articulations are stabilized. Clearly, the so called focalized activity is only part of the motor command structure. As the contraction strength is increased, it is a common observation that activity irradiates to other muscles. This is presumably due, at least in part, to the intracortical connectivity we have described. The irradiation of activity is not pathological, it is sensible as was understood by Hughlings-Jackson who wrote

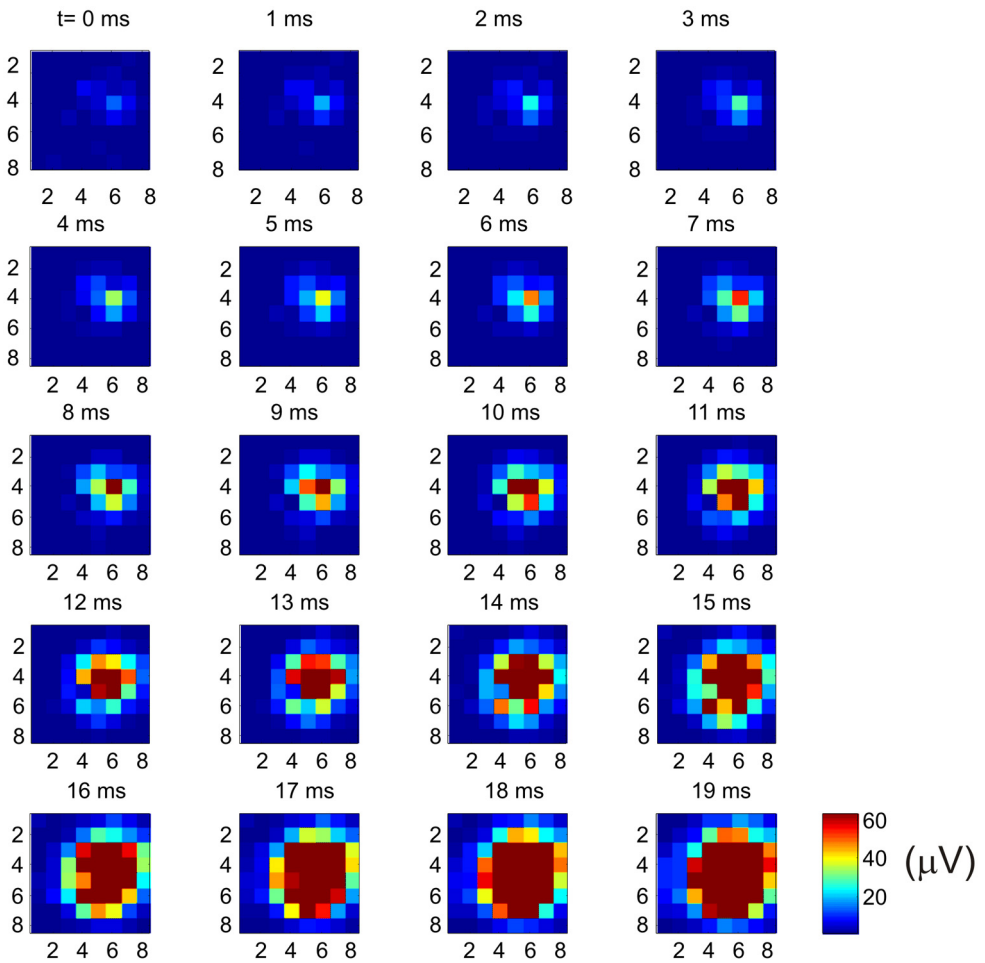

FIGURE 4 | Example of how multi-unit activity (MUA) recorded by an 8 × 8 Utah array propagates from a cortical point. Bursting spike activity in the MCx was produced by focal iontophoretic ejection at array coordinate (6, 4) of the $GABA_A$ receptor antagonist Bicuculline. The maps of neural activity were calculated every millisecond from near the onset ($t = 0$ ms) of spontaneous bursts of ictal neural activity to the time at which the maximum cortical area was recruited ($t = 19$ ms). Activity continues for several tens of millisecond after that. Note the onset of activity at coordinate (6, 4) and the subsequent progressive recruitment of cortical territory with time. In this example activity was evoked at 62 out of 64 possible electrodes. The recruited cortical area was 7.6 mm^2, or 96% of the area covered by the array [reproduced with permission from Capaday et al. (2011)].

"Because the movements of the thumb and fingers could scarcely be developed for any useful purpose without fixation of the wrist (and of parts further and further in automaticity according to the force required), we should a priori be sure that the centre discharged, although it might represent movements in which the thumb had the leading part, must represent also certain other movements of the forearm, upper arm, etc., which serve subordinately."

(In Selected writings of Hughlings-Jackson, 1931, vol. 1, p. 69).

The intracortical connectivity may thus also be viewed as the structural basis of an anticipatory neural network, foreseeing what additional muscles may need to be recruited as the movement evolves, or is perturbed. In the case of coordinated multi-articular movements, a larger cortical territory is likely engaged. The size of the cortical area necessary to evoke such movements is not known, here we speculate that this may involve the area of dense core connectivity. But, if we also consider that the MCx is involved in commanding associated postural adjustments (Massion, 1992), the area is probably much larger. This may explain why various lines of investigation suggest that even for simple finger movements large areas of the MCx appear to be activated (e.g., Sanes et al., 1995; Devanne et al., 2002). In any case, as the input to a particular cortical point is increased and inhibition at surrounding points decreased, the intracortical connectivity insures the synergistic recruitment of muscles required to produce the movement. We do not understand in detailed mechanistic terms how the MCx controls movements, but the intracortical connectivity must be taken into account by any eventual theory. It will also be important for future studies to determine the source and nature of the inputs that initiate activity in the MCx. What seems clear in considering the topography of muscle representations and the intrinsic connectivity is that the MCx contains a large number of potential functional links between widespread muscles. How specific muscle synergies are selected by cortico-cortical and subcortical inputs during voluntary movements is a challenge for the future.

CORTICAL CONTROL OF ANTAGONISTIC MUSCLES

Within the extensive intrinsic connectivity described in the preceding section, motor cortical points representing antagonistic muscles are also synaptically coupled by intrinsic axon collaterals (Capaday et al., 1998). In the example shown in **Figure 5A** biocytin was injected in a cortical point at which the ECR muscle (a physiological flexor) was represented. HRP was injected at another cortical point, about 2.8 mm away, at which its antagonist the palmaris longus muscle (a physiological extensor, or antigravity muscle) was represented. One can see a biocytin stained axon collateral studded with boutons along its course passing through a dense core of HRP staining. The camera lucida reconstruction of all the labeled collaterals coursing through the HRP deposit is shown in **Figure 5B**. The connections are excitatory, but they are normally held in check by local GABAergic inhibition, as we have shown in a subsequent physiological study (Ethier et al., 2007). Additionally, cortically mediated reciprocal inhibition operates at the spinal level when these points are activated, details of which will be discussed further on. Presumably, these interconnections are involved in the flexible control of antagonistic muscles, going from reciprocal activation to co-contraction. However, no studies of the function of this intra-cortical circuit have been done during behavior. Part of our message in this article is that to understand the MCx, is to understand how such circuits actually work during movement. By contrast to spinal circuitry, we are only at the beginning of relating cortical circuitry to motor function.

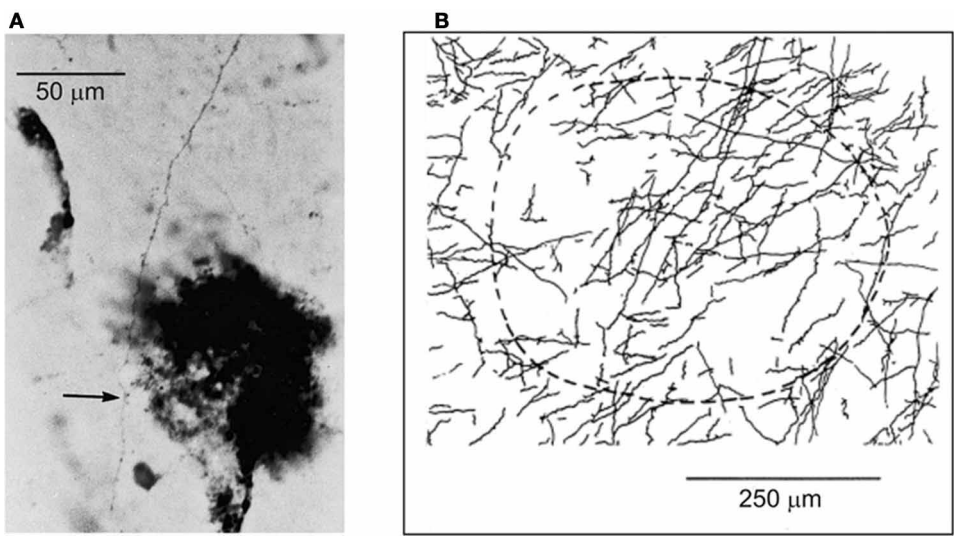

FIGURE 5 | (A) Example of a biocytin stained axon collateral from a pyramidal neuron in a wrist extensor motor cortical point is shown coursing through a wrist flexor point identified by a small deposit of HRP (dark spot). The arrow points to an en-passant synaptic bouton on the axon collateral. **(B)** The camera lucida drawing of all axon collaterals coming from the wrist extensor point and coursing through the identified wrist flexor point. The dashed curve represents an area of approximately 250 mm in radius surrounding the center of the HRP deposit site.

In our original study on the cortical control of antagonistic muscles (Capaday et al., 1998), as in all studies using microstimulation, cortical points that evoke a response in physiological extensor muscles (i.e., anti-gravity muscles) are few in comparison to those that evoke a response in physiological flexor muscles. Why might this be? There are two main reasons, as we discovered (Ethier et al., 2007). First, there is a strong asymmetry of cortically mediated reciprocal inhibition in the spinal cord. Cortically mediated inhibition is much stronger on physiological extensors than flexors (Ethier et al., 2007; see also references therein). This bias is particularly strong for wrist and elbow muscles, but less so for shoulder muscles (Ethier et al., 2007). This may be perhaps related to the functional role of the shoulder in providing a stable anchor for movements of the forelimb. Second, cortical points controlling antagonistic muscles are to a significant extent close together, or even commingled (Ethier et al., 2007). Consequently, the evoked descending volley is mixed; corticospinal fibers going to both flexor and extensor motoneuron pools are discharged. This volley will preferentially evoke a response in flexor motoneurons, because the cortically mediated reciprocal inhibition on the extensor motoneurons is strong. The same principle applies in humans (Capaday, 1997) when the MCx is activated by TMS. The asymmetry of the cortically mediated reciprocal inhibition strongly biases motor cortical maps derived by microstimulation, or TMS.

One should also be cautious of the simplified interpretations derived from such maps. As, for example, that the cat MCx excites forelimb physiological flexors and inhibits physiological extensors, or that by contrast in the baboon the converse is true (e.g., Preston et al., 1967). The latter account implies that for a baboon to reach for a food morsel the MCx controls the extension of the forelimb, but that the subsequent flexion movement to bring the morsel to its mouth would be mediated by a different part of the CNS. We suggest that a too literal interpretation of these otherwise sound data does not represent the true nature of motor cortical control. Preston et al. (1967) insightfully interpreted the strong cortical inhibition of physiological extensors in cats as part of a mechanism to arrest the tonic anti-gravity activity which occurs during standing postures. For the baboon, the interpretation was that it represented a neurophysiological sign of the transition from quadruped to biped posture. In neither case was it implied that motor cortical control has a unidirectional bias. Indeed, recent studies have shown that both types of movements can be elicited by microstimulation of the simian MCx (Graziano et al., 2002, 2004). Yet another factor that may bias cortical maps is the relative excitability of different motoneuron pools. Two factors are involved here; the input resistance of the motoneurons and spontaneous depolarizing drive that may occur in different states. Little is known about motoneuron input resistance differences between motor pools such as those of wrist and shoulder muscles. In principle, pools constituted of motoneurons having a higher input resistance will tend to be preferentially activated by synaptic currents.

FEEDBACK REMAPPING OF CORTICAL OUTPUTS

Graziano et al. (2004) suggested the possibility that the output of cortical points may be remapped by proprioceptive inputs (see also Graziano, 2006). They demonstrated that, for example, microstimulation at a cortical point evoked either activity in the triceps muscle when the elbow was flexed, or activity in the biceps when the elbow is extended. In another example they showed that evoked activity in the triceps increased monotonically as a function of the degree of elbow flexion. In these as well as other examples, examination of the EMG recordings (e.g., Figure 9 in Graziano, 2006) shows that the evoked responses are a function of the background EMG activity in the respective muscle. When the elbow was flexed (triceps is stretched) the background activity increased in the triceps and its microstimulation evoked response also increased. When the elbow was extended (biceps stretched) the background EMG activity of the biceps increased and so too its evoked response. We propose that this can be explained by changes in spinal neural circuit excitability produced by the stretch reflex, the associated reciprocal inhibition and the close grouping or intermingling of the corticospinal neurons controlling the biceps and triceps, respectively. Thus, for example, when the biceps is stretched the increased spindle afferent discharges will increase the activity of the biceps motoneurons via the stretch reflex pathway(s) and reciprocally inhibits the triceps motoneurons. Consequently, the mixed corticospinal volley will evoke a net response in the biceps motoneurons. Graziano (2006) suggested that such observations are evidence for proprioceptive remapping of the output of cortical points by mechanisms intrinsic to the MCx and spinal cord. We suggest that these results depend only on spinal neural mechanisms, as explained. Relatedly, Griffin et al. (2011) have demonstrated that during ongoing voluntary motor activity high-frequency microstimulation of the MCx in macaques has effects which depend on the ongoing level of EMG activity, but not limb position, which can confound interpretation.

Nonetheless, how proprioceptive information is used by the motor cortical circuitry is an important issue that has not received much attention beyond establishing the existence of a trans-motor-cortical stretch reflex in primates, including humans (Phillips, 1969, 1975; Cheney and Fetz, 1984; Capaday et al., 1991). We will discuss the possible role of proprioception in the operations of motor cortical circuits in the final section of this article.

NEURAL MECHANISMS OF LINEAR SUMMATION OF MCx OUTPUTS

We do not know whether the MCx stores motor engrams (i.e., memories of complete movements) or, by contrast, whether it synthesizes a movement on a moment-to-moment basis by selecting multi-purpose muscle synergy modules and if so, how. One possibility, as discussed in the section "On the Nature of the Intrinsic Connectivity of the MCx," is that the dense core of connectivity contains the neural circuitry, or engram, required to evoke a movement. However, as the horizontal connections extend beyond the dense core, it may be possible to functionally link cortical points representing different muscles, or muscle synergies. Such a mechanism would allow creating a rich variety of movements, from a smaller repertoire of stored basic engrams. We discussed in section "On the Nature of the Intrinsic Connectivity of the MCx," how selected excitation and release

from inhibition can functionally link distinct cortical points and produce a synergistic motor output pattern (Schneider et al., 2002). Whatever the mechanisms of muscle synergy selection turn out to be, it seems important to understand quantitatively how cortical points interact and how the net output is thereby modified.

In the study by Ethier et al. (2006) we asked how the outputs of two simultaneously stimulated motor cortical points summate. To this end experiments were done in Ketamine anesthetized cats. Long trains (e.g., 500 ms) of intracortical microstimulation applied to the MCx evoked coordinated movements of the contralateral forelimb, as was first shown by Graziano et al. (2002) in the monkey. Paw kinematics in three dimensions and the EMG activity of eight muscles were simultaneously recorded. The evoked movements were represented as displacement vectors pointing from initial to final paw position. We showed that the EMG outputs of two cortical points simultaneously stimulated sum linearly (**Figure 6**). Additionally, the displacement vector resulting from simultaneous stimulation pointed in nearly the same direction as the algebraic resultant vector. This result is true as long as the individual movement vectors point in different directions and are not due to motion at single joint, which rarely if ever occurs with long duration trains of microstimulation. Importantly, however, the resulting movement during simultaneous stimulation is always a blend of the movements evoked from each cortical point on its own (Ethier et al., 2006). Linear summation of EMG outputs was also found when inhibition at one of the cortical points was reduced by $GABA_A$ receptor antagonists. A simple principle emerges from these results. MCx outputs combine nearly linearly in terms of muscle activation

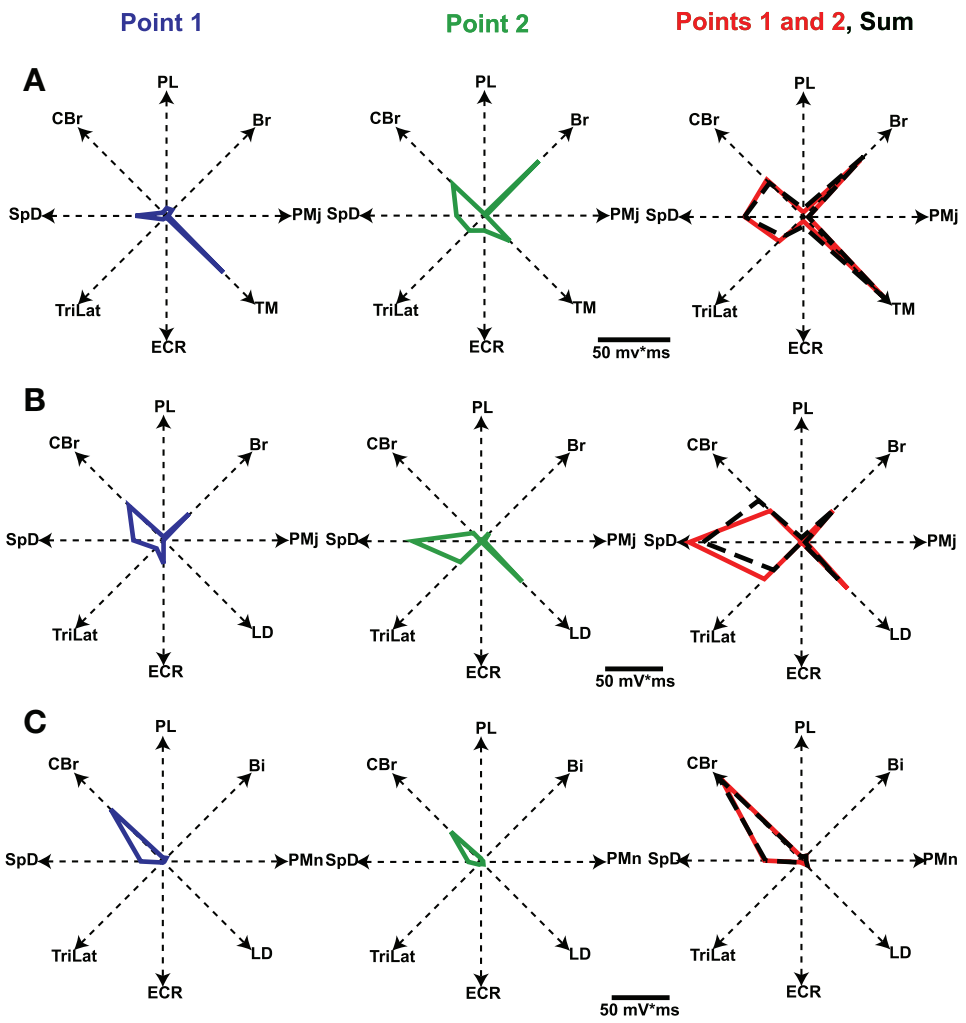

FIGURE 6 | Polar plots of evoked EMG activity and their summation. Each axis represents the integrated EMG activity of a given muscle. Line segments join the points plotted on each axis, thus giving a geometrical representation of the evoked muscle-coordination pattern. Graphs in the first two columns represent the muscle-coordination pattern evoked by separate stimulation of two cortical points. Graphs in the third column represent the muscle coordination pattern obtained when the two points were simultaneously stimulated (Points 1 and 2, red line) and the linear sum expected by addition of the two separate patterns (black dashed lines). Note that the expected and experimentally obtained muscle-coordination patterns are nearly the same in the three examples shown **(A–C)**. Figure from Ethier et al. (2006).

patterns, despite the underlying complex neuronal circuitry and electrophysiological properties of neurons. The summation of muscle activation patterns leads to a blending of the movements evoked from each point. This operational principle may simplify the synthesis of motor commands, as previously discussed. Nonetheless, the linear summation of outputs was unexpected and puzzling. It is even more puzzling given the lack of effect of reducing inhibition at one of the cortical points; a condition in which it should have received the full brunt of inputs from the other cortical point.

There are at least two explanations for the observed linear summation of MCx outputs. The simplest is that the distance between paired cortical points was on average greater than that over which neural activity spreads, which is approximately 1.5 mm in radial distance as discussed in the section "On the Nature of the Intrinsic Connectivity of the MCx." The distances between pairs of microstimulated points ranged between 0.66 and 5.7 mm, with a mean distance of 2.65 mm ($SD = 1.52$ mm). Thus, the separation between cortical points studied by Ethier et al. (2006) was on average greater than that over which activity at a cortical point influences its surround. It is possible, therefore, that we were dealing with effectively functionally isolated cortical points. However, the observation that despite reducing the strength of inhibition at one of the cortical points the outputs still summed linearly is more difficult to explain on these grounds. The distances between pairs of points tested in this way was between 2.65 and 4.62 mm, with a mean distance of 3.4 mm ($SD = 0.92$ mm). Thus, these pairs of cortical points were well within the range over which they can be functionally coupled, i.e., at least 5 mm (Schneider et al., 2002). Yet, despite the fact that in this condition spiking activity initiated at the stimulated point produces spiking activity at the disinhibited point, the outputs still summed linearly. This raises a second and more interesting possibility that the motor cortical circuitry may be wired to produce linear interactions between loci. Balanced neural networks as originally proposed by Van Vreeswijk and Sompolinsky (1996) involve a feedback dependent balance between excitation and inhibition such that, despite non-linear unit properties, the population output is a linear function of the input to the network. More recently, Capaday and Van Vreeswijk (2006) proposed a mechanism by which gain may be modulated by such a balance of excitatory and inhibitory synaptic inputs on dendritic trees. This may allow for the scaling of motor commands.

In a balanced neural network (**Figure 7**) the sum of the excitatory currents from external inputs, as well as from the activity of intrinsic circuit neurons, is balanced nearly exactly by the recurrent inhibitory currents. Spiking occurs at times when noise fluctuations exceed threshold, thereby also explaining spike time variability. The basic idea of the balanced neural network is not unlike the principle used in operational amplifiers, where negative feedback of a portion of the output results in a device with linear input/output properties. Now consider a network consisting of multiple cortical points. The excitatory and inhibitory neuron populations at each point mutually interact and can receive external command inputs (**Figure 7**). The excitatory neurons at one point also projects to excitatory and inhibitory neurons at other cortical points through long range collaterals. If we neglect

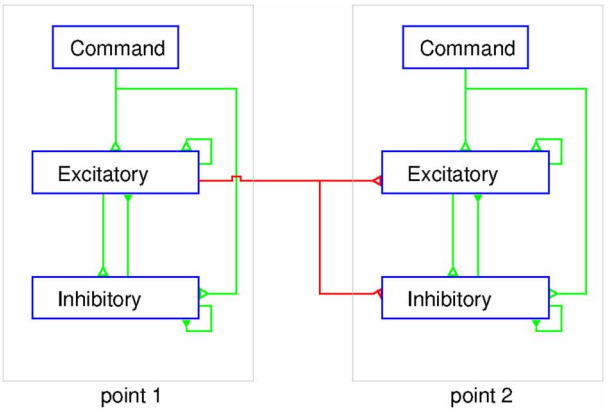

FIGURE 7 | Schematic representation of the balanced network model of MCx. At each point the excitatory and inhibitory populations of neurons are interconnected and receive a command input from outside the MCx. The excitatory neurons also project to both the excitatory and inhibitory neurons in other cortical points. The figure shows two cortical points and for simplicity only the connections from point 1 to point 2 are shown (red lines). The corticospinal axons would emanate from a sub-group of the excitatory neurons at each point. The external command input makes synaptic contact with excitatory and inhibitory neurons simultaneously. The coupling within the intra-motor-cortical network neurons leads to a balanced state and linear summation of the separate outputs, as explained in the text.

the latter for a moment, a command input into a single point would activate the excitatory and inhibitory cells and their activity evolves to a state where, in both populations, the inhibitory feedback roughly cancels the command input and the recurrent excitation. It can be shown that this results in a response in both populations of neurons which is proportional to the command input (Van Vreeswijk and Sompolinsky, 1996, 1998). When considering interacting cortical points, the problem is more complex. A command input into point 1 activates both neuron populations at that point. Through the horizontal connections, however, this produces an input in other points. This will activate the inhibitory cells in these points, and as a result, the excitatory cells receive excitatory inputs through the horizontal connections and local recurrent inhibitory inputs, as shown in **Figure 7**. If the ratio of the strength of synaptic inputs coming from the horizontal connections to the excitatory and inhibitory populations at a given cortical point is just right, this input to the excitatory cells is just canceled by the local inhibitory feedback. Thus, even though cortical points are connected, activation of one point may not recruit the excitatory cells at other points.

How does this explain the twin stimulation experiments? When point 1 is stimulated, it leaves the excitatory cells at point 2 unaffected, and *vice versa* (**Figure 7**). When both points are stimulated simultaneously, each point reacts to the stimulus input and the input from the other point. Since, in the balanced network, the response is linear with the external input, activity of both populations of neurons at each point is just the sum of the activity due to the stimulation and that due to input from the other point. But, since the latter does not affect the activity of the excitatory population, stimulation of one point does not affect the response

of the excitatory population at the other point. As a result, the total output from MCx to the motoneurons in the spinal cord is the sum of the outputs to stimulation of these points separately. This model suggests that the long range connections have been carefully arranged to have no effect. This immediately raises the question of why they exist? We suggest that they serve to couple cortical points as needed for movement production, an idea proposed initially by Schneider et al. (2002). The lack of effect of activity at point 1 on point 2 is due the local inhibitory feedback at that point and vice versa (**Figure 7**). However, if the local inhibitory feedback is modified, for example through disinhibition, the anatomical connections between cortical points can be made physiologically relevant, i.e., cortical points can be functionally coupled. Thus, for example, proprioceptive inputs could by inhibiting inhibitory neurons at a given cortical point, allow it to respond when the command signal arrives.

The anatomical and physiological data are, in broad terms, in agreement with the theory of balanced networks. As discussed in the section "On the Nature of the Intrinsic Connectivity of the MCx," intrinsic and extrinsic inputs to a cortical locus contact local excitatory and inhibitory neurons and the connections between these neurons are recurrent (i.e., there is feedback between them). This suggests that cortical neurons are driven by simultaneous excitatory and inhibitory currents, an idea consistent with recent physiological results (Haider et al., 2006; Okun and Lampl, 2008). The spiking activity of cortical neurons is thus not due to excitatory synaptic inputs alone, but rather the result of simultaneous excitation and inhibition. However, whether balanced network operations in the MCx explain why the output of cortical points sum linearly will require further experimental and theoretical investigations. In particular, the experimental data does not allow us at this time to understand the effects of disinhibition quantitatively. One possibility is that, when the second point is strongly disinhibited it enters into a limit cycle in which the strong local excitatory feedback leads to recurrent bursting activity. The input from point 1 via the horizontal connections is then presumably relatively small in comparison to the local inputs and would only serve to reset the phase of the limit cycle. Consequently, the total input to the motor pool would be the output due to stimulation of point 1 added linearly to the output from the spontaneous activity of point 2, as experimentally observed (Ethier et al., 2006). We are currently re-examining this issue.

The two explanations we have proposed depend, nonetheless, on linear corticospinal transmission. It may also be conjectured that any non-linearity at the cortical level is compensated by a non-linearity of opposite direction at the corticospinal level. However, the results we have obtained from multi-unit-activity (MUA) recordings make this unlikely (Capaday et al., 2011). MUA recordings represent the weighted average of single spike activity recorded within some 100 μm from the microelectrode tip (Buchwald et al., 1965; Buchwald and Grover, 1970; Legatt et al., 1980). Importantly, MUA recordings obtained from multiple cortical sites, when taken together, yielded more accurate predictions of movement parameters than any other intracortical signal (Stark and Abeles, 2007). **Figure 8C** shows an example of an averaged MUA burst from layer V neurons of the cat MCx. Recurrent multi-unit bursts were induced by iontophoretic ejection of Bicuculline, a $GABA_A$ receptor antagonist, at a motor cortical point (Capaday et al., 2011). The figure also shows the

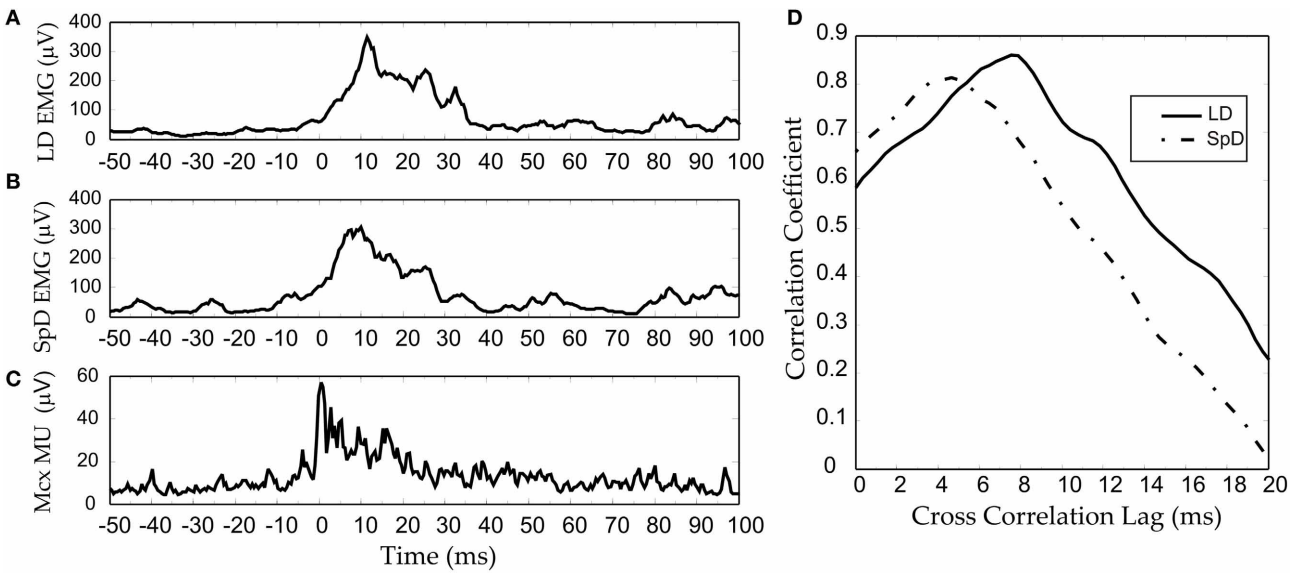

FIGURE 8 | An example of an RMS-smoothed multi-unit (MU) burst (C) recorded recorded from the cat MCx and simultaneously recorded EMG activity (A,B) of the two muscles in which activity was evoked. **(D)** The cross-correlation function between the MCx waveform and the respective EMG waveforms. Bursting spike activity in the MCx was produced by focal iontophoretic ejection at a cortical point of the $GABA_A$ receptor antagonist Bicuculline (see Capaday et al., 2011). The EMG recording where low-pass filtered at 100 Hz, whilst the MCx spiking activity was filtered at 1 KHz. The waveforms are averages of eight consecutive responses.

averaged EMG activity of the two muscles in which activity was evoked by the cortical burst (**Figures 8B**,**C**). Note the similarity of all three waveforms. The cross-correlation function confirms the high degree of linear correlation between the MCx waveform and the respective EMG waveforms (**Figure 8D**). To a first order approximation, therefore, the corticospinal stage of synaptic transmission may be characterized as linear, or threshold-linear to be more precise (see also Townsend et al., 2006).

A HYPOTHESIS ON THE BASIC MODE OF OPERATION OF THE MCx

Ultimately we want to relate neural circuitry to function. However, without an understanding of the global function of the MCx such an undertaking will not be possible. In this final section we develop our current working hypothesis on the basic mode of operation of the MCx. By basic mode of operation, we mean the most elementary purpose for which it exists, which is to willfully move a limb from one position to another.

We hypothesize that the command inputs to the MCx are, whatever their origin, kinematic in nature. This is a base assumption, but it is consistent with a large body of evidence. Cortical areas having direct, or indirect, inputs to MCx encode spatial features such as, the location of visual and cutaneous stimuli in various reference frames, or the combined position of limb segments with respect to the body (e.g., see Rizzolatti and Kalaska, 2013). In the simplest case, we propose that the kinematic inputs specify where, for example, the arm must be moved to. The output of the MCx is related to muscle forces, those necessary to move the limb and those required for its postural support. We thus further hypothesize that a transformation from a kinematic to a kinetic (muscle) frame of reference occurs within the MCx. This is consistent with several studies (e.g., Ajemian et al., 2000; Trainin et al., 2007). We suggest that this does not occur in stages but automatically as a consequence of the projection of the external inputs onto the local connectivity. Consequently, unless one can manage to record from the axons of the input pathways, neural activity explicitly related to kinematic variables will not be experimentally observed. All MCx spike activities which can be recorded with present technology will be de facto related to muscle forces, that is coded in a muscle based reference frame, because the output layer V is strongly interconnected with the other cortical layers (Weiler et al., 2008). The essentially kinetic nature of MCx output is consistent with Evart's original finding that MCx neuron discharges are related to the muscular effort required to move inertial loads (Evarts, 1968), that under isometric conditions MCx neuron discharges are related to the exerted force (e.g., Smith et al., 1975) and that when the limb is free to move MCx neuron discharges are related to joint power (Scott et al., 2001), the product of force/torque and velocity. The linear correlation between MUA in MCx and EMG outputs shown in **Figure 8** is fully consistent with these key studies. The penultimate element of our hypothesis is that the transformation of kinematic command input to a muscle output pattern is based on the recruitment of embedded muscle synergies, according to the various schemes we have discussed in previous sections. The recurrent connectivity of the MCx is such that it can function as an attractor neural network (e.g., see Dayan and Abbott, 2001; Trappenberg, 2002). The input command to MCx will produce transient neural activity that, because of the recurrent connectivity, will settle to a steady-state activity pattern, the attractor state. In the process, this neural activity generates the required components of a motor command. A transient component that will drive the limb to the desired position and a steady-state, or tonic, component that will hold the limb in place. The transient component may recruit different muscles than those recruited by the tonic component. For example one may point to a location along the body's midline, but the arm may be initially located either to the left or to the right of that location. The muscle activities required to move the arm (transient component) is different in each case, but those required to hold the arm (tonic component) at that location are the same. The final element of our hypothesis is that the trajectory taken by the neural activity in the MCx as it settles to the steady-state depends on proprioceptive inputs to the MCx. This explains how different transient motor commands can be generated for the same kinematic input command.

Our hypothesis implies that there should be some relation between spatial position and muscle activation pattern. Our study of the arm's posture at the end of pointing movements made by humans demonstrates such a relation. Limb posture is an indirect but accurate reflection of the muscle activation pattern, our tonic component, when the limb is held in place after a movement. We therefore measured the posture of the arm at six different locations (targets) in the workspace. The subjects were instructed to move the hand at a comfortable speed twice from each of seven widely spaced initial start positions to place the pad of the index tip slightly above the center of target cylinders. These were positioned at six different locations on a table-top in front of the subject. The arm elevation (angle of the humeral segment relative to its projection in the horizontal plane) and forearm yaw (angle of the forearm projected onto the horizontal plane) angles for the 14 movements to each target were similar. That is, the upper limb (arm and forearm) orientations were about the same for any one target location despite the varied start positions (**Figure 9**). As can be seen in **Figure 9**, the variability of the arm elevation and forearm yaw angles at each target location are relatively small and in fact independent of the initial start position. Put simply, regardless of where the arm is located before moving the fingertip to a given spatial location, the posture of the arm at that spatial location is relatively constant. This means that, by and large, Donder's law is obeyed for pointing movements of the arm. That is, a given location of the arm endpoint (index finger tip) is achieved with the same orientations of the upper limb joints. Our results and conclusion differ from those of Soechting et al. (1995). In their study, large variations of some 25–30 degrees in average angle of the vector perpendicular to the plane of arm were observed at four of the five target locations after movements from widely spaced starting positions. However, in their study the subjects were instructed to "*move their arm to touch the tip of the pointer*." This leaves considerable freedom as to how to orient the fingertip relative to the pointer tip. In our task, there was no such ambiguity, as subjects were asked to place the pad of the index finger slightly over the center of the top of a short cylinder ∼2.5 cm in diameter.

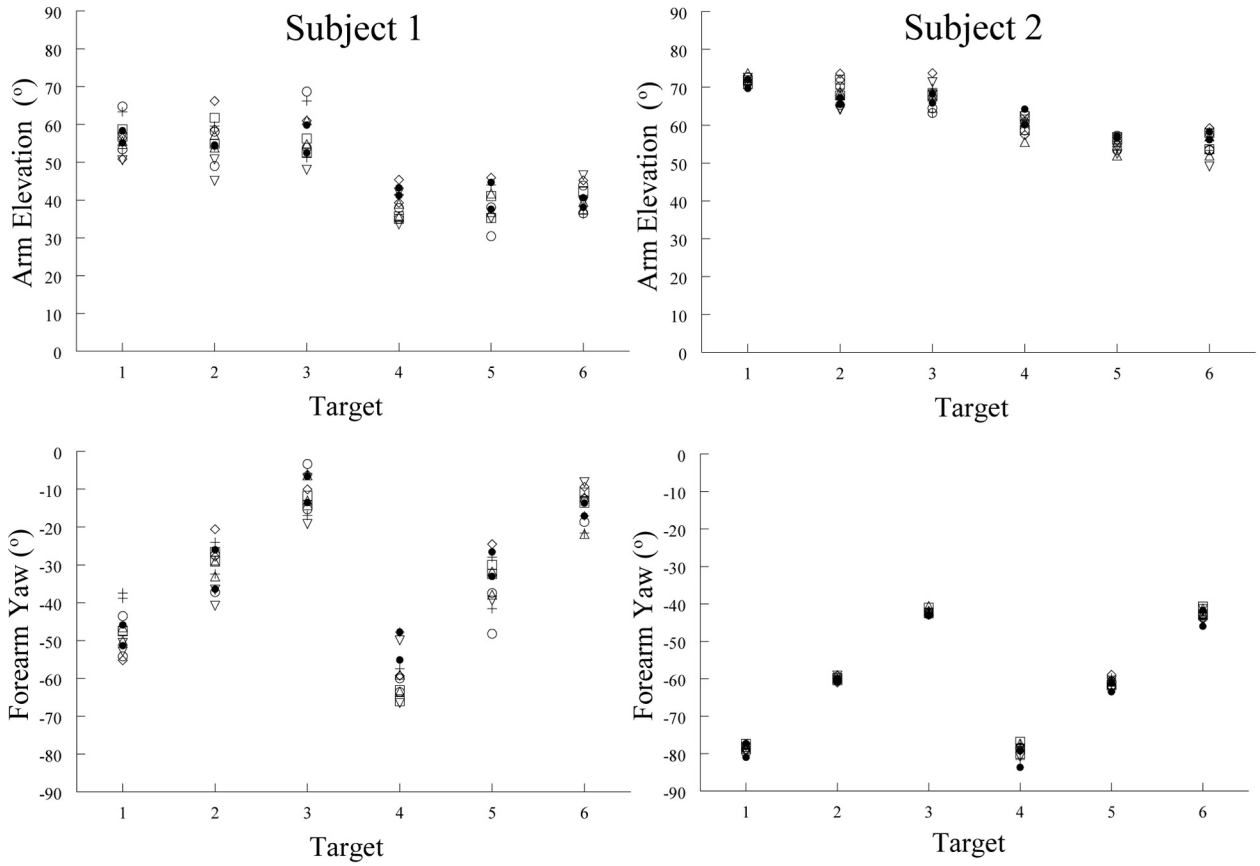

FIGURE 9 | Examples of arm elevation and forearm yaw angles characterizing arm posture at the end of pointing movements made to six different targets from seven different starting positions. Note the low variability of these angular measures at each target locations. This demonstrates that arm posture at the end of a pointing movement to a given location was essentially the same, regardless of the starting position of the arm. Each symbol represents a movement made from one of the seven starting positions.

The observation that the posture of the human arm at a given spatial location is essentially the same regardless of the starting position is consistent with our hypothesis. The findings of Aflalo and Graziano (2006) are also accordant with our hypothesis. They showed that, in monkeys, the discharge of MCx neurons is significantly related to the posture attained by the arm at the end of freely made spontaneous movements. Furthermore, microstimulation of a cortical point evoked arm postures that matched the postures to which the neurons at that point were best tuned.

EPILOGUE

In summary, it is the recurrent nature of the connectivity that makes it possible for a simple command input coded in a kinematic reference frame to set the MCx into action and automatically generate the transient and steady-state portions of the motor command. The computational scheme we propose would be difficult to implement in non-recurrent networks.

ACKNOWLEDGMENTS

The work described in this article was funded by grants from the Canadian Institutes of Health Research, the Natural Sciences and Engineering Research Council of Canada (NSERC) and the Canadian Foundation for Innovation to Charles Capaday. We thank Justin Capaday for his aid in editing the manuscript.

REFERENCES

Aflalo, T., and Graziano, M. S. (2006). Partial tuning of motor cortex neurons to final posture in a free-moving paradigm. *Proc. Natl. Acad. Sci. U.S.A.* 103, 2909–2914.

Ajemian, R., Bullock, D., and Grossberg, S. J. (2000). Kinematic coordinates in which motor cortical cells encode movement direction. *J. Neurophysiol.* 84, 2191–2203.

Alexander, M. R. (1992). *The Human Machine*. New York, NY: Columbia University Press.

Armstrong, D. M., and Drew, T. (1985). Forelimb electromyographic responses to motor cortex stimulation during locomotion in the cat. *J. Physiol.* 367, 327–351.

Baker, S. N., Spinks, R., Jackson, A., and Lemon, R. N. (2001). Synchronization in monkey motor cortex during a precision grip task. I. Task-dependent modulation in single-unit synchrony. *J. Neurophysiol.* 85, 869–885.

Buchwald, J. S., and Grover, F. S. (1970). Amplitudes of background fast activity characteristic of specific brain sites. *J. Neurophysiol.* 33, 148–159.

Buchwald, J. S., Halas, E. S., and Schramm, S. (1965). Comparison of multiple-unit and electroencephalogram activity recorded from the same brain sites during behavioural conditioning. *Nature* 205, 1012–1014.

Capaday, C. (1997). Neurophysiological methods for studies of the motor system in freely moving human subjects. *J. Neurosci. Methods* 74, 201–218.

Capaday, C. (2004). The integrated nature of motor cortical function. *Neuroscientist* 10, 207–220.

Capaday, C., Devanne, H., Bertrand, L., and Lavoie, B. A. (1998). Intracortical connections between motor cortical zones controlling antagonistic muscles in the cat: a combined anatomical and physiological study. *Exp. Brain Res.* 120, 223–232.

Capaday, C., Ethier, C., Brizzi, L., Sik, A., Van Vreeswijk, C., and Gingras, D. (2009). On the nature of the intrinsic connectivity of the cat motor cortex: evidence for a recurrent neural network topology. *J. Neurophysiol.* 102, 2131–2141.

Capaday, C., Forget, R., Fraser, R., and Lamarre, Y. (1991). Evidence for a contribution of the motor cortex to the long-latency stretch reflex of the human thumb. *J. Physiol.* 440, 243–255.

Capaday, C., and Van Vreeswijk, C. (2006). Direct control of firing rate gain by dendritic shunting inhibition. *J. Integr. Neurosci.* 5, 199–222.

Capaday, C., Van Vreeswijk, C., Ethier, C., Ferkinghoff-Borg, J., and Weber, D. (2011). Neural mechanism of activity spread in the cat motor cortex and its relation to the intrinsic connectivity. *J. Physiol.* 589, 2515–2528.

Cheney, P. D., and Fetz, E. E. (1984). Corticomotoneuronal cells contribute to long-latency stretch reflexes in the rhesus monkey. *J. Physiol.* 349, 249–272.

Dayan, P., and Abbott, L. F. (2001). *Theoretical Neuroscience*. The MIT Press.

Devanne, H., Cassim, F., Ethier, C., Brizzi, L., Thevenon, A., and Capaday, C. (2006). The comparable size and overlapping nature of upper limb distal and proximal muscle representations in the human motor cortex. *Eur. J. Neurosci.* 23, 2467–2476.

Devanne, H., Cohen, L. G., Kouchtir-Devanne, N., and Capaday, C. (2002). Integrated motor cortical control of task-related muscles during pointing in humans. *J. Neurophysiol.* 87, 3006–3017.

Donoghue, J. P., Leibovic, S., and Sanes, J. N. (1992). Organization of the forelimb area in squirrel monkey motor cortex: representation of digit, wrist, and elbow muscles. *Exp. Brain Res.* 89, 1–19.

Ethier, C., Brizzi, L., Darling, W. G., and Capaday, C. (2006). Linear summation of cat motor cortex outputs. *J. Neurosci.* 26, 5574–5581.

Ethier, C., Brizzi, L., Giguere, D., and Capaday, C. (2007). Corticospinal control of antagonistic muscles in the cat. *Eur. J. Neurosci.* 26, 1632–1641.

Evarts, E. V. (1968). Relation of pyramidal tract activity to force exerted during voluntary movement. *J. Neurophysiol.* 31, 14–27.

Gould, H. J. 3rd., Cusick, C. G., Pons, T. P., and Kaas, J. H. (1986). The relationship of corpus callosum connections to electrical stimulation maps of motor, supplementary motor, and the frontal eye fields in owl monkeys. *J. Comp. Neurol.* 247, 297–325.

Graziano, M. S. (2006). The organization of behavioral repertoire in motor cortex. *Ann. Rev. Neurosci.* 29, 105–134.

Graziano, M. S., Patel, K. T., and Taylor, C. S. (2004). Mapping from motor cortex to biceps and triceps altered by elbow angle. *J. Neurophysiol.* 92, 395–407.

Graziano, M. S., Taylor, C. S., Moore, T., and Cooke, D. F. (2002). The cortical control of movement revisited. *Neuron* 36, 349–362.

Griffin, D. M., Hudson, H. M., Belhaj-Saif, A., and Cheney, P. D. (2011). Hijacking cortical motor output with repetitive microstimulation. *J. Neurosci.* 31, 13088–13096.

Haider, B., Duque, A., Hasenstaub, A. R., and McCormick, D. A. (2006). Neocortical network activity *in vivo* is generated through a dynamic balance of excitation and inhibition. *J. Neurosci.* 26, 4535–4545.

Huntley, G. W., and Jones, E. G. (1991). Relationship of intrinsic connections to forelimb movement representations in monkey motor cortex: a correlative anatomic and phylogical study. *J. Neurophysiol.* 66, 390–413.

Jackson, A., Gee, V. J., Baker, S. N., and Lemon, R. N. (2003). Synchrony between neurons with similar muscle fields in monkey motor cortex. *Neuron* 38, 115–125.

Jackson, J. H. (1931). *Selected Writings of John Hughlings Jackson*. London: Hodder and Stoughton.

Keller, A. (1993). Intrinsic connections between representation zones in the cat motor cortex. *Neuroreport* 4, 515–518.

Krings, T., Naujokat, C., and von Keyserlingk, D. G. (1998). Representation of cortical motor function as revealed by stereotactic transcranial magnetic stimulation. *Electroencephalogr. Clin. Neurophysiol.* 109, 85–93.

Lacquaniti, F., and Soechting, J. F. (1982). Coordination of arm and wrist motion during a reaching task. *J. Neurosci.* 2, 399–408.

Legatt, A. D., Arezzo, J., and Vaughan, H. G., Jr. (1980). Averaged multiple unit activity as an estimate of phasic changes in local neuronal activity: effects of volume-conducted potentials. *J. Neurosci. Methods* 2, 203–217.

Lund, J. S., Yoshioka, T., and Levitt, J. B. (1993). Comparison of intrinsic connectivity in different areas of macaque monkey cerebral cortex. *Cereb. Cortex* 3, 148–162.

Massion, J. (1992). Movement, posture and equilibrium: interaction and coordination. *Prog. Neurobiol.* 38, 35–56.

Matsumura, M., Chen, D., Sawaguchi, T., Kubota, K., and Fetz, E. E. (1996). Synaptic interactions between primate precentral cortex neurons revealed by spike-triggered averaging of intracellular membrane potentials *in vivo*. *J. Neurosci.* 16, 7757–7767.

McKiernan, B. J., Marcario, J. K., Karrer, J. H., and Cheney, P. D. (1998). Corticomotoneuronal post-spike effects in shoulder, elbow, wrist, digit, and intrinsic hand muscles during a reach and prehension task. *J. Neurophysiol.* 80, 1961–1980.

Okun, M., and Lampl, I. (2008). Instantaneous correlation of excitation and inhibition during ongoing and sensory-evoked activities. *Nat. Neurosci.* 11, 535–537.

Park, M. C., Belhaj-Saif, A., Gordon, M., and Cheney, P. D. (2001). Consistent features in the forelimb representation of primary motor cortex in rhesus macaques. *J. Neurosci.* 21, 2784–2792.

Penfield, W., and Rasmussen, T. (1950). *The Cerebral Cortex of Man: A Clinical Study of Localization of Function*. New York, NY: McMillan.

Phillips, C. G. (1969). The ferrier lecture, 1968. Motor apparatus of the baboon's hand. *Proc. R. Soc. Lond. B Biol. Sci.* 173, 141–174.

Phillips, C. G. (1975). Laying the ghost of 'muscles versus movements'. *Can. J. Neurol. Sci.* 2, 209–218.

Preston, J. B., Shende, M. C., and Uemura, K. (1967). "The motor cortex–pyramidal system: patterns of facilitation and inhibition on motoneuronns innervating limb musculature of cat and baboon and their possible adaptive significance," in *Neurophysiological Basis of Normal and Abnormal Motor Activities*, eds M. D. Yahr and D. P. Purpura (Hewlett, NY: Raven Press), 61–74.

Rathelot, J. A., and Strick, P. L. (2006). Muscle representation in the macaque motor cortex: an anatomical perspective. *Proc. Natl. Acad. Sci. U.S.A.* 103, 8257–8262.

Rizzolatti, G., and Kalaska, J. F. (2013). "Voluntary movement: the parietal and premotor cortex," in *Principles of Neural Science*, eds E. R. Kandel, J. H. Schwartz, T. M. Jessel, S. A. Siegelbaum, and A. J. Hudspeth (Mc Graw Hill), 865–882.

Sanes, J. N., Donoghue, J. P., Thangaraj, V., Edelman, R. R., and Warach, S. (1995). Shared neural substrates controlling hand movements in human motor cortex. *Science* 268, 1775–1777.

Schneider, C., Devanne, H., Lavoie, B. A., and Capaday, C. (2002). Neural mechanisms involved in the functional linking of motor cortical points. *Exp. Brain Res.* 146, 86–94.

Schneider, C., Zytnicki, D., and Capaday, C. (2001). Quantitative evidence for multiple widespread representations of individual muscles in the cat motor cortex. *Neurosci. Lett.* 310, 183–187.

Scott, S. H., Gribble, P. L., Graham, K. M., and Cabel, D. W. (2001). Dissociation between hand motion and population vectors from neural activity in motor cortex. *Nature* 413, 161–165.

Smith, A. M., Hepp-Reymond, M. C., and Wyss, U. R. (1975). Relation of activity in precentral cortical neurons to force and rate of force change during isometric contractions of finger muscles. *Exp. Brain Res.* 23, 315–332.

Smith, W. S., and Fetz, E. E. (2009). Synaptic linkages between corticomotoneuronal cells affecting forelimb muscles in behaving primates. *J. Neurophysiol.* 102, 1040–1048.

Soechting, J. F., Buneo, C. A., Herrmann, U., and Flanders, M. (1995). Moving effortlessly in three dimensions: does Donders' law apply to arm movement? *J. Neurosci.* 15, 6271–6280.

Stark, E., and Abeles, M. (2007). Predicting movement from multiunit activity. *J. Neurosci.* 27, 8387–8394.

Townsend, B. R., Paninski, L., and Lemon, R. N. (2006). Linear encoding of muscle activity in primary motor cortex and cerebellum. *J. Neurophysiol.* 96, 2578–2592.

Trainin, E., Meir, R., and Karniel, A. (2007). Explaining patterns of neural activity in the primary motor cortex using spinal cord and limb biomechanics models. *J. Neurophysiol.* 97, 3736–3750.

Trappenberg, T. P. (2002). *Fundamentals of Computational Neuroscience*. Oxford University Press.

Van Vreeswijk, C., and Sompolinsky, H. (1996). Chaos in neuronal networks with balanced excitatory and inhibitory activity. *Science* 274, 1724–1726.

Van Vreeswijk, C., and Sompolinsky, H. (1998). Chaotic balanced state in a model of cortical circuits. *Neural Comput.* 10, 1321–1372.

Walshe, F. M. R. (1943). On the mode of representation of movements in the motor cortex with special reference to convulsions beginning unilateraly (Jackson). *Brain* 66, 104–142.

Wassermann, E. M., McShane, L. M., Hallett, M., and Cohen, L. G. (1992). Noninvasive mapping of muscle representations in human motor cortex. *Electroencephalogr. Clin. Neurophysiol.* 85, 1–8.

Weiler, N., Wood, L., Yu, J., Solla, S. A., and Shepherd, G. M. (2008). Top-down laminar organization of the excitatory network in motor cortex. *Nat. Neurosci.* 11, 360–366.

White, E. L. (1989). *Cortical Circuits.* Basel: Birkhauser.

Conflict of Interest Statement: The authors declare that the research was conducted in the absence of any commercial or financial relationships that could be construed as a potential conflict of interest.

Received: 02 December 2012; accepted: 27 March 2013; published online: 18 April 2013.

Citation: Capaday C, Ethier C, Van Vreeswijk C and Darling WG (2013) On the functional organization and operational principles of the motor cortex. Front. Neural Circuits 7:66. doi: 10.3389/fncir.2013.00066

frontiers in
NEURAL CIRCUITS

ORIGINAL RESEARCH ARTICLE
published: 04 April 2013
doi: 10.3389/fncir.2013.00051

Heterogeneous neural coding of corrective movements in motor cortex

Adam S. Dickey[1], Yali Amit[1,2] and Nicholas G. Hatsopoulos[1,3]*

[1] Committee on Computational Neuroscience, University of Chicago, Chicago, IL, USA
[2] Department of Statistics, University of Chicago, Chicago, IL, USA
[3] Department of Organismal Biology and Anatomy, University of Chicago, Chicago, IL, USA

Edited by:
Michael Brecht, Humboldt University Berlin, Germany

Reviewed by:
Scott Hooper, Ohio University, USA
David J. Margolis, Rutgers University, USA

***Correspondence:**
Nicholas G. Hatsopoulos, Department of Organismal Biology and Anatomy, University of Chicago, 1025 East 57th Street, Chicago, IL 60637, USA.
e-mail: nicho@uchicago.edu

During a reach, neural activity recorded from motor cortex is typically thought to linearly encode the observed movement. However, it has also been reported that during a double-step reaching paradigm, neural coding of the original movement is replaced by that of the corrective movement. Here, we use neural data recorded from multi-electrode arrays implanted in the motor and premotor cortices of rhesus macaques to directly compare these two hypotheses. We show that while a majority of neurons display linear encoding of movement during a double-step, a minority display a dramatic drop in firing rate that is predicted by the replacement hypothesis. Neural activity in the subpopulation showing replacement is more likely to lag the observed movement, and may therefore be involved in the monitoring of the sensory consequences of a motor command.

Keywords: double-step, reaching, motor cortex, neural coding, target jump

INTRODUCTION

There is a long tradition of investigating motor control by using a double-step reaching paradigm, where a target jumps to a new location after a movement is initiated (Georgopoulos et al., 1981; Soechting and Lacquaniti, 1983; Goodale et al., 1986; Pelisson et al., 1986; Paulignan et al., 1991; Prablanc and Martin, 1992). For example, this double-step paradigm was used to implicate posterior parietal cortex (PPC) in monitoring the error between the hand and target position, because online corrections are not made in response to a double-step when this area is inactivated by transcranial magnetic stimulation (Desmurget et al., 1999; Reichenbach et al., 2011) or by a lesion (Grea et al., 2002).

Only a few studies have used extracellular recordings in cerebral cortex to investigate neural coding during a double-step reaching paradigm (Georgopoulos et al., 1983; Archambault et al., 2009, 2011). These studies found that in primary motor (MI) and dorsal premotor (PMd) cortices (Archambault et al., 2011), and in area 5 of the PPC (Archambault et al., 2009), neural activity during a double-step was well-explained by replacing the original neural activity with neural activity corresponding to the correction elicited by the target jump.

However, this idea of replacement is at odds with the traditional view in the motor cortical encoding literature, which describes neural activity during reaching as a linear function of hand kinematics, particularly the instantaneous direction and speed (Georgopoulos et al., 1982; Schwartz et al., 1988; Moran and Schwartz, 1999; Wang et al., 2007). These models would not predict anything different during a double-step reach.

Here, we use multi-electrode arrays to record neural data from MI, PMd, and ventral premotor (PMv) cortices from rhesus macaques performing reaches, and directly compare the default, linear encoding hypothesis to the replacement hypothesis previously proposed in cortical double-step studies. The replacement hypothesis (Archambault et al., 2009, 2011) was developed in the context of a standard center-out task, requiring reaches from a center target to one of eight peripheral targets arranged in a circle. The double-step involved jumping from the original target to a target located 180° opposite on the circle. Double-step activity was fit by starting with the original neural activity for movement from the center to the first target and replacing it with neural activity for movement from the center to the second target, which predicted the observed neural activity better than replacing it with neural activity associated with movement from the center to a randomly selected target (Archambault et al., 2009, 2011). Though these studies found that a linear encoding model generalized poorly from single-step to double-step trials (Archambault et al., 2009, 2011), the prediction of the "Replacement" hypothesis was not directly compared to the alternative of linear encoding of observed kinematics. This is because the "Replacement" prediction was derived from the directly observed, trial-averaged neural activity, instead of the prediction of a linear model fit using single-trials. Thus it is not clear that the replacement model predicts double-step neural activity better than a standard linear encoding model of observed kinematics.

Here, we use the concept of superposition to allow a direct comparison of the two hypotheses. It has been previously shown that the kinematics during a double-step can be expressed as the superposition (or vector sum) of the original, unperturbed movement and a corrective movement from the original target location to the new target location (Flash and Henis, 1991). We define the "Replaced" hypothesis to mean that, during a double-step trial, neurons first encode the kinematics of the original movement, and then switch to encode the kinematics of the corrective movement. To test this prediction, the observed movement first needs to be decomposed into a linear combination of its two constituent parts: the original movement and the corrective movement. To allow a direct and fair comparison to the standard linear encoding model,

we define an alternative "Summed" hypothesis which states that neurons encode the summed kinematics of the two constituent movements, which should closely match the observed movement.

The difference between the "Replaced" and "Summed" hypotheses can be best understood in the context of a double-step movement in one dimension, where the target is simply perturbed farther in the direction of the original movement (**Figure 1**). If the target jump happens soon after movement onset, the correction will be triggered before the original movement ends. This means that the velocity profile will be double-peaked, and it will not return to 0 between the peaks (**Figure 1A**, top). This double-peaked profile can be decomposed into the sum of two overlapping single-peaked speed profiles. If we assume that neurons linearly encode the velocity in the neuron's preferred direction at a single leading time delay, then the firing rate profile should also be double-peaked (**Figure 1A**, middle). That is the "Summed" prediction. In contrast, in the "Replaced" prediction, the firing rate first follows the original, single-peaked profile and then switches to the second, corrective single-peaked profile at some time prior to the start of the second movement (**Figure 1A**, bottom). This switch produces a sharp drop in firing rate back to the baseline level, before rising again to match the corrective velocity profile.

If instead neuronal firing lags the velocity profile, the "Summed" prediction simply shifts to the right but is otherwise unchanged (**Figure 1B**, middle). However, if the switch time happens at the same time point, then the "Replaced" hypothesis predicts an extended silent period where the firing rate drops to the baseline level, before rising again to track the corrective movement (**Figure 1B**, bottom). The predictions of the "Summed" and "Replaced" hypotheses are quite different, so we should be able to resolve on a neuron by neuron basis which hypothesis better fits single-trial neural activity.

MATERIALS AND METHODS

NEURAL RECORDINGS

Three rhesus macaques (*Macaca mulatta*) were implanted with a total of five Utah 100-microelectrode arrays (Blackrock Microsystems, Salt Lake City, UT, USA) in MI, PMv, or PMd cortices in the right hemisphere (contralateral to the arm used for the task). Subject CO had arrays in MI, PMd, and PMv, subject MK had an array in MI, and subject BO had an array in PMd (**Figure 2**). The length of the electrodes on subject CO's MI array was 1.5 mm, while the length on the other four arrays was 1 mm. All electrode tips were sputter-coated with platinum, except for subject MK's MI electrode tips, which were coated with iridium oxide. The procedure for implanting the Utah array has been described elsewhere (Rousche and Normann, 1992; Maynard et al., 1999). During a recording session, signals from 96 electrodes were amplified (gain of 5,000), band-pass filtered between 0.3 Hz and 7.5 kHz, and recorded digitally (14-bit) at 30 kHz per channel using a Cerberus acquisition system (Blackrock Microsystems Inc., Salt Lake City, UT, USA). Only waveforms (duration, 1.6 ms; 48 sample time points per waveform) that crossed a voltage threshold were stored for off-line sorting. This voltage threshold was set just outside the noise band, so that all potential spike waveforms were recorded for later off-line spike sorting. Spike waveform data were sorted in Offline Sorter (Plexon, Dallas, TX, USA) using a user-defined unit template, which was a single waveform shape to which all potential spike waveforms were compared. All waveforms whose mean square error from this template fell below a

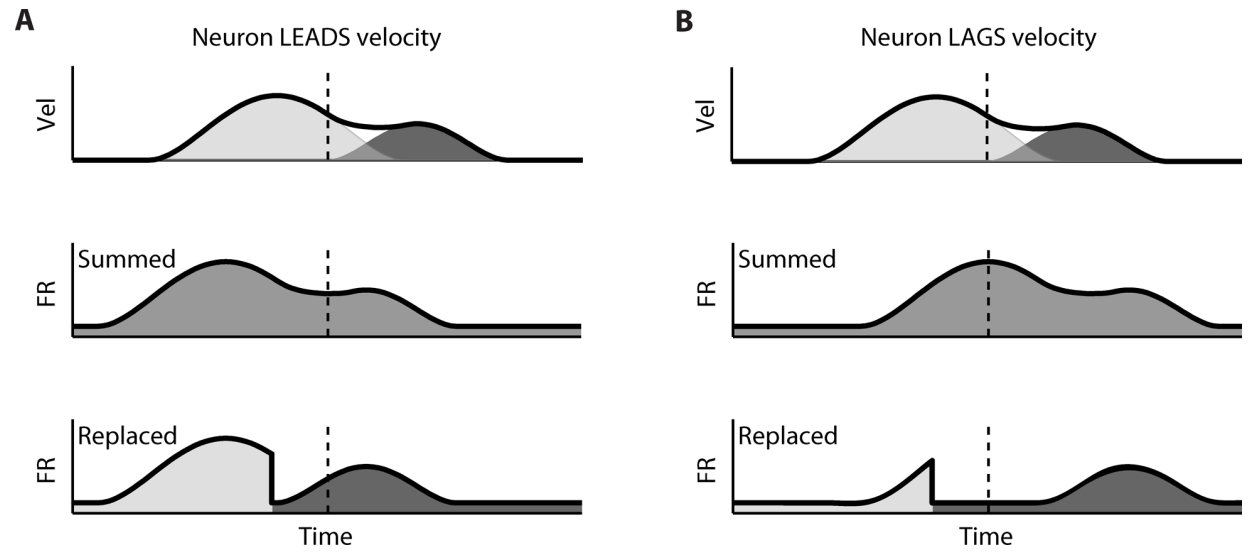

FIGURE 1 | Schematic of the two hypotheses for neural coding during a double-step. (A) *Top*: The theoretical double-peaked velocity profile of a double-step trial (black) can be decomposed into the sum of a primary velocity profile (light gray) and an overlapping, secondary velocity profile (dark gray); *middle*: Under the default "Summed" hypothesis, neural firing is predicted to track the observed velocity profile, preceding it at a fixed lead; *bottom*: The alternative "Replaced" hypothesis predicts that the neural firing will track the primary velocity profile (light gray), before replacing this with coding of the secondary profile (dark gray). **(B)** The predictions under the "Summed" and "Replaced" hypotheses if neuronal firing instead lags the observed velocity. The replacement between coding of the primary and secondary movements is assumed to happen at a fixed delay that we call the *neural offset*, prior to the start of the second movement (dashed line).

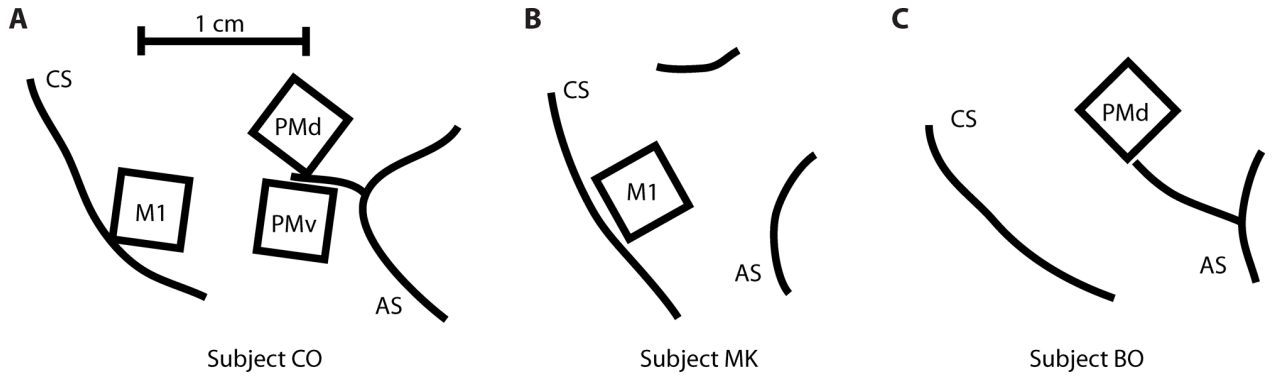

FIGURE 2 | Location of the five multi-electrode arrays relative to the central sulcus (CS) and the arcuate sulcus (AS). (A) Subject CO had arrays in primary motor cortex (MI), dorsal premotor cortex (PMd), and ventral premotor cortex (PMv). **(B)** Subject MK had one array in MI. **(C)** Subject BO had one array in PMd.

user-defined threshold were classified as spikes belonging to that unit.

BEHAVIORAL TASK

Subjects were operantly conditioned to perform a behavioral task requiring planar reaching movements using a two-link robotic exoskeleton (KINARM, BKIN Technologies, Kingston, ON, Canada) that sampled X and Y positions of the hand at 500 Hz. However, for these experiments, the shoulder angle was locked, so only one-dimensional, elbow flexion and extension movements were possible. Control (single-step) trials of the behavioral task involved maneuvering a cursor controlled by the hand position to acquire a target within 1,500 ms of its appearance and then holding on it for a random hold period (uniformly distributed from 300 to 700 ms). There was no instructed delay, so subjects were free to move to the target as soon as it appeared. There were five discrete target locations (numbered 1–5), equally spaced at 1.35, 1.5, 1.65, 1.8, and 1.95 radians, respectively. Here, 0 radians indicates a fully extended elbow and an increasing angle indicates elbow flexion. The target width was 0.05 radians. Since the subjects forearm lengths were approximately 20 cm, this corresponds to an approximately 1 cm wide target.

In addition to these single-step control trials, up to one-third of trials requiring movement between targets 2, 3, or 4 were perturbed to become double-step trials. The target shifted its position when the cursor moved more than 0.075 radians from the original target center.

In the three "Forward Jump" datasets, the target was perturbed in the same direction as the initial movement by 0.15 radians (for example, a movement starting at location 2 to a target at location 4 was perturbed by moving the target to location 5). In the four "Reverse Jump" datasets, the target was perturbed in the opposite direction of the initial movement by 0.15 radians. More details of the seven datasets analyzed are given below (**Table 1**). Of note, subject CO had all three arrays implanted simultaneously, and datasets #1 and #5 were recorded simultaneously. Each dataset represents all neurons recorded from one cortical area in a given day's training session. All of the surgical and behavioral procedures were approved by the University of Chicago Institutional Animal Care and Use Committee and conform to the principles outlined in the *Guide for the Care and Use of Laboratory Animals.*

DATA PROCESSING

The raw angular position traces were first low-pass filtered forward and backward using a fourth order Butterworth filter and a 10-Hz cutoff frequency. These were then differentiated to obtain the angular velocity traces. For single-step trials, spike times were aligned on the first crossing of a 0.3-radians/s velocity threshold after target appearance. For double-step trials, spike times were aligned on the jump time (when the change in target location occurred). Mean trajectories and peri-event time histograms (PETHs) were computed by averaging kinematics and spike counts across all trials with the same starting and ending locations in a time window from −300 ms before the velocity threshold crossing (or jump time for the double-step trials) to 800 ms afterward.

ENCODING MODEL

Previous studies have reported that motor cortical firing is linearly related to both the Cartesian velocity and speed of the hand at a single time lag (Moran and Schwartz, 1999), but also that cortical

Table 1 | Details are provided for the seven datasets reported here.

#	Area	Subject	Jump Dir.	Single	Double	Neurons	Analyzed
1	MI	CO	Forward	1,626	167	26	17
2	MI	MK	Reverse	1,276	228	70	41
3	MI	CO	Reverse	1,428	242	36	17
4	PMd	BO	Reverse	1,645	280	115	67
5	PMd	CO	Forward	1,626	167	88	30
6	PMd	CO	Reverse	1,407	299	128	56
7	PMv	CO	Forward	1,943	275	90	54

From left to right, the columns list the dataset number (#), the cortical area recorded from (Area), the subject ID (Subject), whether the dataset had a "Forward" or "Reverse" double-step (Jump Dir.), the number of single-step trials (Single), double-step trials (Double), sorted neurons (Neurons), and neurons analyzed in the Section "Results" (Analyzed).

discharge is better explained by joint angular velocity than Cartesian velocity (Reina et al., 2001). For our 1-D behavioral task, we combine these two results and assume that during single-step trials motor cortical firing rate FR(t) is a linear function of the elbow joint angular velocity $V(t)$ and speed $|V(t)|$ at a single time delay δ. The baseline firing rate is b_0, and b_1 and b_2 are the coefficients for velocity and speed tuning, respectively.

$$\mathrm{FR}(t-\delta) = b_0 + b_1 V(t) + b_2|V(t)|. \tag{1}$$

Although in 1-D angular velocity and speed can differ only in sign, they are uncorrelated and the linear prediction is better when using both. Spike times for each neuron from all successful single-step trials were binned every 10 ms, and the resulting spike counts were smoothed by convolving them with a Gaussian kernel with a standard deviation of 30 ms, similar to the Archambault et al.'s (2009; 2011) studies. These smoothed spike counts were fit as a linear function of the elbow angular velocity and speed, sampled every 10 ms and delayed by the parameter δ. We tested all possible delays from −300 to +300 ms in 10 ms increments, and kept the delay with the highest correlation coefficient between the predicted and actual binned spike counts. We also fit a logistic version of Eq. 1, using standard generalized linear model techniques, relating kinematics to binary spike counts in 10 ms bins (the 0.2% bins containing more than one spike were treated as having one spike).

Of the 553 neuron samples which were originally recorded across the seven datasets, we excluded from analysis the 190 neurons which had an encoding delay of greater than +175 ms. This is due to the fact that these neurons tended to respond precisely to the visual appearance of the target, usually 100 ms following target appearance (Reimer and Hatsopoulos, 2010), rather than in anticipation of future velocity or response to past velocity. For the remaining neurons, we compared the prediction of the encoding model (Eq. 1) to the mean PETHs computed for each combination of starting and end point by computing a correlation coefficient between the observed and predicted PETHs. We rejected an additional 81 neurons whose correlation coefficient was less than 0.5. This left 282 neurons for further analysis. The number of neurons analyzed in each dataset is given in **Table 1**. These are neurons for which the linear encoding model (Eq. 1) provides an adequate prediction of the firing rate on control, single-step motions between pairs of targets.

DECOMPOSING DOUBLE-STEP KINEMATICS

It has been previously shown that kinematics during a target jump can be decomposed into the sum of two minimum jerk movements (Flash and Henis, 1991; Henis and Flash, 1995). If the inter-stimulus interval between the original target presentation and the target jump is greater than 100 ms, then the original movement is directed from the start point to the original target location, and the secondary movement is directed from the original target to the new target location (Henis and Flash, 1995).

We first fit the control, single-step movements to a single minimum jerk trajectory. The minimum jerk velocity profile is mathematically described below (Eq. 2) for a movement starting at time t_0 with duration d and with an amplitude a, which is the change in position from the beginning to the end of the movement (Hogan, 1984; Flash and Hogan, 1985). Note that velocity is defined to be 0 before the start point t_0 or after the endpoint $t_0 + d$.

$$V(t; t_0, a, d) = \left\{ \begin{array}{c} 30\frac{a}{d}\left(\tau^4 - 2\tau^3 + \tau^2\right), \tau = \frac{(t-t_0)}{d} \ \text{ for } t_0 \le t \le t_0 + d \\ 0 \text{ otherwise} \end{array} \right\}. \tag{2}$$

The angular velocity during a double-step trial $V_{JUMP}(t)$ was fit as a sum of a primary (V_1) and secondary (V_2) minimum jerk velocity profile (Eq. 3). Thus the double-step velocity can be described with six parameters.

$$\begin{aligned} V_{\mathrm{JUMP}}(t) &\approx V_{\mathrm{SUM}}(t; t_1, a_1, d_1, t_2, a_2, d_2) \\ &= V_1(t; t_1, a_1, d_1) + V_2(t; t_2, a_2, d_2). \end{aligned} \tag{3}$$

We found the optimal set of six parameters to fit a given double-step velocity profile $V_{\mathrm{JUMP}}(t)$ by minimizing the cost function expressed below (Eq. 4).

$$\begin{aligned} C(t_1, a_1, d_1, t_2, a_2, d_2) = \\ \frac{(1-\alpha)}{(\sigma_{\mathrm{ERR}})^2}\left[\sum_t \left(V_{\mathrm{JUMP}}(t) - V_{\mathrm{SUM}}(t; t_1, a_1, d_1, t_2, a_2, d_2)\right)^2\right] \\ + \alpha\left[\sum_{i=1}^{2}\left(a_i - a_i^*\right)^2/(\sigma_a)^2 + \sum_{i=1}^{2}\left(d_i - d_i^*\right)^2/ \right. \\ \left. (\sigma_d)^2 + \left(t_2 - t^*\right)^2/(\sigma_t)^2\right]. \end{aligned} \tag{4}$$

We make the assumption that the parameters of two component movements will be similar to the corresponding single-step motions. Thus, for a double-step which starts at location 2 where the target jumps from location 4 to 5, we assume the primary motion V_1 is similar to the single-step movement from 2 to 4, and the secondary motion V_2 is similar to the single-step movement from 4 to 5. The values of the coefficients were constrained by including a squared error term relative to a reference value, multiplied by a scaling factor. These reference values and scaling factors were derived from single-step trials. We fit the velocity profiles from single-step trials to a minimum jerk velocity profile (Eq. 2) by minimizing the sum of squared errors. The reference amplitudes (a_1^*, a_2^*) and durations (d_1^*, d_2^*) were set to the median of the amplitudes and durations fit to the corresponding single-step trials, and so these values varied from dataset to dataset. The remaining parameters (t^*,σ_a, σ_b, σ_t, σ_{ERR}) were set constant for all datasets, and were derived from the "well-fit" single-step trials from one dataset (#7) whose correlation between actual and fit velocity was above 0.9 for 1,694 of 1,943 trials (87%). The start time of the first movement was unconstrained, but the reference start time of the second movement (relative to the jump

time) was set as the mean of the reaction time of these well-fit single-step trials ($t^\star = 220$ ms), with scaling factor given by their standard deviation ($\sigma_t = 50$ ms). Similarly, the scale factor for the amplitude and duration was again set to the pooled estimate of their standard deviations for the well-fit single-step trials ($\sigma_a = 0.3$ radians, $\sigma_d = 90$ ms). The sum squared error between the actual and fit velocity was normalized by the mean squared error of the well-fit single-step trials ($\sigma_{ERR} = 0.08$ radians/s). There was also an arbitrary weight constant ($\alpha = 0.95$) added to prevent the velocity error term from dominating the coefficient error terms.

"SUMMED" vs. "REPLACED" HYPOTHESIS

Under the default "Summed" hypothesis, the same encoding model (Eq. 1) that was fit to single-step trials was applied to double-step trials. However, rather than applying this encoding model to the observed velocity profile V_{JUMP}, the firing rate was predicted using the fit velocity profile V_{SUM}:

$$FR_{SUM}(t-\delta) = b_0 + b_1 V_{SUM}(t) + b_2 |V_{SUM}(t)| . \quad (5)$$

The "Summed" prediction is based on the fit velocity V_{SUM} to allow a direct comparison to the alternative "Replaced" hypothesis, where neurons instead encode the constituent movements V_1 and V_2 which comprise V_{SUM}. The "Replaced" hypothesis states that neurons will first encode the primary movement, and then switch to encoding the secondary movement at some time after the target jump (Eq. 6). We assume that this switch time is fixed to the start of the second movement t_2 minus some constant neural offset t_N. To prevent over-fitting, we fixed the neural offset to a constant for each cortical area before comparing the prediction to the "Summed" hypothesis.

$$FR_{REPLACE}(t) = \left\{ \begin{array}{l} b_0 + b_1 V_1(t+\delta) + b_2 |V_1(t+\delta)| \text{ for } t < t_2 - t_N \\ b_0 + b_1 V_2(t+\delta) + b_2 |V_2(t+\delta)| \text{ for } t \geq t_2 - t_N \end{array} \right\} . \quad (6)$$

We compared the "Summed" (Eq. 5) and the "Replaced" (Eq. 6) predictions in terms of their fit to observed neural activity during a double-step trial. We predicted the spike count in 10 ms bins for each trial, and assessed the goodness of fit of these predictions by computing the root-mean-square error (RMSE) between the prediction and the smoothed spike train (after convolution with a Gaussian kernel with a 30-ms standard deviation). The calculation of the RMSE metric was limited to a time interval from the jump time to 500 ms after the jump, as the predictions of the two hypotheses were very similar outside of this window. The RMSE metric includes data, from double-step trials from all the movement conditions. Predicted firing rates less than 1 spike/s were replaced with replaced with 1 spike/s. This thresholding was performed to prevent the linear model from predicting a negative or zero firing rate. A paired t-test was then used to determine if the mean RMSE was significantly different between the two predictions.

We also compared the predictions for the "Summed" and "Replaced" hypotheses using the logistic version of Eq. 1. For the logistic prediction of firing rate, $FR^\star(t)$, we computed a log-likelihood of observed binary spike counts in 10 ms bins, given the "Summed" or "Replaced" predictions. We assume spike counts are conditionally independent Bernoulli random variables. If the binary spike count for a given neuron at time t is denoted $x(t)$, then the log-likelihood of a spike train given the "Summed" hypothesis (L_{SUM}) is given in Eq. 7. A similar expression holds for log-likelihood of the "Replaced" hypothesis ($L_{REPLACED}$).

$$L_{SUM} = \sum_t x(t) \log\left(FR^*_{SUM}(t)\right) + (1 - x(t)) \log\left(1 - FR^*_{SUM}(t)\right) . \quad (7)$$

RESULTS

A decomposition algorithm was used (see Decomposing Double-step Kinematics) to fit the double-step velocity profiles to the sum of two minimum jerk velocity profiles (**Figure 3**). For a single trial (**Figure 3A**), the fit velocity profile does a good job matching the bulk of the observed double-peak profile, though it does not fit the reversal in velocity, which comes after the second movement. The fraction of variance (R^2) of the actual velocity explained by the fit velocity was 0.986. The decomposition performed similarly well for all 52 double-step trials for this movement condition from dataset #7 (**Figure 3B**), where the starting point was location 2, and the target jumped from location 4 to 5. The main difference is that the fit velocity is constant at 0 before and after the double-peaked velocity profile. The median R^2 for these trials was also 0.986, and the mean was 0.983 (standard deviation 0.015). For the 1,658 successful double-step trials from all datasets, the median R^2 was 0.982, with a mean of 0.970 (standard deviation 0.0357).

We can use the parameters of the fit velocity profile as an estimate of the reaction time, either from the target appearance or the target jump (**Table 2**, left). The average reaction time of all single-step trials (with amplitude 0.15 radians) of a given dataset varied from 203 to 230 ms. However, when looking across the seven datasets, the mean of these single-step reaction times was not significantly different from the mean of the first or second double-step reaction times (paired t-test, $p > 0.05$). The average movement duration for single-step trials (with amplitude 0.15 radians) varied from 405 to 457 ms (**Table 2**, right). Similarly, when looking across the seven datasets, the mean of these single-step durations was not significantly different from the mean of the first or second double-step durations (paired t-test, $p > 0.05$).

Given the decomposition, we still need one extra parameter to predict the neural firing under the "Replaced" hypothesis: the neural offset t_N. This is a constant which represents how soon before the start of the secondary movement (t_2) the neurons show the replacement effect. We first assumed that the neural offset for each neuron was constant for all movement conditions, but different across neurons. We then tested a range of offsets for each neuron, from 0 to 250 ms in 10 ms increments, and picked the offset which minimized the RMSE of the data given the "Replaced" prediction. Within this range, we are trying to find a change in

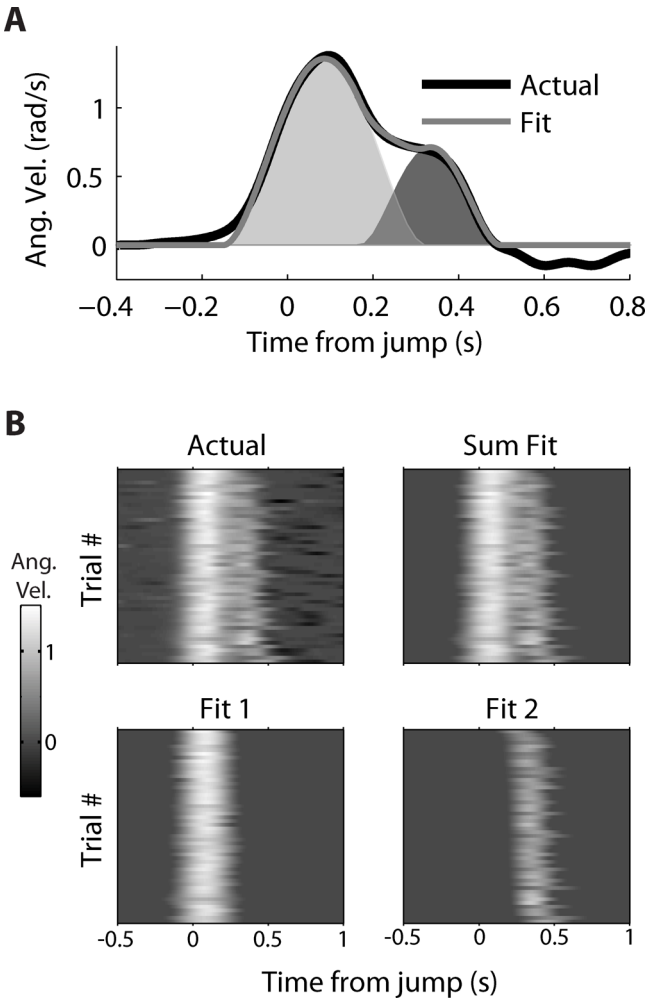

FIGURE 3 | Decomposition of actual kinematics observed during a double-step. (A) The actual kinematics of a double-step trail (black line) are well-approximated by the sum (gray line) of a primary (light gray) and secondary (dark gray) single-peaked profiles. **(B)** The single-trial velocity profiles are displayed as heat maps, with the vertical axis representing different trials, and the horizontal axis representing time elapsed within a given trial. The actual kinematics (top left) can be compared to the fit kinematics (top right), which is the sum of the single-trial primary (bottom left) and secondary (bottom right) motions.

Table 2 | The mean and standard deviation of the reaction times (RT) and movement durations of the single-step (SS), the first double-step (DS 1), and the second double-step (DS 2) movements for all seven datasets.

#	RT mean (±SD) in ms			#	Duration mean (±SD) in ms		
	SS	DS 1	DS 2		SS	DS 1	DS 2
1	228 (47)	207 (40)	222 (34)	1	416 (66)	418 (68)	366 (51)
2	203 (71)	202 (57)	201 (50)	2	457 (102)	469 (83)	446 (82)
3	231 (53)	224 (42)	181 (48)	3	405 (71)	399 (61)	416 (85)
4	221 (84)	253 (46)	248 (44)	4	406 (105)	404 (100)	409 (119)
5	228 (47)	207 (40)	222 (34)	5	416 (67)	418 (68)	366 (51)
6	230 (55)	221 (40)	174 (43)	6	413 (71)	396 (51)	413 (77)
7	223 (50)	208 (43)	217 (39)	7	430 (76)	420 (55)	389 (84)

Data are reported for all single-step trials with an amplitude of 0.15 radians, and all double-step trials where each component has an amplitude of 0.15 radians. Outlying reaction times >400 ms (6% of original data) and durations >700 ms (7%) were removed before the mean and standard deviation were computed.

neural activity in the reaction time period, between the change in target position but before the onset of movement. We then compared the distributions of neural offsets across cortical regions, from neurons which were better fit by the "Replaced" prediction (lower mean RMSE, $p < 0.05$, t-test) and whose neural offset was greater than 0 ms and less than 250 ms.

The distribution of neural offsets was markedly different between MI and premotor cortices, i.e., PMd and PMv cortices (**Figure 4**). The mean neural offset of the 26 eligible MI cortical neurons (53 ms) was significantly less ($p < 0.01$, t-test) than the mean of neural offset of the 91 eligible premotor neurons (84 ms). This indicates that premotor cortex shows an earlier response to the double-step target jump than MI cortex, consistent with previous results (Archambault et al., 2011). There was no significant difference in mean neural offsets between neurons in PMd and PMv ($p > 0.05$, t-test). To compare the "Replaced" prediction to the "Summed" prediction, we did not want the neural offset to be a free parameter, because this could lead to over-fitting of the "Replaced" neural prediction and would represent an unfair comparison between the two hypotheses. Thus, we rounded the mean neural offsets up to the nearest 10 ms, so that all MI neurons had a neural offset of 60 ms, and all premotor neurons had a neural offset of 90 ms. Recall that the neural offset specifies when the neural replacement happens relative to start of movement. It is different that the encoding delay, which specifies whether neural firing lags or leads observed movement.

We observed that the response profiles of some neurons were consistent with the "Summed" hypothesis while others were more consistent with the "Replaced" hypothesis during the double-step

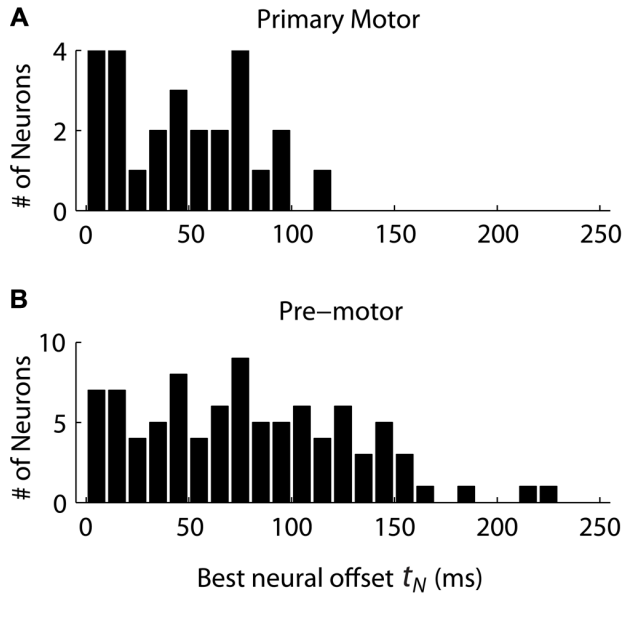

FIGURE 4 | The distribution of neural offsets is compared between neurons from the primary motor cortex (A) and the premotor cortex (B), including both dorsal and ventral premotor cortices. The neural offset describes the time at which the "Replaced" hypothesis predicts a shift from coding the primary movement to coding the secondary movement (see **Figure 1**).

trials, even among neurons that were recorded simultaneously. For an example PMv neuron (from dataset #7), the prediction of a linear encoding model (fit on all single-step trials) closely matched the PETH for single-step movements from location 2 to 4 (**Figure 5A**). The R^2 between the actual PETH (**Figure 5A**, solid black) and predicted PETH (**Figure 5A**, gray dot dash) was 0.96 for this movement condition. Fitting a linear encoding model to all single-step trials gave an optimal encoding delay δ of +30 ms, meaning this neuron's firing led the observed velocity.

The corresponding double-step condition also involved starting at location 2 and moving to location 4, but the visual target was switched to location 5 after the original movement was initiated. This resulted in a double-peaked velocity (see **Figure 3**) where the constituent velocity profiles overlapped. For a neuron which leads velocity, the "Summed" hypothesis predicts the firing rate should follow the shape of the double-peaked profile, while the "Replaced" hypothesis predicts a temporary reset to baseline after the target jump (see **Figure 1A**). For this neuron, the "Summed" prediction much better fit to the observed double-step PETH than did the "Replaced" prediction (**Figure 5B**).

This neuron's spike times from individual trials of the single-step (**Figure 5C**) and double-step (**Figure 5D**) conditions show a similar smooth rise and fall in firing rate. The raw double-step rasters (**Figure 5D**) can be visually compared to the single-trial predictions of the "Summed" (**Figure 5E**) and "Replaced" (**Figure 5F**) predictions. These are displayed as heat maps, where black indicates a high firing rate and white indicates a low firing rate. There is a sharp drop in firing rate (seen as a black to white transition) in the "Replaced" prediction (**Figure 5F**) around 100 ms after the target jump. However, this predicted drop in firing rate is not seen in the raw double-step rasters (**Figure 5D**) or the observed PETH (**Figure 5B**). Instead, the neuron reaches a similar peak firing rate as the single-step condition (23 spikes/s) at the jump time (0 s), before gradually decreasing its firing rate over the next 500 ms. Note that the double-step rasters and predictions (**Figures 5D–F**) are sorted by the start of the second constituent motion (as defined by the decomposition algorithm). This is why the reset to baseline is predicted to occur later for trials near the bottom for the "Replaced" hypothesis (**Figure 5F**). The R^2 between the actual double-step PETH and the "Summed" prediction is 0.94, compared to 0.62 for the "Replaced" prediction. For this neuron, across all trials of all double-step conditions, the average RMSE for the "Summed" prediction (7.6 spikes/s) was significantly less ($p < 0.001$, paired-test) than the average RMSE of the "Replaced" prediction (8.2 spikes/s).

In contrast, the firing of a different but simultaneously recorded PMv neuron was clearly better fit by the "Replaced" hypothesis (**Figure 6**). The single-step PETH (**Figure 6A**, black) from target 2 to 4 showed a smooth increase and decrease in firing rate. The firing rate profile was wider than that predicted by the linear encoding model (gray dot dash), but the R^2 between the actual and fit PETH was still 0.80. This neuron's optimal delay δ was −70 ms, indicating that neural firing lagged hand velocity. During the corresponding double-step profile, the "Summed" hypothesis failed to predict the neuron's response (**Figure 6B**, gray dotted). It predicted that the neural firing rate should reach a peak of 20 spikes/s 200 ms after the target jump. Instead,

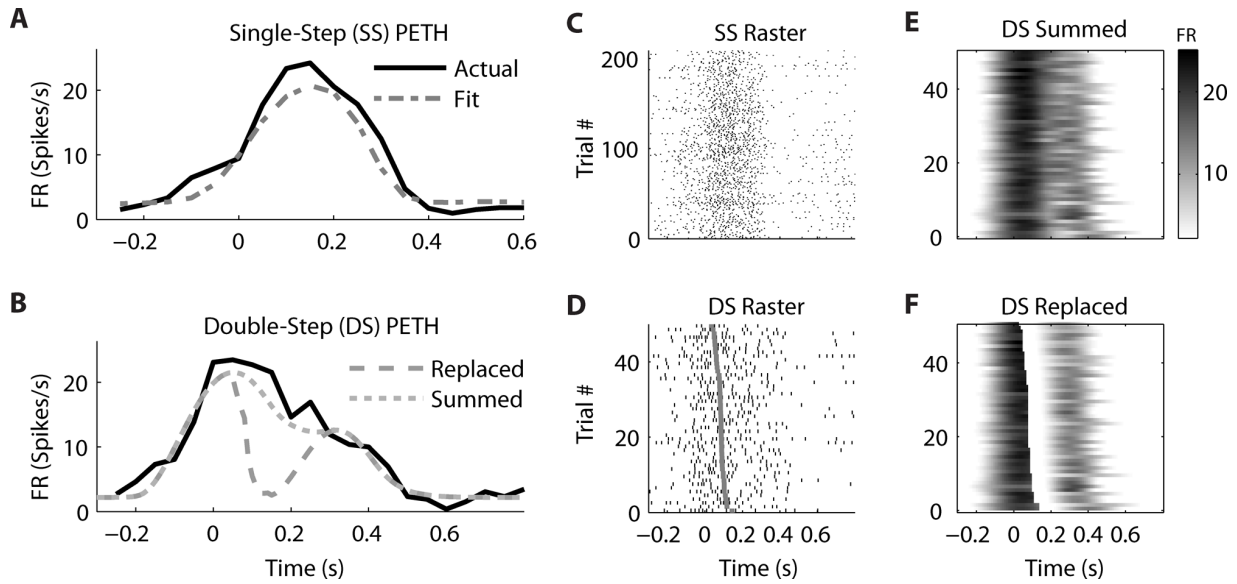

FIGURE 5 | A neuron from ventral premotor cortex is better fit by the "Summed" hypothesis. (A) During single-step (SS) trials, the observed peri-event time histogram (PETH, black) is well fit by a model assuming linear encoding of velocity and speed (gray dot dash). Zero time refers to the time of target appearance. **(B)** During double-step (DS) trials, the observed PETH (black) is well fit by the "Summed" prediction (gray dotted) but not the "Replaced" prediction (gray dashed). Zero time refers to the time of the target jump. **(C)** The single-trial spike time rasters for the SS trials. **(D)** The single-trial spike time rasters for the DS trials, arranged by the predicted replacement time (gray). **(E)** The DS single-trial prediction of the "Summed" hypothesis, displayed as a heat map. **(F)** The DS single-trial prediction of the "Replaced" hypothesis.

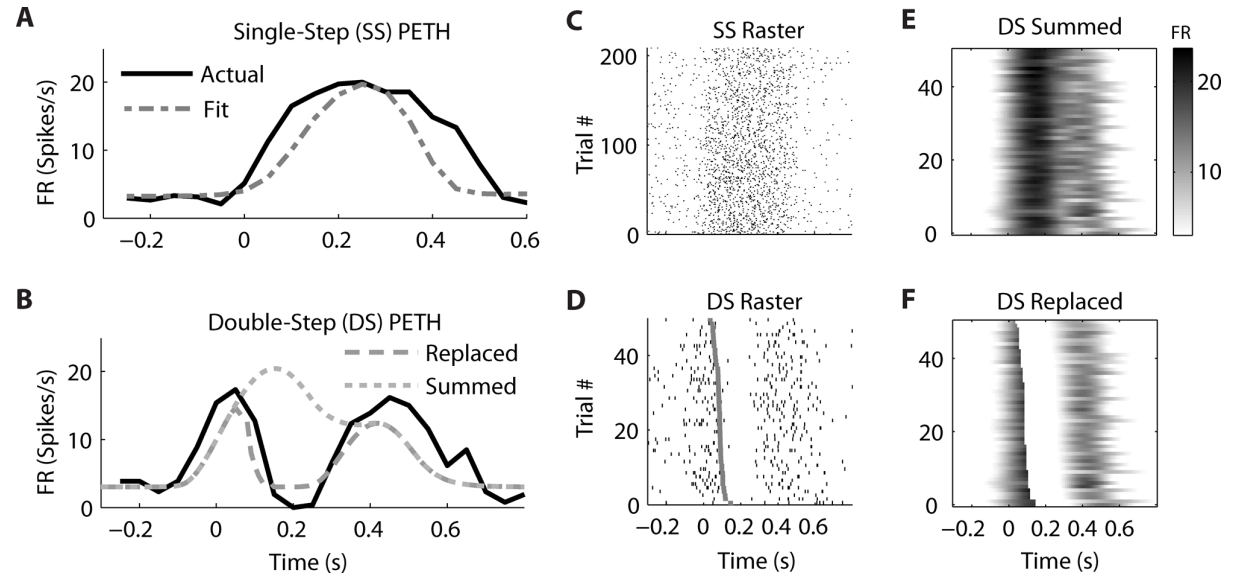

FIGURE 6 | A neuron from ventral premotor cortex is better fit by the "Replaced" hypothesis. Format follows **Figure 5**.

the actual neural firing dropped below 2 spikes/s from 150 to 250 ms after the target jump. Unlike the "Summed" prediction, the "Replaced" prediction (gray dashed) successfully predicted this transient drop in firing rate for the double-step condition. The R^2 between the actual and predicted double-step PETH was 0.80 for the "Replaced" hypothesis, but 0.05 for the "Summed" hypothesis.

While the single-trial spike times for the control, single-step trials (**Figure 6C**) showed a smooth increase and decrease in firing rate, each individual trial in the double-step condition showed an abrupt cessation of spiking activity (**Figure 6D**). This drop is not seen in the single-trial predictions of the "Summed" hypothesis (**Figure 6E**), but it is seen in the predictions of the "Replaced" hypothesis (**Figure 6F**). Across all trials of all

double-step conditions, the mean RMSE for the "Replaced" prediction (7.5 spikes/s) was significantly less ($p < 0.001$, paired-test) than the mean RMSE of the "Summed" prediction (8.8 spikes/s).

Similar examples of "Replaced" neurons can be found in MI (**Figure 7**) and PMd (**Figure 8**). The MI neuron (from dataset #2) had an optimal encoding delay δ of −90 ms, and the R^2 between the actual and predicted single-step PETH for movement from location 2 to 4 was 0.86 (**Figure 7B**). The R^2 between double-step PETH and the "Replaced" prediction was 0.68, and between the PETH and "Summed" prediction was 0.08. The RMSE was significantly less for the "Replaced" than the "Summed" prediction (14.2 vs. 15.7 spikes/s, $p < 0.001$, paired-test). In this dataset, the jump involved a reversal in the direction of movement (see Materials and Methods), but this neuron increased its firing rate for movements in both directions, so the "Replaced" prediction was similar to the previous example. The PMd neuron (from dataset #5) had an optimal encoding delay δ of −100 ms, and the R^2 between the actual

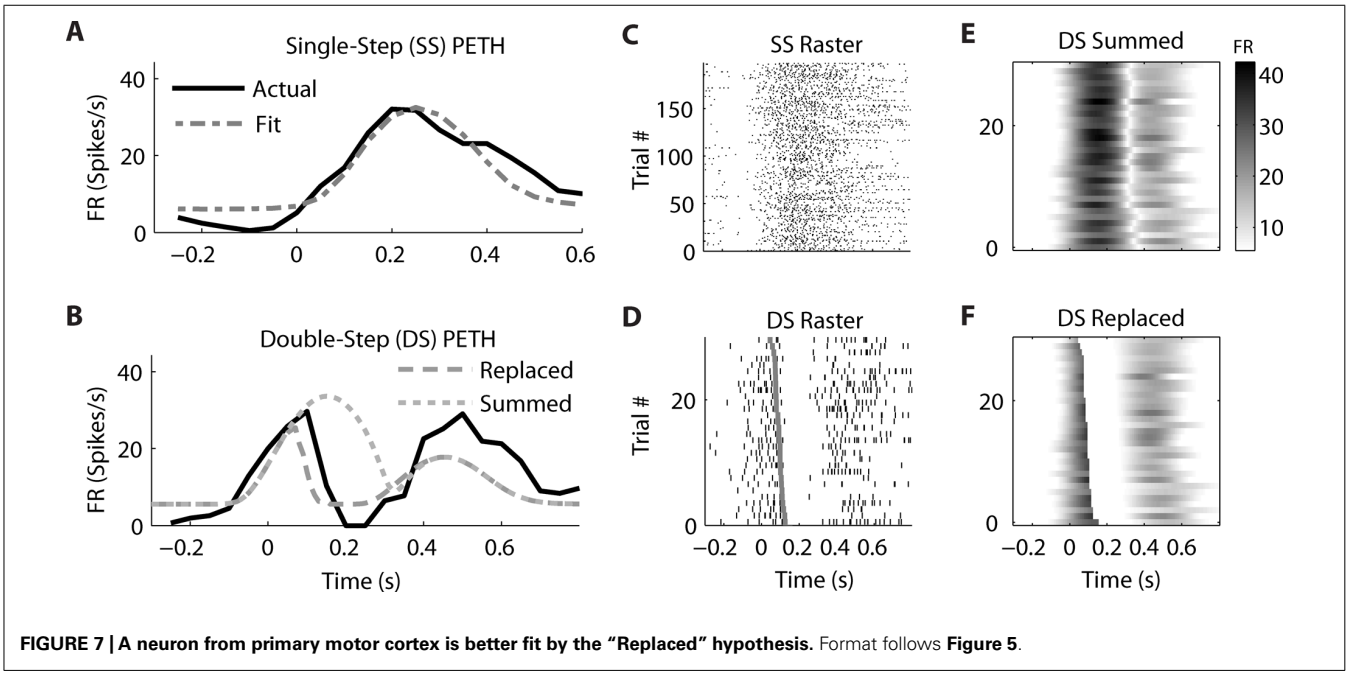

FIGURE 7 | A neuron from primary motor cortex is better fit by the "Replaced" hypothesis. Format follows **Figure 5**.

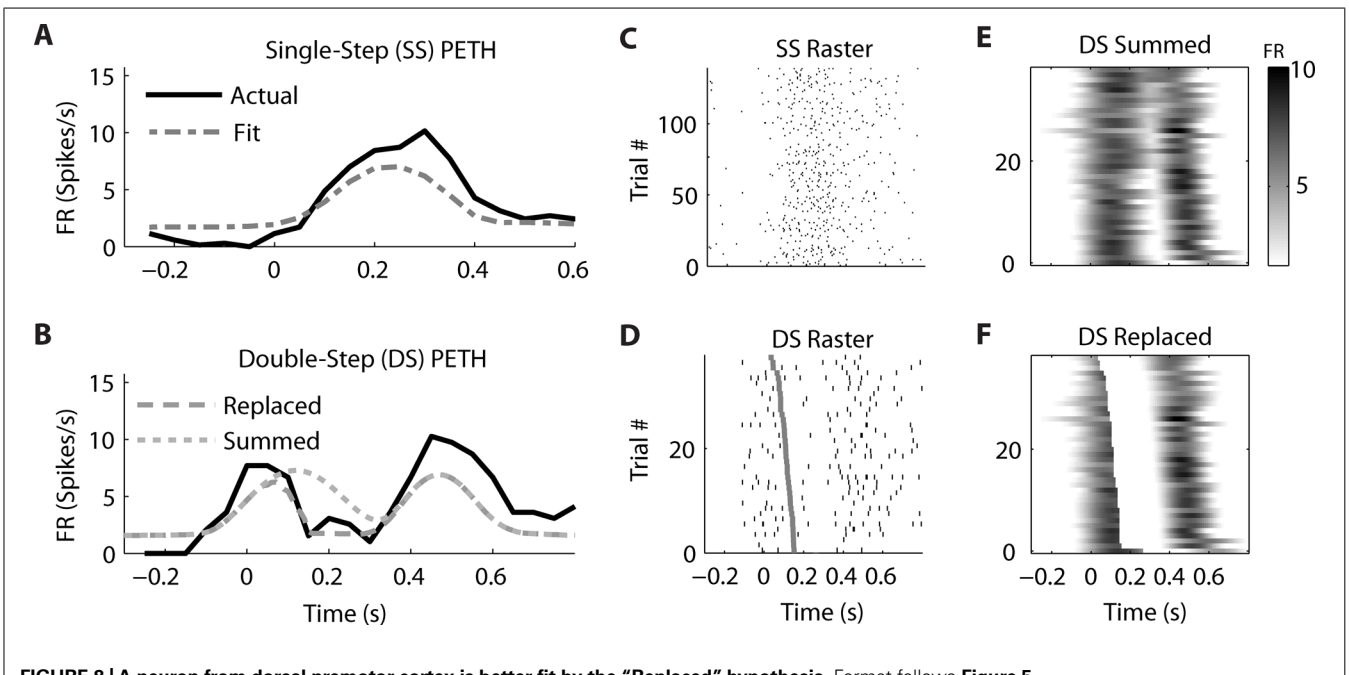

FIGURE 8 | A neuron from dorsal premotor cortex is better fit by the "Replaced" hypothesis. Format follows **Figure 5**.

and predicted single-step PETH for movement from location 2 to 3 was 0.89 (**Figure 8B**). The R^2 between double-step PETH and the "Replaced" prediction was 0.81, and between the PETH and "Summed" prediction was 0.40 (**Figure 8F**). The RMSE was significantly less for the "Replaced" than the "Summed" prediction (5.5 vs. 6.2 spikes/s, $p < 0.001$, paired-test).

Across all neurons, two-thirds were better fit with the "Summed" prediction, and one-third were better fit with the "Replaced" prediction (**Table 3**). For the linear version of Eq. 1, we defined the better prediction as having a lower average RMSE, while for the logistic version, the better prediction had a higher log-likelihood (see Materials and Methods). The percentage of cells which were better fit with the "Replaced" prediction (using RMSE) did not differ significantly between MI cortex (29/75, 39%) and premotor cortex (82/207, 40%).

Interestingly, we found that "Replaced" neurons were more likely to lag movement velocity while "Summed" neurons tended to lead movement velocity. Specifically, the percentage of neurons with an encoding delay δ less than 0 was significantly different for "Summed" and "Replaced" neurons, as were the mean and median lags (**Table 3**). Recall that the encoding lag is fit only to single-step trials, while the determination of "Replaced" vs. "Summed" is made on the double-step trials. This difference in the distribution of encoding delays was most dramatic when we looked at the 128 neurons that exhibited a significant difference ($p < 0.01$, t-test) in the mean RMSE between the "Summed" and "Replaced" predictions (**Figure 9**). Of these cells, 46 (36%) were better "Replaced" and 82 (64%) were better "Summed." Again, the "Replaced" neuronal firing was significantly more likely ($p < 0.001$, chi-square test) to lag observed velocity (35/46 or 76% with $\delta < 0$) than was "Summed" neuronal firing (42/82 or 51% with $\delta < 0$).

Table 3 | Neurons which were better "Replaced" were more likely to lag the kinematics (encoding delay <0) than neurons better "Summed."

	Replaced	Summed	*p*-Value
Linear			
Percentage of cells	39% (111)	61% (171)	
Percentage lagging	58% (64)	30% (66)	0.01
Mean delay	−49 ms	13 ms	<0.001
Median delay	−70 ms	30 ms	<0.001
Logistic			
Percentage of cells	36% (108)	64% (194)	
Percentage lagging	56% (61)	43% (83)	0.02
Mean delay	−116 ms	−11 ms	0.01
Median delay	−140 ms	−10 ms	0.03

The top rows list the percentage (and number) of cells better "Replaced" or better "Summed," while the subsequent rows show the percentage of those cells with a lagging delay, the mean delay, and median delay. The percentages were compared using a chi-square test, the mean delays were compared with a t-test, and the median delays were compared with a Wilcoxon rank-sum test.

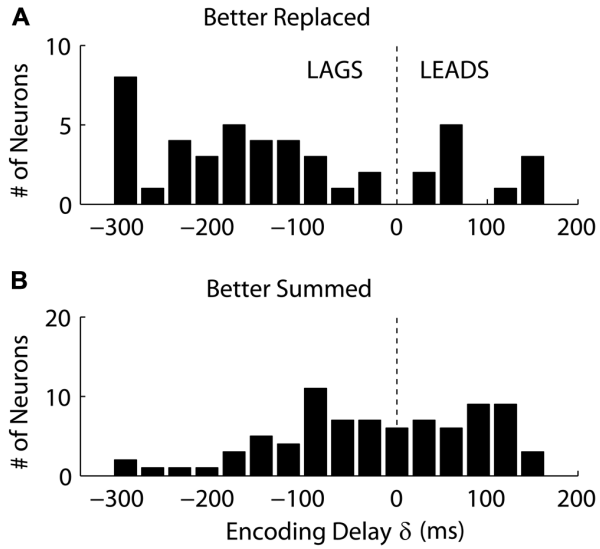

FIGURE 9 | The distribution of the encoding time delay δ is compared between neurons which were better fit with the "Replaced" hypothesis (A), versus neurons better fit with the "Summed" hypothesis (B). Only neurons which showed a significant difference in single-trial root-mean-square error between the two hypotheses are shown (see Results for details).

DISCUSSION

We found that for a third of the neurons analyzed from MI and premotor cortices, single-trial neural activity during a double-step was better explained with the "Replaced" rather than "Summed" encoding hypothesis. In some cases, the drop in firing rate predicted by the "Replaced" hypothesis was dramatic and readily visible in the single-trial raster plots (see **Figure 6**). Thus we were able to replicate the replacement phenomenon described previously (Georgopoulos et al., 1983; Archambault et al., 2009, 2011), though we saw it in only a minority of cells. The majority of neurons was consistent with the "Summed" hypothesis and conformed to the model of linear encoding of velocity (Schwartz et al., 1988; Moran and Schwartz, 1999).

Why did we only observe the "Replaced" phenomenon in a minority of cells? One potential difference from the studies by Archambault et al. (2009, 2011) is that we used a 1-D reaching paradigm rather than 3-D unconstrained reaching. We chose the 1-D paradigm to make the decomposition algorithm as simple as possible (see Decomposing Double-step Kinematics). However, we do not expect the change in the degrees of freedom to affect the results – the "Replaced" hypothesis was described for both 2-D planar reaching (Georgopoulos et al., 1983) and 3-D unconstrained reaching (Archambault et al., 2009, 2011). Likewise, linear encoding models have been used to describe motor cortical firing both for 2-D planar reaching (Moran and Schwartz, 1999) and 3-D unconstrained reaching (Wang et al., 2007).

We feel the difference from the Archambault et al.'s (2009; 2011) studies is simply one of methodology. The previous studies were documenting the existence of a phenomenon, so the "Replaced" hypothesis was compared to a null condition. This null condition replaced neural firing with a randomly selected firing pattern,

while the alternative condition replaced with a firing pattern corresponding to the direction of the correction. That is an appropriate technique, but it does not address the question of whether the "Replaced" hypothesis is better than the existing linear encoding models (the "Summed" hypothesis). We wanted to know the prevalence of "Replaced" phenomenon, not just whether it existed. That is a higher threshold of evidence to cross, and only one-third of neurons crossed it.

That said, we tested a fairly restrictive form of the "Replaced" hypothesis, where the prediction of neuronal firing at one time point was instantaneously replaced with another firing rate, usually leading to a sharp drop in predicted firing rate back to baseline. This was done deliberately, because it helped ensure that the neurons found to be better "Replaced" were not simply being over-fit. However, it did mean that other neurons might be well-described with the "Replaced" hypothesis using a more gentle transition. Thus the number of "Replaced" neurons might be underestimated.

We also found that the firing of neurons better fit by the "Replaced" hypothesis was more likely to lag velocity than lead it (see **Figure 9**). This suggests that this population is monitoring on-going movement as opposed to causally driving it. However, it is unclear why these lagging neurons would shut-off during the target jump. The simplest interpretation is that the firing of these lagging neurons is related to incoming sensory information, but that this neuronal firing is inhibited after the target jump. This might be analogous to saccadic suppression, where sensory responses are dampened in primary visual cortex during a saccade (Vallines and Greenlee, 2006) to avoid the trouble of processing a blurry image. Perturbation experiments during voluntary movement have suggested that the proprioceptive effects on MI neurons are highly attenuated during large ballistic movements as compared to finer movement adjustments (Evarts and Fromm, 1977). Therefore, modulation in this "sensory" population of MI neurons might be expected to temporarily shut-off during the early ballistic portion of the corrective movement.

Another possibility is these "Replaced" neurons are participating in a larger cortical network which monitors of the consequences of motor actions, particularly whether or not the action is successful. For example, the anterior cingulate cortex (ACC) is known to have projections to MI cortex (Dum and Strick, 1991), and the ACC has been implicated in the monitoring of the consequences of one's actions. One proposal is that the ACC encodes the "surprise related to the non-occurrence of a predicted event" (Alexander and Brown, 2011). Neurons in the ACC have been found that show an error-related phasic increase in firing rate peaking around 200 ms after the initiation of an inappropriate saccade (Ito et al., 2003). If these neurons (or similar neurons) directly inhibited the pool of "Replaced" neurons described here, it would explain the sudden drop in firing rate following a target jump.

We focused on kinematics for this study, because our single-trial "Replaced" prediction relied on a kinematic decomposition assuming summation of the original movement and a second corrective movement. One drawback of this focus is that we did not record forces, torques, or muscle activity. The lack of force data means we were unable to investigate alternatives to kinematic summation, such as the proposal that a target jump elicits a stereotyped force pulse made in the direction of the new target (Massey et al., 1986).

Another limitation is that we excluded a fair number of neurons from analysis. We excluded 190 of 553 neurons (34%) for having a predictive encoding lag greater than +175 ms. This was done purposely to exclude neurons firing in relation to the previous target appearance (Reimer and Hatsopoulos, 2010), rather than anticipation of future velocity. We did not want to consider target encoding effects here. We also excluded an additional 81 of 553 neurons (15%) because they were not well fit by the linear encoding model. However, such neurons might still encode relevant information, particularly if they use a temporal rather than a rate code. By focusing on the two main classes of neurons, "Summed" and "Replaced," we are underestimating the heterogeneity of neural coding.

We used the double-step reaching paradigm in these experiments to reliably induce corrections, so that we could average across trials with similar corrections. However, we view this as a model system for corrections and motor variability in general. Corrective submovements are often observed when reaches require accuracy (Crossman and Goodeve, 1983; Milner and Ijaz, 1990; Novak et al., 2000) or when infants are first learning to reach (Berthier, 1997). We predict that these "Replaced" neurons would also show a sharp change in firing rate for these naturally occurring corrections as well as those resulting from a target jump. Decomposing submovements in naturalistic movement is a difficult problem if the exact nature of the submovement is uncertain (Krebs et al., 1999). However, unpredictable gain or rotation perturbations could be applied on a single-trial basis to reliably induce corrections without the need for a sudden shift in visual target location.

The existence of a subpopulation of "Replaced" neurons is relevant for the design of brain machine interfaces. Standard techniques, such as the linear filter (Serruya et al., 2002) or the Kalman filter (Wu et al., 2002), tend to only look at the neuronal firing with leading encoding delays. This means such techniques may ignore the lagging "Replaced" neurons entirely. However, this subpopulation might be used to identify the presence of a correction, which would indicate the need for a dramatic adjustment to the estimate of hand position. Additionally, the "Replaced" subpopulation could be used to identify trials where a correction was necessary, which could be used as a teaching signal in an adaptive decoding algorithm. If the "Replacement" phenomenon is replicated in situations involving more natural corrections, then we should be able to leverage the information they contain to make brain machine interface algorithms more accurate and easier to control during real-time, closed loop control.

ACKNOWLEDGMENTS

We would like to thank Aaron Suminski for help in creating images and Josh Coles for help in training subjects. This work was supported by National Institute of Neurological Disorders and Stroke at the National Institutes of Health (R01 NS045853).

REFERENCES

Alexander, W. H., and Brown, J. W. (2011). Medial prefrontal cortex as an action-outcome predictor. *Nat. Neurosci.* 14, 1338–1344.

Archambault, P. S., Caminiti, R., and Battaglia-Mayer, A. (2009). Cortical mechanisms for online control of hand movement trajectory: the role of the posterior parietal cortex. *Cereb. Cortex* 19, 2848–2864.

Archambault, P. S., Ferrari-Toniolo, S., and Battaglia-Mayer, A. (2011). Online control of hand trajectory and evolution of motor intention in the parietofrontal system. *J. Neurosci.* 31, 742–752.

Berthier, N. E. (1997). "Analysis of reaching for stationary and moving objects in the human infant," in *Neural Network Models of Cognition: Biobehavioral Foundations*, eds J. W. Donohoe and V. P. Dorsel (Amsterdam: Elsevier), 283–301.

Crossman, E. R., and Goodeve, P. J. (1983). Feedback control of hand-movement and Fitts' law. *Q. J. Exp. Psychol. A* 35, 251–278.

Desmurget, M., Epstein, C. M., Turner, R. S., Prablanc, C., Alexander, G. E., and Grafton, S. T. (1999). Role of the posterior parietal cortex in updating reaching movements to a visual target. *Nat. Neurosci.* 2, 563–567.

Dum, R. P., and Strick, P. L. (1991). The origin of corticospinal projections from the premotor areas in the frontal lobe. *J. Neurosci.* 11, 667–689.

Evarts, E. V., and Fromm, C. (1977). Sensory responses in motor cortex neurons during precise motor control. *Neurosci. Lett.* 5, 267–272.

Flash, T., and Henis, E. (1991). Arm trajectory modifications during reaching towards visual targets. *J. Cogn. Neurosci.* 3, 220–230.

Flash, T., and Hogan, N. (1985). The coordination of arm movements: an experimentally confirmed mathematical model. *J. Neurosci.* 5, 1688–1703.

Georgopoulos, A. P., Kalaska, J. F., Caminiti, R., and Massey, J. T. (1982). On the relations between the direction of two-dimensional arm movements and cell discharge in primate motor cortex. *J. Neurosci.* 2, 1527–1537.

Georgopoulos, A. P., Kalaska, J. F., Caminiti, R., and Massey, J. T. (1983). Interruption of motor cortical discharge subserving aimed arm movements. *Exp. Brain Res.* 49, 327–340.

Georgopoulos, A. P., Kalaska, J. F., and Massey, J. T. (1981). Spatial trajectories and reaction times of aimed movements: effects of practice, uncertainty, and change in target location. *J. Neurophysiol.* 46, 725–743.

Goodale, M. A., Pelisson, D., and Prablanc, C. (1986). Large adjustments in visually guided reaching do not depend on vision of the hand or perception of target displacement. *Nature* 320, 748–750.

Grea, H., Pisella, L., Rossetti, Y., Desmurget, M., Tilikete, C., Grafton, S., et al. (2002). A lesion of the posterior parietal cortex disrupts on-line adjustments during aiming movements. *Neuropsychologia* 40, 2471–2480.

Henis, E., and Flash, T. (1995). Mechanisms underlying the generation of averaged modified trajectories. *Biol. Cybern.* 72, 407–419.

Hogan, N. (1984). An organizing principle for a class of voluntary movements. *J. Neurosci.* 4, 2745–2754.

Ito, S., Stuphorn, V., Brown, J. W., and Scall, J. D. (2003). Performance monitoring by the anterior cingulate cortex during saccade countermanding. *Science* 302, 120–122.

Krebs, H. I., Aisen, M. L., Volpe, B. T., and Hogan, N. (1999). Quantization of continuous arm movements in humans with brain injury. *Proc. Natl. Acad. Sci. U.S.A.* 96, 4645–4649.

Massey, J. T., Schwartz, A. B., and Georgopoulos, A. P. (1986). On information processing and performing a movement sequence. *Exp. Brain Res.* 15, 242–251.

Maynard, E. M., Hatsopoulos, N. G., Ojakangas, C. L., Acuna, B. D., Sanes, J. N., Normann, R. A., et al. (1999). Neuronal interactions improve cortical population coding of movement direction. *J. Neurosci.* 19, 8083–8093.

Milner, T. E., and Ijaz, M. M. (1990). The effect of accuracy constraints on three-dimensional movement kinematics. *Neuroscience* 35, 365–374.

Moran, D. W., and Schwartz, A. B. (1999). Motor cortical representation of speed and direction during reaching. *J. Neurophysiol.* 82, 2676–2692.

Novak, K. E., Miller, L. E., and Houk, J. C. (2000). Kinematic properties of rapid hand movements in a knob turning task. *Exp. Brain Res.* 132, 419–433.

Paulignan, Y., MacKenzie, C., Marteniuk, R., and Jeannerod, M. (1991). Selective perturbation of visual input during prehension movements. 1. The effects of changing object position. *Exp. Brain Res.* 83, 502–512.

Pelisson, D., Prablanc, C., Goodale, M. A., and Jeannerod, M. (1986). Visual control of reaching movements without vision of the limb. II. Evidence of fast unconscious processes correcting the trajectory of the hand to the final position of a double-step stimulus. *Exp. Brain Res.* 62, 303–311.

Prablanc, C., and Martin, O. (1992). Automatic control during hand reaching at undetected two-dimensional target displacements. *J. Neurophysiol.* 67, 455–469.

Reichenbach, A., Bresciani, J. P., Peer, A., Bulthoff, H. H., and Thielscher, A. (2011). Contributions of the PPC to online control of visually guided reaching movements assessed with fMRI-guided TMS. *Cereb. Cortex* 21, 1602–1612.

Reimer, J., and Hatsopoulos, N. G. (2010). Periodicity and evoked responses in motor cortex. *J. Neurosci.* 30, 11506–11515.

Reina, G. A., Moran, D. W., and Schwartz, A. B. (2001). On the relationship between joint angular velocity and motor cortical discharge during reaching. *J. Neurophysiol.* 85, 2576–2589.

Rousche, P. J., and Normann, R. A. (1992). A method for pneumatically inserting an array of penetrating electrodes into cortical tissue. *Ann. Biomed. Eng.* 20, 413–422.

Schwartz, A. B., Kettner, R. E., and Georgopoulos, A. P. (1988). Primate motor cortex and free arm movements to visual targets in three-dimensional space. I. Relations between single cell discharge and direction of movement. *J. Neurosci.* 8, 2913–2927.

Serruya, M. D., Hatsopoulos, N. G., Paninski, L., Fellows, M. R., and Donoghue, J. P. (2002). Instant neural control of a movement signal. *Nature* 416, 141–142.

Soechting, J. F., and Lacquaniti, F. (1983). Modification of trajectory of a pointing movement in response to a change in target location. *J. Neurophysiol.* 49, 548–564.

Vallines, I., and Greenlee, M. W. (2006). Saccadic suppression of retinotopically localized blood oxygen level-dependent responses in human primary visual area V1. *J. Neurosci.* 26, 5965–5969.

Wang, W., Chan, S. S., Heldman, D. A., and Moran, D. W. (2007). Motor cortical representation of position and velocity during reaching. *J. Neurophysiol.* 97, 4258–4270.

Wu, W., Black, M. J., Gao, Y., Bienenstock, E., Serruya, M., and Donoghue, J. P. (2002). "Inferring hand motion from multi-cell recordings in motor cortex using a Kalman filter," in *SAB'02-Workshop on Motor Control in Humans and Robots: On the Interplay of Real Brains and Artificial Devices*, August 10, 2002, Edinburgh, 66–73.

Conflict of Interest Statement: The authors declare that the research was conducted in the absence of any commercial or financial relationships that could be construed as a potential conflict of interest.

Received: 30 November 2012; paper pending published: 17 January 2013; accepted: 08 March 2013; published online: 04 April 2013.

Citation: Dickey AS, Amit Y and Hatsopoulos NG (2013) Heterogeneous neural coding of corrective movements in motor cortex. Front. Neural Circuits ***7****:51. doi: 10.3389/fncir.2013.00051*

frontiers in
NEURAL CIRCUITS

ORIGINAL RESEARCH ARTICLE
published: 01 April 2013
doi: 10.3389/fncir.2013.00055

In vivo optogenetic tracing of functional corticocortical connections between motor forelimb areas

Riichiro Hira[1,2,3†], Fuki Ohkubo[1,2,3,4†], Yasuhiro R. Tanaka[1,2], Yoshito Masamizu[1,2], George J. Augustine[5,6], Haruo Kasai[3] and Masanori Matsuzaki[1,2,3,4]*

[1] Division of Brain Circuits, National Institute for Basic Biology, Okazaki, Japan
[2] CREST, Japan Science and Technology Agency, Saitama, Japan
[3] Laboratory of Structural Physiology, Center for Disease Biology and Integrative Medicine, Graduate School of Medicine, University of Tokyo, Tokyo, Japan
[4] Department of Basic Biology, School of Life Science, The Graduate University for Advanced Studies (SOKENDAI), Myodaiji, Okazaki, Japan
[5] Center for Functional Connectomics, Korea Institute of Science and Technology, Seoul, Republic of Korea
[6] Program in Neuroscience and Behavioral Disorder, Duke-NUS Graduate Medical School, Singapore

Edited by:
Gordon M. Shepherd, Northwestern University, USA

Reviewed by:
Johannes J. Letzkus, Friedrich Miescher Institute for Biomedical Research, Switzerland
John Martin, The City College of the City University of New York, USA

***Correspondence:**
Masanori Matsuzaki, Division of Brain Circuits, National Institute for Basic Biology, Myodaiji, Okazaki, 444-8585, Japan.
e-mail: mzakim@nibb.ac.jp

† These authors have contributed equally to this work.

Interactions between distinct motor cortical areas are essential for coordinated motor behaviors. In rodents, the motor cortical forelimb areas are divided into at least two distinct areas: the rostral forelimb area (RFA) and the caudal forelimb area (CFA). The RFA is thought to be an equivalent of the premotor cortex (PM) in primates, whereas the CFA is believed to be an equivalent of the primary motor cortex. Although reciprocal connections between the RFA and the CFA have been anatomically identified in rats, it is unknown whether there are functional connections between these areas that can induce postsynaptic spikes. In this study, we used an *in vivo* Channelrhodopsin-2 (ChR2) photostimulation method to trace the functional connections between the mouse RFA and CFA. Simultaneous electrical recordings were utilized to detect spiking activities induced by synaptic inputs originating from photostimulated areas. This method, in combination with anatomical tracing, demonstrated that the RFA receives strong functional projections from layer 2/3 and/or layer 5a, but not from layer 5b (L5b), of the CFA. Further, the CFA receives strong projections from L5b neurons of the RFA. The onset latency of electrical responses evoked in remote areas upon photostimulation of the other areas was approximately 10 ms, which is consistent with the synaptic connectivity between these areas. Our results suggest that neuronal activities in the RFA and the CFA during movements are formed through asymmetric reciprocal connections.

Keywords: motor cortex, Channelrhodopsin-2, optogenetics, corticocortical connections, photostimulation mapping

INTRODUCTION

The coordinated activities of motor cortex network are thought to be essential for elaborate movements. There are two spatially segregated motor forelimb areas in rodents: the rostral forelimb area (RFA) and the caudal forelimb area (CFA), which can be identified by intracortical microstimulation (ICMS) (Neafsey et al., 1986; Rouiller et al., 1993; Tennant et al., 2011) or Channelrhodopsin-2 (ChR2) photostimulation mapping (Hira et al., 2013). When rodents participate in reaching, grasping, and lever-pulling tasks, the RFA and the CFA show similar neuronal activities (Hyland, 1998; Hira et al., 2013). Nevertheless, the largest peaks of neuronal activities in the RFA and the CFA occurred before reach onset and around the time of reach end, respectively (Hyland, 1998). To understand how such activities in the RFA and the CFA are coordinated during movement, it needs to clarify synaptic connections between the RFA and the CFA.

By using anterograde and retrograde tracers, Rouiller et al. (1993) found that neurons in layers above the cluster of the corticospinal neurons of the CFA have dense projections to layers 5 (L5) and 6 (L6) of the RFA, while neurons in L5 and L6 of the RFA project to all layers of the CFA. Projections from lower to higher sensory areas originate from neurons predominantly located in layer 4 (L4) and layer 2/3 (L2/3), while projections from higher to lower sensory areas originate from neurons located in L5 (Van Essen and Maunsell, 1983; Coogan and Burkhalter, 1990; Shipp, 2005). Thus, it is thought that the RFA is a higher motor area than the CFA, although both areas lack L4 (Neafsey et al., 1986; Rouiller et al., 1993; Smith et al., 2010; Tennant et al., 2011). However, whether activation of the RFA induces the CFA activity, or vice versa, has not yet been examined. Recently, both we and another group reported that scanning of light beams across the surface of the cortex can induce cortical activity around the photostimulated points in transgenic mice that express ChR2 mainly in layer 5b (L5b) pyramidal neurons (Ayling et al., 2009; Hira et al., 2009). With this optogenetic approach, the motor areas where photostimulation induces limb movements can be rapidly and reproducibly mapped. Furthermore, another study used this ChR2-photostimulation mapping method, combined with whole-cortical voltage-sensitive dye imaging, to reveal the output regions of each stimulated cortical area (Lim et al., 2012). However, the functional connections between the RFA and the CFA have not yet been examined by any method. In addition,

in mice that express ChR2 in L5b the projections originating from upper layers [L2/3 and layer 5a (L5a); Hooks et al., 2013] cannot be examined. In this study, we circumvented this issue by combining *in vivo* ChR2-based photostimulation mapping with *in vivo* electrical recording of neurons. This was done in either ChR2 transgenic mice, where the L5b neurons express ChR2 (Wang et al., 2007), or in mice where both the upper layers and L5b were transfected with an adeno-associated virus (AAV) that encoded ChR2-EYFP (Yizhar et al., 2011). We found that L5 neurons in the RFA receive functional projections from L2/3 and/or L5a, but not L5b, of the CFA. Conversely, L5 neurons in the CFA receive functional projections from L5b of the RFA.

MATERIALS AND METHODS

ANIMAL PREPARATIONS

C57BL/6 and C57BL/6 (Thy1-ChR2-EYFP) mice [line 9; (Arenkiel et al., 2007; Wang et al., 2007)] aged 4–6 months were used in this study. For photostimulation, mice were anesthetized by intraperitoneal injection of ketamine (74 mg/kg) and xylazine (10 mg/kg) and then an incision was made in the skin that covered the neocortex. Once the exposed skull was cleaned, a head plate was attached to the skull with dental cement (Fujiryu-to; GC, Tokyo, Japan). Mice were then either subjected to experimentation immediately after the surgery or were allowed to recover for several days. In cases where the animals were given time to recover, the surface of the intact skull was coated with clear acrylic dental resin (Super bond; Sun Medical, Shiga, Japan) to prevent drying (Hira et al., 2009). The animal experimental committee of the School of Medicine, University of Tokyo and the Okazaki animal committee approved all experiments in this study.

INTRACORTICAL MICROSTIMULATION (ICMS)

ICMS was performed as described (Hira et al., 2009, 2013). Briefly, wild-type mice were anesthetized by intraperitoneal injection of ketamine (74 mg/kg) and xylazine (10 mg/kg). The area of the skulls that covered either the left or the right cortical hemisphere was then removed. Tungsten or elgiloy microelectrodes (WPI, Sarasota, FL) were inserted to a depth of more than 0.6 mm beneath the cortical surface. The cortex was then stimulated with a 45 ms train of 0.4 ms cathodal pulses of 30–200 μA at 333 Hz.

VIRUS INJECTIONS

ChR2 was introduced into neurons in wild-type mouse brains by intracortical injections of rAAV2/9-Syn-hChR2 (H134R)-EYFP (AAV-ChR2-EYFP; 8.58×10^{12} vector genomes/ml; provided by the University of Pennsylvania Gene Therapy Program Vector core), as previously described (Masamizu et al., 2011). Mice were anesthetized with either isoflurane (0.8–1.1% for induction and maintenance) or ketamine (74 mg/kg) and xylazine (10 mg/kg), and then 0.5–2.0 μl of virus solution was injected into one, two, or three sites at depths of 300–500 μm below the pia in either the RFA (2.5 mm rostral; 0.8 mm lateral from bregma, left hemisphere) or the CFA (0.2 mm rostral; 1.2 mm lateral from bregma, left hemisphere) through a glass pipette (20–30 μm open tip diameter) at 8–10 psi pressure (T25-15-900; Toohey Spritzer, Fairfield, NJ). The mice were then returned to their homecages and were allowed to recover for more than 2 weeks. This recovery period allowed for sufficient levels of ChR2 to express.

OPTOGENETIC TRACINGS

ChR2 transgenic and AAV-ChR2-EYFP transfected mice with headplates were anesthetized with isoflurane (0.7–1.1%). The skull that covered either the left or right cortical hemisphere (including both the stimulation and recording sites) was then removed. Photostimulation was performed with a blue laser at 473 nm using an upright microscope (BX61WI; Olympus, Tokyo, Japan) and a FV1000-MPE laser-scanning microscope system (Olympus). Either the entire, or just a portion, of the field of view (6.4 × 6.4 mm when using a 2× objective, numerical aperture [NA] of 0.08, PlanApo, Olympus; or 2.6 × 2.6 mm when using a 5× objective, NA of 0.10, MPLan, Olympus) of the cortical surface was divided into two-dimensional pixel arrays. Each pixel was then individually illuminated. The order of illumination was pseudo-randomly programmed (Hira et al., 2009). Assuming that the refractive index of the brain tissue was 1.38 (Binding et al., 2011), and that the laser beam entered the brain with a half-angle of arcsin[0.10/1.38], then the diameter of the laser spot was 29 μm {$= 2 \times 200$ μm tan[arcsin(0.10/1.38)]} at a depth of 200 μm, and 87 μm {$= 2 \times 600$ μm tan[arcsin(0.10/1.38)]} at a depth of 600 μm, from the vasculature. These are lower estimates that do not account for the effects of light scattering. The distance between the center of the mapping area and the recording site in **Figure 4** was 2.46 ± 0.27 mm ($n = 5$ sites from which a photostimulation-induced response was detected), which was not significantly different from the distance between the center of the RFA and the center of the CFA determined by ChR2 photostimulation mapping (Hira et al., 2013; 2.39 ± 0.19 mm, $n = 4$, $P = 0.67$; Student's t-test). For electrical recordings, tungsten microelectrodes with impedances of 1.5–2 MΩ (TM33B20KT; WPI) were inserted to the RFA or the CFA. As the electrode was inserted, the rate of spontaneous activity suddenly changed from 3.3 ± 2.4 Hz to 12.0 ± 7.3 Hz (8 penetrations) at depths of ∼400–500 μm, which presumably corresponded to the border between L2/3 and L5. When the recording was performed in L5, the recording sites were approximately 50–150 μm deeper than the border (524–662 μm from the cortical surface). When the recording was performed in L2/3, the recording sites were searched at a depth of less than 350 μm from the cortical surface, where the rate of spontaneous activity was low. The signals from the electrodes were amplified (DAM-80 amplifier; WPI), filtered at 300–1000 Hz (SIM900; Stanford Research Systems, Sunnyvale, CA), and sampled at 5 kHz (FV1000 system; Olympus). For pharmacological experiments, 1 mM 6-cyano-7-nitroquinoxaline-2,3-dione (CNQX; a competitive AMPA/kainite receptor antagonist; Tocris, Bristol, UK) or 3 μM tetrodotoxin (TTX; a selective blocker of sodium channels that prevents action potentials; Nacalai Tesque, Kyoto, Japan) was dissolved in a solution that contained 125 mM NaCl, 4 mM KCl, and 5 mM HEPES, and was applied directly to the cortical surface. Recodings were made 30 min after the applications of the CNQX or the TTX.

IMMUNOHISTOCHEMISTRY OF AAV-ChR2-EYFP-POSITIVE NEURONS

More than 2 weeks after injection of 0.5 μl AAV-ChR2-EYFP into one site, the mice were deeply anesthetized with ketamine (74 mg/kg) and xylazine (10 mg/kg) and were then transcardially perfused with 40 ml of phosphate buffered saline (PBS) and 40 ml of 4% paraformaldehyde in PBS (Wako, Osaka, Japan). The brains were removed and then post-fixed with the same fixative for at least 12 h at 4°C. The brains were then embedded in 3% agar in PBS and cut into sagittal sections with a thickness of 50 μm. Sections were incubated with a rabbit anti-GFP antibody (Invitrogen, A6455, 1:500) in PBS containing 0.3% Triton X-100 and 1% normal donkey serum (Millipore, S30-100ML) (PBS-XD) for 9–12 h at room temperature. After washed twice (>10 min each) with PBS containing 0.3% Triton X-100 (PBS-X), sections were incubated with a secondary antibody (Invitrogen, A11034, goat anti-rabbit IgG, Alexa Fluor 488 conjugate, 1:200) in PBS-X for 1 h at room temperature. After washing two times with PBS-X, sections were counterstained with red fluorescent Nissl (propidium iodide 536/617, Invitrogen), mounted on glass slides, and coverslipped. Fluorescence was visualized through a fluorescence microscope (BX53F; Olympus) or by confocal laser scanning microscopy (LSM510; Carl Zeiss, Gottingen, Germany). Layer boundaries were determined as the sites where cell body size or density suddenly changed after performing Nissl staining of the same slices. GFP-positive and GFP-negative neurons were determined according to the averaged fluorescent intensity within the Nissl-stained neuronal somata with clearly visible nucleoli.

FLUORESCENT TRACING USING CHOLERA TOXIN B SUBUNIT

Alexa Fluor 594-conjugated cholera toxin B subunit (CTB; CTB-Alexa 594; Invitrogen) was used as a retrograde tracer. The injection of CTB-Alexa 594 was performed, as described before with slight modifications (Tanaka et al., 2011). Briefly, a glass pipette with CTB-Alexa 594 in PBS was inserted into either the RFA or the CFA. Approximately 0.5 μl of the solution was injected through a pipette tip with a diameter at approximately 40 μm and at a pressure of 5–10 psi. One to seven days after injection of the CTB conjugate, mice were deeply anesthetized and transcardially perfused, and the brains were cut into sections, as described above. Sections were incubated with a goat anti-CTB antiserum (List Biological Laboratories, #703, 1:60,000) in PBS-XD overnight at room temperature. After washing twice (>10 min each) with PBS-X, sections were incubated with a secondary antibody (Invitrogen, A11058, donkey anti-goat IgG, Alexa Fluor 594 conjugate, 1:1000) in PBS-XD for 1 h at room temperature. Sections were counterstained with green fluorescent Nissl (NeuroTrace 500/525, Invitrogen), mounted on glass slides, and coverslipped. For ChR2 transgenic mice, the sections were incubated overnight with a mixture of 1/500-diluted rabbit anti-GFP antibody and 1/60,000-diluted goat anti-CTB antibody in PBS-XD. After washing twice (>10 min each) with PBS-X, sections were incubated for 1 h with 1/200-diluted Alexa Fluor 488 conjugated donkey anti-rabbit IgG (Invitrogen, A21206) and 1/1000-diluted Alexa Fluor 594 conjugated donkey anti-goat IgG (Invitrogen, A11058) in PBS-XD at room temperature. Sections were counterstained with deep red fluorescent Nissl (TO-PRO-3 iodide 642/661, Invitrogen), mounted on glass slides, and coverslipped. Fluorescence was visualized through a fluorescence microscope or confocal laser scanning microscopy. The labeled neurons were counted stereologically in confocal stacks (Howard and Reed, 1998) from the most densely labeled part of each of L2/3, L5a, and L5b of the RFA or the CFA.

DATA ANALYSES

All analyses were conducted using Matlab (version 7; MathWorks, MA). Spiking activity was determined to have occurred when at least two successive signals from 0 to 20 ms after the stimulation were less than −4 SD plus the baseline value. Latency was defined as the time from the start of the photostimulation until the start of the spiking activity. In cases where a series of spontaneous activities occurred prior to the photostimulation, these data were removed from the latency analyses.

STATISTICS

Data are presented as mean ± SD. Student's *t*-tests were used for statistical comparisons.

RESULTS

DETERMINATION OF RFA AND CFA LOCATIONS BY ICMS

We began by using ICMS to locate the RFA and the CFA. They were determined to be the areas where ICMS induced contralateral forelimb movements. The rostral area was approximately 2.5 mm rostral and 0.8 mm lateral from the bregma (RFA), and the caudal area was approximately 0.2 mm rostral and 1.2 mm lateral from the bregma (CFA) (**Figures 1A,B**). This is consistent with our previous study, which used photostimulation mapping in ChR2 transgenic mice expressing a high level of ChR2 in pyramidal neurons in L5b (ChR2 Tg mice; **Figure 2A**; Wang et al., 2007; Hira et al., 2013). In that study, the center of the RFA and the center of the CFA were approximately 2.5 mm rostral and 1 mm lateral, and 0.5 mm rostral and 1.2 mm lateral, respectively. Throughout the study, we performed electrical recording and injected AAV-ChR2-EYFP based on these coordinate.

OPTOGENETIC STIMULATION OF CORTICAL NEURONS

To reveal the functional projections originating from the upper layers (L2/3 and L5a) and L5b, we used two distinct approaches to express ChR2. The first approach was to use ChR2 Tg mice (**Figure 2A**). The second approach was to use AAV-ChR2-EYFP to express ChR2 in both the upper layers and L5b in the injected region (AAV-ChR2 mice; **Figure 2B**).

First, we determined whether blue laser illumination of the cortical surfaces evoked spiking activity in L5 nearest to the illumination points (horizontal distance of less than 300 μm) in both ChR2 Tg mice and AAV-ChR2 mice (**Figure 3A**). Photostimuli that lasted 2–10 ms induced spiking activities near the photostimulation points in both the ChR2 Tg mice and the AAV-ChR2 mice. Light intensities of ≥1.5 mW induced spiking activities in every trial in both the ChR2 Tg mice and the AAV-ChR2 mice (**Figure 3B**). The mean onset latencies of spiking activities evoked near the photostimulation points were 1.4 ± 1.6 ms ($n = 9$ sites in 4 mice) for the ChR2 Tg mice and 2.2 ± 0.8 ms ($n = 5$ sites in 3 mice) for the AAV-ChR2 mice (**Figures 3C,D**). This activity

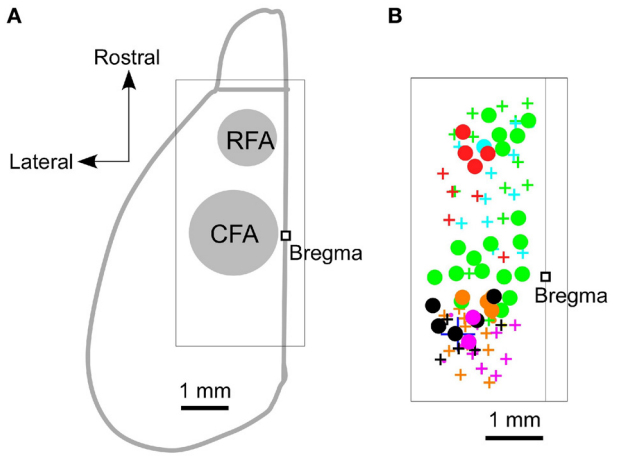

FIGURE 1 | Locations of the RFA and the CFA. (A) A schematic dorsal view of the left hemisphere of the mouse neocortex and olfactory bulb. A square was used to denote the location of the bregma. The approximate locations of the RFA and the CFA are labeled and indicated in gray. The boxed region indicates the expanded area shown in **(B)**. **(B)** Circles denote the sites where ICMS induced contralateral forelimb movements, and the crosses denote the sites where the maximum ICMS current injections (200 μA) failed to induce contralateral forelimb movements. Different colors indicate the different animals that were used in these experiments ($n = 6$ mice).

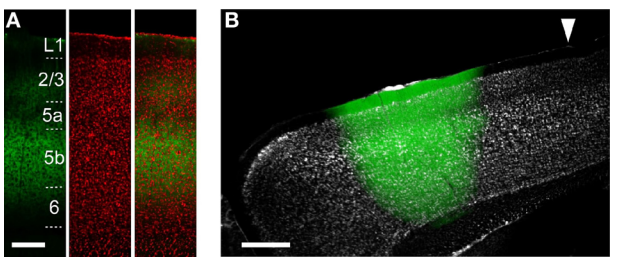

FIGURE 2 | ChR2 expression in ChR2 Tg and AAV-ChR2 mice. (A) Anti-GFP immunofluorescence (left), Nissl staining (middle), and the overlay (right) in the CFA in a sagittal section from a ChR2 Tg mouse. Scale bar, 200 μm. **(B)** Overlay of EYFP fluorescence (green) and Nissl staining (gray) in a sagittal section of a mouse in which AAV-ChR2-EYFP was injected into the RFA. Arrowhead indicates 0 mm anterior and 0.8 mm lateral from the bregma. Scale bar, 500 μm.

reflected action potentials, rather than some sort of photoelectric artifact, because it was completely inhibited by application of TTX in both lines of mice (**Figures 3C,E**). Furthermore, spiking activity with short latency was still apparent upon application of CNQX to both the ChR2 Tg and AAV-ChR2 mice (**Figures 3C,E**). Thus, spiking activity was rapidly induced near the photostimulation points due to direct photostimulation of nearby neurons.

OPTOGENETIC TRACING OF FUNCTIONAL CONNECTIONS BETWEEN THE RFA AND THE CFA

If the activated neurons near the photostimulation points sent sufficient synaptic projections to a remote area, then the postsynaptic neurons in that remote area should also fire (**Figure 3F**). Thus, we next assessed whether photostimulation of either the RFA or the CFA induced spiking activity in the other area. We assessed multiple illumination points within and around the RFA and the CFA by simultaneously measuring spiking activity in the other area (**Figures 4A,B**). Interestingly, photostimulation of the RFA in ChR2 Tg mice reproducibly induced spiking activity in L5 in the CFA (**Figures 4A–D**). The mean onset latency of responses in the CFA following photostimulation of the RFA was 12.6 ± 1.9 ms ($n = 8$ sites in 4 mice; **Figures 3D,F**). In contrast, stimulation of the CFA did not induce any detectable spiking in L5 in the RFA of four ChR2 Tg mice (**Figure 4B**). Thus, there seems to be asymmetry in the functional connections between neurons in the RFA and the CFA. Spiking activity was not detected in L2/3 in either the RFA (two mice) or the CFA (three mice) after photostimulation of the other area.

However, photostimulation of either the RFA or the CFA in the AAV-ChR2 mice induced spiking in L5 in the other area (**Figure 4B**). The mean onset latencies of spiking activities were 11.0 ± 2.4 ms ($n = 3$ sites in 2 mice) in the CFA in response to photostimulation of the RFA and 9.6 ± 3.1 ms ($n = 4$ sites in 2 mice) in the RFA in response to photostimulation of the CFA (**Figure 3D**). These latencies of spiking activities (in response to photostimulation of the other area) were significantly greater than the latencies of spiking activities evoked near the photostimulation points (ChR2 Tg mice: $P = 1.1 \times 10^{-9}$; Student's t-test; $n = 9$ sites from four mice for stimulation and recording of the same areas; $n = 8$ sites from four mice for stimulation and recording from different areas; AAV-ChR2 mice: $P = 8.6 \times 10^{-5}$; $n = 5$ sites from three mice for stimulation and recording from the same areas; and $n = 7$ sites from four mice for stimulation and recording from different areas). By contrast, spiking activity was not detected in L2/3 in either the RFA or the CFA when the other area was photostimulated in AAV-ChR2 mice (two mice for the RFA and two mice for the CFA), although activity was detected in L2/3 near the photosimulation sites (four sites in two mice).

In contrast to the activity evoked near the photostimulation sites, spiking activity in the remote areas did not originate from the neurons that had been directly photostimulated (the antidromically stimulated neurons) because the activities were completely abolished upon application of CNQX (**Figures 3E,F**). Substantial delays in firing activities (approximately 10 ms) due to synaptically transmitted signals were observed when the CFA was photostimulated and responses were compared in the RFA and the CFA. In addition, similar substantial delays were also apparent when comparing responses in the CFA and the RFA following photostimulation of the RFA. Taken together, these results indicate that neurons in the upper layers, but not L5b, of the CFA induce strong postsynaptic responses in L5 of the RFA, and that RFA neurons in L5b induce strong postsynaptic responses in L5 of the CFA.

ANATOMICAL TRACING OF CONNECTIONS BETWEEN THE RFA AND THE CFA

We next examined whether this asymmetric functional connectivity between the RFA and the CFA was consistent with the anatomical projections between these two areas. For this

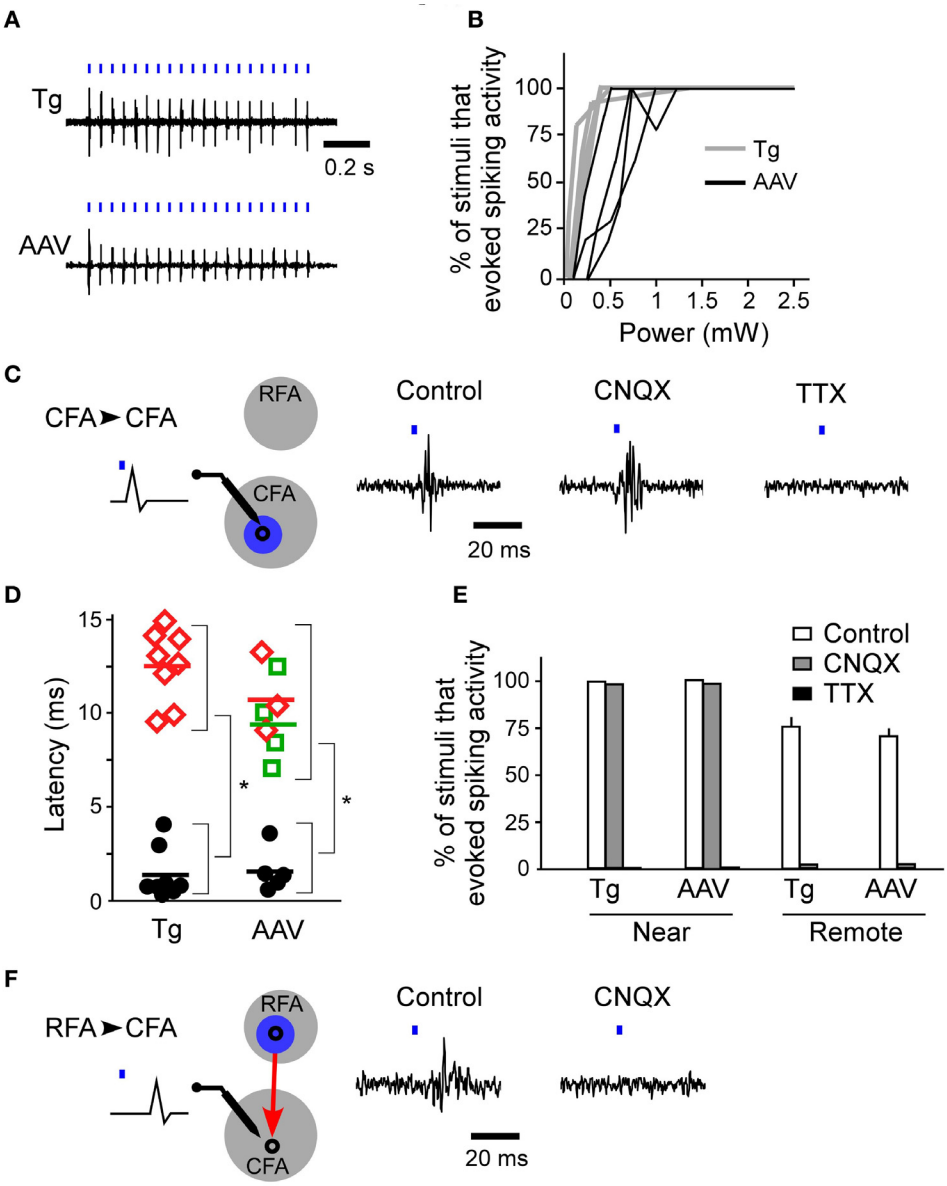

FIGURE 3 | Firing activities evoked by ChR2 photostimulation of the RFA and CFA. (A) Representative spiking activities induced by photostimulation of the CFA in the ChR2 Tg and AAV-ChR2 mice. Both traces were recorded in L5 of the CFA. The horizontal distances between the photostimulation points and the recording sites were approximately 200 μm. The blue bars represent the photostimuli (10 ms durations at a frequency of 20 Hz). The laser intensity was 2.5 mW. **(B)** Relationship between the laser power and the percentage of trials in which firing activities were evoked near the photostimulation points (gray, six sites in four ChR2 Tg mice; black, four sites in three AAV-ChR2 mice). The duration of photostimulation was 10 ms. **(C)** Left, A schematic of the experimental arrangement for photostimulation (blue) of the CFA (gray) with simultaneous electrical recording in the CFA. CFA photostimulation directly evoked firing of neurons in the CFA. Right, Representative data showing spike activities recorded in the CFA when the CFA was photostimulated in control conditions, upon CNQX application, and upon TTX application. The data were obtained from the same recording site and the same photostimulation site in a ChR2 Tg mouse. The duration of photostimulation was 2 ms. **(D)** Latencies of evoked spiking activities. Black circles indicate the electrical recordings that were made near the photostimulation points (horizontal distance of approximately 200 μm) in the RFA and the CFA. Red diamonds indicate the electrical recordings in the CFA that were responses to RFA photostimulation. Green squares indicate the electrical recordings in the RFA that were responses to CFA photostimulation. Each colored bar indicates the mean latency for the condition presented in the corresponding color. $*P < 10^{-4}$ by Student's *t*-tests. **(E)** The percentage of trials that evoked spiking activities in control, CNQX application, and TTX application conditions in ChR2 Tg mice (near: control, $n = 6$; CNQX, $n = 2$; and TTX, $n = 2$; remote: control, $n = 4$; and CNQX, $n = 2$) and AAV-ChR2 mice (near: control, $n = 4$; and CNQX, $n = 2$; and TTX, $n = 2$; remote: control, $n = 4$; and CNQX, $n = 2$). Error bars indicate SEM. **(F)** Left, A schematic of the experimental arrangement for photostimulation (blue) of the RFA (gray) with simultaneous electrical recording in the CFA. RFA photostimulation evoked postsynaptic firing activities in the CFA via the synaptic projection (red). Right, Representative data showing evoked activities in the CFA when the RFA was photostimulated. Control conditions and application of CNQX to the CFA are shown. The data were obtained from the same recording site and the same photostimulation site in a ChR2 Tg mouse. The duration of photostimulation was 2 ms.

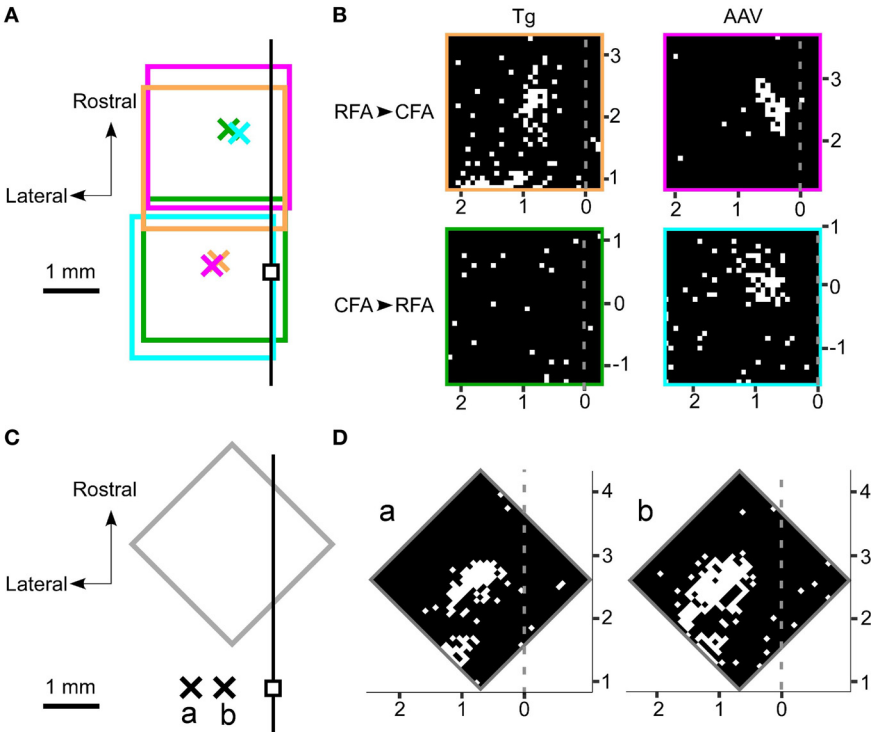

FIGURE 4 | Photostimulation mapping of functional connections between the RFA and the CFA. (A) The four rectangles represent the regions mapped by photostimulation. In each region, 32 × 32 points were pseudo-randomly stimulated with a blue laser. The laser intensity was 2.5 mW and the illumination duration was 10 ms. The crosses represent the recording sites. Each color represents one set of recording and photostimulation. The small black square denotes the bregma. The black line represents the midline. **(B)** The laser was used to stimulate 32 × 32 points that are indicated as pixels throughout the RFA and the CFA. White pixels indicate points where photostimulation induced spiking activities and black pixels reflect areas that did not induce spiking activities. The gray dotted lines represent the midline. The mapping was performed in four different mice. The top panels indicate photostimuli that were presented to the RFA while simultaneous recordings were made in the CFA. The bottom panels indicate photostimuli that were presented to the CFA while simultaneous recordings were made in the RFA. The experiments in the left panels were conducted in ChR2 Tg mice, while the experiments in the right panels were conducted in AAV-ChR2 mice. The four areas mapped are indicated by the colored rectangles in **(A)**. **(C)** A gray rectangle indicates the region mapped in **(D)**. The crosses labeled as a and b represent the corresponding recording sites in **(D)**. The recordings were made from the same ChR2 Tg mouse. The black line represents the midline. **(D)** Photostimulation maps of the RFA showed similar patterns of evoked activities even if the recording sites were changed within the CFA. The horizontal distance between the two recording sites shown here was 600 μm.

purpose, we performed anterograde tracing of the AAV-ChR2-EYFP transfected neurons, using an anti-GFP antibody to detect the EYFP-tagged ChR2. After AAV-ChR2-EYFP injection into the RFA (**Figure 2B**), axonal fibers were densely labeled in layer 1, L5b and upper L6 of the CFA (**Figures 5A–C**), consistent with a previous report (Smith et al., 2010). AAV-ChR2-EYFP injection into the CFA yielded labeling of axonal fibers densely in L5a of the RFA (**Figures 5D–G**). The results obtained with the anterograde tracer were consistent with spiking activity occurring in L5, but not in L2/3, when the other area was photostimulated.

To anatomically determine the layer of the projection neurons in the RFA and the CFA, we used CTB subunit as a retrograde tracer. CTB injection into the RFA yielded denser CTB-positive neurons in the upper layers of the CFA than in L5b (the ratio of CTB-positive neurons to Nissl-stained neurons: 24.1 ± 6.2% in L2/3, 13.5 ± 2.9% in L5a, 3.1 ± 1.1% in L5b, $n = 3$ mice; **Figures 6A–D**). In addition, when CTB was injected into the RFA in ChR2 Tg mice, CTB labeling was detected in 4.3% (3/70) of ChR2-EYFP-positive neurons and 5.1% (3/59) of ChR2-EYFP-negative neurons in L5b of the CFA (**Figure 6E**). Thus, it was unlikely that a subset of ChR2-EYFP-negative neurons, instead of ChR2-EYFP-positive neurons, in L5b of the CFA strongly projected to the RFA. Thus, the major origin of the projection from the CFA to the RFA was the upper layers. By contrast, after CTB injection into the CFA, the ratio of CTB-positive neurons to Nissl-stained neurons was higher in L5b of the RFA than in the upper layers (6.5 ± 1.0% in L2/3, 4.4 ± 1.4% in L5a, 15.8 ± 1.4% in L5b, $n = 3$ mice; **Figures 6F–H**). Thus, the dominant direct projection to the CFA originates from L5b of the RFA. All anatomical tracings indicate that the RFA and the CFA communicate with each other through distinct, asymmetric connections (**Figure 7**).

DISCUSSION

OPTOGENETIC TRACINGS OF FUNCTIONAL CONNECTIONS

In this study, we used an optogenetic mapping method to investigate the connectivity between the RFA and the CFA in mice.

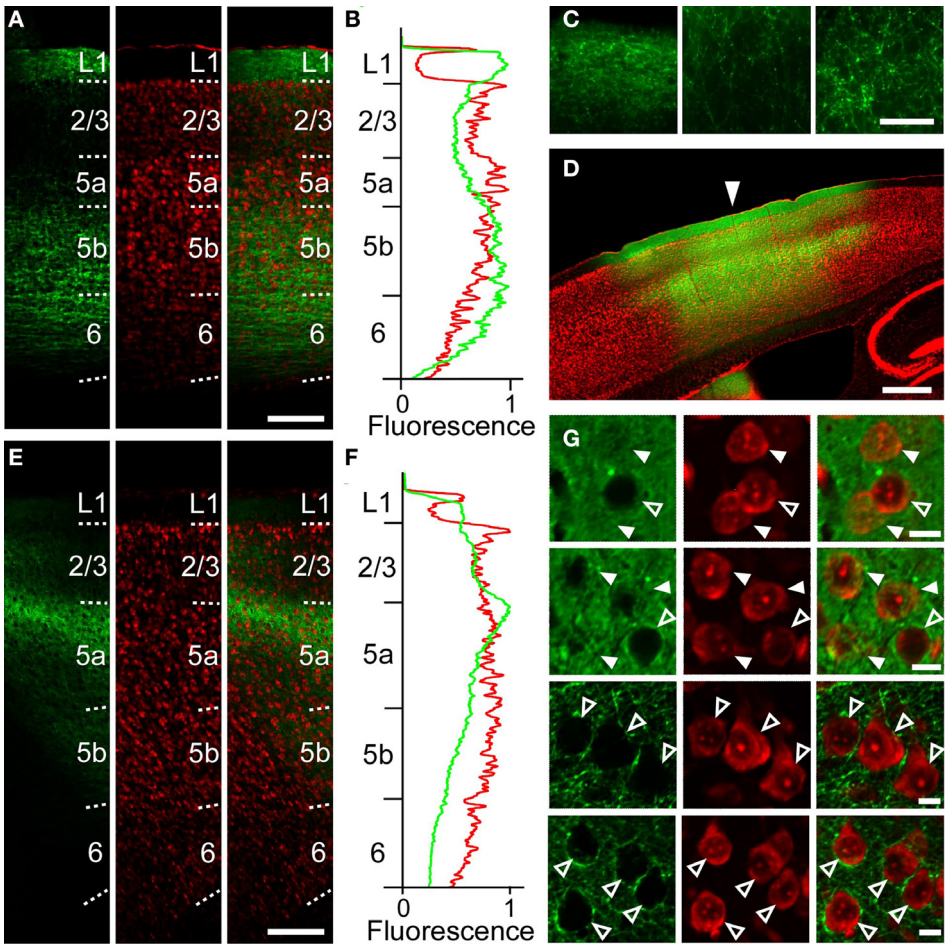

FIGURE 5 | Anatomical tracings of axonal fibers between the RFA and the CFA. (A) Anti-GFP immunofluorescence (left), Nissl staining (middle), and the overlay (right) in the CFA in a sagittal section after AAV-ChR2-EYFP injection into the RFA in **Figure 2B**. Scale bar, 200 μm. **(B)** Profiles of anti-GFP immunofluorescence (green) and Nissl staining (red) in **(A)** as a function of laminar depth. Fluorescence was background subtracted and normalized. **(C)** Higher magnification of GFP-immunofluorescence in **(A)**. Left, L1. Middle, L2/3. Right, L5b. Scale bar, 50 μm. **(D)** Overlay of EYFP fluorescence (green), Nissl staining (red) in a sagittal section of a mouse in which AAV-ChR2-EYFP was injected into the CFA. Arrowhead indicates 0 mm anterior and 1.2 mm lateral from the bregma. Scale bar, 500 μm. **(E)** Anti-GFP immunofluorescence (left), Nissl staining (middle), and the overlay (right) in the RFA in a sagittal section after AAV-ChR2-EYFP injection into the CFA in **(D)**. **(F)** Normalized profiles of anti-GFP immunofluorescence (green) and Nissl staining (red) in **(E)** as a function of laminar depth. **(G)** Higher magnification of the images in **(D)**. Top row, L2/3 at the injection site. Second row, L5a at the injection site. Third row, L2/3 1.2 mm anterior from the injection site. Bottom row, L5a 1.2 mm anterior from the injection site. Closed arrowheads indicate ChR2-EYFP-positive neurons. Open arrowheads indicate ChR2-EYFP-negative neurons. Scale bars, 10 μm.

Pharmacological experiments and analyses of response latencies demonstrated that spikes evoked in these cortical areas by photostimulation of the other cortical area were postsynaptic responses, rather than directly activated or antidromic action potentials. The transgenic mice that were used in the present study expressed ChR2 in the L5b pyramidal neurons, while AAV transfection introduced ChR2 into neurons in both the upper layers (L2/3 and L5a) and L5b throughout the injected regions. This combination of experiments allowed us to compare projections that originate from L5b to projections that originate from the upper layers and L5b between these cortical areas. In future studies, it will be necessary to limit ChR2 expression to only L2/3 or L5a by using other promoters, such as Wolfram syndrome 1 (Wfs1) or ETS-domain transcription factor (Etv1) (O'Connor et al., 2009). In addition, the number of photostimulated neurons could be further restricted by expressing ChR2 only in a very small subset of neurons (Ako et al., 2011) or by using two-photon ChR2 stimulation methods (Rickgauer and Tank, 2009; Andrasfalvy et al., 2010; Papagiakoumou et al., 2010). Retrograde and anterograde trans-synaptic virus tracers may also be promising ways to yield more specific photostimulation (Miyamichi et al., 2010; Lo and Anderson, 2011). In the *in vivo* electrical recording, it was difficult to determine whether the recorded activity came from L5a or L5b neurons. Synaptic inputs to L5a and L5b neurons could be identified by combining whole-cell recording of target neurons in neocortical brain slices and photostimulation of ChR2-expressing axons from the other area (Petreanu et al., 2009; Hooks et al., 2013).

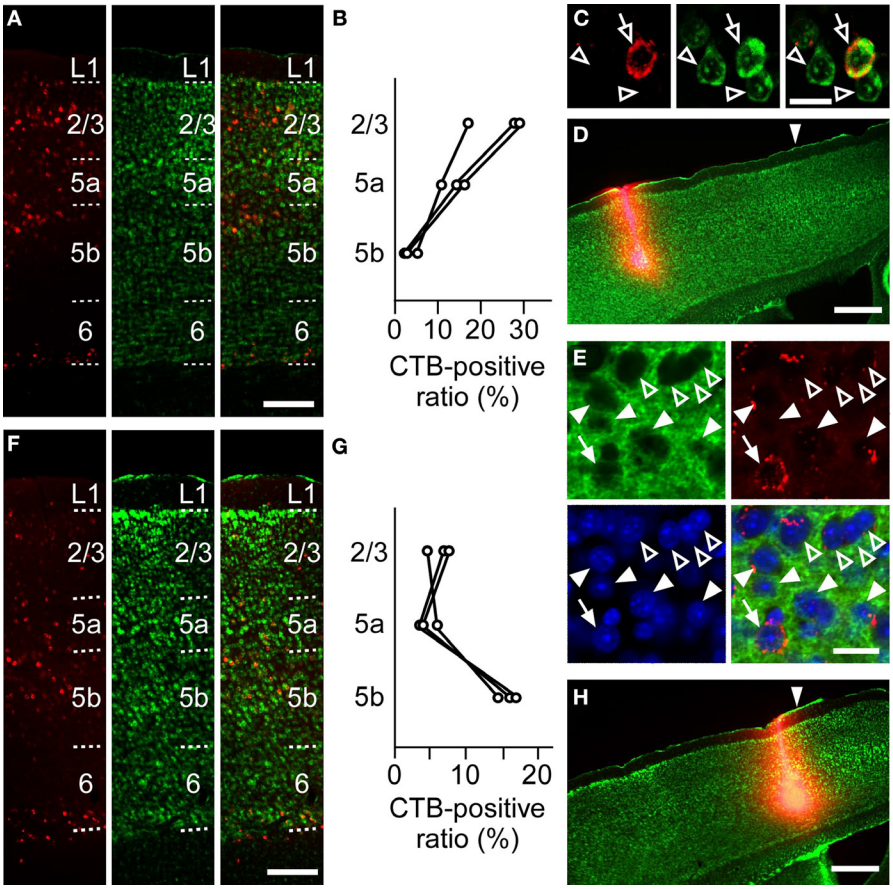

FIGURE 6 | Anatomical tracings of projection neurons between the RFA and the CFA. (A) Anti-CTB immunofluorescence (left), Nissl staining (middle), and the overlay (right) in the CFA after CTB-Alexa 594 injection into the RFA in **(D)**. Scale bar, 200 μm. **(B)** Ratios of CTB-positive neurons to Nissl-stained neurons in L2/3, L5a, and L5b of the CFA after CTB-Alexa 594 injection into the RFA. Each line indicates one mouse. **(C)** Higher magnification of the images in L5a in **(A)**. Open arrows indicate a CTB-positive neuron. Open arrowheads indicate CTB-negative neurons. Scale bar, 20 μm. **(D)** Anti-CTB immunofluorescence and Nissl staining of the RFA injected with CTB-Alexa 594 are overlaid. Arrowhead indicates 0 mm anterior and 0.9 mm lateral from the bregma. Scale bar, 500 μm. **(E)** High magnification of the images of anti-GFP immunofluorescence (green), Anti-CTB immunofluorescence (red), Nissl staining (blue), and the overlay in the L5b CFA after CTB-Alexa 594 injection into the RFA of a ChR2 Tg mouse. Closed arrows indicate a ChR2-EYFP-positive and CTB-positive neurons. Closed arrowheads indicate ChR2-EYFP-positive and CTB-negative neurons. Open arrowheads indicate ChR2-EYFP-negative and CTB-negative neurons. Scale bar, 20 μm. **(F)** Anti-CTB immunofluorescence (left), Nissl staining (middle), and the overlay (right) in the RFA after CTB-Alexa 594 injection into the CFA in **(H)**. Scale bar, 200 μm. **(G)** Ratios of CTB-positive neurons to Nissl-stained neurons in L2/3, L5a, and L5b of the RFA after CTB-Alexa 594 injection into the CFA. Each line indicates one mouse. **(H)** Anti-CTB immunofluorescence and Nissl staining of the CFA are overlaid. Arrowhead indicates 0 mm anterior and 1.0 mm lateral from the bregma. Scale bar, 500 μm.

LAMINAR CONNECTIVITY PATTERNS BETWEEN THE RFA AND THE CFA

We detected responses in the CFA when the neurons in L5b of the RFA were photostimulated in the ChR2 Tg mice. Although these results did not allow us to determine whether the upper layers of the RFA also projects to the CFA, our retrograde tracer experiments showed that axons originating from neurons in L5b of the RFA provided the dominant projections to the CFA.

By contrast, responses were absent in the RFA when the CFA was photostimulated in the ChR2 Tg mice, but were clearly present when the AAV-ChR2 mice were used. This difference demonstrated that while L5b of the CFA does not strongly project to the RFA, L2/3 and/or L5a of the CFA strongly does. These results are also consistent with our anatomical tracing experiments.

Synaptic projections that originate from L2/3 predominantly innervate the deeper parts of L5 and there is differentiation between corticostriatal and corticospinal outputs (Morishima and Kawaguchi, 2006; Brown and Hestrin, 2009; Anderson et al., 2010). Corticospinal neurons in L5b, which are the final outputs of motor cortical networks, receive excitatory inputs from corticostriatal neurons, but the corticostriatal neurons do not receive inputs from the corticospinal neurons (Kiritani et al., 2012). Therefore, information is unidirectionally transmitted from L2/3 neurons and L5a corticostriatal neurons to L5b corticospinal neurons within the RFA and the CFA. Our results indicate that L5b of the CFA does not strongly project to L5 of the RFA, but L5b of the RFA has strong projections to L5 of the CFA. Therefore, information that is processed in the upper layers of the CFA is

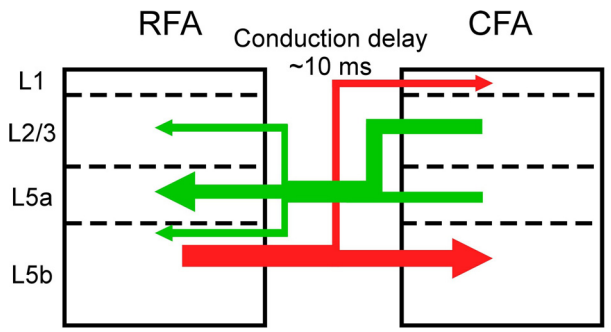

FIGURE 7 | Asymmetric synaptic connectivity between the RFA and the CFA. The RFA receives stronger functional projections from L2/3 and/or L5a of the CFA than from L5b of the CFA (green). The CFA receives stronger functional projections from L5b of the RFA than from L2/3 and L5a of the RFA.

transmitted to the RFA and the final outputs of L5b of the CFA are likely determined by integration of signals from the upper layers of the CFA and L5b of the RFA. Considering the asymmetric information flow between the RFA and the CFA (**Figure 7**), our results support the idea that the RFA is a higher motor area than the CFA (Neafsey et al., 1986; Rouiller et al., 1993; Smith et al., 2010; Tennant et al., 2011).

However, the laminar connection patterns among the supplementary motor cortex (SMA), the premotor cortex (PM), and the primary motor cortex (M1) in the primate are not hierarchical (Dum and Strick, 2005). The PM and M1 project to the spinal cord (Dum and Strick, 1991). Similarly, the corticospinal axons originate from both the RFA and CFA in the rat (Rouiller et al., 1993). Thus, it remains unclear whether the motor cortex network is comparable between rodents and primates. Nevertheless, the next step will be to find what signals are transmitted between the RFA and the CFA. Individual neurons that project to the other area can be retrogradely labeled (Sato and Svoboda, 2010). Furthermore, individual neurons that are activated in the remote area by ChR2 photostimulation could potentially be identified by expressing calcium-sensitive fluorescent molecules in these neurons. Therefore, two-photon calcium imaging of these neurons during a motor task like the lever-pull movement task (Hira et al., 2013) should reveal the characteristics of their activities during movement and allow us to understand how multiple motor output channels are organized by corticocortical interactions during elaborate movements.

CONDUCTION DELAY BETWEEN THE RFA AND THE CFA

We found that it took approximately 10 ms to transmit corticocortical information from the RFA to the CFA or from the CFA to the RFA. Given the dense anatomical projections between the RFA and the CFA, we were not surprised to observe direct synaptic connections between these cortical areas. However, the latency may be longer than expected for a direct monosynaptic connection. For example, neurons in the motor cortex respond to whisker stimuli approximately 8 ms later than neurons in the somatosensory barrel cortex in the mouse and this motor cortex response is thought to be mediated by direct synaptic projections from the somatosensory cortex (Ferezou et al., 2007). The distance between these areas is approximately 4 mm, which is longer than the approximately 2 mm between the RFA and the CFA. Therefore, it remains possible that indirect connections, such as cortico-thalamo-cortical connections, are responsible for signaling between the RFA and the CFA. It remains unknown whether the 10 ms delay that we observed between the RFA and the CFA is mediated by monosynaptic or polysynaptic connections.

Whatever its origins, this delay cannot be ignored because the temporal order of action potentials is important for information processing (Izhikevich, 2006) and spike timing-dependent plasticity (Froemke and Dan, 2002; Wolters et al., 2003). Thus, how the activity of the RFA and the CFA are temporally coordinated with these substantial conduction delays during movements could potentially be determined by simultaneous multi-electrode recording in both areas (Isomura et al., 2009).

SUMMARY

In this study, we combined *in vivo* ChR2 photostimulation mapping with *in vivo* electrical recording. This approach allowed us to demonstrate functional connections between the RFA and the CFA with conduction delay of approximately 10 ms in the mouse motor cortex. We found that the RFA receives strong functional projections from L2/3 and/or L5a, but not L5b, of the CFA, while the CFA receives strong functional projections from L5b of the RFA. Our results suggest that the neuronal activity that occurs in the RFA and the CFA during movement is generated through asymmetric reciprocal connections. The *in vivo* optogenetic mapping method will be useful to further clarify corticocortical functional connections.

ACKNOWLEDGMENTS

We thank M. Himeno, J. Saito, and T. Sugiyama for technical assistance. We thank Y. H. Tanaka for technical advice. We are grateful to the Spectrography and Bioimaging Facility at NIBB for allowing the equipment use. We thank Dr. K. Deisseroth, Stanford University for providing pAAV-Syn-hChR2 (H134R)-EYFP-WPRE, and Dr. J. M. Wilson, University of Pennsylvania for providing helper plasmid pAAV2-9. This work was supported by Grants-in-Aids for Scientific Research on Innovative Areas "Mesoscopic Neurocircuitry" (no. 22115005 to Masanori Matsuzaki), for Scientific Research (B) (no. 23300148 to Masanori Matsuzaki), for JSPS Fellows (Riichiro Hira), for Research Activity Start-up (no. 23800071 to Yoshito Masamizu), and for Specially Promoted Areas (no. 2000009 to Haruo Kasai), and the Strategic Research Program for Brain Sciences ("Bioinformatics for Brain Sciences" to Haruo Kasai) from the Ministry of Education, Culture, Sports, Science, and Technology (MEXT), Japan; by Takeda foundation and Toyoaki foundation grants to Masanori Matsuzaki; by CREST of JST to Haruo Kasai; and by a CRP grant from the National Research Foundation of Singapore and by the World Class Institute (WCI) Program of the National Research Foundation of Korea (NRF) funded by the Ministry of Education, Science and Technology of Korea (MEST) (NRF Grant Number: WCI 2009-003).

REFERENCES

Ako, R., Wakimoto, M., Ebisu, H., Tanno, K., Hira, R., Kasai, H., et al. (2011). Simultaneous visualization of multiple neuronal properties with single-cell resolution in the living rodent brain. *Mol. Cell. Neurosci.* 48, 246–257.

Anderson, C. T., Sheets, P. L., Kiritani, T., and Shepherd, G. M. G. (2010). Sublayer-specific microcircuits of corticospinal and corticostriatal neurons in motor cortex. *Nat. Neurosci.* 13, 739–744.

Andrasfalvy, B. K., Zemelman, B. V., Tang, J., and Vaziri, A. (2010). Two-photon single-cell optogenetic control of neuronal activity by sculpted light. *Proc. Natl. Acad. Sci. U.S.A.* 107, 11981–11986.

Arenkiel, B. R., Peca, J., Davison, I. G., Feliciano, C., Deisseroth, K., Augustine, G. J., et al. (2007). *In vivo* light-induced activation of neural circuitry in transgenic mice expressing channelrhodopsin-2. *Neuron* 54, 205–218.

Ayling, O. G. S., Harrison, T. C., Boyd, J. D., Goroshkov, A., and Murphy, T. H. (2009). Automated light-based mapping of motor cortex by photoactivation of channelrhodopsin-2 transgenic mice. *Nat. Methods* 6, 219–224.

Binding, J., Ben Arous, J., Léger, J. F., Gigan, S., Boccara, C., and Bourdieu, L. (2011). Brain refractive index measured *in vivo* with high-NA defocus-corrected full-field OCT and consequences for two-photon microscopy. *Opt. Express* 19, 4833–4847.

Brown, S. P., and Hestrin, S. (2009). Intracortical circuits of pyramidal neurons reflect their long-range axonal targets. *Nature* 457, 1133–1136.

Coogan, T. A., and Burkhalter, A. (1990). Conserved patterns of cortico-cortical connections define areal hierarchy in rat visual cortex. *Exp. Brain Res.* 80, 49–53.

Dum, R. P., and Strick, P. L. (1991). The origin of corticospinal projections from the premotor areas in the frontal lobe. *J. Neurosci.* 11, 667–689.

Dum, R. P., and Strick, P. L. (2005). Frontal lobe inputs to the digit representations of the motor areas on the lateral surface of the hemisphere. *J. Neurosci.* 25, 1375–1386.

Ferezou, I., Haiss, F., Gentet, L. J., Aronoff, R., Weber, B., and Petersen, C. C. H. (2007). Spatiotemporal dynamics of cortical sensorimotor integration in behaving mice. *Neuron* 56, 907–923.

Froemke, R. C., and Dan, Y. (2002). Spike-timing-dependent synaptic modification induced by natural spike trains. *Nature* 416, 433–438.

Hira, R., Honkura, N., Noguchi, J., Maruyama, Y., Augustine, G. J., Kasai, H., et al. (2009). Transcranial optogenetic stimulation for functional mapping of the motor cortex. *J. Neurosci. Methods* 179, 258–263.

Hira, R., Ohkubo, F., Ozawa, K., Isomura, Y., Kitamura, K., Kano, M., et al. (2013). Spatiotemporal dynamics of functional clusters of neurons in the mouse motor cortex during a voluntary movement. *J. Neurosci.* 33, 1377–1390.

Hooks, B. M., Mao, T., Gutnisky, D. A., Yamawaki, N., Svoboda, K., and Shepherd, G. M. G. (2013). Organization of cortical and thalamic input to pyramidal neurons in mouse motor cortex. *J. Neurosci.* 33, 748–760.

Howard, C. V., and Reed, M. G. (1998). *Unbiased Stereology: Three-Dimensional Measurement in Microscopy*. Oxford: Bios Scientific Publishers.

Hyland, B. (1998). Neural activity related to reaching and grasping in rostral and caudal regions of rat motor cortex. *Behav. Brain Res.* 94, 255–269.

Isomura, Y., Harukuni, R., Takekawa, T., Aizawa, H., and Fukai, T. (2009). Microcircuitry coordination of cortical motor information in self-initiation of voluntary movements. *Nat. Neurosci.* 12, 1586–1593.

Izhikevich, E. M. (2006). Polychronization: computation with spikes. *Neural Comput.* 18, 245–282.

Kiritani, T., Wickersham, I. R., Seung, H. S., and Shepherd, G. M. G. (2012). Hierarchical connectivity and connection-specific dynamics in the corticospinal–corticostriatal microcircuit in mouse motor cortex. *J. Neurosci.* 32, 4992–5001.

Lim, D. H., Mohajerani, M. H., Ledue, J., Boyd, J., Chen, S., and Murphy, T. H. (2012). *In vivo* large-scale cortical mapping using channelrhodopsin-2 stimulation in transgenic mice reveals asymmetric and reciprocal relationships between cortical areas. *Front. Neural Circuits* 6:11. doi: 10.3389/fncir.2012.00011

Lo, L., and Anderson, D. J. (2011). A cre-dependent, anterograde transsynaptic viral tracer for mapping output pathways of genetically marked neurons. *Neuron* 72, 938–950.

Masamizu, Y., Okada, T., Kawasaki, K., Ishibashi, H., Yuasa, S., Takeda, S., et al. (2011). Local and retrograde gene transfer into primate neuronal pathways via adeno-associated virus serotype 8 and 9. *Neuroscience* 193, 249–258.

Miyamichi, K., Amat, F., Moussavi, F., Wang, C., Wickersham, I., Wall, N. R., et al. (2010). Cortical representations of olfactory input by trans-synaptic tracing. *Nature* 472, 191–196.

Morishima, M., and Kawaguchi, Y. (2006). Recurrent connection patterns of corticostriatal pyramidal cells in frontal cortex. *J. Neurosci.* 26, 4394–4405.

Neafsey, E., Bold, E., Haas, G., Hurley-Gius, K., Quirk, G., Sievert, C., et al. (1986). The organization of the rat motor cortex: a microstimulation mapping study. *Brain Res.* 11, 77–96.

O'Connor, D. H., Huber, D., and Svoboda, K. (2009). Reverse engineering the mouse brain. *Nature* 461, 923–929.

Papagiakoumou, E., Anselmi, F., Bègue, A., de Sars, V., Glückstad, J., Isacoff, E. Y., et al. (2010). Scanless two-photon excitation of channelrhodopsin-2. *Nat. Methods* 7, 848–854.

Petreanu, L., Mao, T. Y., Sternson, S. M., and Svoboda, K. (2009). The subcellular organization of neocortical excitatory connections. *Nature* 457, 1142–1145.

Rickgauer, J. P., and Tank, D. W. (2009). Two-photon excitation of channelrhodopsin-2 at saturation. *Proc. Natl. Acad. Sci. U.S.A.* 106, 15025–15030.

Rouiller, E. M., Moret, V., and Liang, F. (1993). Comparison of the connectional properties of the two forelimb areas of the rat sensorimotor cortex: support for the presence of a premotor or supplementary motor cortical area. *Somatosens. Mot. Res.* 10, 269–289.

Sato, T. R., and Svoboda, K. (2010). The functional properties of barrel cortex neurons projecting to the primary motor cortex. *J. Neurosci.* 30, 4256–4260.

Shipp, S. (2005). The importance of being agranular: a comparative account of visual and motor cortex. *Philos. Trans. R. Soc. B* 360, 797–814.

Smith, N. J., Horst, N. K., Liu, B., Caetano, M. S., and Laubach, M. (2010). Reversible inactivation of rat premotor cortex impairs temporal preparation, but not inhibitory control, during simple reaction-time performance. *Front. Integr. Neurosci.* 4:124. doi: 10.3389/fnint.2010.00124

Tanaka, Y. R., Tanaka, Y. H., Konno, M., Fujiyama, F., Sonomura, T., Okamoto-Furuta, K., et al. (2011). Local connections of excitatory neurons to corticothalamic neurons in the rat barrel cortex. *J. Neurosci.* 31, 18223–18236.

Tennant, K. A., Adkins, D. L., Donlan, N. A., Asay, A. L., Thomas, N., Kleim, J. A., et al. (2011). The organization of the forelimb representation of the C57BL/6 mouse motor cortex as defined by intracortical microstimulation and cytoarchitecture. *Cereb. Cortex* 21, 865–876.

Van Essen, D. C., and Maunsell, J. H. R. (1983). Hierarchical organization and functional streams in the visual cortex. *Trends Neurosci.* 6, 370–375.

Wang, H., Peca, J., Matsuzaki, M., Matsuzaki, K., Noguchi, J., Qiu, L., et al. (2007). High-speed mapping of synaptic connectivity using photostimulation in Channelrhodopsin-2 transgenic mice. *Proc. Natl. Acad. Sci. U.S.A.* 104, 8143–8148.

Wolters, A., Sandbrink, F., Schlottmann, A., Kunesch, E., Stefan, K., Cohen, L. G., et al. (2003). A temporally asymmetric Hebbian rule governing plasticity in the human motor cortex. *J. Neurophysiol.* 89, 2339–2345.

Yizhar, O., Fenno, L. E., Davidson, T. J., Mogri, M., and Deisseroth, K. (2011). Optogenetics in neural systems. *Neuron* 71, 9–34.

Conflict of Interest Statement: The authors declare that the research was conducted in the absence of any commercial or financial relationships that could be construed as a potential conflict of interest.

Received: 28 November 2012; accepted: 11 March 2013; published online: 01 April 2013.

Citation: Hira R, Ohkubo F, Tanaka YR, Masamizu Y, Augustine GJ, Kasai H and Matsuzaki M (2013) In vivo optogenetic tracing of functional corticocortical connections between motor forelimb areas. Front. Neural Circuits 7:55. doi: 10.3389/fncir.2013.00055

frontiers in
NEURAL CIRCUITS

ORIGINAL RESEARCH ARTICLE
published: 27 March 2013
doi: 10.3389/fncir.2013.00048

Mapping the spatio-temporal structure of motor cortical LFP and spiking activities during reach-to-grasp movements

Alexa Riehle[1,2]*, Sarah Wirtssohn[1†], Sonja Grün[2,3,4,5] and Thomas Brochier[1]

[1] Institut de Neurosciences de la Timone, UMR 7289, Centre National de la Recherche Scientifique - Aix-Marseille Université, Marseille, France
[2] Riken Brain Science Institute, Wako-Shi, Japan
[3] Institute of Neuroscience and Medicine (INM-6), Computational and Systems Neuroscience, Research Center Jülich, Jülich, Germany
[4] Institute for Advanced Simulation (IAS-6), Theoretical Neuroscience, Research Center Jülich, Jülich, Germany
[5] Theoretical Systems Neurobiology, RWTH Aachen University, Aachen, Germany

Edited by:
Nicholas Hatsopoulos, University of Chicago, USA

Reviewed by:
Nicholas Hatsopoulos, University of Chicago, USA
Marc Schieber, University of Rochester, USA

***Correspondence:**
Alexa Riehle, Institut de Neurosciences de la Timone, UMR 7289, Centre National de la Recherche Scientifique - Aix-Marseille Université, Campus Santé Timone, 27, Boulevard Jean Moulin, 13885 Marseille Cedex 05, France.
e-mail: alexa.riehle@univ-amu.fr

[†]Present address:
Sarah Wirtssohn, Institute of Biology, Behavioural Physiology, Humboldt-Universität zu Berlin, Berlin, Germany.

Grasping an object involves shaping the hand and fingers in relation to the object's physical properties. Following object contact, it also requires a fine adjustment of grasp forces for secure manipulation. Earlier studies suggest that the control of hand shaping and grasp force involve partially segregated motor cortical networks. However, it is still unclear how information originating from these networks is processed and integrated. We addressed this issue by analyzing massively parallel signals from population measures (local field potentials, LFPs) and single neuron spiking activities recorded simultaneously during a delayed reach-to-grasp task, by using a 100-electrode array chronically implanted in monkey motor cortex. Motor cortical LFPs exhibit a large multi-component movement-related potential (MRP) around movement onset. Here, we show that the peak amplitude of each MRP component and its latency with respect to movement onset vary along the cortical surface covered by the array. Using a comparative mapping approach, we suggest that the spatio-temporal structure of the MRP reflects the complex physical properties of the reach-to-grasp movement. In addition, we explored how the spatio-temporal structure of the MRP relates to two other measures of neuronal activity: the temporal profile of single neuron spiking activity at each electrode site and the somatosensory receptive field properties of single neuron activities. We observe that the spatial representations of LFP and spiking activities overlap extensively and relate to the spatial distribution of proximal and distal representations of the upper limb. Altogether, these data show that, in motor cortex, a precise spatio-temporal pattern of activation is involved for the control of reach-to-grasp movements and provide some new insight about the functional organization of motor cortex during reaching and object manipulation.

Keywords: cortical map, high-density recordings, monkey motor cortex, spiking activity, LFP

INTRODUCTION

The motor cortex is undoubtedly the first cortical area to be functionally examined in the history of neuroscience. In 1870, Fritsch and Hitzig did the first electrical stimulation experiments describing the topographical structure of motor cortex related to body segments (Fritsch and Hitzig, 1870). Almost 100 years later, Evarts (1964, 1966) started the first electrophysiological experiments in the awake behaving monkey to relate cortical activity to upper limb movements. Electrophysiological and anatomical studies have demonstrated the complex organization of body representation in the motor cortex of human and non-human primates. The motor effects evoked by intra-cortical micro-stimulation (ICMS) show systematic variations along the medio-lateral axis of the primary motor cortex (M1): ICMS at medial cortical sites in the precentral gyrus evokes lower limb movements, whereas ICMS at more lateral sites generate upper limb and head movements (Woolsey et al., 1952; Asanuma and Rosén, 1972; Kwan et al., 1978; Humphrey, 1986). Complementary studies revealed some additional variations in M1 and dorsal premotor (PMd) cortical organization along the antero-posterior axis. These observations suggest a clearly delineated somatotopic parcellation of motor cortical areas (Raos et al., 2003; Boudrias et al., 2010). However, converging evidence shows that body representation is not so strictly organized but characterized by a great degree of overlap between the cortical zones within M1 controlling nearby body parts (Park et al., 2001, 2004). This is particularly true within the distal upper limb representation in which there is little evidence of independent representation of the fingers (Schieber and Hibbert, 1993; Schieber, 2001).

On the functional side, it remains unclear how motor cortical organization as revealed by ICMS mapping relates to the activity of this cortical area during complex movements involving multiple body segments. Reach-to-grasp movements are particularly well suited to address this issue. These movements require the coordinated activation of arm and hand muscles to move the proximal and distal segments of the upper limb in a coherent way (Jeannerod, 1984; Jeannerod et al., 1995). Reaching requires activation of the arm muscles to transport the hand toward target objects, whereas grasping involves the activation of extrinsic and intrinsic hand muscles for hand preshaping and force control

(Brochier et al., 2004; Stark et al., 2007). Following object contact, grasping also requires a fine adjustment of grasp forces for secure manipulation. Earlier studies suggest that the control of hand shaping and grasp force involves partially segregated motor cortical networks both during preparation and execution (Tokuno and Tanji, 1993; Rubino et al., 2006; Umilta et al., 2007; Vargas-Irwin et al., 2010; Bansal et al., 2012). However, it is still unclear how information originating from these networks is processed and integrated over motor cortical areas to give rise to a unified motor command.

One way to study the spatio-temporal modulations of neural activity during reach-to-grasp movements is to record simultaneously from an extended cortical territory through implanted microelectrode arrays. Vargas-Irwin et al. (2010) used 4 mm × 4 mm 100-electrode Utah arrays implanted in the upper limb representation just anterior to the central sulcus to analyze the spiking activity of single neurons during reach-to-grasp movements. They did not observe any systematic spatial dependence of neuronal firing with arm and hand movements, nor any related spatial partitioning of neuronal populations. However, Hatsopoulos and colleagues (Rubino et al., 2006; Hatsopoulos et al., 2011; Takahashi et al., 2011) used the same type of arrays to analyze the properties of local field potential (LFP) oscillatory activity in the beta frequency range (15–30 Hz) along the cortical surface close to the central sulcus. They described propagating waves of beta oscillations along the dominant axes of the motor cortex with respect to the proximal and distal motor representations in both humans and monkeys. These partially conflicting observations may be related to the observation that spiking activity and LFPs are not tightly correlated neuronal signals (Poulet and Petersen, 2008; Okun et al., 2010) and thus likely carry different information. LFPs can be recorded from the same electrode as single neurons and reflect mainly the spatially averaged synaptic input to neurons within a small volume around the electrode tip (Mitzdorf, 1985). It is plausible that the global LFP signal is more appropriate to capture gradual transitions within motor cortical maps than highly localized spiking activity.

Besides their oscillatory properties, LFPs are known to modulate in the time domain in relation to specific behaviorally relevant events. In motor cortical areas, LFPs exhibit a large multi-component movement-related potential (MRP) around movement onset (Donchin et al., 2001; Roux et al., 2006; Kilavik et al., 2010). However, little is known about the spatio-temporal distribution of MRPs across motor cortex in relation to task requirements. It is assumed that negative deflections of the LFP reflect excitatory inputs to the neurons in the local vicinity of the electrode tip and as such may promote an increase in spiking activity (Arieli et al., 1995; Destexhe et al., 1999). Following this assumption, one can hypothesize that the modulation of the amplitudes of the different MRP components may be characterized by specific spatio-temporal structures related to the motor cortical internal map.

In this paper, we use high-density intra-cortical recordings to study the temporal and spatial modulations of LFP and spiking activity during a delayed reach-to-grasp task. Neuronal activity was recorded by using a 100-electrode "Utah" array, chronically implanted in the precentral gyrus convexity. We first used the LFP signal to analyze the distinct MRP components and to explore how their peak amplitudes and latencies are spatially distributed over the cortical surface covered by the electrode array. Using this mapping approach, we showed for the first time that during movement execution, the spatio-temporal structure of the MRP reflects the complex physical properties of reach-to-grasp movement. In addition, we explored how the MRP structure relates to two other measures of neuronal activity: (i) the temporal profile of single neuron spiking activity at each electrode site and (ii) the somatosensory receptive field (RF) properties of single neuron activities. We observed that the spatial representations of LFP and spiking activities overlap extensively and relate to the spatial distribution of proximal and distal representations of the upper limb in motor cortex. Altogether, these data show that, in motor cortex, a precise spatio-temporal pattern of activation is involved for the control of reach-to-grasp movements and provide some new insight about the functional organization of motor cortex during reaching and object manipulation. Preliminary data were presented in Brochier and Riehle (2011) and Riehle and Brochier (2012).

MATERIALS AND METHODS

BEHAVIORAL TASK

One adult female macaque monkey (*Macaca mulatta*), weighing 4.5 kg, was used in the experiment. All animal procedures were approved by the local ethical committee (authorization A1/10/12) and conformed to the European and French government regulations.

The monkey was trained to perform an instructed delay reach-to-grasp task to obtain a food reward (apple sauce), using the left hand, and sat in a custom-made primate chair in front of the experimental apparatus with the non-working arm loosely restrained in a semi-flexed position. The unrestrained working hand rested on a switch positioned at waist-level, 5 cm lateral to the midline. The target object was a stainless steel parallelepiped (40 mm × 16 mm × 10 mm) attached to the anterior end of a low-friction horizontal shuttle and rotated at a 45° angle from the vertical axis (see **Figure 1A**). It was located 13 cm away from the switch at 14 cm height. The object had to be grasped and pulled with the working hand using one of two different grips: a precision grip (PG) by placing the tips of the index and the thumb in a groove on the upper and lower sides of the object, respectively, or a side grip (SG), by placing the tip of the thumb and the lateral surface of the index on the right and left sides, respectively (**Figure 1A**). The object weight could be set to one of two different values (100 or 200 g) by means of an electromagnet inside the apparatus. Thus, the force required to pull the object was either low force (LF) or high force (HF) when the magnet was turned off or on, respectively. Changes in object weight occurred between trials and were undetectable by the monkey. The apparatus provided a continuous measure of the grip and pulling load forces by means of force sensitive resistances (FSR). In addition, a hall-effect sensor measured the horizontal displacement of the object over a maximal distance of 15 mm.

A square of four red light-emitting diodes (LEDs) with one yellow LED in its center was used to display the instruction cues (**Figure 1B**). The LEDs were inserted in the apparatus just above

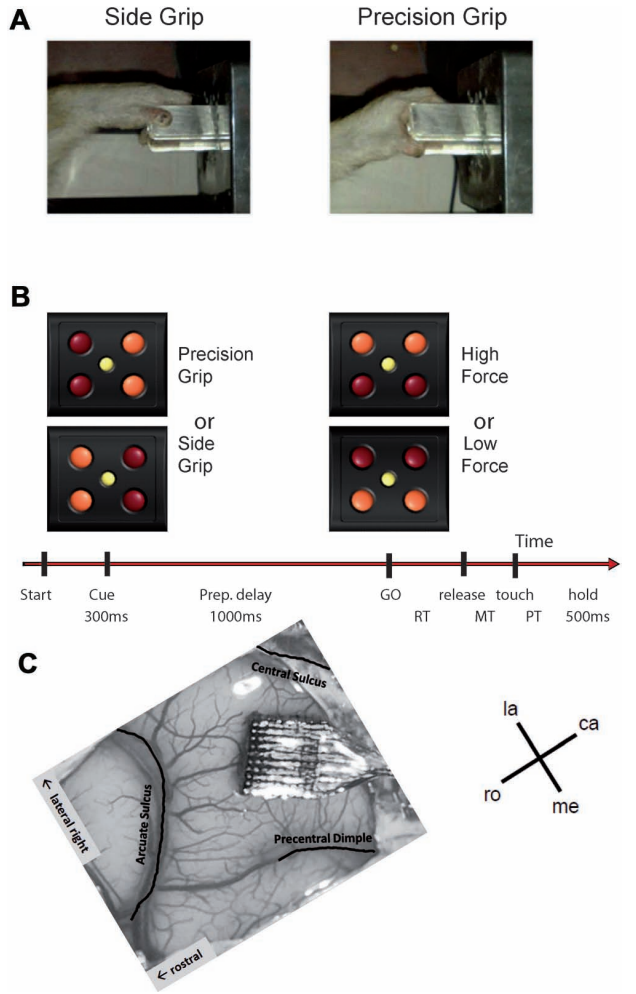

FIGURE 1 | (A,B) Experimental design (see text for details). **(C)** Implanted Utah array in the motor cortex of our monkey. The picture is rotated such that the array is oriented in the same way as the maps shown in **Figures 4, 8,** and **9**. la, lateral; me, medial; ro, rostral; ca, caudal.

the target object. Illumination of the two left or right red LEDs instructed the monkey to perform a SG or a PG, respectively. Illumination of the two bottom or top LEDs instructed the monkey that pulling the object required a LF or HF, respectively.

The task was programed and controlled using LabVIEW (National Instruments Corporation, Austin, TX, USA). The trial sequence was as follows (see **Figure 1B**). The monkey had to close the switch with the hand to initiate a trial. After 400 ms, the central yellow LED was illuminated for another 400 ms, followed by the preparatory cue, illuminated for 300 ms, which instructed the monkey about the grip (PG or SG) required to perform the trial. Cue extinction was followed by a 1-s preparatory delay. At the end of this delay, the GO signal provided the remaining information about the force and also served as imperative signal instructing the monkey to release the switch to reach and grasp the object. Following object grasp, the monkey had to pull the object into a narrow position window (4–14 mm) and to hold it there for 500 ms to obtain the reward. In case of grip error, the trial was aborted and all four LEDs were flashed as a negative feed-back. The reaction time (RT) was defined as the time between the GO signal and switch release and the movement time (MT) the time between switch release and grip force onset as detected by the FSR by using a fixed threshold. The monkey was required to keep RT and MT below 700 ms to be rewarded. Five to 10 recording subsessions of about 10–15 min each were recorded per recording session, one session per day, up to five sessions per week. During each subsession, the four trial types, i.e., a combination of SG–LF, SG–HF, PG–LF, and PG–HF, were presented at random with equal probability. The monkey usually achieved a total of 100–200 successful trials/subsession.

SURGERY

When the monkey was fully trained in the task and obtained 85% of correct trials, a 100-electrode Utah array (Blackrock Microsystems, Salt Lake City, UT, USA) was surgically implanted in the motor cortex contralateral to the working hand. The array had an arrangement of 10 × 10 iridium oxide electrodes, each of them 1.5 mm long, with an inter-electrode distance of 400 μm. The surgery was performed under deep general anesthesia using full aseptic procedures. Anesthesia was induced with 10 mg/kg i.m. ketamine and maintained with 2–2.5% isoflurane in 40:60 O_2–air. To prevent cortical swelling, 2 ml/kg of mannitol i.v. was slowly injected over a period of 10 min. A 20 mm × 20 mm craniotomy was performed over the motor cortex and the dura was incised and reflected. The array was positioned on the cortical surface 3 mm anterior to the central sulcus at the level of the spur of the arcuate sulcus (**Figure 1C**). The array was inserted using a pneumatic inserter (Array Inserter, Blackrock Microsystems) and covered with a sheet of an artificial non-absorbable dura (Goretex). The real dura was sutured back and covered with a piece of an artificial absorbable dura (Seamdura, Codman). The bone flap was put back at its original position and attached to the skull by means of a 4 mm × 40 mm strip of titanium (Bioplate, Codman). The array connector was fixed to the skull on the opposite side with titanium bone screws (Bioplate, Codman). The skin was sutured back over the bone flap and around the connector. The monkey received a full course of antibiotics and analgesic before returning to the home cage.

RECORDINGS

Data were recorded using the 128-channel Cerebus acquisition system (Blackrock Microsystems, Salt Lake City, UT, USA). The signal from each active electrode (96 out of the 100 electrodes were connected) was pre-processed by a head stage with unity gain and then amplified with a gain of 5000. The signal was filtered in two different frequency bands to split into LFPs (0.3–250 Hz) and spiking activity (0.5–7.5 kHz). The LFPs were sampled at 1 kHz and saved on disk. On every channel, the experimenter set a threshold online for spike selection. All waveforms crossing the threshold were sampled at 30 kHz and snippets of 1.6 ms duration were saved for offline spike sorting. All behavioral data such as stimuli, switch release, force traces for thumb and index fingers, and object displacement were fed into the Cerebus, sampled at 1 kHz and stored for offline analysis. During the offline spike sorting (Offline Spike Sorter, version 3, Plexon Inc., Dallas,

TX, USA), spike clusters which were separated significantly from each other and with less than 1% of inter-spike intervals (ISIs) of 2 ms and less were considered as single units (single-unit activity, SUA), whereas less well separated clusters and/or more than 1% of 2 ms ISIs were considered as multi-unit (multi-unit activity, MUA) recordings.

DATA SELECTION

Data were obtained from 57 recording sessions over a period of more than 7 months. For LFP analysis, we selected 18 recording subsessions from different sessions. Three criteria guided the selection. Each selected subsession had to contain a sufficient number of trials (at least 100), it should show as few artifacts as possible and the selected subsessions should homogeneously span the entire 7 months of recording. For spike data, 11 recording subsessions were selected using the same criteria. These subsessions were different from the LFP subsessions since they were also selected to get as many (at least 80) recorded single neurons as possible per subsession.

DATA ANALYSIS

All data were analyzed using Matlab (The MatWorks Inc., Natick, MA, USA).

The timing of the behavioral events in the different tasks was calculated offline. The object touch was calculated from the first derivative of the grip force measured at the thumb (i.e., the grip force rate, GFR). In each trial, it corresponded to the time after switch release at which the GFR passed a threshold arbitrarily set to $\max_{GFR}/25$ (where $\max_{GFR}$ corresponds to the peak of GFR in the current trial). The object pull was computed from the object displacement measure and corresponded to the time at which the object entered the position window. The time difference between switch release, object touch, object pull, and reward corresponded to the RT, MT, and hold time (Hold), respectively.

Local field potential signals from each electrode and from each recording subsession were processed independently. For some subsessions, visual inspection of the data showed that in very few electrodes, the signal was corrupted by recurrent artifacts in almost all trials. These electrodes were excluded from the analysis. For each remaining electrode, the raw LFP signal was band-pass filtered in the range of 3–15 Hz (fourth order Butterworth filter). This frequency range corresponds to the main frequency band of the MRPs (Kilavik et al., 2010) excluding both the prominent beta oscillations (20–30 Hz; Kilavik et al., 2012a) and slow frequency modulations (<2 Hz) such as the contingent negative variation (CNV) occurring during an instructed delay (Walter et al., 1964; Zaepffel and Brochier, 2012). In each trial, the LFP was aligned to switch release and cut in a time window starting 500 ms before and ending 1000 ms after switch release, and then *z*-scored across all trials. At every time point in this window, the mean and standard deviation of the LFP signal was computed across all trials of each trial type. We discarded each individual trial in which the signal exceeded the mean LFP ± 2 standard deviations at any time point. This procedure was used to reject outlier trials that may be corrupted by non-physiological artifacts. Mean LFPs on each electrode exhibited a large MRP with three positive components alternating with two negative components (**Figure 2**, only −250 to 550 ms with respect to switch release are shown here). We labeled these components P1, N1, P2, N2, and P3. In some sessions, the P2 component for PG trials was divided in two distinct subcomponents. We labeled these two subcomponents P2-1 and P2-2. Each component of each trial type was analyzed separately. We first determined its absolute peak amplitude and its peak latency in relation to switch release for each electrode in each subsession in appropriate time windows covering the component. We then analyzed how the peak amplitude and latency across all subsessions varied spatially between electrodes. To do so, we used a 10 × 10 matrix to represent the cortical surface covered by the 100-electrode array. In all figures, we oriented this matrix so that the top row is parallel to the central sulcus (see **Figure 1C**), and the left upper corner represents the lateral electrodes, the left lower corner of the matrix being closer to the arcuate sulcus (toward PM), representing the rostral electrodes. The right upper and lower corners of the matrix represent the caudal and medial electrodes, respectively. We used a color code to represent the peak amplitudes of the component at each electrode location on the matrix. In **Figure 3A**, an example of peak amplitude maps can be seen, computed from SG–HF trials, in which the largest and smallest amplitudes were represented in red and blue, respectively. To represent the spatial modulation of the peak latencies (see **Figure 3B**) we used another matrix for display. On the peak latency map, earliest and latest peaks with respect to switch release were represented in red and

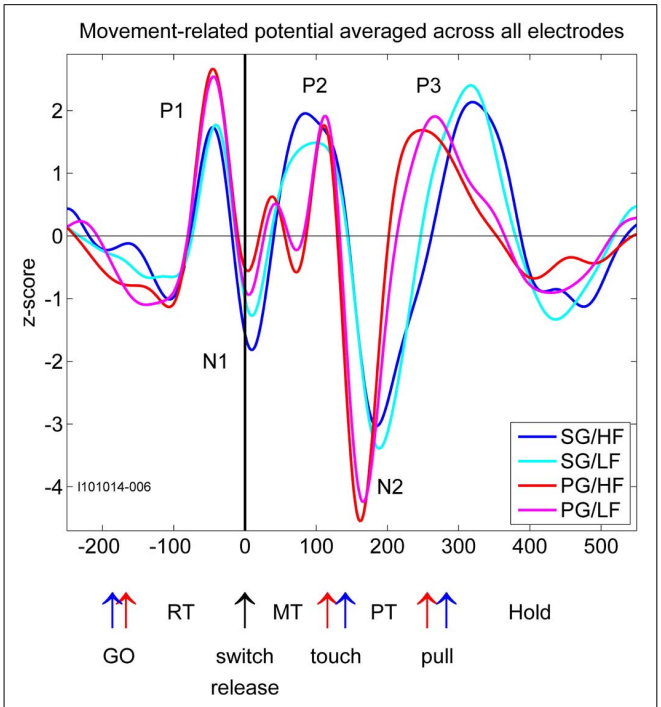

FIGURE 2 | Movement-related potentials (MRPs) of the LFP for each of the four trial types averaged across all electrodes recorded in one selected subsession. Time in millisecond around switch release (t0). SG, side grip; PG, precision grip; LF, low force; HF, high force; RT, reaction time; MT, movement time; PT, pulling time; GO, GO signal occurrence; touch, touching the object; pull, arriving in the hold window. The red and blue arrows correspond to the timing of the trial averaged events during PG and SG trials, respectively.

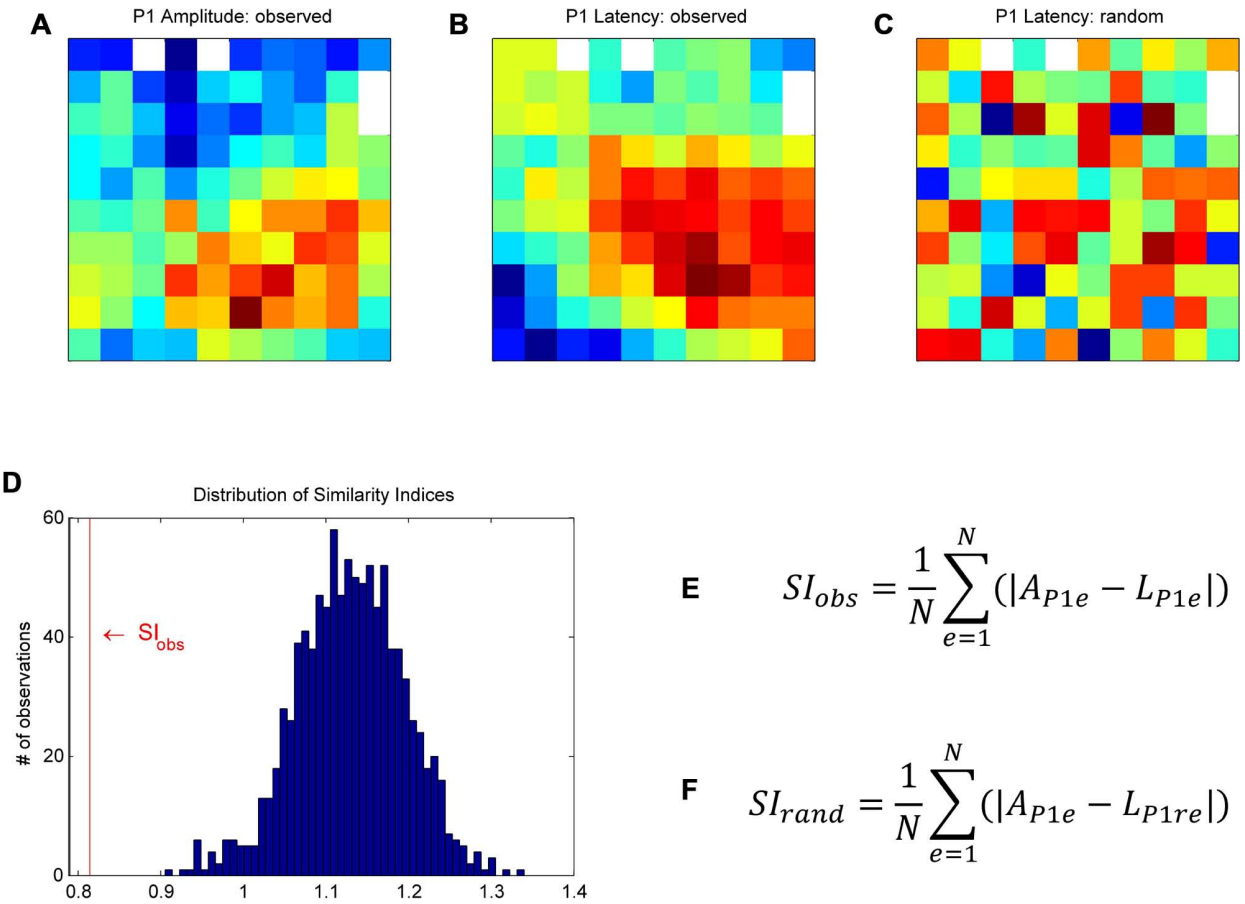

FIGURE 3 | Bootstrap procedure to assess whether the similarity between a given pair of maps could have occurred by chance (for more details, see Materials and Methods). As an example, we used the maps of the P1 peak amplitudes **(A)** and their latencies **(B)**. First, in order to homogenize the data to be compared between maps, we *z*-scored the data on each map individually. We then calculated a similarity index (SI) between the two maps of observations. At each electrode, we computed the absolute difference between the P1 amplitude and the P1 latency, and averaged these values across all electrodes to obtain the similarity index, SI_{obs} **(E)**, where A_{P1e} is the peak amplitude of the P1 component at electrode e, L_{P1e} the peak latency of the P1 at the same electrode, and *N* the number of electrodes. For the bootstrap, the P1 latency values of the original map were randomly shuffled in space to create a "random P1 latency map" **(C)**. We calculated the SI between this "random latency map" and the original P1 amplitude map, SI_{rand} **(F)**. This procedure was repeated 1000 times to build a distribution of SI_{rand} **(D)**. SI_{obs} was compared to the distribution of SI_{rand} to assess if the similarity between the two observed maps was significant.

blue, respectively. We repeated the same procedure to create an amplitude and latency map for each of the five MRP components and for each of the four trial types across all subsessions.

In each recording subsession, these maps showed that the five MRP components varied in amplitude and latency across the array. In a first analysis, we tested for each MRP component if the layout of these maps was consistent across recording subsessions. For this purpose, we compared the MRP map in each subsession to the map in all the other subsessions, one by one. For each pair of subsessions, we computed the pairwise correlation coefficient between the amplitudes of the component on each electrode in the two subsessions. We then counted the number of significant correlations ($p < 0.05$) across all possible pairs of subsessions. The same method was applied to quantify the consistency of the peak latency maps of each MRP component. The consistency across subsessions of the amplitude/latency map of a given component was considered to be significant if more than 95% of the subsession pairs showed a significant correlation (see black fields in **Figure 5**).

Since the maps were highly consistent across subsessions (see Consistency of Maps Across Sessions and **Figure 5**), the following analyses were done on peak amplitude and latency maps averaged across all 18 subsessions. We raised three different issues: Were the peak amplitude maps different for the four trial types? Did the spatial modulation of MRP peak amplitude relate to the spatial modulation of its latency? Was there any similarity between the amplitude maps of the five MRP components? To address these issues, we used a bootstrap procedure to assess whether the similarity between a given pair of maps could have occurred by chance. This procedure is described below by using, as an example, the comparison between the P1 amplitude and the P1 latency maps (see **Figure 3**). First, in order to compare two maps, we had to normalize the two data sets to obtain a similar scale. To do so, we *z*-scored the P1 peak amplitude at each electrode by the mean and

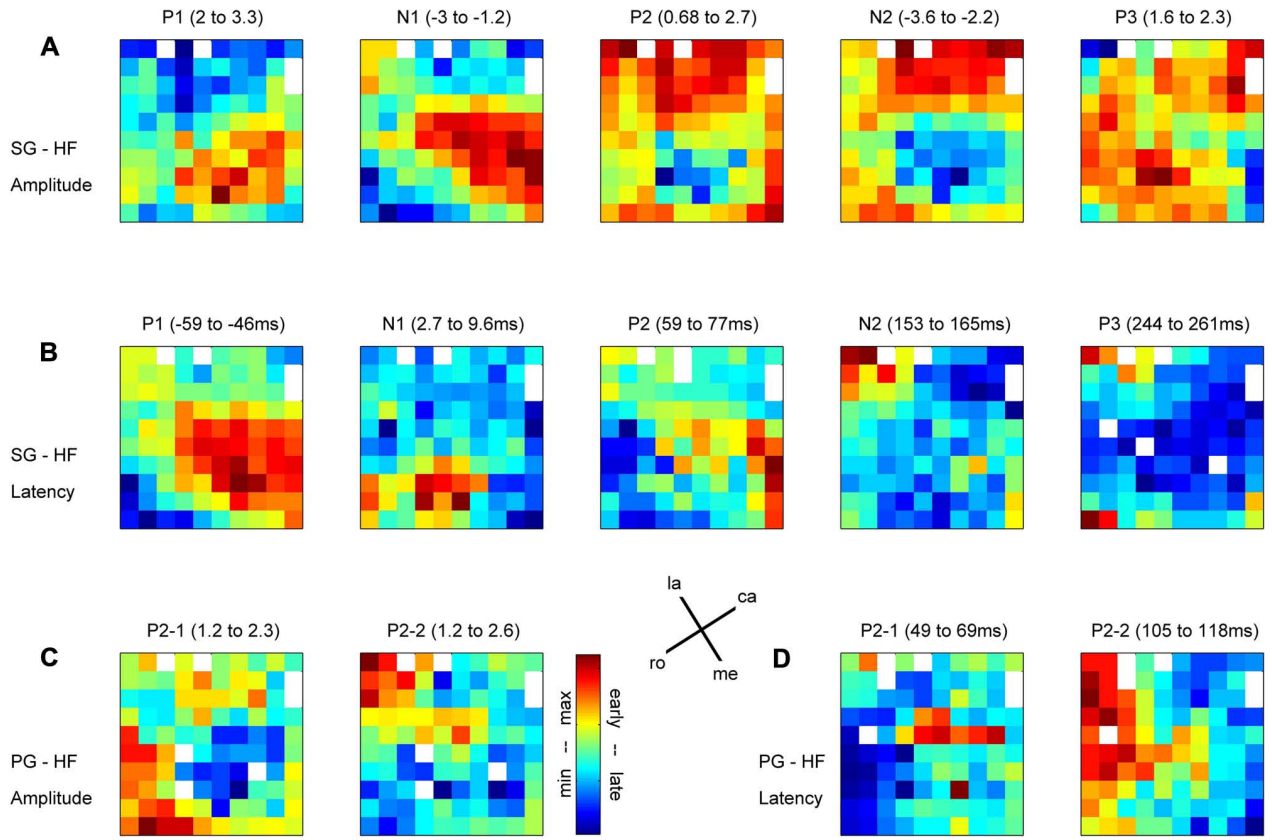

FIGURE 4 | Maps of peak amplitudes (A,C) and latencies (B,D) of the different components of the MRP averaged across all selected subsessions; *n* = 18 in (A,B); *n* = 12 in (C,D). Color code is in absolute values and adapted to each component separately. Above each map, the MRP component and the min–max values are indicated in *z*-score for the amplitudes **(A,C)** and in millisecond with respect to switch release for the latencies **(B,D)**. **(A,B)** Side grip–high force; **(C,D)** precision grip–high force. White squares are either the four inactive electrodes (see their position in A) or eliminated electrodes because of outliers. la, lateral; me, medial; ro, rostral; ca, caudal; see **Figure 1C**.

standard deviation of the P1 peak amplitudes computed across all electrodes. The same normalization was applied to the P1 peak latency map. We then calculated a similarity index (SI) between the two maps of observations. At each electrode, we computed the absolute difference between the P1 amplitude and the P1 latency, both normalized and in arbitrary units. These values were then averaged across all electrodes to obtain the SI (SI_{obs}).

$$SI_{obs} = \frac{1}{N}\sum_{e=1}^{N} |A_{ple} - L_{ple}|.$$

Where A_{P1e} is the peak amplitude of the P1 component at electrode e, L_{P1e} the peak latency of the P1 at the same electrode, and N the number of electrodes. For the bootstrap, the normalized P1 latency values of the original map were randomly shuffled in space to create a "random P1 latency map" (see **Figure 3C** for an example map). We calculated the SI between this "random latency map" and the original P1 amplitude map (SI_{rand}). This procedure was repeated 1000 times to build a distribution of SI_{rand} (see **Figure 3D**). The 25th and 975th SI_{rand} defined the upper and lower limits of the confidence interval. SI_{obs} was compared to the distribution of SI_{rand} to assess if the similarity between the two observed maps was significant. If SI_{obs} is at the lower tail of the distribution, as in **Figure 3D**, the two maps match positively, that is they significantly cover the same/similar space on the matrices. If SI_{obs} is at the upper tail of the distribution, the two maps match inversely, that is when a value is high on one map, it is rather low on the other map. The same bootstrap procedure was used to compare the peak amplitude and latency maps for the five MRP components, the peak amplitude and latency maps of each component to the peak amplitude and latency maps of the other components and the peak amplitude maps of the different trial types.

RESULTS

LOCAL FIELD POTENTIALS

Maps of peak amplitudes and latencies on the cortical surface covered by the array

In relation to our complex reach-to-grasp task, the MRP of the LFP contains five distinct components around movement onset (switch release). **Figure 2** shows an example of MRPs averaged across all electrodes of the array recorded during one recording subsession for each of the four trial types. The five components occur at specific time points during reaching and grasping: P1 occurs between

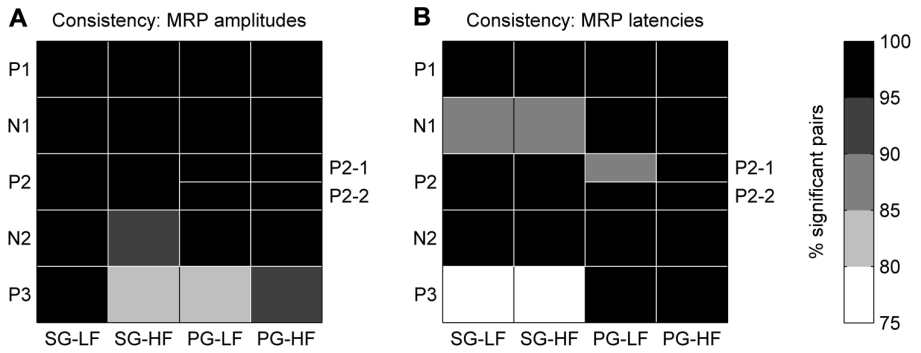

FIGURE 5 | Consistency of peak amplitude (A) and peak latency (B) maps across all selected subsessions. The gray color code corresponds to the percentage of significant data pairs for each component and behavioral condition. The black fields indicate that more than 95% ($p < 0.05$) of the pairs were statistically significant. Note, for PG the P2 component is split in two subcomponents, P2-1 and P2-2.

the GO onset and switch release, N1 around switch release, P2 between switch release and object touch, N2 during object pulling, and finally P3 during the object hold. Although this temporal sequence could suggest that each component is linked to a specific task event, we observed that the average MRPs of all five components are the largest when single trial LFPs are aligned to switch release. Therefore, all our analyses included here were done using LFPs aligned to switch release. **Figure 4** shows the peak amplitude (**Figure 4A**) and peak latency (**Figure 4B**) maps for each of the five components during SG–HF trials, averaged across the 18 selected subsessions of recording (see Materials and Methods for details). **Figures 4C,D** show the amplitude and latency maps, respectively, for the two P2 subcomponents in PG–HF trials. The spatial layout of these maps shows clear differences between the individual components. The highest amplitudes and the earliest peak latencies of P1 and N1 are localized mainly in the lower part of the maps, representing the rostral electrode positions closer to the precentral dimple (see **Figure 1C**). In contrast, the later components, P2 and N2, are largest in the upper part of the map, representing the electrode positions closer to the central sulcus. P3 has no clear localization. The two P2 subcomponents could clearly be separated in 12 out of the 18 subsessions and were analyzed separately as shown in **Figures 4C,D**. Interestingly, striking differences are observed between the map layouts of the two subcomponents. The amplitude of the first subcomponent is largest at the bottom of the map whereas the amplitude of the second subcomponent is largest at the top. The latency maps also show that for these two subcomponents, the peak occurs earlier on specific electrodes at the center and on the left border of the map for P2-1 and P2-2, respectively. In the following section, we questioned if the spatial organization of these average maps results from a systematic spatial distribution of the five LFP components in individual recording subsessions.

Consistency of maps across sessions

In order to test the consistency of the peak amplitude and latency maps from subsession to subsession, we calculated the correlation between the maps for each possible pair taken from the 18 subsessions ($n = 153$). The correlation between maps of the P2-1 and P2-2 subcomponents in PG trials could be calculated only in 12 subsessions ($n = 66$; see Maps of Peak Amplitudes and Latencies on the Cortical Surface Covered by the Array). **Figure 5A** shows that for all components but P3, the between subsession correlation of the amplitude maps is significant in more than 95% of the pairs (black fields). Also, for all components but the N1 and P3 during SG (see **Figure 5B**) the between subsession correlation of the latency maps was significant in more than 95% of the pairs. The lowest amount of significant pairs was found for the P3 latencies in SG, being nevertheless higher than 75%. In other words, the maps of both peak amplitudes and latencies were highly consistent over the 7 months of recording and, thus, we performed the following analyses on the data sets averaged across all recording subsessions.

Spatial representation of behavioral conditions

In order to test if the different behavioral parameters such as grip and force are differently represented on the motor cortical surface covered by the array, we used a bootstrap procedure with 1000 iterations (see Materials and Methods, **Figure 3**). This procedure quantifies the likelihood that the similarity between maps could have occurred by chance. Here we compared the peak amplitude maps of each component between trial types. For the P2 component in PG we chose the larger subcomponent, i.e., the P2-2. This comparison reveals that the maps for both the two grip types and the two force types are almost identical ($p < 0.001$). For that reason, we selected only HF trial types for further analyses. However, since the shapes of the MRPs related to SG and PG strongly varied (see **Figure 2**), we analyzed SG and PG separately.

Spatial relation between peak amplitude and latency

In order to determine if there is any spatial relationship between the peak amplitude and its latency for individual MRP components, we used the same bootstrap procedure as described in Section "Spatial Representation of Behavioral Conditions" with 1000 iterations (see Materials and Methods). The main result is that there is a significant ($p < 0.05$) match between amplitude and latency for the P1 component obtained for the two grip types (black squares in **Figure 6A**), meaning that the higher the P1 amplitude, the earlier it occurs. Less systematic effects are observed for the other components. The N1 component shows a significant inversed match between the amplitude and latency maps,

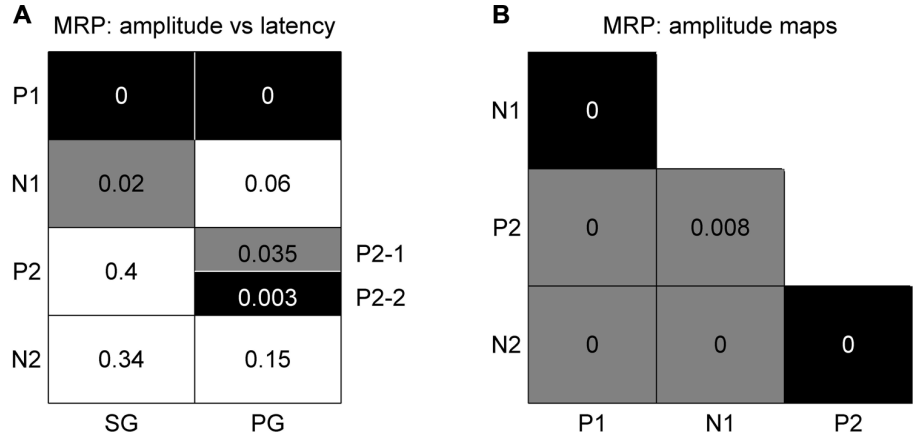

FIGURE 6 | Significance levels of comparisons between maps of MRP components for high force trial types only. Black: statistically significant ($p < 0.05$) positive match; gray: statistically significant negative match; white: not significant. The numbers correspond to the *p*-value for each combination. **(A)** Peak amplitude vs peak latency maps. **(B)** Comparison between peak amplitude maps of different components. The results for SG and PG are identical.

but only for SG trials (gray square in **Figure 6A**). This inversed match indicates that the higher the amplitude of the N1 peak, the later it occurs. The two subcomponents of the P2 in PG trials show opposite effects. The P2-2 amplitude map matches the latency map, whereas P2-1 amplitude and latency maps show a inversed match. The spatial organization of the P3 component is very poor (see **Figure 4**) and thus it is not further considered for comparison.

Different spatial representations of the individual components

We again used the same bootstrap procedure as described above to test the similarity between the amplitude maps of the different MRP components (see **Figure 6B**). A black square indicates that the maps are significantly more similar than predicted by chance, i.e., that the maps significantly match. A gray square indicates the reverse, i.e., that the maps show a significant reversed layout. This comparison shows that all combinations were statistically significant, where the two early components (P1–N1) and the two late components (P2–N2) share the same spatial representations. On the other hand, the maps of P1–P2, P1–N2, N1–N2, and N1–P2 have an opposite representation on the cortical surface. The same result was obtained for both SG and PG. As in the previous comparison, the poor spatial organization of the P3 component precludes it from further comparison.

MAPPING THE SINGLE NEURON SPIKING ACTIVITY ACROSS THE CORTICAL SURFACE

In the 11 subsessions of data selected for the analysis of the spike data (see Materials and Methods), single neuron activities were recorded from almost all electrodes, leading to 83–119 well-sorted single neurons (SUA) and 27–90 MUAs. Across these 11 recording subsessions, a total of 1058 SUAs and 809 MUAs were discriminated. The similarity of the SUAs across sessions was not systematically assessed. However, visual inspection of the spike waveforms, inter-spike-interval histograms and post-stimulus time histograms (PSTHs) in the task suggested that most of the SUAs isolated in different recording subsessions actually corresponded to different neurons. Therefore for the purpose of this study, all neurons in all subsessions were considered as independent neurons and included in the analysis. **Figure 7** shows five examples of the activity of single neurons recorded during some of the selected subsessions. Spiking data were aligned to switch release, as were the MRPs of the LFP. It can clearly be seen, that each neuron exhibits only one peak of activity, but peaks at a different moment in time around switch release. **Figure 8A** shows the numbers of neurons (SUAs and MUAs) discriminated on each electrode across the 11 subsessions which had a peak in their firing rate during a window of ±500 ms around switch release ($n = 1677$ out of the 1867 recorded neurons). These numbers appear evenly distributed across the array. Here we investigated the relationship between spiking activity and MRP modulations (**Figure 4**). More specifically, we questioned if the peak activity of single neurons could be related in space and time to the peaks of the different MRP components. We restricted this comparative analysis to the first three MRP components, P1, N1, and P2, which temporally best related to the peak occurrences of the spiking activity (**Figure 8B**). After aligning spike data in each trial to switch release (t0), we computed the mean firing rate across all trials (PSTH) with a temporal resolution of 1 ms, which was smoothed with a Gaussian filter (length 50 ms) and converted to spikes per second. We then determined for each neuron the latency of the peak firing rate with respect to switch release. **Figure 8B** presents the distribution of the peak latencies for the 1673 neurons (SUA and MUA). This distribution shows that although the peak activity of most neurons occurs after t0, an important proportion of neurons do actually peak before t0. We analyzed if the proportion of neurons peaking before and after t0 is equally distributed in space across the array. In relation to the MRPs, we selected three discrete time windows around the peak latency of the three MRP components, win1 from −200 to −10 ms (P1), win2 from −10 to 40 ms (N1), and win3 from 40 to 140 ms (P2). We then calculated the percentage of neurons

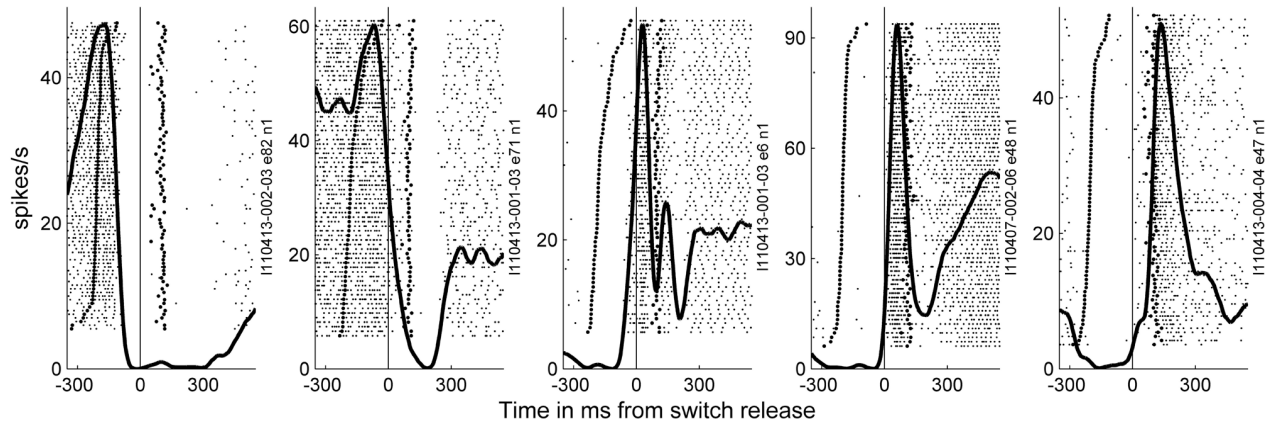

FIGURE 7 | Examples of the activity of neurons recorded during a few of the selected subsessions. Spiking data were aligned to switch release (t0) as the MRPs of the LFP. In the raster displays, each horizontal line corresponds to a trial, and each small dot to the occurrence of a spike. Trials were aligned according to increasing reaction times. In each example, the data recorded during 59–82 trials during SG–HF are shown. The first raw of large dots corresponds to the occurrence of the GO signal in each trial, and the large dots in the second raw correspond to object touch. Spiking data were averaged across all trials and represented as post-stimulus time histogram (PSTH, thick line). It can clearly be seen, that each neuron exhibits only one peak of activity, but peaks at a different moment in time around switch release.

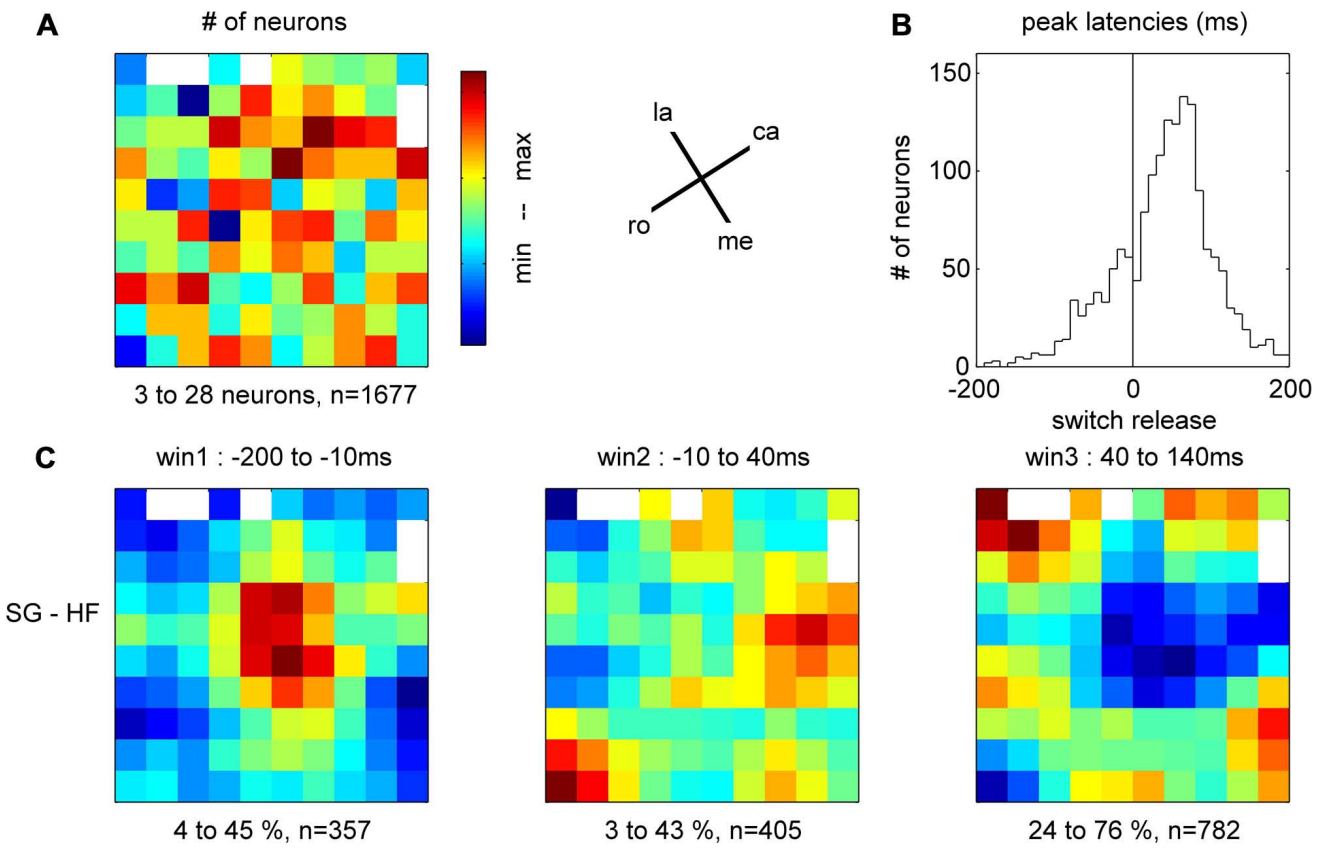

FIGURE 8 | (A) Total number of neurons recorded on each electrode during the 11 selected subsessions, peaking during ±500 ms around switch release. la, lateral; me, medial; ro, rostral; ca, caudal; see **Figure 1C**. **(B)** Peak latencies of all neurons with respect to switch release (t0). **(C)** Amount of neurons peaking during one of the three time windows corresponding to the first three components of the MRP of the LFP, expressed as percentage of neurons from all neurons peaking around switch release (± 500 ms, $n = 1677$) on each electrode. For the color code, the min (blue)–max (red) values of the percentages are indicated below each map, as well as the total number of neurons peaking during the respective window.

recorded at a given electrode peaking during a given time windows with respect to the total number of all recorded neurons peaking in relation to switch release ($n = 1677$). The result of this analysis is presented in **Figure 8C** for the three time windows. The data were smoothed over the array by averaging the values obtained on each electrode with those obtained on all directly adjacent electrodes and color coded. It can be seen that the neurons peaking during the first time window (win1) are mostly located in the center right part of the array. A reverse pattern is observed in the third time window (win3) during which most of the neurons that are peaking were recorded on the array borders.

SOMATOSENSORY PROPERTIES OF SPIKING ACTIVITY

To better characterize the functional properties of the cortical zone covered by the array, we explored the somatosensory RFs of all the recorded neurons in three sessions over three consecutive days. To do so, we applied passive movements or tactile stimulations on different parts of the left upper limb (i.e., the limb used during the task) while recording the spiking activity on all electrodes simultaneously. Each particular stimulation was tested separately. It was applied about 30 times at 0.3 Hz and synchronized with a trigger signal generated by the experimenter for offline analysis of the evoked responses. The trigger consisted of a switch operated by the experimenter's foot when applying the stimulus. We grouped the stimulations into three categories with respect to their location on the upper limb (see inset in **Figure 9A**). *Distal* stimulations were applied on different parts of the hand and fingers and included light touch of the thumb tip, of the inner side of thumb, of the index tip; of digits 2–5 tips, of the hand palm; passive thumb adduction, abduction, or flexion; passive index abduction or extension, passive digits 2–5 flexion or extension; simultaneous flexion of the thumb and index in a passive PG. *Proximo-distal* stimulations were applied to the wrist and included passive wrist flexion, pronation or ulnar deviation. *Proximal* stimulations were applied to the elbow or shoulder and included passive elbow flexion or extension and passive shoulder elevation or lowering. In each of the three recording sessions, we tested up to nine different stimulations using at least one stimulation of each category (distal, proximo-distal, and proximal). In the three sessions in which we tested the RFs, we recorded 90, 91, and 103 SUAs and 78, 79, and 69 MUAs, respectively. For each neuron (SUA and MUA), we computed a PSTH for each stimulation type separately. **Figure 9A** illustrates the responses of three simultaneously recorded neurons to the nine stimulation types used in the first recording session. The spiking activity evoked by each stimulus was analyzed in a $\pm$400 ms window around the experimenter's trigger (dashed lines). The mean spike count was computed with a temporal resolution of 1 ms across all trials ($N \sim 30$), smoothed with a Gaussian filter (length 50 ms) and converted to spikes per second. Each PSTH was then z-scored by the mean and standard deviation of the firing rate across all stimulation types. By doing so, the relative amplitude of the responses could be directly compared between neurons. Neuron 1 responds strongly to the elbow flexion, moderately to the wrist stimulation and very weakly to the distal stimulation. In contrast, the response of the second neuron is specific to wrist stimulation and the response of the third neuron to the tactile stimulation of the thumb or index finger. To quantify the response evoked by each stimulation type, we computed the difference between the minimum and the maximum value of the PSTH in the $\pm$400 ms window. The maps in **Figures 9B–D** illustrate the spatial distribution of the response amplitudes for proximal (elbow, shoulder, **Figure 9B**), proximo-distal (wrist, **Figure 9C**), and distal (hand, fingers, **Figure 9D**) stimulations, respectively. The response amplitude at each electrode is averaged across all SUAs and MUAs discriminated at this electrode location. Red and blue squares indicate strong and weak evoked responses, respectively. As in Section "Mapping the Single Neuron Spiking Activity Across the Cortical Surface," the three maps were spatially smoothed by averaging the amplitude at each electrode with the amplitudes at all directly adjacent electrodes. **Figure 9** shows a clear distinction between proximal and distal upper limb representations over the cortical surface covered by the electrode array. The neurons at the bottom of the array (medial on the cortical surface) respond much more vigorously to proximal stimulation whereas those in the top left corner (lateral on the cortical surface) are more responsive to distal stimulation. The responses to proximo-distal stimulation are more distributed over the array.

COMPARISON OF MAPS OBTAINED WITH DIFFERENT SIGNAL TYPES

In a final analysis we looked for a relationship between the MRP maps, the RF maps and the maps of peak spiking activity. We used our bootstrap procedure to compare these different maps. In summary (**Figure 10**), a significant match was observed between all combinations of (i) the representation of proximal somatosensory RFs and passive movements around elbow and shoulder (**Figure 9B**), (ii) the amplitude maps of the P1 component of the MRP (**Figure 4A**), and (iii) the map of the percentages of neurons peaking during the corresponding time window (win1 in **Figure 8C**). Furthermore, there is a close match between (i) the maps of the distal somatosensory RFs on hand and fingers (**Figure 9D**), (ii) the representation of the late component (P2) of the MRP (**Figure 4A**), and (iii) the distribution of the percentages of neurons peaking during the same time window (win3 in **Figure 8C**).

DISCUSSION

We showed that, in motor cortex, the MRPs of the LFP are characterized by complex spatio-temporal properties during the execution of reach-to-grasp movements. Although our data are only from one monkey, our results obtained over more than 7 months of recording (see Data Selection) were highly reproducible, suggesting a general finding. For each individual MRP component, the peak amplitude and its latency with respect to movement onset vary along the cortical surface following a precise structure. We observed that these spatial modulations are related to the firing properties of the single neurons recorded in the same cortical area. In addition, we also showed that the spatio-temporal properties of both the LFP and the spiking activity may be linked to the spatial organization of the somatosensory inputs to motor cortex, as estimated by RF testing.

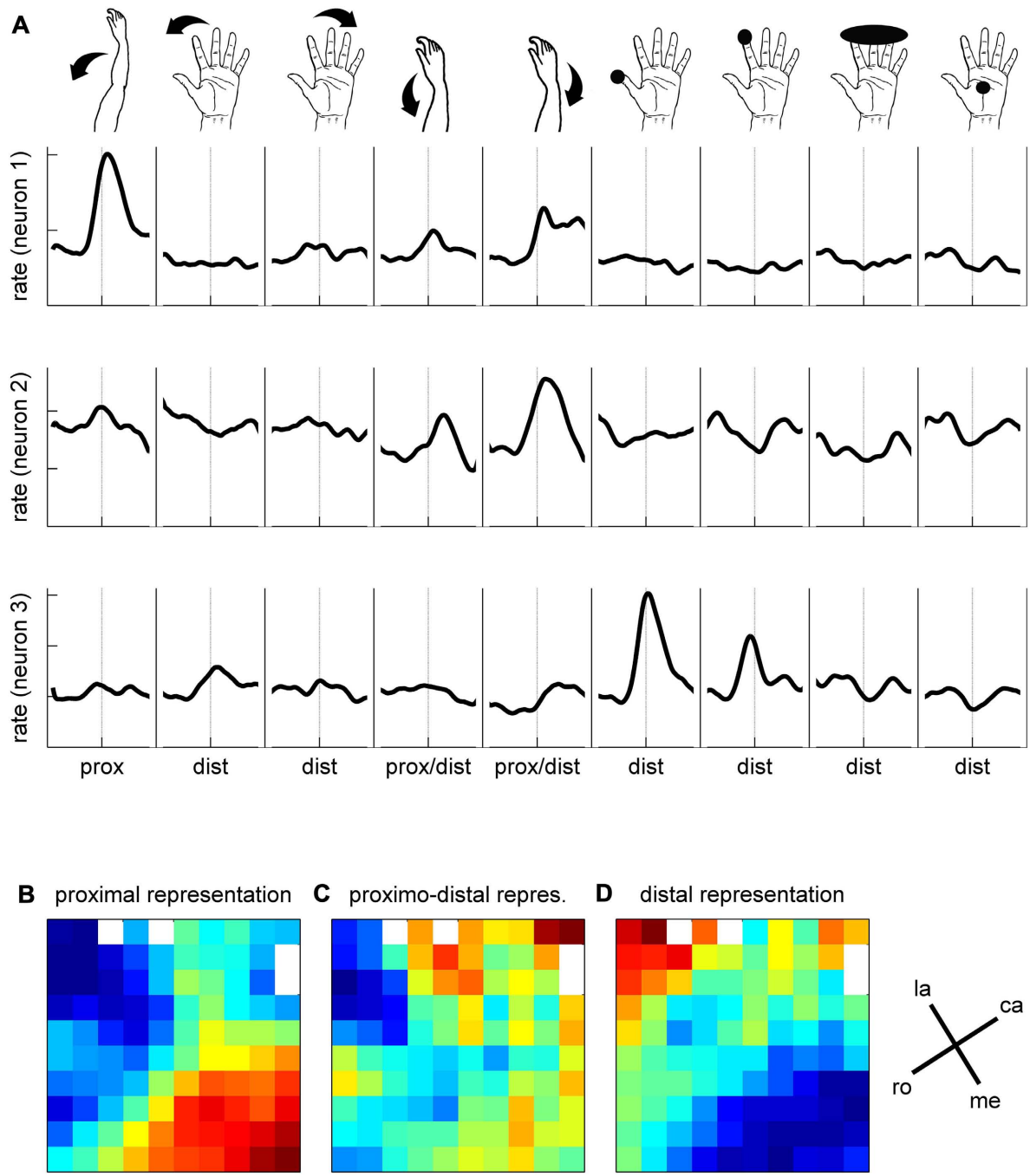

FIGURE 9 | Somatosensory properties of spiking activity.
(A) Responses of three simultaneously recorded neurons to nine stimulus conditions, as indicated by the drawings above. Mean firing rates are indicated in *z*-score, averaged across ~30 trials. For each stimulation condition, the mean firing rate is presented ±400 ms around the trigger signal (dashed lines). **(B–D)** Maps of somatosensory properties. Color code indicates min (blue) to max (red) activation, averaged across all neurons recorded during 3 days on each electrode of the array. White squares correspond to the inactive electrodes of the array. la, lateral; me, medial; ro, rostral; ca, caudal; see **Figure 1C**.

COMPLEX SPATIO-TEMPORAL PROPERTIES OF THE MRPS DURING REACH-TO-GRASP MOVEMENTS

It has previously been shown that during reaching movements, LFPs exhibit a large MRP around movement onset containing three to four clearly distinguishable components (Donchin et al., 2001; Roux et al., 2006; Kilavik et al., 2010). In the present study, we show that even five distinct components can be identified during reach-to-grasp movements. We suggest that the striking difference in the MRP structure between reaching and reach-to-grasp movements relates to their difference in complexity. When compared

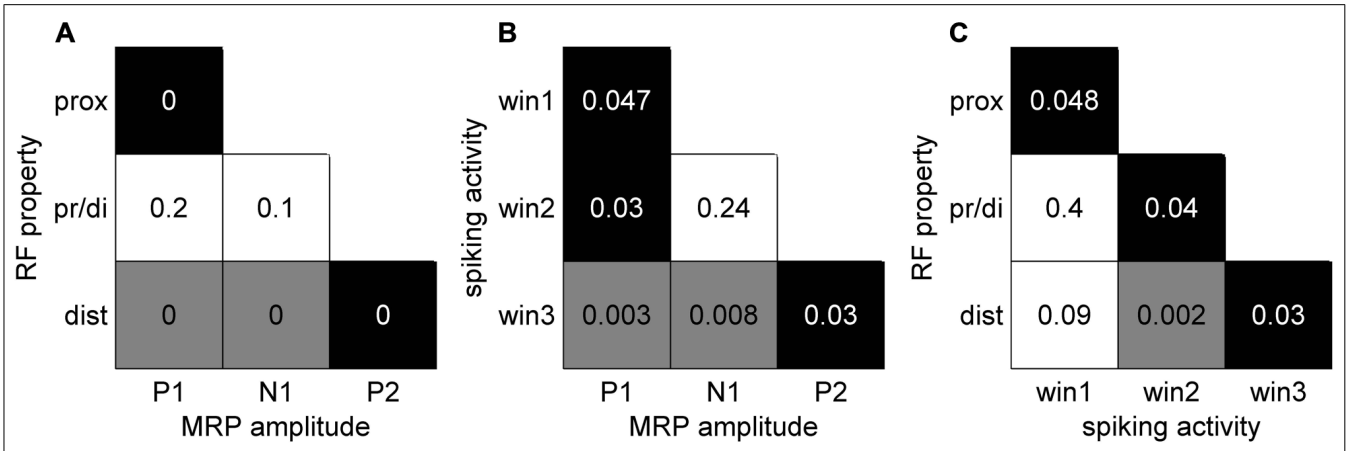

FIGURE 10 | Significance levels of comparisons between maps of different signal types of neuronal activity. Black: statistically significant ($p < 0.05$) positive map; gray: statistically significant negative map; white: not significant. The numbers correspond to the *p*-value for each combination. **(A)** MRP maps (**Figure 4**) vs RF property maps (**Figure 9**). **(B)** MRP maps vs spiking activity maps (**Figure 8**). **(C)** Spiking activity maps vs RF property maps.

to a reaching movement, reach-to-grasp movements additionally involve a tight coordination between arm and hand movements so that the hand is already preshaped when contacting the object (Jeannerod, 1984). Grasping movements also require a fine control of the contact forces for object manipulation and this control is closely dependent upon the cortical processing of somatosensory inputs from the hand and fingers (Picard and Smith, 1992; Brochier et al., 1999; Salimi et al., 1999). These additional processes activate dedicated cortical circuits projecting onto the hand area of motor cortex (Tokuno and Tanji, 1993; Dum and Strick, 2005) where they directly modulate the activity of layer V neurons during grasp (Tokuno and Nambu, 2000; Kraskov et al., 2011). In the present study, two additional observations support the assumption that the complexity of the MRP reflects the movement-related modulations of motor cortical activity. First, we showed that the spatial distribution of the peak amplitude and its latency differs between the early (P1/N1) and late components (P2/N2/P3) of the MRP (**Figures 4A,B**). This difference suggests that the processes giving rise to the early and late components are, at least in part, spatially segregated. Since the early components are systematically observed in both reaching and reach-to-grasp tasks, they are probably related to unspecific preparatory motor processes (Roux et al., 2006) or the motor control of the reaching part of upper limb movements (Gemba et al., 1981). The later components (P2/N2/P3) are more specific of reach-to-grasp movements and would reflect the activation of grasp-related local networks in M1. Second, we observed that the structure of the MRP was consistently more complex during execution of PG rather than SG trials. In particular, the P2 component could be subdivided in two subcomponents with distinct topographies (**Figures 4C,D**). Previous work in human and non-human primates indicate that PG is characterized by a greater level of complexity and is more demanding in terms of neural control (Ehrsson et al., 2000; Begliomini et al., 2007). Grasping an object between the tip of the thumb and the index finger leads to more instability than grasping an object with a whole hand grip and requires additional sensorimotor control mechanisms (Johansson, 1996). In line with this idea, the subdivision of the P2 component occurs right before the object touch (**Figure 2**) and may indicate the activation of specific processes for the control of a PG.

SPATIO-TEMPORAL RELATIONSHIP BETWEEN SPIKING ACTIVITY AND MRP COMPONENTS

Previous works suggest that during LFP oscillations, spiking activity increases during the negative peaks of the LFP, indicating that LFP reflects the synchronization of excitatory inputs to the neurons around the electrode tip (Baker et al., 1997; Destexhe et al., 1999; Denker et al., 2011). Following this hypothesis, the motor command originating from layer V in the motor cortex should produce a sustained negativity in the recordings. However, to our knowledge, there is no evidence that the relationship between spike rate and LFP negativity holds for the MRPs (see Discussion in Roux et al., 2006). We observe that the MRP presents a robust alternation of positive and negative peaks throughout movement execution. **Figure 8B** shows that a majority of the recorded neurons are maximally active between 40 and 140 ms after switch release, in close temporal relationship with the P2 component of the MRP (**Figure 4**). Many fewer neurons are showing a peak of activity later than 140 ms after switch release, when the large N2 component of the MRP is observed. Although we did not assess the direct temporal coupling between spike and LFP, our observations suggest a non-systematic relationship between LFPs and firing rate during movement execution. In particular, the comparison of LFP and spiking data shows that the MRP expresses at least five distinct components (see **Figure 2**), whereas neurons tend to present a single peak of spiking activity around movement onset (see **Figure 7**).

RELATION TO PROXIMAL–DISTAL REPRESENTATIONS

In agreement with earlier studies (Rosén and Asanuma, 1972; Lemon, 1981), we observed that a large proportion of motor cortical neurons were responsive to passive stimulation of the upper limb. RF testing with the 100-electrode Utah array presented two additional advantages. First, the RFs were tested simultaneously on

all electrodes, making thus sure that the same mechanical stimuli were used for all neurons. Second, we could directly reconstruct the spatial distribution of the RFs at all electrode locations and compare the RF maps for distal and proximal stimuli. Using this approach, we demonstrated that the proximal and distal parts of the upper limb were preferentially represented toward the medial and lateral sides of the array, respectively. This spatial organization is reminiscent of motor cortical maps obtained by ICMS in which a representation of the hand and fingers close to the central sulcus is surrounded by a representation of the arm toward the arcuate sulcus (Kwan et al., 1978; Park et al., 2001). Although ICMS effects were not tested in the current experiment, the comparison between our RF maps and ICMS maps in earlier studies confirm a close match between the afferent input and motor maps in the motor cortex (Rosén and Asanuma, 1972; Lemon, 1981).

Furthermore, we analyzed how this spatial organization of the motor cortex is modulated during complex reach-to-grasp movements. Our results show a clear shift of neural activity from medial to lateral motor cortex during the course of the movement that is revealed both in the MRP and in single neuron firing rates. This shift of activity occurs between the N1 and P2 components of the MRP and between the corresponding temporal windows for the peak spiking activity. In terms of behavior, these temporal windows correspond to the MT between movement onset and object touch (Jeannerod, 1984). Importantly, the spatio-temporal structure of the MRPs and spiking activities closely match the spatial distribution of the RFs. During the early part of the movement (corresponding to the P1 and N1 components of the MRP), the neural activity predominates in the areas receiving somatosensory input from the arm, whereas during the later parts (corresponding the P2, N2, and P3 components), the activity shifts to the hand-related areas. These observations suggest that the underlying organization of motor cortex in terms of body representation strongly influences the modulation of neuronal activity during movement execution. It is, however, important to stress that these spatial modulations are only relative, so that the lateral motor cortex is not entirely silent when the medial part is active and vice-versa. For instance in the MRP, we observed a clear P1 component on all the electrodes, but this component was substantially larger toward the medial electrodes. This indicates that the whole motor cortex covered by the array is activated during the task and that the global pattern of activity is locally modulated in relation to the functional requirements of the different parts of the task. Such organization would be adapted to enable the tight coupling between proximal and distal upper limb segments during reach-to-grasp movements (Wing et al., 1986; Jakobson and Goodale, 1991; Chieffi and Gentilucci, 1993).

It has been proposed that proximo-distal coupling for upper limb movements may be mediated by traveling waves of LFP beta oscillations across the surface of the motor cortex (data filtered at 10–45 Hz in Rubino et al., 2006; Hatsopoulos et al., 2011; Takahashi et al., 2011). In these studies, oscillations were analyzed both in the delay period preceding the movement and during movement execution itself, a period in which beta oscillations are known to be almost suppressed (Kilavik et al., 2012a,b). An attractive hypothesis would be that the transfer of information during movement execution is also mediated by traveling waves in the low frequency range of the MRP (3–15 Hz). This hypothesis would predict that the latency of each MRP component should vary along a given trajectory across the array, but that the amplitude of the peak at these different latencies should remain constant. We observed instead that the MRP peaks varied in amplitude in direct relationship with the peak latency, i.e., the smaller the peak, the later the latency. This correlation rather suggests that each MRP component derives from a local source and that the peak at a remote electrode from the source occurs later and is of smaller amplitude. However, more detailed analyses will be required to confirm this hypothesis.

Altogether, our results show a clear spatio-temporal structure of the MRP and spiking activities over the motor cortex that relates to the proximo-distal organization of this cortical area. This organization would provide the essential substrate for the control of complex reach-to-grasp movements involving the coordination of multiple segments of the upper limb. However, it is likely that other properties of the recorded area are also contributing to the spatio-temporal representation of the neuronal activity. In particular, since our electrode array was implanted over M1 and PMd (see **Figure 1C**), area-specific activity modulations may also come into play. But this issue cannot be directly addressed, since our data do not allow a clear distinction between these two areas.

ACKNOWLEDGMENTS

The authors thank William A. MacKay for critically reading the manuscript, Ivan Balansard for surgical help, Marc Martin for animal care, and Joel Baurberg, Alain De Moya, and Xavier Degiovanni for technical assistance. This work was partly supported by Helmholtz Alliance on Systems Biology, European Union (FP7-ICT-2009-6, BrainScales), Collaborative Research Agreement Riken-CNRS, ANR GRASP, CNRS (PEPS, Neuro_IC2010) and DAAD.

REFERENCES

Arieli, A., Shoham, D., Hildesheim, R., and Grinvald, A. (1995). Coherent spatiotemporal patterns of ongoing activity revealed by real-time optical imaging coupled with single-unit recording in the cat visual cortex. *J. Neurophysiol.* 73, 2072–2093.

Asanuma, H., and Rosén, I. (1972). Topographical organization of cortical efferent zones projecting to distal forelimb muscles in the monkey. *Exp. Brain Res.* 14, 243–256.

Baker, S. N., Olivier, E., and Lemon, R. N. (1997). Coherent oscillations in monkey motor cortex and hand muscle EMG show task-dependent modulation. *J. Physiol.* 501.1, 225–241.

Bansal, A. K., Truccolo, W., Vargas-Irwin, C. E., and Donoghue, J. P. (2012). Decoding 3D reach and grasp from hybrid signals in motor and premotor cortices: spikes, multiunit activity, and local field potentials. *J. Neurophysiol.* 107, 1337–1355.

Begliomini, C., Wall, M. B., Smith, A. T., and Castiello, U. (2007). Differential cortical activity for precision and whole-hand visually guided grasping in humans. *Eur. J. Neurosci.* 25, 1245–1252.

Boudrias, M. H., McPherson, R. L., Frost, S. B., and Cheney, P. D. (2010). Output properties and organization of the forelimb representation of motor areas on the lateral aspect of the hemisphere in rhesus macaques. *Cereb. Cortex* 20, 169–186.

Brochier, T., Boudreau, M. J., Paré, M., and Smith, A. M. (1999). The effects of muscimol inactivation of small regions of motor and somatosensory cortex on independent finger movements and force control in the precision grip. *Exp. Brain Res.* 128, 31–40.

Brochier, T., and Riehle, A. (2011). Monkey primary motor cortex activity for anticipatory and feed-back

force control during grasp. *Soc. Neurosci. Abstr.* 2011, 591.12.

Brochier, T., Spinks, R. L., Umilta, M. A., and Lemon, R. N. (2004). Patterns of muscle activity underlying object-specific grasp by the macaque monkey. *J. Neurophysiol.* 92, 1770–1782.

Chieffi, S., and Gentilucci, M. (1993). Coordination between the transport and the grasp components during prehension movements. *Exp. Brain Res.* 94, 471–477.

Denker, M., Roux, S., Lindén, H., Diesmann, M., Riehle, A., and Grün, S. (2011). The local field potential reflects surplus spike synchrony. *Cereb. Cortex* 21, 2681–2695.

Destexhe, A., Contreras, D., and Steriade, M. (1999). Spatiotemporal analysis of local field potentials and unit discharges in cat cerebral cortex during natural wake and sleep phases. *J. Neurosci.* 19, 4595–4608.

Donchin, O., Gribova, A., Steinberg, O., Bergman, H., Cardoso de Oliveira, S., and Vaadia, E. (2001). Local field potentials related to bimanual movements in the primary and supplementary motor cortices. *Exp. Brain Res.* 140, 46–55.

Dum, R. P., and Strick, P. L. (2005). "Motor areas in the frontal lobe: the anatomical substrate for the central control of movement," in *Motor Cortex in Voluntary Movements: A Distributed System for Distributed Functions*, eds A. Riehle and E. Vaadia (Boca Raton, FL: CRC Press), 3–47.

Ehrsson, H. H., Fagergren, A., Jonsson, T., Westling, G., Johansson, R. S., and Forssberg, H. (2000). Cortical activity in precision- versus power-grip tasks: an fMRI study. *J. Neurophysiol.* 83, 528–536.

Evarts, E. V. (1964). Temporal patterns of discharge of pyramidal tract neurons during sleep and waking in the monkey. *J. Neurophysiol.* 27, 152–171.

Evarts, E. V. (1966). Pyramidal tract activity associated with a conditioned hand movement in the monkey. *J. Neurophysiol.* 29, 1011–1027.

Fritsch, G., and Hitzig, E. (1870). Über die elektrische Erregbarkeit des Grosshirns. *Arch. Anat. Physiol. Wissen. Med.* 37, 300–332.

Gemba, H., Hashimoto, S., and Sasaki, K. (1981). Cortical field potentials preceding visually initiated hand movements in the monkey. *Exp. Brain Res.* 42, 435–441.

Hatsopoulos, N. G., Olmedo, L., and Takahashi, K. (2011). "Proximal-to-distal sequencing behavior and motor cortex," in *Motor Control: Theories, Experiments, and Applications*, eds F. Danion and M. L. Latash (New York: Oxford University Press), 159–176.

Humphrey, D. R. (1986). Representations of movements and muscles within the primate precentral motor cortex: historical and current perspectives. *Fed. Proc.* 45, 2687–2699.

Jakobson, L. S., and Goodale, M. A. (1991). Factors affecting higher-order movement planning: a kinematic analysis of human prehension. *Exp. Brain Res.* 86, 199–208.

Jeannerod, M. (1984). The timing of natural prehension movements. *J. Mot. Behav.* 16, 235–254.

Jeannerod, M., Arbib, M. A., Rizzolatti, G., and Sakata, H. (1995). Grasping objects: the cortical mechanisms of visuomotor transformation. *Trends Neurosci.* 18, 314–320.

Johansson, R. S. (1996). "Sensory control of dexterous manipulation in humans," in *Hand and Brain*, eds A. M. Wing, P. Haggard, and J. R. Flanagan. (New York: Academic), 381–414.

Kilavik, B. E., Confais, J., Ponce-Alvarez, A., Diesmann, M., and Riehle, A. (2010). Evoked potentials in motor cortical local field potentials reflect task timing and behavioral performance. *J. Neurophysiol.* 104, 2338–2351

Kilavik, B. E., Ponce-Alvarez, A., Trachel, R., Confais, J., Takerkart, S., and Riehle, A. (2012a). Context-related frequency modulations of macaque motor cortical LFP beta oscillations. *Cereb. Cortex* 22, 2148–2159.

Kilavik, B. E., Zaepffel, M., Brovelli, A., MacKay, W. A., and Riehle, A. (2012b). The ups and downs of beta oscillations in sensorimotor cortex. *Exp. Neurol.* doi: 10.1016/j.expneurol.2012.09.014 [Epub ahead of print].

Kraskov, A., Prabhu, G., Quallo, M. M., Lemon, R. N., and Brochier, T. (2011). Ventral premotor – motor cortex interactions in the macaque monkey during grasp: response of single neurons to intracortical microstimulation. *J. Neurosci.* 31, 8812–8821.

Kwan, H. C., MacKay, W. A., Murphy, J. T., and Wong, Y. C. (1978). Spatial organization of precentral cortex in awake primates. II. Motor outputs. *J. Neurophysiol.* 41, 1120–1131.

Lemon, R. N. (1981). Functional properties of monkey motor cortex neurones receiving afferent input from the hand and fingers. *J. Physiol.* 311, 497–519.

Mitzdorf, U. (1985). Current source-density method and application in cat cerebral cortex: investigation of evoked potentials and EEG phenomena. *Physiol. Rev.* 65, 37–100.

Okun, M., Naim, A., and Lampl, I. (2010). The subthreshold relation between cortical local field potential and neuronal firing unveiled by intracellular recordings in awake rats. *J. Neurosci.* 30, 4440–4448.

Park, M. C., Belhaj-Saif, A., and Cheney, P. D. (2004). Properties of primary motor cortex output to forelimb muscles in rhesus monkeys. *J. Neurophysiol.* 92, 2968–2984.

Park, M. C., Belhaj-Saif, A., Gordon, M., and Cheney, P. D. (2001). Consistent features in the forelimb representation of primary motor cortex in rhesus monkeys. *J. Neurosci.* 21, 2784–2792.

Picard, N., and Smith, A. M. (1992). Primary motor cortical activity related to the weight and texture of grasped objects in the monkey. *J. Neurophysiol.* 68, 1867–1881.

Poulet, J. F. A., and Petersen, C. C. H. (2008). Internal brain state regulates membrane potential synchrony in barrel cortex of behaving mice. *Nature* 454, 881–885.

Raos, V., Franchi, G., Gallese, V., and Fogassi, L. (2003). Somatotopic organization of the lateral part of area F2 (dorsal premotor cortex) of the macaque monkey. *J. Neurophysiol.* 89, 1503–1518.

Riehle, A., and Brochier, T. (2012). "Mapping the spatio-temporal structure of motor cortical LFP and spiking activity during reach and grasp movements," in *22nd Annual Meeting of NCM*, Venice.

Rosén, I., and Asanuma, H. (1972). Peripheral afferent inputs to the forelimb area of the monkey motor cortex: input–output relations. *Exp. Brain Res.* 14, 257–273.

Roux, S., MacKay, W. A., and Riehle, A. (2006). The pre-movement component of motor cortical local field potentials reflects the level of expectancy. *Behav. Brain Res.* 169, 335–351.

Rubino, D., Robbins, K. A., and Hatsopoulos, N. G. (2006). Propagating waves mediate information transfer in the motor cortex. *Nat. Neurosci.* 12, 1549–1557.

Salimi, I., Brochier, T., and Smith, A. M. (1999). Neuronal activity in somatosensory cortex of monkeys using a precision grip. I. Receptive fields and discharge patterns. *J. Neurophysiol.* 81, 825–834.

Schieber, M. H. (2001). Constraints on somatotopic organization in the primary motor cortex. *J. Neurophysiol.* 86, 2125–2143.

Schieber, M. H., and Hibbert, L. S. (1993). How somatotopic is the motor cortex hand area? *Science* 261, 489–492.

Stark, E., Asher, I., and Abeles, M. (2007). Encoding of reach and grasp by single neurons in premotor cortex is independent of recording site. *J. Neurophysiol.* 97, 3351–3364.

Takahashi, K., Saleh, M., Penn, R. D., and Hatsopoulos, N. G. (2011). Propagating waves in human motor cortex. *Front. Hum. Neurosci.* 5:40. doi: 10.3389/fnhum.2011.00040

Tokuno, H., and Nambu, A. (2000). Organization of nonprimary motor cortical inputs on pyramidal and nonpyramidal tract neurons of primary motor cortex: an electrophysiological study in the macaque monkey. *Cereb. Cortex* 10, 58–68.

Tokuno, H., and Tanji, J. (1993). Input organization of distal and proximal forelimb areas in the monkey primary motor cortex: a retrograde double labeling study. *J. Comp. Neurol.* 333, 199–209.

Umilta, M. A., Brochier, T., Spinks, R. L., and Lemon, R. N. (2007). Simultaneous recording of macaque premotor and primary motor cortex neuronal populations reveals different functional contributions to visuomotor grasp. *J. Neurophysiol.* 98, 488–507.

Vargas-Irwin, C. E., Shakhnarovich, G., Yadollahpour, P., Mislow, J. M. K., Black, M. J., and Donoghue, J. P. (2010). Decoding complete reach and grasp actions from local primary motor cortex populations. *J. Neurosci.* 30, 9659–9669.

Walter, W. G., Cooper, R., Aldridge, V. J., McCallum, W. C., and Winter, A. L. (1964). Contingent negative variation: an electric sign of sensorimotor association and expectancy in the human brain. *Nature* 203, 380–384.

Wing, A. M., Turton, A., and Fraser, C. (1986). Grasp size and accuracy of approach in reaching. *J. Mot. Behav.* 18, 245–260.

Woolsey, C. N., Settlage, P. H., Meyer, D. R., Sencer, W., Pinto-Hamuy, T., and Travis, A. M. (1952). Patterns of localization in precentral and "supplementary" motor areas and their relation to the concept of premotor area. *Res. Publ. Assoc. Res. Nerv. Ment. Dis.* 30, 238–264.

Zaepffel, M., and Brochier, T. (2012). Planning of visually guided reach-to-grasp movements: inference from reaction time and contingent negative variation (CNV). *Psychophysiology* 49, 17–30.

Conflict of Interest Statement: The authors declare that the research was conducted in the absence of any commercial or financial relationships that could be construed as a potential conflict of interest.

Received: 12 December 2012; paper pending published: 21 January 2013; accepted: 06 March 2013; published online: 27 March 2013.
Citation: Riehle A, Wirtssohn S, Grün S and Brochier T (2013) Mapping the spatio-temporal structure of motor cortical LFP and spiking activities during reach-to-grasp movements. Front. Neural Circuits **7***:48. doi: 10.3389/fncir.2013.00048*

frontiers in
NEURAL CIRCUITS

ORIGINAL RESEARCH ARTICLE
published: 01 March 2013
doi: 10.3389/fncir.2013.00033

Cortical output to fast and slow muscles of the ankle in the rhesus macaque

Heather M. Hudson†, Darcy M. Griffin†, Abderraouf Belhaj-Saïf and Paul D. Cheney*

Department of Molecular and Integrative Physiology, University of Kansas Medical Center, Kansas City, KS, USA

Edited by:
Nicholas Hatsopoulos, University of Chicago, USA

Reviewed by:
C. J. Heckman, Northwestern University, USA
Lee E. Miller, Northwestern University, USA

***Correspondence:**
Paul D. Cheney, Department of Molecular and Integrative Physiology, University of Kansas Medical Center, G011 Wahl Hall East, 3901 Rainbow Blvd., Kansas City, KS 66160, USA.
e-mail: pcheney@kumc.edu

†Present address:
Heather M. Hudson Department of Neurology, University of Minnesota, 2001 6th St. SE, LRB 419, Minneapolis, MN 55455, USA.
Darcy M. Griffin, Systems Neuroscience Institute, University of Pittsburgh School of Medicine, 3501 Fifth Ave., BST3 4074, Pittsburgh, PA 15260, USA.

The cortical control of fast and slow muscles of the ankle has been the subject of numerous reports yielding conflicting results. Although it is generally agreed that cortical stimulation yields short latency facilitation of fast muscles, the effects on the slow muscle, soleus, remain controversial. Some studies have shown predominant facilitation of soleus from the cortex while others have provided evidence of differential control in which soleus is predominantly inhibited from the cortex. The objective of this study was to investigate the cortical control of fast and slow muscles of the ankle using stimulus triggered averaging (StTA) of EMG activity, which is a sensitive method of detecting output effects on muscle activity. This method also has relatively high spatial resolution and can be applied in awake, behaving subjects. Two rhesus macaques were trained to perform a hindlimb push-pull task. Stimulus triggered averages (StTAs) of EMG activity (15, 30, and 60 μA at 15 Hz) were computed for four muscles of the ankle [tibialis anterior (TA), medial gastrocnemius (MG), lateral gastrocnemius (LG), and soleus] as the monkeys performed the task. Poststimulus facilitation (PStF) was observed in both the fast muscles (TA, MG, and LG) as well as the slow muscle (soleus) and was as common and as strong in soleus as in the fast muscles. However, while poststimulus suppression (PStS) was observed in all muscles, it was more common in the slow muscle compared to the fast muscles and was as common as facilitation at low stimulus intensities. Overall, our results demonstrate that cortical facilitation of soleus has an organization that is very similar to that of the fast ankle muscles. However, cortical inhibition is organized differently allowing for more prominent suppression of soleus motoneurons.

Keywords: soleus, tibialis anterior, cortical facilitation, EMG, stimulus triggered averaging

INTRODUCTION

The existence of fast and slow motor units is well known (Eccles et al., 1958; Andersen and Sears, 1964; Kugelberg and Edstrom, 1968; Ranvier, 1874; Kronecker and Stirling, 1878). The ankle muscles have been a particular focus of many studies investigating the distribution, metabolism, and physiology of fast and slow motor units. This work has established that the soleus muscle consists exclusively of slow motor units while tibialis anterior (TA), an ankle flexor, consists largely of fast motor units. MG and LG are mixed but with a predominance of fast motor units (Burke, 1967; Burke et al., 1970, 1971; Burke and Tsairis, 1974). The hypothesis of differential cortical control of these exclusively or predominantly fast and slow muscles has been the subject of numerous studies in cats, primates and humans yielding conflicting results.

Monosynaptic linkages have been established between corticospinal neurons and hindlimb motoneurons in primates (Preston and Whitlock, 1963; Muir and Porter, 1973; Shapovalov and Kurchavyi, 1974; Jankowska et al., 1975; Asanuma et al., 1979; Edgley et al., 1997). Preston and Whitlock (1963) and Uemura and Preston (1965), studying monosynaptic reflex conditioning in the "pyramidal" monkey preparation, in which the brainstem is destroyed leaving only the pyramidal tract intact, reported corticospinal output to soleus motoneurons was predominantly inhibitory while output to motoneurons of fast muscles (gastrocnemius and TA) was excitatory. Jankowska et al. (1975) reported EPSPs in soleus, but found the EPSPs in soleus and gastrocnemius were half the size of EPSPs in TA in the monkey. Kawai (1982), in the "pyramidal" cat preparation, demonstrated largely excitatory postsynaptic potentials (EPSPs) to fast motoneurons and inhibitory postsynaptic potentials (IPSPs) to slow motoneurons. Also in the cat, Binder et al. (1998) measured effective synaptic currents in fast and slow motoneurons of triceps surae associated with stimulating the contralateral pyramidal tract. They reported that more than 60% of putative slow motoneurons received a net hyperpolarizing effective synaptic current from pyramidal tract stimulation compared to only 33% of fast motoneurons. Consistent with this result, they also found that pyramidal tract stimulation increased the discharge rate of motoneurons receiving depolarizing effective currents while decreasing the rate of those receiving hyperpolarizing currents.

Transcranial magnetic stimulation (TMS) and transcranial electrical stimulation (TES) have been used in numerous human subject studies yielding varied results. TMS of motor cortex in humans consistently reveals a clear, short latency facilitation of the ankle flexor, TA (Brouwer and Ashby, 1990, 1992; Valls-Solé et al., 1994; Brouwer and Qiao, 1995; Ertekin et al., 1995; Goulart

and Valls-Solé, 2001; Bawa et al., 2002; Geertsen et al., 2010). However, the results for the slow ankle extensor, soleus, have been more varied. Several studies have reported either non-existent or weak facilitation of soleus from TMS or electrical stimulation of the cortex (Cowan et al., 1986; Ashby and Advani, 1990; Brouwer and Ashby, 1990, 1992; Brouwer and Qiao, 1995), while other studies have shown that TMS does yield short latency facilitation of soleus (Valls-Solé et al., 1994; Goulart and Valls-Solé, 2001; Bawa et al., 2002; Geertsen et al., 2010).

Despite numerous studies in animals and humans, the cortical control of fast and slow muscles of the ankle remains controversial. The goal of this study was to investigate the cortical control of fast and slow muscles of the ankle in the rhesus macaque using stimulus triggered averaging (StTA) of EMG activity recorded from TA, MG, LG, and soleus (SOL) muscles during a hindlimb push-pull task. StTAing of EMG activity is a potentially more sensitive and higher resolution approach to delineating cortical motor output effects on muscle activity than the methods applied in previous studies. Also, unlike intracellular recording, it can be applied in awake, behaviorally active subjects thus avoiding the complicating effects of anesthesia or central lesions used with intracellular recording studies.

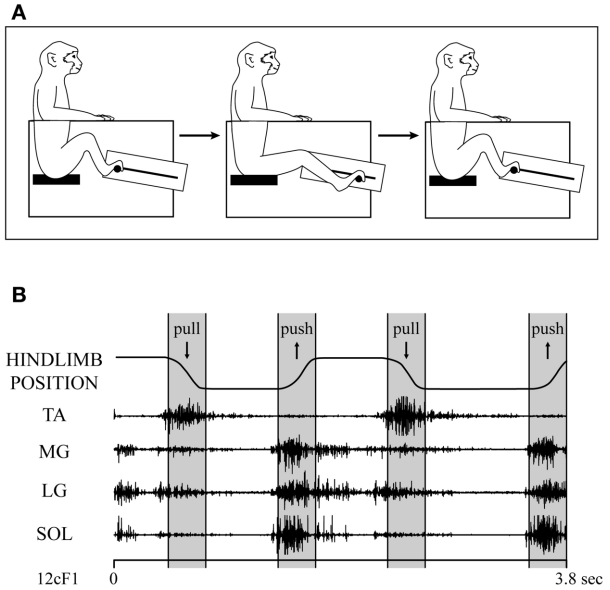

FIGURE 1 | (A) Hindlimb push-pull task. The monkey is seated in a custom-built primate chair with both arms and the left leg restrained. The monkey gripped the push-pull device's manipulandum (horizontal post) with the right foot and pushed it to a target zone. After a hold period of 500 ms in the target zone, the monkey pulled the manipulandum to a second target zone and held for 500 ms. Upon successful completion of each push-pull trial, the monkey was given an applesauce reward. The behavioral task was guided by visual and auditory cues. **(B)** EMG records of ankle muscles during two cycles of the hindlimb push-pull task. TA, tibialis anterior; MG, medial gastrocnemius; LG, lateral gastrocnemius; SOL, soleus. Figure adapted from Hudson et al. (2010).

MATERIALS AND METHODS

BEHAVIORAL TASK

Data were collected from the left primary motor cortex (M1) of two male rhesus macaques (*Macaca mulatta*, ∼10 kg, 6–7 years old). The monkeys were trained to perform a hindlimb push-pull task (**Figure 1A**) engaging both proximal and distal muscles in reliable and stereotyped patterns of activation (Hudson et al., 2010). Seated in a custom primate chair within a sound-attenuating chamber, both arms and the left leg were restrained. With the right foot, the monkey gripped the manipulandum (horizontal post) and extended the leg until the target zone was achieved. After a hold period of 500 ms in the target zone, the monkey flexed the leg pulling the manipulandum to a second target zone. Following a second hold period of 500 ms, the monkey was given an applesauce reward. The behavioral task was guided by visual and auditory cues.

MRI

The monkey's head was placed in an MRI-compatible stereotaxic apparatus and structural MRIs in the sagittal, coronal and horizontal planes were obtained using a Siemens Allegra 3T system. A 3-dimensional reconstruction of each monkey's brain was produced using CARET software (Computerized Anatomical Reconstruction and Editing Tool Kit). This enabled highly accurate targeting of the hindlimb representation of M1 for the cortical chamber implant.

SURGICAL PROCEDURES

Upon completion of training, each monkey was implanted with a titanium cortical recording chamber (30 mm inside diameter) centered at anterior 13.5 mm, lateral 0 mm and 0° angle to the midsagittal plane (Paxinos et al., 2000), targeting the hindlimb representation of M1. In a second surgery, pairs of insulated, multi-stranded stainless steel wire (Cooner Wire, AS632) were implanted in 19 muscles of the right hindlimb (Hudson et al., 2010). Briefly, pairs of wires were tunneled subcutaneously to their target muscles from either an external circular connector (Amphenol) affixed to the skull using dental acrylic and titanium screws (cranial-mounted subcutaneous implant, monkey C) or four external connector modules (ITT Canon) affixed to the upper arm with elastic medical adhesive tape (arm-mounted subcutaneous implant, monkey F). Proper placement of electrode pairs in each muscle was tested by stimulating through the electrodes with brief stimulus trains (biphasic pulse, 0.2 ms/phase, ∼50 Hz) while observing appropriate evoked movements. Wires were removed and reinserted if proper placement was not confirmed. Similar stimulation tests were performed at various times after implantation to confirm electrode location. Within weeks of implantation, loops of extra wire length tucked into a subcutaneous pocket in the back became embedded in connective tissue rigidly anchoring the electrodes in place. While 19 hindlimb muscles were implanted in each monkey, this paper focuses on the results of EMGs recorded from four ankle muscles: TA, medial gastrocnemius (MG), lateral gastrocnemius (LG) and soleus (SOL) (**Figure 1B**).

All procedures were in accordance with the standards outlined by the *Guide for the Care and Use of Laboratory Animals* published by the US Department of Health and Human Services and the National Institutes of Health. All surgeries were performed in

an Association for Assessment and Accreditation of Laboratory Animal Care (AAALAC) accredited facility using full aseptic procedures. Postoperative analgesics (buprenorphine, 0.01 mg/kg) were administered for 5 days. Wound edges were inspected daily and treated with Betadine (10% povidone-iodine) and topical antibiotic when necessary.

DATA COLLECTION

EMG activity, cortical activity and task-related signals were simultaneously monitored. Glass and mylar-insulated platinum-iridium electrodes (0.5–1.5 MΩ impedances, Frederick Haer) were used to record cortical unit activity and for stimulation. The electrode was positioned in the recording chamber using a custom-made x–y positioner and advanced using a manual hydraulic microdrive (Frederick Haer). Electrode penetrations were systematically made at 1 mm intervals in the precentral cortex of the left hemisphere encompassing the entire hindlimb M1 representation. Data were collected from putative sites in layer V of the cortex, as determined by depth from first cortical activity and size and nature of neuronal spikes. Data were collected from putative layer V sites in the bank of the medial wall and central sulcus at 0.5 mm intervals over the extent of the electrode track.

DATA ANALYSIS

At each putative layer V site, stimulus triggered averages (StTAs) (15, 30, and 60 μA at 15 Hz) of EMG activity were computed for 19 muscles of the hindlimb as the monkey performed the push-pull task. Individual stimuli were symmetrical biphasic pulses, 0.2 ms negative pulse followed by a 0.2 ms positive pulse, applied throughout all phases of the task. EMGs were generally filtered at 30 Hz to 1 kHz, digitized at 4 kHz and full-wave rectified. StTAs were compiled over an 80 ms epoch, 20 ms pre-trigger and 60 ms post-trigger, and consisted of at least 500 trigger events. To prevent averaging periods where EMG activity was minimal or non-existent, segments of EMG activity associated with each stimulus were evaluated and accepted for averaging only when the average of all EMG data points over the entire 80 ms epoch was ≥5% of full-scale input (McKiernan et al., 1998).

For this study, we analyzed StTAs from the four ankle muscles at each cortical site. Poststimulus facilitation (PStF) and suppression (PStS) effects were computer measured as described by Mewes and Cheney (1991). Each average consisted of an 80 ms epoch, 20 ms pre-trigger and 60 ms post-trigger. A poststimulus effect (PStE) was defined as a peak or trough of EMG activity that rose or fell from baseline and maintained a level exceeding two standard deviations of baseline for a period equal to or greater than 0.75 ms. Baseline EMG activity was measured as the 12 ms period preceding the onset of the effect initially determined by visual inspection. Baseline statistics were then used to determine the onset of the effect as the point where the envelope of the record exceeded two standard deviations of baseline. The magnitude of PStEs was expressed as the peak percentage increase (+ppi) or peak percentage decrease (−ppi) in EMG activity above (PStF) or below (PStS) baseline. To avoid skewing of the data from very weak effects, only PStF effects with a ppi ≥15 and PStS effects with a ppi ≤ −15 were included in the analysis (**Figure 2**).

Cross-talk between muscles was evaluated by computing EMG-triggered averages (Cheney and Fetz, 1980). Averages of EMG activity were compiled for each muscle using one muscle's EMG activity as a trigger and repeated using all 19 muscles as triggers. If the ratio of the cross-talk peak in the test versus trigger muscle exceeded the ratio of their PStEs by a factor of two or more, a muscle was considered to have an unacceptable level

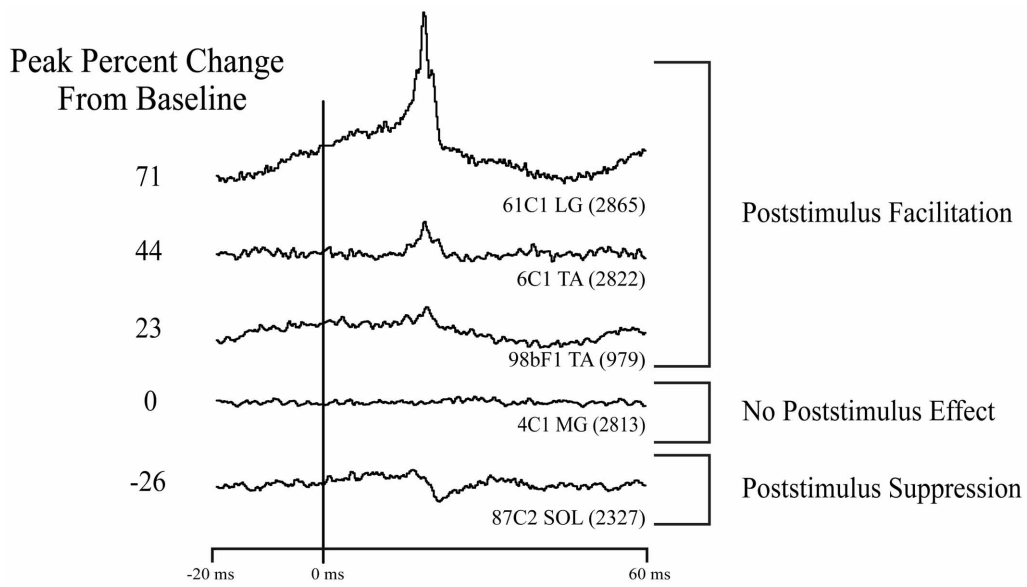

FIGURE 2 | Types of effects observed in stimulus triggered averages of ankle muscle EMG activity. Column on left: magnitude of the primary poststimulus facilitation (PStF) or poststimulus suppression (PStS) measured as peak percent change from baseline EMG value just before the onset of the effect. Stimulation at 60 μA and 15 Hz repetition rate.

of cross-talk (Buys et al., 1986). No muscle in this study showed significant cross-talk using this criterion.

UNFOLDING THE CORTEX

A two-dimensional representation of cortical layer V of the cortex in the medial wall of the hemisphere, the anterior bank of the central sulcus and the surface cortex required flattening and unfolding the curvature of the cortex. This process has been described in detail by Park et al. (2001). Briefly, the cortex was unfolded and 2-dimensional maps were generated based on known architectural landmarks, observations during the cortical chamber implant surgery, MRI images, electrode track x-y coordinates, electrode penetration depth and properties of recorded neurons.

RESULTS

EMG ACTIVITY DURING BEHAVIORAL TASK

Figure 1B shows the EMG activity of TA, MG, LG, and SOL throughout different phases of the hindlimb task. The extensors (MG, LG, and SOL) all showed a similar pattern of modulation with the strongest activity during the extension (push) phase of the task but continuing at a lower level through the hold phase of extension and also at a lower level yet during leg flexion (pull). The flexor muscle (TA) showed a more focused pattern with activity confined primarily to the flexion (pull and hold) phase of the task.

DATASET

StTA of EMG activity from four ankle muscles was performed systematically from sites in the left M1 cortex of two rhesus macaques. **Figure 2** illustrates the types of PStEs obtained (facilitation, suppression, no effect). A total of 312 electrode tracks were made (monkey F, 170; monkey C, 142). Data collection is summarized in **Table 1**. StTA was performed at 259 putative layer V sites at 15 μA, 292 sites at 30 μA and 317 sites at 60 μA. Twenty-seven putative layer V sites yielded PStEs at 15 μA, 73 at 30 μA and 134 at 60 μA. Both PStF and PStS were observed in each of the four ankle muscles. Data from all sites were used to analyze the distribution of effects (**Table 2A**). Data from sites with PStEs in the same muscle at all three stimulus intensities are shown separately (**Table 2B**). Although the number of effects is somewhat limited, these data provide a purer measure of changes in magnitude with stimulus intensity.

LATENCY AND MAGNITUDE

At 15 μA, the average PStF onset latency across all ankle muscles was 18.5 ± 3.0 ms compared with an average PStS onset latency of 19.9 ± 3.8 ms (**Table 2A**). The latency difference between PStF and PStS increased to 2.2 ms at 30 μA and 3.7 ms at 60 μA. There were no significant differences in PStF onset latency between muscles at any stimulus intensity (Kruskal–Wallis test, n.s.). As expected, the PStF onset latency decreased with stimulus intensity and this difference became statistically significant in some cases (TA at 15 μA compared to 30 and 60 μA; SOL at 15 μA compared to 60 μA; Wilcoxon signed ranks test, $p < 0.05$). For a given muscle, PStS onset latency was not different at any stimulus intensity although the numbers of effects for MG and LG at 15 μA were too small for comparison (**Table 2A**, Friedman's test, n.s.) At 60 μA, TA PStS onset latency was greater than MG, LG, and SOL (Mann–Whitney's U test, TA-MG $p = 0.001$, TA-LG $p < 0.05$, TA-SOL $p < 0.001$).

Figure 3 shows the distribution of PStF onset latencies for the ankle muscles at 15, 30, and 60 μA (all effects included). There was a similar distribution of latencies among all muscles, although TA had a clear suggestion of bimodality that was not present in the distributions for other muscles. The minimum onset latency of PStF decreased by 1.9 ms from 15 to 30 μA and by 0.3 ms from 30 to 60 μA (**Table 2A**). Regardless of muscle, the minimum latency was approximately 12–13 ms (30 and 60 μA). The only exceptions were two effects in MG at 60 μA that were 8 and 10 ms.

At 15 μA, the overall mean PStF magnitude, expressed as peak percent increase (ppi) above baseline, was 24.4 ± 8.7 compared with a peak percent decrease of −19.0 ± 3.6 for PStS (**Table 2A**). When comparing mean PStF magnitude across muscles, there were no significant differences between muscles at 15 and 30 μA (Kruskal–Wallis test, n.s.). However, at 60 μA MG had a significantly weaker PStF magnitude than LG, TA, and SOL

Table 1 | Summary of data collected from ankle muscles.

Electrode tracks	Monkey F			Monkey C			Total		
	170			142			312		
	15 μA	30 μA	60 μA	15 μA	30 μA	60 μA	15 μA	30 μA	60 μA
Layer V* sites stimulated	117	150	167	142	142	150	259	292	317
Sites yielding PStEs	4	17	55	23	56	79	27	73	134
Sites yielding PStF	4	15	47	14	35	66	18	50	113
Sites yielding PStS	0	2	11	11	22	29	11	24	40
PStEs obtained	4	20	99	29	89	179	33	109	278
PStF effects	4	18	84	17	61	136	21	79	220
PStS effects	0	2	15	12	28	43	12	30	58

PStE, poststimulus effect; PStF, poststimulus facilitation; PStS, poststimulus suppression.

**Putative layer V sites identified based on criteria given in the text.*

Table 2 | Latency and magnitude of PStEs.

A. All effects

	Onset latency, ms						Magnitude, %					
	15 μA		30 μA		60 μA		15 μA		30 μA		60 μA	
Muscle	***n***	**Mean**	***n***	**Mean**	***n***	**Mean**	***n***	**Mean**	***n***	**Mean**	***n***	**Mean**
PStF												
TA	6	20.3 ± 3.3	18	16.3 ± 3.2	54	17.3 ± 3.9	6	23.7 ± 4.3	18	26.2 ± 10.0	54	29.9 ± 10.5
SOL	7	19.3 ± 3.1	21	16.9 ± 1.9	68	16.6 ± 2.0	7	24.6 ± 10.9	21	25.6 ± 8.2	68	30.9 ± 14.7
LG	3	16.3 ± 0.9	29	16.2 ± 1.1	65	15.6 ± 1.3	3	19.0 ± 0.7	29	21.8 ± 4.8	65	33.4 ± 16.3
MG	5	16.5 ± 1.4	11	17.6 ± 3.4	33	15.8 ± 2.4	5	28.2 ± 11.6	11	28.9 ± 18.8	33	24.2 ± 8.6
Total	21	18.5 ± 3.0	79	16.6 ± 2.3	220	16.3 ± 2.6	21	24.4 ± 8.7	79	24.8 ± 9.9	220	30.4 ± 13.8
PStS												
TA	3	24.9 ± 1.1	7	21.9 ± 3.3	17	23.2 ± 2.8	3	−19.9 ± 3.6	7	−17.8 ± 2.2	17	−22.2 ± 5.5
SOL	7	18.6 ± 3.1	15	17.6 ± 2.1	22	18.3 ± 1.4	7	−19.4 ± 3.8	15	−24.3 ± 7.6	22	−24.2 ± 7.8
LG	1	17.8	4	18.6 ± 0.8	8	19.0 ± 0.8	1	−15.7	4	−19.3 ± 3.5	8	−22.2 ± 5.2
MG	1	16.8	4	18.3 ± 2.1	11	19.0 ± 2.4	1	−16.6	4	−18.3 ± 2.4	11	−20.3 ± 5.1
Total	12	19.9 ± 3.8	30	18.8 ± 2.8	58	20.0 ± 2.9	12	−19.0 ± 3.6	30	−21.3 ± 6.3	58	−22.6 ± 6.4

B. Effects present in the same muscle at 15, 30, and 60 μA

PStF												
TA	5	19.5 ± 2.9	5	18.8 ± 3.0	5	19.2 ± 3.0	5	24.5 ± 4.3	5	34.8 ± 15.8	5	41.9 ± 5.6
SOL	3	17.9 ± 2.0	3	17.8 ± 2.0	3	18.2 ± 2.3	3	24.2 ± 10.9	3	31.9 ± 11.7	3	57.3 ± 30.1
LG	3	16.3 ± 0.9	3	16.9 ± 0.1	3	15.9 ± 1.0	3	19.0 ± 0.7	3	29.5 ± 4.3	3	51.0 ± 14.4
MG	1	17.5	1	17.8	1	17.0	1	20.8	1	31.8	1	27.8
Total	12	18.1 ± 2.4	12	18.0 ± 2.2	12	17.9 ± 2.5	12	22.8 ± 5.9	12	32.5 ± 11.1	12	46.8 ± 17.1
PStS												
TA	0	–	0	–	0	–	0	–	0	–	0	–
SOL	5	17.2 ± 1.4	5	17.5 ± 1.4	5	17.5 ± 1.2	5	−18.0 ± 1.6	5	−25.9 ± 7.4	5	−33.5 ± 9.9
LG	1	17.8	1	17.8	1	17.8	1	−15.7	1	−16.3	1	−26.0
MG	0	–	0	–	0	–	0	–	0	–	0	–
Total	6	17.3 ± 1.3	6	17.5 ± 1.3	6	17.5 ± 1.1	6	−17.6 ± 1.7	6	−24.3 ± 7.7	6	−32.3 ± 9.4

Values are mean ± SD. %, peak percent change from baseline; PStE, poststimulus effect; PStF, poststimulus facilitation; PStS, poststimulus suppression.

(Mann–Whitney's U test, $p < 0.01$). There were no significant differences between muscles for PStS magnitude at any stimulus intensity (Kruskal–Wallis test, n.s.). Changes in magnitude of effects with stimulus intensity are best appreciated from a subset of cortical sites in which effects were present at each of the three stimulus intensities (**Table 2B**). Although the number of sites is somewhat limited, the data show increases in PStF magnitude ranging from 7.7–11.0% in going from 15 to 30 μA and 7.1–25.4% in going from 30 to 60 μA. Corresponding increases for PStS were 0.6–7.9% for 15–30 μA and 7.6–9.7% for 30–60 μA. Magnitudes based on all effects (**Table 2A**) are not appropriate for examining relationships between magnitude and intensity because higher intensity stimulation recruits new muscles with weak effects that dilute the mean magnitude.

There was a similar distribution of magnitudes of PStF among all muscles with a consistent trend toward skewing in the direction of the weakest magnitudes (**Figure 4**), a trend also observed in the primate forelimb (Park et al., 2004). The strongest effects observed for each muscle were in the range of 60–70 ppi (60 μA). Effects in soleus were equally as strong as those in TA, MG, and LG. In fact, the two strongest effects observed were in soleus.

DISTRIBUTION OF PStEs

Figure 5 shows the distribution of PStF and PStS effects observed in each of the ankle muscles sampled at 15, 30, and 60 μA. Both PStF and PStS effects were observed in each muscle at each stimulus intensity. Overall, PStF was more common than PStS in all four muscles. PStS was most common in SOL, especially at 15 μA where the incidence of PStS was equal to the incidence of PStF. At higher intensities the incidence of PStF compared to PStS in SOL shifted in favor of PStF. Both monkeys exhibited these trends. However, it should be noted that the increased incidence of facilitation with increasing stimulus intensity is likely to be a consequence of the fact that, for clarity, we based the sign of an effect (facilitation or suppression) on the earliest latency component. Because output zones in cortex are mixed and PStF has a shorter latency than PStS, as stimulus intensity increases, changes in the incidence of facilitation and suppression will be biased

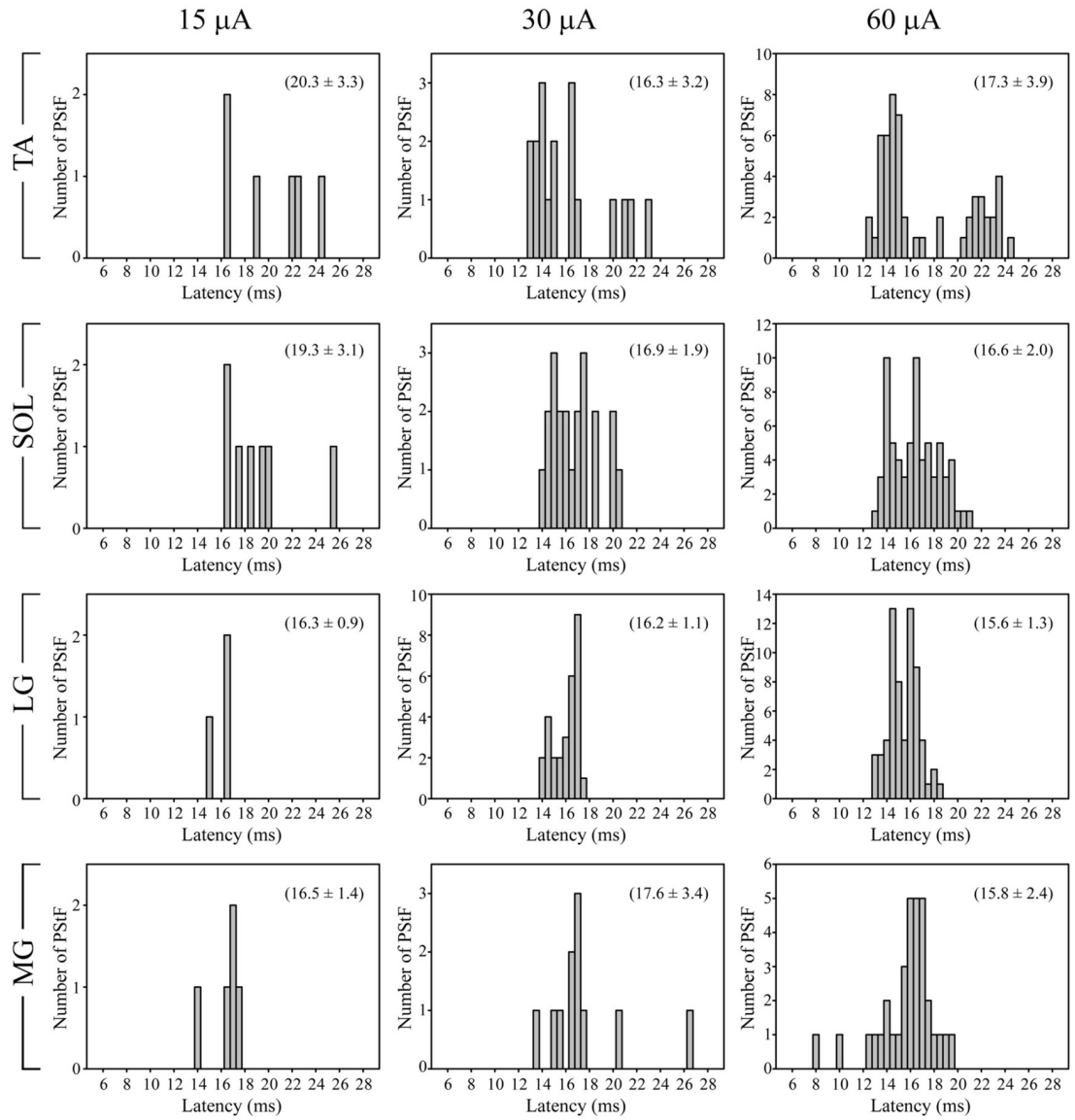

FIGURE 3 | Distribution of PStF onset latencies for ankle muscles at 15, 30, and 60 μA stimuli. The values given in parentheses for each graph represent the mean ± SD of the onset latency of the PStF. Muscle abbreviations are the same as in **Figure 1**.

toward facilitation. Accordingly, results at the 15 μA intensity are likely to be most meaningful relative to questions about the prevalence of facilitation versus suppression in different muscles.

Suggestions in previous studies of differential control of fast and slow muscles from motor cortex (Preston and Whitlock, 1963) prompted us to examine this issue with our data. It was proposed that cortically initiated movements could be enhanced through cortical inhibition of soleus as a slow, tonically contracting postural muscle, coupled with excitation of its agonists—MG and LG. We examined this issue by determining the relative prevalence of PStS and PStF in the gastrocnemius muscles and TA when (1) PStS was present in soleus, and (2) PStF was present in soleus. The results show that in all cases and at all intensities, the effect in soleus tends to be matched by a similar effect in MG and LG. For instance, at 60 μA, there were 22 PStS effects in soleus. In these cases, there was one PStF effect in the gastrocnemius muscles and 15 PStS effects. The opposite pattern was evident for TA which followed a reciprocal innervation plan with 8 PStF effects and 2 PStS effects.

MUSCLE REPRESENTATION

Figure 6 shows the representation of each muscle in M1 of both monkeys based on PStF effects. All muscles were represented in both monkeys. There was massive overlap in the territories for

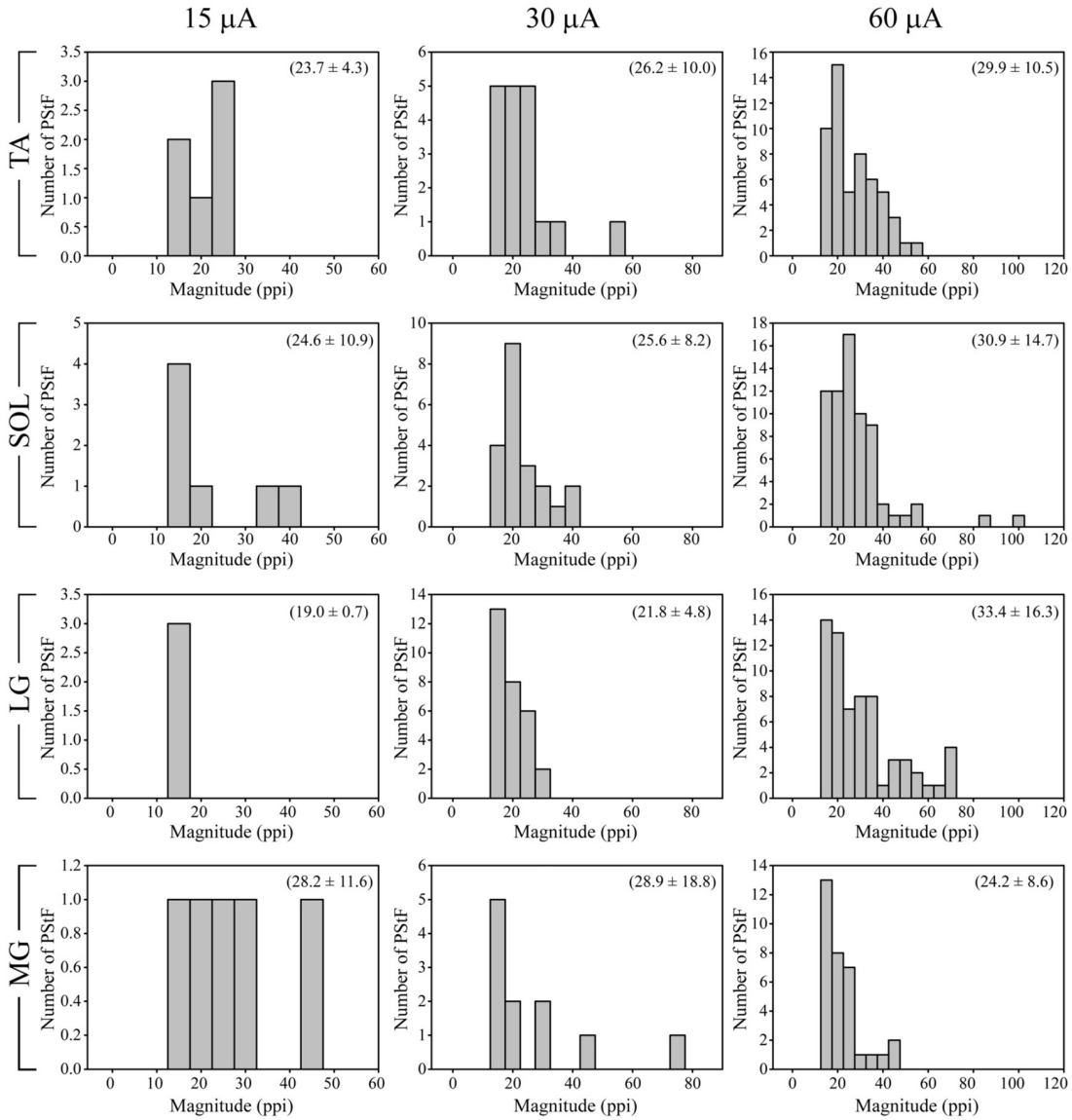

FIGURE 4 | Distribution of PStF magnitudes for ankle muscles at 15, 30, and 60 μA stimuli. The magnitudes are expressed as peak percent increase (ppi) above baseline. The values given in parentheses for each graph represent the mean ± SD of the magnitude of the PStF. Muscle abbreviations are the same as in **Figure 1**.

each muscle, not only of the extensors (MG, LG, and SOL) but also of the flexor muscle, TA. While monkey F had considerably fewer effects than monkey C, the same trends were apparent in both monkeys.

DISCUSSION

Early studies in the primate and more recent studies in human subjects have yielded conflicting results regarding the role of motor cortex in the control of slow muscles such as soleus. While it is well established that the motor cortex has a dominant excitatory effect on fast muscles, the cortical control of the slow muscle, soleus, has remained contentious. In this study, we investigated the cortical control of fast (TA, MG, and LG) and slow (SOL) muscles of the ankle using StTA of EMG activity (Cheney and Fetz, 1985; Park et al., 2001). With this method, microstimuli are superimposed on a background of EMG activity associated with task performance. The effects of single stimuli are subthreshold for overt EMG responses but the evoked EPSPs and IPSPs in motoneurons influence the firing probability of motoneurons and this can be revealed with signal averaging of EMG over thousands of stimuli. This provides a highly sensitive method capable of revealing both excitatory and inhibitory effects.

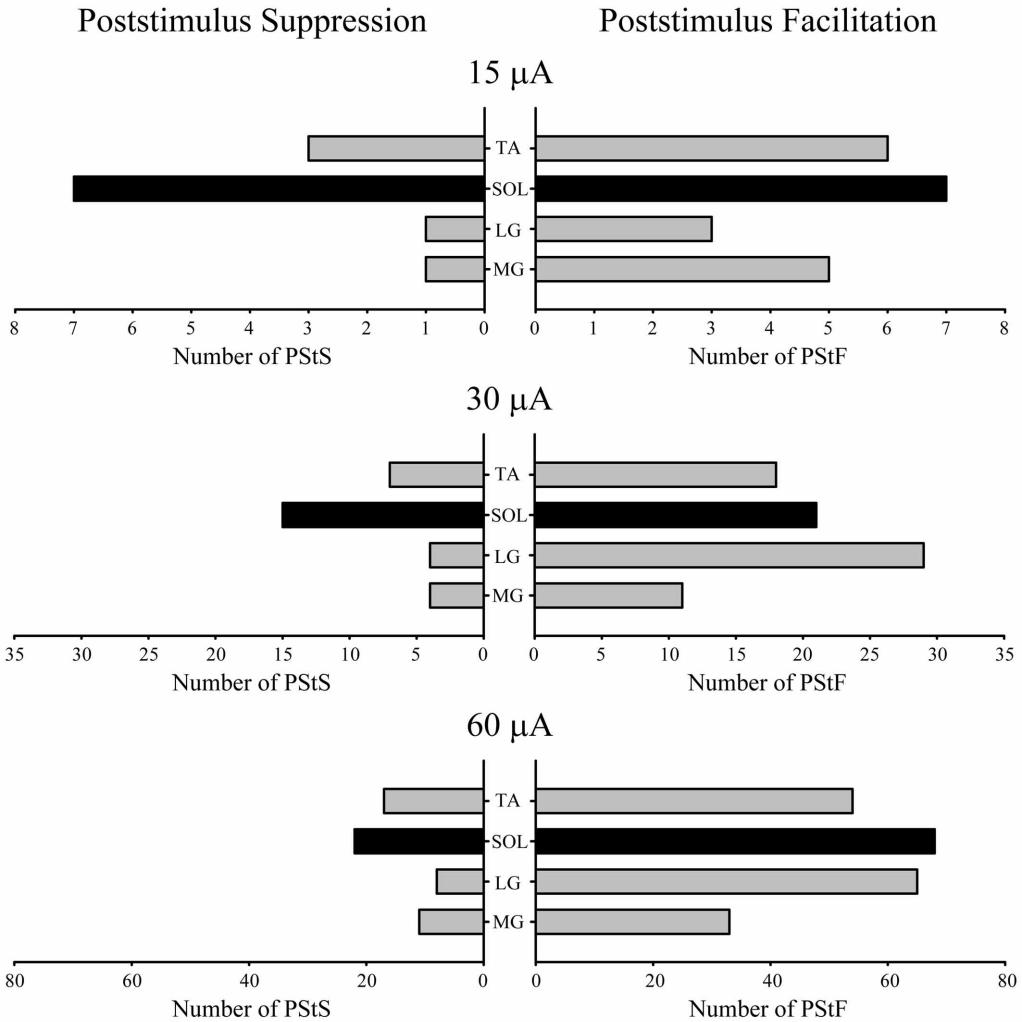

FIGURE 5 | Distribution of PStF (right) and PStS (left) effects obtained from four ankle muscles of the hindlimb at 15, 30, and 60 μA stimuli. Gray bars: fast muscles. Black bars: slow muscle. Muscle abbreviations are the same as in **Figure 1**.

PStF was observed in all muscles and was as common in the slow muscle, soleus, as in the fast muscles. The mean onset latencies of PStF effects were similar among the fast and slow muscles. The mean magnitudes of PStF effects were also similar among the fast and slow muscles. The distributions of PStF magnitudes were similar among all muscles, demonstrating a consistent trend toward the weakest magnitudes being the most common. Poststimulus suppression (PStS) was observed in all muscles; however, it was more common in soleus than in the fast muscles, especially at lower stimulus intensities where it was as common as facilitation. This was not true of fast muscles at any stimulus intensity.

The question arises as to why previous studies in the primate and some studies in human subjects have reported weak to absent excitatory effects on soleus or predominantly inhibitory effects from motor cortex in contrast to our own results. The early studies of Preston and Whitlock (1963) and Uemura and Preston (1965) used the monkey "pyramidal" preparation, which involves lesioning the brainstem sparing only the pyramidal tract, while the monkeys in our study were awake, with an intact nervous system, and performing a trained motor behavioral task. It should be noted that while Preston and Whitlock (1963) emphasized the predominant, almost pure inhibitory, nature of the effect of cortical stimulation on motoneurons of soleus determined with monosynaptic reflex conditioning, early weak facilitation peaks were evident but considered equivocal (their **Figure 3**). They characterized their results as showing "quantitatively greater cortical inhibition impinging on soleus motoneurons when compared with the synergistic motoneurons of the medial head of the gastrocnemius muscle" and this statement is consistent with our results.

In human subjects, Bawa et al. (2002) found that a higher stimulus intensity was needed to elicit a short latency facilitation in soleus compared to TA. Moreover, Valls-Solé et al. (1994) found that TMS effects in soleus were difficult to elicit unless the subjects were standing on their toes which would produce a large

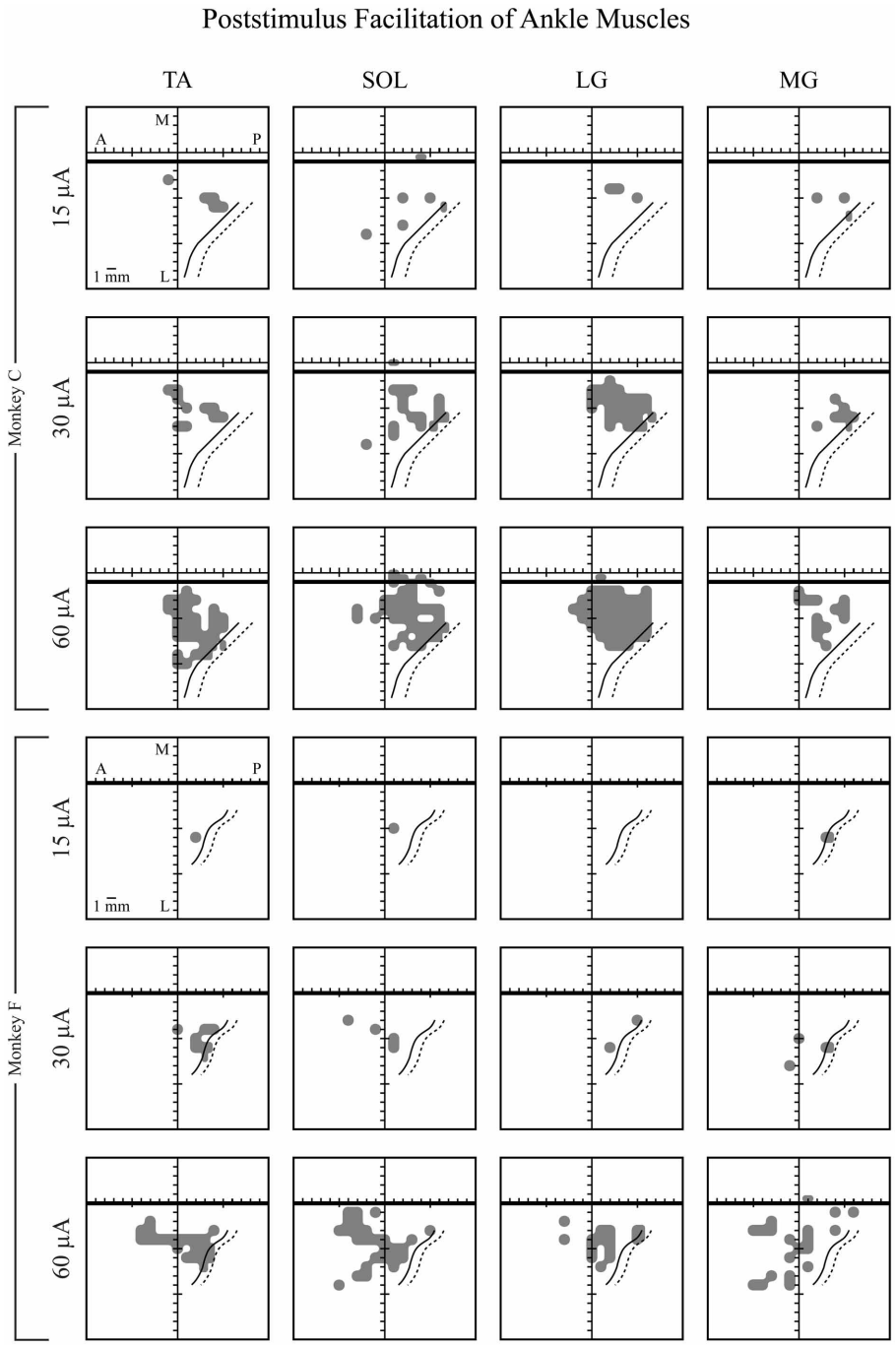

FIGURE 6 | Maps of individual ankle muscle representations in hindlimb primary motor cortex in two monkeys (F and C), represented in two dimensions after unfolding the medial wall and central sulcus. Maps of hindlimb muscles were based on PStF effects at 15, 30, and 60 μA. Heavy horizontal black line: midline, above the heavy black line represents the bank of the medial wall of the hemisphere. Solid black curved line: central sulcus. Dotted black curved line: fundus of the central sulcus. A, anterior; P, posterior; M, medial; and L, lateral. Muscle abbreviations are the same as in **Figure 1**.

excitability increase in soleus motoneurons. Consistent with this finding, Goulart and Valls-Solé (2001) reported that facilitation of soleus was stronger when subjects were in standing position rather than seated. Geertsen et al. (2010) found that facilitation of soleus occurred during voluntary ankle extension and flexion. Reports of weak or non-existent soleus excitation may have been due to low stimulus intensities (Brouwer and Qiao, 1995) or inadequate background excitability of soleus motoneurons. In this study, we used three stimulus intensities and found the relative number of suppression and facilitation effects in soleus to be similar at low intensities (15 μA). At higher intensities, facilitation of soleus was more common than suppression.

The results obtained in this study for hindlimb muscles are of interest in comparison with results obtained with similar methods for forelimb muscles. Park et al. (2004) examined M1 output effects in 24 muscles of the macaque forelimb using 15 μA StTA. Although there are no pure slow muscles acting at the wrist for comparison with our data on soleus, it is possible to compare effects on ankle muscles obtained in this study with those for wrist muscles from Park et al., 2004. In general, wrist PStF effects were considerably greater in magnitude compared to ankle PStF effects. At 15 μA, the average wrist PStF magnitude (ppi) was 73.7 ± 81.1 compared to an ankle muscle average PStF magnitude of 24.4 ± 8.7. PStS showed a similar pattern, although the disparity was not as great. At 15 μA, the average wrist PStS magnitude was −30.8 ± 15.2 compared to an ankle muscle average PStS magnitude of −19.0 ± 3.6. The magnitude of ankle muscle PStS was 78% of that for PStF, whereas for wrist muscles it was only 42%. As for the distribution of excitatory and inhibitory effects, PStF was more common than PStS in all wrist muscles at 15 μA (77 vs. 33%). Other intensities were not tested. The same was true of ankle muscles at 15 μA except soleus, where PStF and PStS were equally common. At higher stimulus intensities, facilitation in soleus was more common than suppression. However, this would be expected from the mixed cortical representations of facilitation and suppression coupled with the fact that facilitation effects are shorter latency and we used the shortest latency effect to define the sign (facilitation or suppression) of the effect.

Based on our results, there can be no doubt that motor cortex in primates is capable of powerful excitatory effects on soleus motoneurons equal to that of fast muscles. However, it should be emphasized that motor cortex is also capable of significant inhibitory effects on soleus and the inhibitory effects are more prominent in the slow muscle, soleus, than the fast muscles. In fact, at low stimulus intensities, inhibitory effects in soleus were as common as excitatory effects. Overall, our results support the findings of recent TMS studies in human subjects demonstrating short latency facilitation of both fast and slow muscles of the ankle (Valls-Solé et al., 1994; Goulart and Valls-Solé, 2001; Bawa et al., 2002; Geertsen et al., 2010), but also leave open the possibility for a unique role of cortical inhibition of soleus in the control of movement.

REFERENCES

Andersen, P., and Sears, T. A. (1964). The mechanical properties and innervation of fast and slow motor units in the intercostal muscles of the cat. *J. Physiol.* 173, 114–129.

Asanuma, H., Zarzecki, P., Jankowska, E., Hongo, T., and Marcus, S. (1979). Projection of individual pyramidal tract neurons to lumbar motor nuclei of the monkey. *Exp. Brain Res.* 34, 73–89.

Ashby, P., and Advani, A. (1990). Corticospinal control of soleus motoneurons in man. *Can. J. Pharmacol.* 68, 1231–1235.

Bawa, P., Chalmers, G. R., Stewart, H., and Eisen, A. A. (2002). Responses of ankle extensor and flexor motoneurons to transcranial magnetic stimulation. *J. Neurophysiol.* 88, 124–132.

Binder, M. D., Robinson, F. R., and Powers, R. K. (1998). Distribution of effective synaptic currents in cat triceps surae motoneurons. VI. Contralateral pyramidal tract. *J. Neurophysiol.* 80, 241–248.

Brouwer, B., and Ashby, P. (1990). Corticospinal projections to upper and lower limb spinal motoneurons in man. *Electroencephalogr. Clin. Neurophysiol.* 76, 509–519.

Brouwer, B., and Ashby, P. (1992). Corticospinal projections to the lower limb motoneurons in man. *Exp. Brain Res.* 89, 649–654.

Brouwer, B., and Qiao, J. (1995). Characteristics and variability of lower limb motoneuron responses to transcranial magnetic stimulation. *Electroencephalogr. Clin. Neurophysiol.* 97, 49–54.

Burke, R. E. (1967). Motor unit types of cat triceps surae muscle. *J. Physiol.* 193, 141–160.

Burke, R. E., Jankowska, E., and ten Bruggencate, G. (1970). A comparison of peripheral and rubrospinal synaptic input to slow and fast twitch motor units of triceps surae. *J. Physiol.* 207, 709–732.

Burke, R. E., Levine, D. N., and Zajac, F. E. (1971). Mammalian motor units: physiological-histochemical correlation in three types in cat gastrocnemius. *Science* 174, 709–712.

Burke, R. E., and Tsairis, P. (1974). The correlation of physiological properties with histochemical characteristics in single muscle units. *Ann. N.Y. Acad. Sci.* 228, 145–159.

Buys, E. J., Lemon, R. N., Mantel, G. W., and Muir, R. B. (1986). Selective facilitation of different hand muscles by single corticospinal neurons in the conscious monkey. *J. Physiol.* 381, 529–549.

Cheney, P. D., and Fetz, E. E. (1980). Functional classes of primate corticomotoneuronal cells and their relation to active force. *J. Neurophysiol.* 44, 773–791.

Cheney, P. D., and Fetz, E. E. (1985). Comparable patterns of muscle facilitation evoked by individual corticomotoneuronal (CM) cells and by single intracortical microstimuli in primates: evidence for functional groups of CM cells. *J. Neurophysiol.* 53, 786–804.

Cowan, J. M. A., Day, B. L., Marsden, C., and Rothwell, J. C. (1986). The effect of percutaneous motor cortex stimulation on H reflexes in muscles of the arm and leg in intact man. *J. Physiol.* 377, 333–347.

Eccles, J. C., Eccles, R. M., and Lundberg, A. (1958). The action potentials of the alpha motoneurones supplying fast and slow muscles. *J. Physiol.* 142, 275–291.

Edgley, S. A., Eyre, J. A., Lemon, R. N., and Miller, S. (1997). Comparison of activation of corticospinal neurons and spinal motor neurons by magnetic and electrical transcranial stimulation in the lumbosacral cord of the anaesthetized monkey. *Brain* 120, 839–853.

Ertekin, C., Ertaş, M., Efendi, H., Larsson, L. E., Sirin, H., Araç, N., et al. (1995). A stable late soleus EMG response elicited by cortical stimulation during voluntary ankle dorsiflexion. *Electroenchepalogr. Clin. Neurophysiol.* 97, 275–283.

Geertsen, S. S., Zuur, A. T., and Nielsen, J. B. (2010). Voluntary activation of ankle muscles is accompanied by subcortical facilitation of their antagonists. *J. Physiol.* 588, 2391–2402.

Goulart, F., and Valls-Solé, J. (2001). Reciprocal changes of excitability between tibialis anterior and soleus during the sit-to-stand movement. *Exp. Brain Res.* 139, 391–397.

Hudson, H. M., Griffin, D. M., Belhaj-Saïf, A., Lee, S. P., and Cheney, P. D. (2010). Methods for chronic recording of EMG activity from large numbers of hindlimb muscles in awake rhesus macaques. *J. Neurophysiol.* 189, 153–161.

Jankowska, E., Padel, Y., and Tanaka, R. (1975). Projections of pyramidal tract cells to alpha-motoneurones innervating hind-limb muscles in the monkey. *J. Physiol.* 249, 637–667.

Kawai, Y. (1982). [Motor cortex control of fast and slow motoneurons innervating forelimb muscles of the cat]. *Nihon Seirigaku Zasshi* 44, 587–599.

Kronecker, H., and Stirling, W. (1878). The genesis of tetanus. *J. Physiol.* 1, 384–420.

Kugelberg, E., and Edstrom, L. (1968). Differential histochemical effects of muscle contractions on phosphorylase and glycogen in various types of fibres: relation to fatigue. *J. Neurol. Neurosurg. Psychiatry* 31, 415–423.

McKiernan, B. J., Marcario, J. K., Karrer, J. H., and Cheney, P. D. (1998). Corticomotoneuronal postspike effects in shoulder, elbow, wrist, digit, and intrinsic hand muscles during a reach and prehension task. *J. Neurophysiol.* 80, 1961–1980.

Mewes, K., and Cheney, P. D. (1991). Facilitation and suppression of wrist and digit muscles from single rubromotoneuronal cells in the awake monkey. *J. Neurophysiol.* 66, 1965–1977.

Muir, R. B., and Porter, R. (1973). The effect of a preceding stimulus on temporal facilitation at corticomotoneuronal synapses. *J. Physiol.* 228, 749–763.

Park, M. C., Belhaj-Saïf, A., and Cheney, P. D. (2004). Properties

of primary motor cortex output to forelimb muscles in rhesus macaques. *J. Neurophysiol.* 92, 2968–2984.

Park, M. C., Belhaj-Saïf, A., Gordon, M., and Cheney, P. D. (2001). Consistent features in the forelimb representation of primary motor cortex in rhesus macaques. *J. Neurosci.* 21, 2784–2792.

Paxinos, G., Huang, X. F., and Toga, A. W. (2000). *The Rhesus Monkey Brain in Stereotaxic Coordinates*. California, CA: Academic Press.

Preston, J. B., and Whitlock, D. G. (1963). A comparison of motor cortex effects on slow and fast muscle innervations in the monkey. *Exp. Neurol.* 7, 327–341.

Ranvier, L. (1874). De quelques faits relatifs à l'histologie et à la physiologie des muscles stries. *Arch. Physiol. Norm. Pathol.* 7, 5–15.

Shapovalov, A. I., and Kurchavyi, G. G. (1974). Effects of trans-membrane polarization and TEA injection on monosynaptic actions from motor cortex, red nucleus and group Ia afferents on lumbar motoneurons in the monkey. *Brain Res.* 82, 49–67.

Uemura, K., and Preston, J. B. (1965). Comparison of motor cortex influences upon various hind-limb motoneurons in pyramidal cats and primates. *J. Neurophysiol.* 28, 398–412.

Valls-Solé, J., Alvarez, R., and Tolosa, E. S. (1994). Responses of the soleus muscle to transcranial magnetic stimulation. *Electroencephalogr. Clin. Neurophysiol.* 93, 421–427.

Conflict of Interest Statement: The authors declare that the research was conducted in the absence of any commercial or financial relationships that could be construed as a potential conflict of interest.

Received: 05 December 2012; paper pending published: 02 January 2013; accepted: 12 February 2013; published online: 01 March 2013.

Citation: Hudson HM, Griffin DM, Belhaj-Saïf A and Cheney PD (2013) Cortical output to fast and slow muscles of the ankle in the rhesus macaque. Front. Neural Circuits ***7****:33. doi:* ***10.3389/fncir.2013.00033***

frontiers in
NEURAL CIRCUITS

ORIGINAL RESEARCH ARTICLE
published: 27 February 2013
doi: 10.3389/fncir.2013.00030

Cell and neuron densities in the primary motor cortex of primates

Nicole A. Young, Christine E. Collins and Jon H. Kaas*

Department of Psychology, Vanderbilt University, Nashville, TN, USA

Edited by:
Gordon M. G. Shepherd, Northwestern University, USA

Reviewed by:
Chet C. Sherwood, George Washington University, USA
Guy Elston, Centre for Cognitive Neuroscience, Australia
Kathleen S. Rockland, Massachusetts Institute of Technology, USA

***Correspondence:**
Jon H. Kaas, Department of Psychology, Vanderbilt University, 301 Wilson Hall, 111 21st Avenue South, Nashville, TN 37240, USA.
e-mail: jon.h.kaas@vanderbilt.edu

Cell and neuron densities vary across the cortical sheet in a predictable manner across different primate species (Collins et al., 2010b). Primary motor cortex, M1, is characterized by lower neuron densities relative to other cortical areas. M1 contains a motor representation map of contralateral body parts from tail to tongue in a mediolateral sequence. Different functional movement representations within M1 likely require specialized microcircuitry for control of different body parts, and these differences in circuitry may be reflected by variation in cell and neuron densities. Here we determined cell and neuron densities for multiple sub-regions of M1 in six primate species, using the semi-automated flow fractionator method. The results verify previous reports of lower overall neuron densities in M1 compared to other parts of cortex in the six primate species examined. The most lateral regions of M1 that correspond to face and hand movement representations, are more neuron dense relative to medial locations in M1, which suggests differences in cortical circuitry within movement zones.

Keywords: M1, flow fractionator, isotropic fractionator, movement

INTRODUCTION

The cerebral cortex is a heterogeneous structure that contains multiple sensory and motor information-processing systems (e.g., Van Essen et al., 2011). A hallmark of the mammalian cerebral cortex is the regular arrangement of sensory and motor areas across its surface. Primary sensory areas are topographically organized to represent sensory receptor arrays and primary motor cortex has a general somatotopic organization of motor movement representations. It is reasonable to presume that numbers of cells and neurons in functionally distinct cortical areas vary according to information-processing demands. However, the majority of studies on this issue have only reported the total number of cells and neurons for the cerebral cortex as a whole (e.g. Pakkenberg and Gundersen, 1997; Christensen et al., 2007; Herculano-Houzel et al., 2008).

To date, only one study has detailed the total numbers of cells and neurons across the entire cortical expanse after dissection of the cortex into small tissue pieces (Collins et al., 2010b). This study not only demonstrated a clear, non-uniform distribution of cells and neurons across the cortex of all four primate species examined, it also illustrated a pattern of distribution of cells and neurons that was consistent across all of the primate species that were studied. The features of the typical primate pattern of cell and neuron distribution and number are (1) the highest cell and neuron densities are found in primary visual cortex, V1; (2) extrastriate cortical areas have relatively high cell and neuron densities; (3) primary auditory and somatosensory areas have relatively high cell and neuron densities compared to surrounding areas; and (4) motor cortex, M1, appears to have low neuron densities compared to other areas of cortex. These results are consistent with the earlier findings of Beaulieu and Colonnier (1989) who determined neuron number in the cortex below 1 mm^2 of cortical surface in four visual areas, somatosensory area 3b, and two motor areas (4 gamma, 6a alpha) of the cortex of cats, and found that motor areas have the smallest number of neurons per column, while sensory areas contain more neurons, with the greatest number found in the binocular region of visual area 17. Skoglund et al. (1996) later investigated the number of neurons in primary motor, primary somatosensory and the second visual area in rats, and found significant differences in the number of neurons under a fixed amount of cortical surface area. They found that neuron density was highest in the second visual area (not V1), followed by primary somatosensory cortex. Primary motor cortex was the least neuron-dense cortical area. Despite the comprehensive evaluation of cortical cell and neuron number and distribution in the study by Collins and colleagues, the number of species examined in detail was limited and the dissection techniques used in that study had not been refined to allow evaluation of variation in cell and neuron density in different parts of topographically organized cortical areas, and in cases where functional areas were dissected from the cortex, areal boundaries were estimated from surface landmarks and sulcal patterns.

The present study was designed to examine the neuron densities in additional species of primates, to determine whether different representational zones within M1 have variable cell and neuron densities, and to compare estimated areal border locations with those determined electrophysiologically. We use the semi-automated flow fractionator method (Collins et al., 2010a; Young et al., 2012) to contrast M1 cell and neuron densities with the overall average densities across the cortex, and also to another specific primary cortical area, V1, to determine if M1 is contains relatively fewer neurons, as previously reported using other counting techniques. Here we also report estimates of neuron and total cell densities for different movement representation zones in

M1 for three primate species. Variation in neuron and total cell densities within a sub-region of M1 may correspond to the type of movement produced in the sub-region.

MATERIALS AND METHODS

TISSUE

Prosimian galago (*Otolemur garnetti*, $n = 3$), New World owl monkey (*Aotus nancymae*, $n = 1$), and squirrel monkey (*Saimiri sciuresis*, $n = 1$) brains were obtained from ongoing experiments of other investigators at Vanderbilt University. Galago and New World monkey brains were perfused with 0.1 MPBS. Old World macaque (*Macaca nemenstrina*, $n = 2$) and baboon (*Papio cynocephalus anubis*, $n = 1$) brains were purchased from the Washington National Primate Research Center. An additional baboon (*Papio hamadryas anubis*, $n = 1$) brain and a Hominid chimpanzee (*Pan troglodytes*, $n = 1$) brain were purchased from the Texas Biomedical Research Institute. These brains were perfused with 0.1 MPBS, and shipped to us overnight in the same solution. All brains were bisected and one cortical hemisphere was separated from the subcortical structures, the pia was removed and the sulci were opened to flatten the cortical sheet. The flat hemispheres were fixed within 4% paraformaldehyde (PFA). Macaque 2, however, remained intact and was post-fixed in 4% PFA. M1 was dissected from the flattened hemispheres and separated from the remaining cortex after viewing the flattened hemispheres on a light box to identify myelin-dense sensory areas that appear darker relative to surrounding cortical areas, which is an effective means to quickly visualize cortical areas for this method of dissection (see Collins et al., 2010b; Campi et al., 2011). Boundaries of M1 were identified relative to the estimated boundaries of these areas, sulcal landmarks, and in reference to previously published studies that identify boundaries of M1 and its internal organization (Gould et al., 1986; Huang et al., 1988; Waters et al., 1990; Huntley and Jones, 1991; Donoghue et al., 1992; Gaspar et al., 1992; Nudo et al., 1992; Stepniewska et al., 1993, 2005; Preuss et al., 1997; Jain et al., 2000; Qi et al., 2000, 2010; Wu et al., 2000; Fang et al., 2008; Wong and Kaas, 2010; Gharbawie et al., 2011; Kaas, 2012). M1 boundaries in the intact brain of baboon case 09–04 were identified according to intact sulcal landmarks and data from a previous report (Waters et al., 1990). In the galago, owl monkey, squirrel monkey, and baboon cases, the boundary of primary visual cortex (V1) is visible on the fixed brain surface, whether the cortex is flattened or not. Dissection cuts were placed along the visible, readily identifiable boundary. Remaining cortex in all species was dissected into approximately 5×5 mm cortical pieces. All cortical pieces were weighed, and surface areas were measured when possible using freely available NIH Image J software (NIH, Bethesda, MD, USA).

MOTOR AND SOMATOSENSORY MAPPING OF A GALAGO

The primary motor map was derived for one galago (galago 3) using short-train intracortical microstimulation (ICMS). This mapping was undertaken to verify our estimation of M1 boundaries and its internal organization in comparison to estimates in other cases. Some sensory mapping was completed to further confirm the location of the caudal boundary of M1. Detailed methods for surgical preparation, and motor and sensory mapping, are described in previously published reports (see Wu et al., 2000; Wu and Kaas, 2003; Stepniewska et al., 2009; Qi et al., 2011). All surgical procedures were conducted in accordance with the National Institutes of Health Guide for the Care and Use of Laboratory Animals and with the approval and guidance of the Vanderbilt University Animal Care and Use Committee.

In brief, surgical mapping procedures were performed under isoflurane anesthesia. After the skull was opened, the dura was retracted and the cortex digitally photographed. Isoflurane anesthesia was replaced with ketamine hydrochloride diluted with physiological saline (1:4) delivered intravenously with an infusion pump to maintain a stable level of anesthesia (30–50 mg/kg/h). Ketamine did not profoundly suppress cortical responsiveness. The blood vessel pattern on the cortical surface was used to guide electrode penetrations, which were marked on a printed copy of the digital photograph. The frontal cortex was explored with ICMS to identify the locations of the representations of body movements in area M1. In the ICMS procedure a stimulating electrode is lowered into the cortex to cortical layer 5 and the minimal electrical current necessary to elicit body movements is delivered to identify the motor representations for the cortical motor area. The microstimulation currents were delivered in 60-ms trains, with a pulse duration of 0.2 ms, and a pulse frequency of 300 Hz, which are the optimal parameters for eliciting movement in primates and other mammals (see Gould et al., 1986; Preuss et al., 1992; Wu et al., 2000; Young et al., 2011), without tissue damage. Stimulation was delivered with a low-impedance tungsten microelectrode inserted perpendicular to the cortical surface to a depth of 1.5–1.8 mm. This depth was found to be optimal for eliciting responses in prosimian galagos (Wu et al., 2000). Stimulating currents were generated with a Master 8 stimulator (AMPI) with a biphasic stimulus isolator (Bak Electronics Inc.). The entire body of the animal was monitored for ICMS-evoked movements by two observers during the mapping session. The face representation area of M1 was defined by eliciting any movements involving the mouth, tongue, jaw, nose, ears, and eyelids. The forelimb representation area of M1 was defined by eliciting movements involving the shoulder, arm, elbow, wrist, and digits. The trunk representation included movements of the upper and middle torso. Movements were classified as hindlimb when movements of the tail, legs, foot, and toes were made. Somatosensory mapping was undertaken to better identify the caudal boundary of M1. Microelectrode penetrations were made in somatosensory cortex and the magnitudes of neuronal responses to tapping and manipulation of the body surface (face, forelimb, trunk, and hindlimb regions), as indicated by the acoustic strength of neuron firing audio output, were constantly evaluated as the microelectrode passed through the superficial to the middle layers of cortex (up to 1000 μm depth). For each penetration, the receptive field location, size, and stimulus preference to light touch, tapping, and joint movement stimuli at the site where the strongest evoked response occurred were recorded on the photograph of the cortical surface. Boundaries of M1 and S1, and identifiable movement representations areas within M1, were marked with fluororuby tracer (FR) immediately before sacrifice to estimate their location on the cortical surface. Following euthanasia, the brain was removed and the right cortical hemisphere was manually

flattened. The FR landmarks were used to conservatively dissect ICMS-derived M1 representations from remaining cortex for processing with the flow fractionator (Young et al., 2012).

CELL AND NEURON DENSITY ESTIMATES

The isotropic fractionator and flow fractionator cell and neuron counting methods were used to obtain cell and neuron estimates in cortical samples. Detailed processing steps for the isotropic fractionator and flow fractionator are described in previous reports (Herculano-Houzel and Lent, 2005; Collins et al., 2010a; Young et al., 2012). Cell and neuron estimates obtained by the isotropic fractionator and the flow fractionator are in excellent concordance (Collins et al., 2010a; Young et al., 2012), and therefore the two methods can be used interchangeably.

In brief, each cortical piece was homogenized using a glass Tenbroeck tissue grinder (Fisher Scientific) and a dissociation solution of sodium citrate and triton X-100 in distilled water. The resulting homogenized suspensions contained free-floating nuclei. The total suspension volumes were determined based on the sample density, resulting in suspension volumes between 2 and 6 ml. The total number of cells in a nuclear suspension was estimated using DNA staining with 4′,6-diamidino-2-phenylindole (DAPI) that fluoresces bright blue with ultraviolet excitation (460 nm emission). DAPI binds strongly to DNA and labels all nuclei in the suspension, regardless of cell type, thereby providing a means for determining cell number in the homogenized samples. The total cell number estimate includes all DAPI-positive cell types contained within the sample, including glia and endothelial cells, as well as neurons. Free-floating, DAPI-stained nuclei in samples from the main suspension were counted to estimate total cells using either fluorescence microscopy and a glass Neubauer counting chamber and matched coverslip (isotropic fractionator), or a fixed volume of 50 µl of Countbright absolute counting beads (Invitrogen) was added to the sample prior to evaluation using a Becton Dickson (BD) 5-laser LSR II flow cytometer equipped with a 355 nm laser and using BD™ FACSDiva v. 6.1.3 software (flow fractionator). The total number of neurons in a nuclear suspension was estimated by immunolabeling a sample of the main sample suspension for neuronal nuclei with the anti-NeuN antibody (anti-neuronal nuclear antigen) (Millipore, Inc.) to determine the percentage of the total nuclei (DAPI+) that are also NeuN-immunoreactive (NeuN-IR). All samples went through epitope retrieval, which consisted of 30 min in 0.2 M boric acid solution in an oven set at 70°C. After epitope retrieval, samples were washed once with PBS then resuspended in PBS with primary antibody against NeuN added. Alexa Fluor 594 (AF594) goat anti-mouse IgG secondary antibody (Invitrogen, Inc.) was used to fluorescently tag NeuN-IR nuclei for counting on the fluorescence microscope (isotropic fractionator), and Alexa Fluor 647 (AF647) goat anti-mouse IgG secondary antibody (Invitrogen, Inc.) was used to estimate the proportion of NeuN-IR nuclei to the total population of DAPI+ nuclei on the flow cytometer. Detailed procedures for gating the flow cytometry data have been discussed elsewhere (see Collins et al., 2010a; Young et al., 2012). All flow cytometry experiments were conducted in the Vanderbilt University Medical Center Flow Cytometry Shared Resource.

RESULTS

Figure 1 illustrates the locations of M1 on the lateral aspect of the left cerebral hemisphere of the primate species examined in the present study, including prosimian galagos, New World owl monkeys and squirrel monkeys, Old World macaque monkeys and baboons and a Hominid chimpanzee. The location and organization of M1, and the rest of the cortical motor areas, are similar across these species despite differences in the size of the cortex.

PROSIMIAN GALAGOS

In the three galagos analyzed here, the total surface area of the flat cortex was 1782 mm^2 (galago 1), 1850 mm^2 (galago 2), and 1817 mm^2 (galago 3). The total cortex weight for these individuals is also very consistent at 2.86, 2.87, and 2.37 g for galagos 1, 2, and 3, respectively. M1 was identified and dissected in galagos 1 and 2 by visual identification on a lightbox using myelination patterns as reference. Galago 3 (case 10–41) had motor map dissections borders determined by ICMS mapping of M1 (**Figure 2**). Our methods for M1 identification and dissection (lightbox vs. mapping) was shown to produce consistent M1 cell and neuron estimates across individuals, and therefore we believe both dissection methods can be used to accurately identify cortical areas. For example, while the total surface areas for galago 3 (55 mm^2) and galago 2 (78 mm^2) slightly varied, the mapped galago 3 had a total number of 12.7 million cells and 4.9 million neurons within the defined M1 area, while the lightbox-dissected galago 2 had a total number of 11.0 million cells and 4.5 million neurons within M1.

Table 1 shows the results averaged for all three galagos. In galagos, M1 comprised approximately 3.1% of the total cortical mass, and almost 3% of the total cortical surface area. The average cell density in M1 was 118 million cells/g or 181,000 cells per mm^2 of cortical surface area. We found that the average proportion of DAPI-labeled nuclei that were also NeuN-IR was 32.2%, meaning that 32.2% of nuclei in M1 were identified as neuronal. This resulted in the average neuron density in M1 of 29 million neurons/g or 68,742 neurons under 1 mm^2 of cortical surface. To determine the magnitude of the cell and neuron density difference between M1 and V1 within each case, we calculated the average difference within a species for comparison with other species. The overall cortical cell density, averaged across all cortical areas and regions, including M1 and V1, in all three galagos, was 149 million cells/g or 205,398 cells per mm^2 of cortical surface. In contrast with another primary cortical area, the average cell density in V1 was 241 million cells/g or 297,479 cells per mm^2, the highest cell density in the cortex. The overall cortical neuron density across all areas was 64 million neurons/g or 86,231 neurons per mm^2 of surface area. The average neuron density in V1 in galagos was 146 million neurons/g or 182,208 neurons per mm^2 of surface area, approximately five times higher than the neuron density in M1 (29 million neurons/g and 68,742 neurons/mm^2 of cortical surface).

The M1 map derived by ICMS in galago 3 clearly illustrated a mediolateral pattern of the movement map from hindlimb to trunk, forelimb, and face and the boundaries between those movement representations (**Figure 2A**). Each representational zone in M1 was dissected in an effort to evaluate the mediolateral organization of the movement map. The dashed lines in

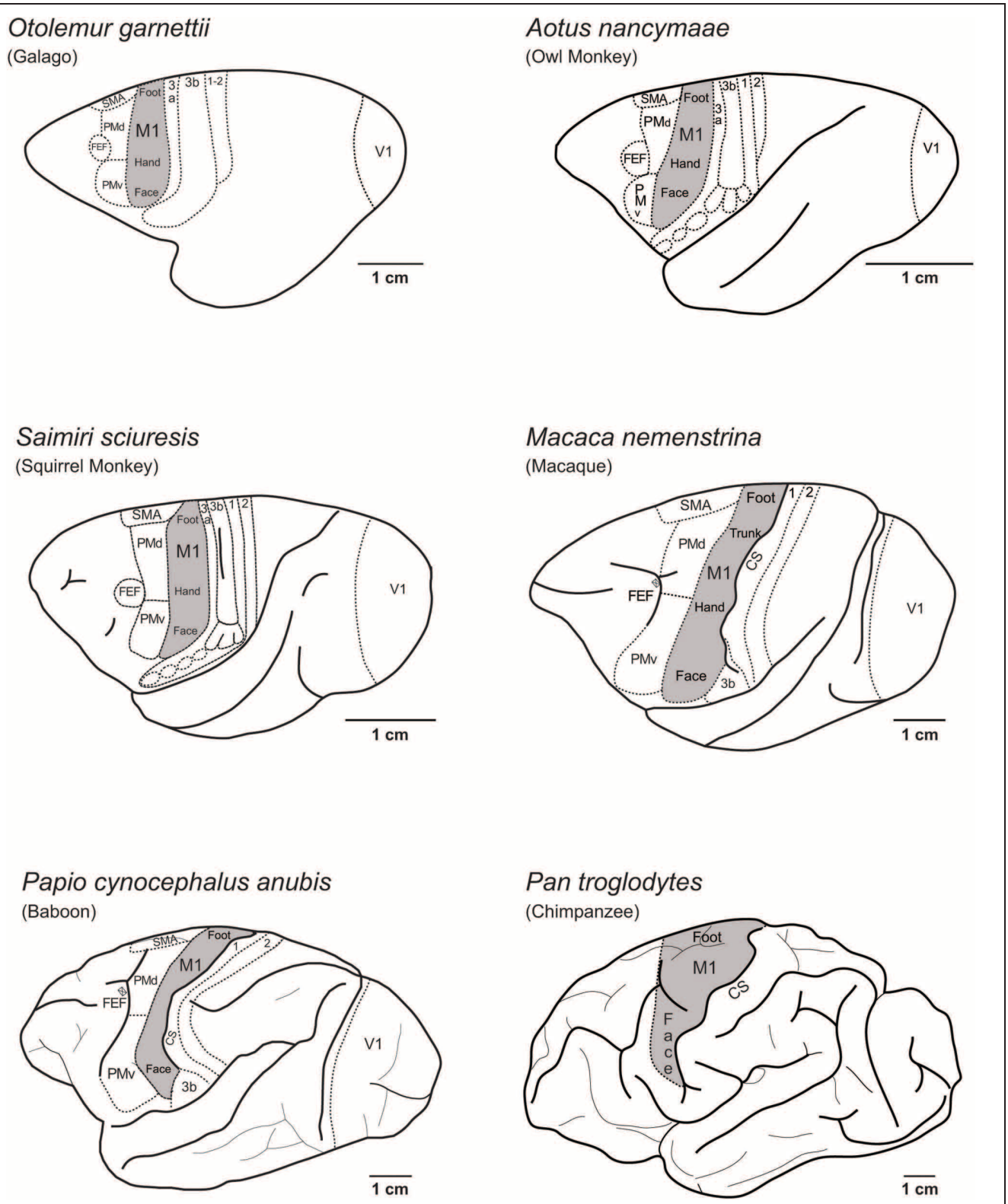

FIGURE 1 | The location of the primary motor cortex (M1) on the lateral view of the left cerebral hemisphere in several of the primate species discussed in this paper. The location and internal organization of M1 in New world and Old World monkeys (Gould et al., 1986; Huang et al., 1988; Waters et al., 1990; Huntley and Jones, 1991; Donoghue et al., 1992; Nudo et al., 1992; Kaas, 2012) and prosimian galagos (Wu et al., 2000) consists of a fractured mosaic of smaller areas devoted to particular movements that are dispersed within a larger somatotopic framework of functional movement domains (see Kaas, 2012; Kaas et al., 2012 for review). **Figure 1** shows the

(Continued)

FIGURE 1 | Continued
locations of M1 in prosimian galagos (Wu et al., 2000; Wong and Kaas, 2010), New World owl monkeys (Gould et al., 1986) and squirrel monkeys (Donoghue et al., 1992; Nudo et al., 1992), Old World macaques (Huntley and Jones, 1991; Preuss et al., 1997) and baboons (Waters et al., 1990), and Great Ape chimpanzees (Bailey et al., 1950). Hindlimb movement representations (foot) are located at the most dorsal-medial aspect of M1, and transitions to movements of the trunk of the body (trunk), forelimb and hand (hand), and finally face at the most ventral-lateral aspect of M1. Cortical areas located rostral to M1 include the dorsal (PMd) and ventral (PMv) premotor areas, the supplementary motor area (SMA), and frontal eye fields (FEF). Somatosensory areas of the anterior parietal cortex (3a, 3b, 1, 2) are caudal to M1. The location of the central sulcus (CS) is indicated in macaque, baboon, and chimpanzee.

Figures 2B,C show where the dissection cuts were placed relative to the physiological motor map. **Figure 2D** illustrates the cell and neuron estimates for each sample according to its location and corresponding movement representation in M1. The data illustrated in the figure show that the more lateral regions of M1, which correspond to the face area, contain a higher density of neurons per mm^2 of surface area than medial M1.

OLD WORLD PRIMATES

One macaque cortical hemisphere used in this study was manually flattened (macaque 1), while the cortical hemisphere of the other macaque brain (macaque 2) remained intact, thus surface area measurements were unavailable for macaque 2. The total surface area of the flattened cortical hemisphere was 15,200 mm^2 (macaque 1) and weighed 116.1 g. M1 was visualized and dissected using the lightbox method for the flat cortical hemisphere in addition to the proximity to sulcal landmarks, while M1 in the intact cortical hemisphere (macaque 2) was estimated using sulcal patterns as landmarks based on previous reports (McGuinness et al., 1980; Wise and Tanji, 1981; Sessle and Wiesendanger, 1982; Huntley and Jones, 1991; Qi et al., 2000, 2010). **Table 1** shows that the average M1 cell density in macaques is 75 million cells/g. The M1 cell density for macaque 1 alone was 84.1 million cells/g and the total cell density averaged across the entire cortex in case macaque 1 was 100 million cells/g. We found that the average proportion of DAPI-labeled nuclei that were also NeuN-IR was 30.9% in macaque monkeys. The average neuron density in M1 was 23.5 million neurons/g for macaques. The M1 neuron density for macaque 1 alone was 22.3 million neurons/g. When averaged across all areas of cortex in macaque 1, the overall neuron density was 48.0 million neurons/g.

For the baboons analyzed in this study, the total surface area of the flat cortex was 18,577 mm^2 (baboon 1), and 23,400 mm^2 (baboon 2). The total cortex weight for these individuals was fairly consistent at 50.0 g in baboon 1 and 56.4 g in baboon 2. M1 was identified and dissected in both baboon cases by visual identification on a lightbox using myelination patterns using sulcal landmarks as reference. **Table 1** shows the summary of M1 data in both individuals. M1 comprised 3.55% (baboon 2) and 4.20% (baboon 1) of the total cortical mass, and 2.72% (baboon 2) and 3.52% (baboon 1) of the total cortical area. The average cell density in M1 was 80 million cells/g or 26,000 cells per mm^2 of cortical surface for baboon 1, and 72.6 million cells/g or 22,800 cells per mm^2 for baboon 2. The average proportion of DAPI-labeled nuclei that we found to also be NeuN-IR was 34.8% in baboon 1 and 38.6% in baboon 2, therefore the M1 neuron densities in these cases were 28.11 million neurons/g (90,000 neurons/mm^2) and 28.10 million/g (88,000 neurons/mm^2), respectively. These results were highly consistent across the two individuals.

We compared the M1 density averages to the overall cortical density average, and also compared them to the density averages for a readily identifiable primary sensory cortical area, V1 (primary visual cortex). The overall cortical cell density, averaged across all cortical areas and regions was 95.9 million cells/g or 251,603 cells per mm^2 (baboon 1) and 78.3 million cells/g or 183,441 cells per mm^2 (baboon 2). The neuron fraction across the cortex was 51% (baboon 1) and 54% (baboon 2), therefore the overall neuron density across the cortex was 51.1 million neurons/g or 128,950 neurons per mm^2 and 42.9 million neurons/g or 97,005 million neurons per mm^2, respectively. To contrast the M1 cell and neuron density data with a primary sensory cortical area, the average cell density in V1 was 144 million cells/g or 283,307 cells per mm^2 (baboon 1) and 139 million cells/g or 223,456 cells per mm^2 (baboon 2). In V1, the fraction of DAPI-labeled nuclei that were also NeuN-IR was 75% (baboon 1) and 72% (baboon 2), therefore the V1 neuron densities in each case were 109 million neurons/g or 210,479 neurons per mm^2 and 101 million neurons/g or 163,100 neurons per mm^2, respectively. Cell and neuron densities in M1 were lower than the overall cortical average, and they were also much lower than cell and neuron density estimates in V1. In this data set, we report the baboon data separately as each case was a hybrid species of baboon, however, there was remarkable consistency in the overall, M1 and V1 data between the two cases in cell and neuron densities, showing a roughly 3-fold decrease in the cell density in M1 compared to V1, and an approximately 5-fold difference in neuron density between M1 and V1.

In each baboon and macaque case, we estimated the locations of M1 movement representations and dissected areas according to those estimates. Without electrophysiological data to support our boundary estimates, we assigned dissected M1 cortical pieces to the likely lower limb, trunk, upper limb, hand, and face representations in a mediolateral sequence. The data in **Figure 3** shows the distribution of cells and neurons within these representations for each individual, in a lateral-to-medial sequence from left to right. The neuron densities was found be higher in lateral parts of M1, corresponding to the face and hand representations, than in medial M1 (**Figure 3D**).

OWL MONKEY, SQUIRREL MONKEY, AND CHIMPANZEE

The total surface area of the flattened owl monkey cortex was 2000 mm^2 with a total weight of 5.21 g. The boundaries of M1 were estimated according to myelination patterns and cortical landmarks and was dissected and processed as a single sample. M1 comprised 5.12% of the total mass of the cortex and 8.6%

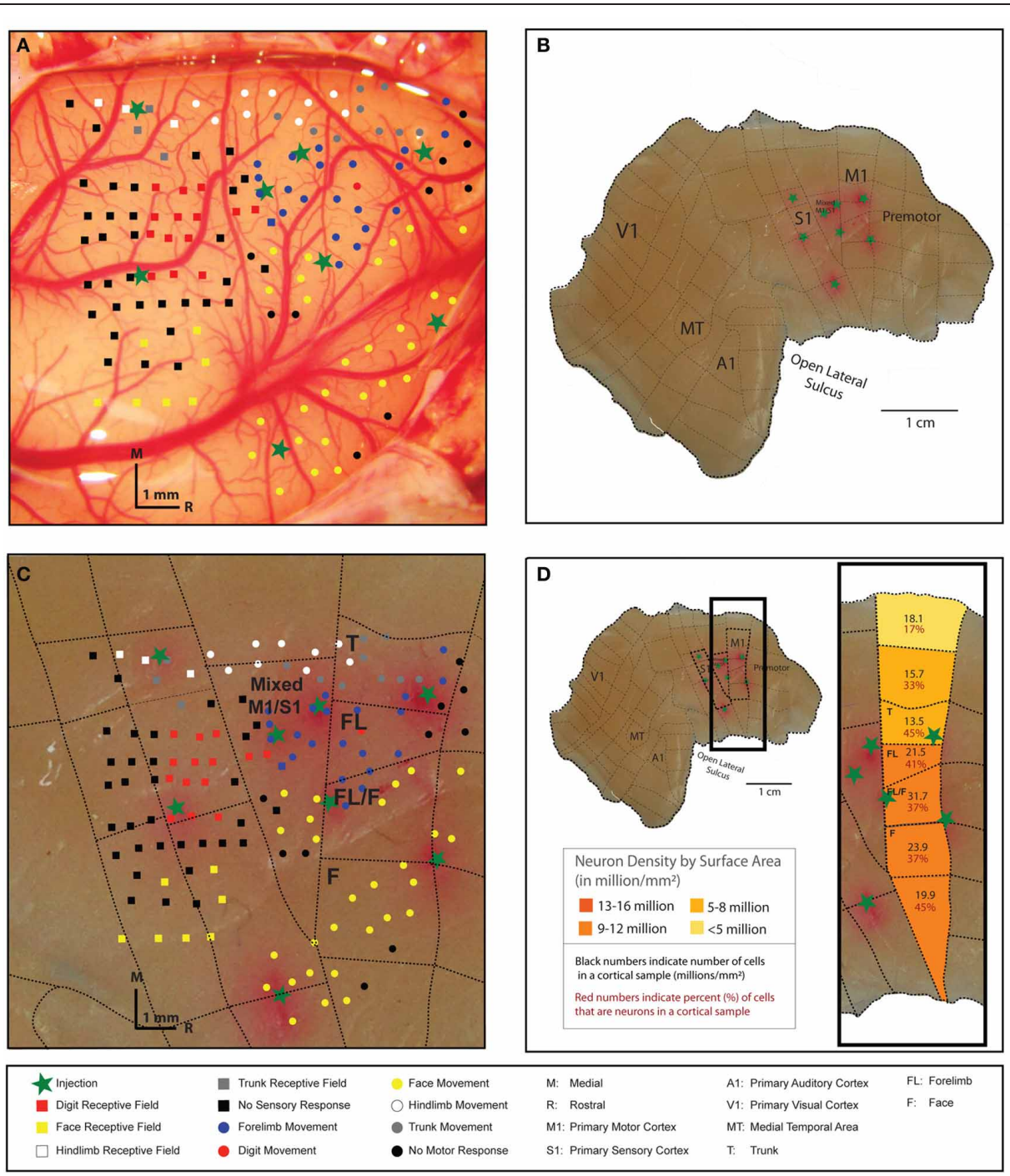

FIGURE 2 | The right cortical hemisphere of a galago (galago 3) was exposed, and movements were evoked at cortical sites in M1 with 60-ms microstimulation trains delivered to layer 5 (A). The locations of stimulation sites where movements were elicited are indicated by color-coded dots on the cortical surface. Somatosensory mapping of receptive fields (layer 4) responsive to tactile stimulation are indicated by color-coded squares on the cortical surface. Somatosensory mapping was undertaken to better identify the caudal boundary of M1. Boundaries of M1 and S1, and identifiable movement representations areas within M1, were marked with a fluororuby tracer (FR) immediately before sacrifice to estimate their location on the cortical surface (green stars). Following sacrifice, the brain was removed and the right cortical hemisphere was manually flattened **(B)**. The FR-indicated areas were used as guidelines to conservatively dissect microstimulation-derived M1representations from remaining cortex. Dashed lines indicate dissections lines that resulted in 84 pieces for the entire cortical hemisphere. The dissection resulted in four pieces identified as M1 by microstimulation mapping **(C)**. Areas dedicated to movements of the trunk, forelimb, and face were readily identified and efforts were made to dissect along these movement representations boundaries within M1. Each M1 piece, as well as cortical pieces medial and lateral to M1, had cell and neuron densities estimated using the flow fractionator method **(D)**. The most lateral aspect of M1, which includes facial movement representations, is the most neuron dense area.

Table 1 | Summary of neuron and cell density in primary motor cortex by mass and surface area.

Species	Mass (g)	Percent total mass	Area (mm^2)	Percent total area	Cell density (millions)		Percent neurons in M1 (%)	Neuron density (millions)		Percent neuron difference from total average (%)
					Cells/g	Cells/mm^2		Neurons/g	Neurons/mm^2	
Otolemur garnettii ($n = 3$)	0.065 ± 0.02	3.13 ± 0.03	43.22 ± 12.70	2.78 ± 0.82	118.84 ± 17.72	0.181 ± 0.038	32.2 ± 5.9	29.04 ± 12.32	0.068 ± 0.041	-7.1 ± 0.2
Aotus nancymaae ($n = 1$)	0.267	5.12	221.83	8.6	114.91	0.138	36.0	41.37	0.050	−3.1
Saimiri sciuresis ($n = 1$)	0.344	3.11	125.1	2.57	91.39	0.251	33.7	30.00	0.082	−21.3
Macaca nemenstrina ($n = 2$)	1.381 ± 0.160	N/A	N/A	2.20	75.06 ± 10.14	N/A	30.9 ± 5.7	23.51 ± 0.49	N/A	N/A
Papio cynocephalus anubis ($n = 1$)	2.102	4.20	653.8	3.52	80.78	0.260	34.8	28.11	0.090	−14.93
Papio hamadryas anubis ($n = 1$)	2.000	3.55	636.4	2.72	72.62	0.228	38.6	28.10	0.088	−12.4
Pan troglodytes ($n = 1$)	7.520	N/A	2700	N/A	73.01	0.203	27.0	19.30	0.055	N/A

All values are reported as mean ± standard deviation where applicable. The n value refers the number of cortical hemispheres available for study. Percent Total Mass refers to the percentage of cortical mass dedicated to M1 within the mass of the cortical hemisphere. Percent Total Area refers to the percentage of cortical area dedicated to M1 across the entire cortical hemisphere. Percent Neuron Difference for Total Average refers to the Percent Neurons in M1 minus the overall percent of neurons averaged across the entire cortical hemisphere.

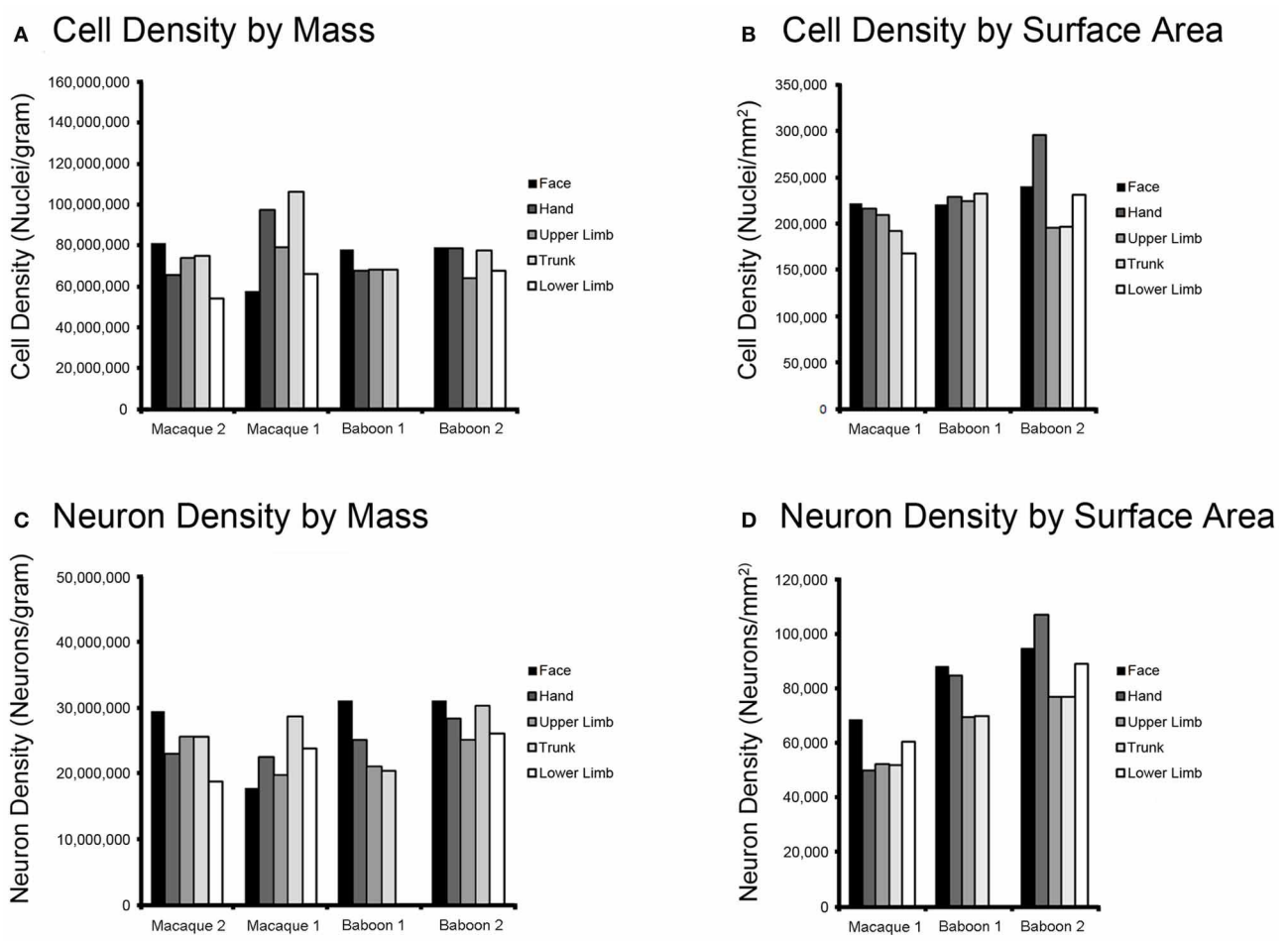

FIGURE 3 | Histograms of cell and neuron density in M1 of Old World monkeys. Movement representation boundaries within M1 were estimated, the motor cortex was dissected along those boundaries, and cell and neuron densities were obtained using the flow fractionator. The results show that distribution of cells by mass **(A)** and by surface area **(B)** does not vary substantially within M1 in either the macaque (macaque 1; macaque 2) or baboon (baboon 1; baboon 2). Neuron density by mass **(C)** and surface area **(D)** shows a trend toward the most lateral aspect within M1, which includes face and hand movement representations, as being the most neuron dense area in both species. Please note that macaque 2 was an intact dissection and, as a result, cortical surface area could not be accurately estimated.

of the total cortical surface area. The M1 cell and neuron density by weight are approximately 115 million cells/g and 41 million neurons/gram of cortical tissue. The M1 cell and neuron densities per mm^2 of cortical surface are 138,000 cells/mm^2 and 50,000 neurons/mm^2. The overall cell density averaged across the entire cortex was 139 million cells/g or 276,595 cells per mm^2. The overall proportion of neurons was 39%, compared to the M1 neuron proportion of 36%, resulting in an overall neuron density of 55.6 million neurons/g or 106,227 neurons per mm^2. The V1 cell density in this case was 165 million cells/g or 270,703 cells per mm^2. The proportion of cells in V1 that were NeuN-IR was 58%, resulting in a neuron density of 96.7 million neurons/g or 158,554 neurons per mm^2 of primary visual cortex. V1 has approximately a two-fold higher neuron density than M1.

The flattened squirrel monkey cortex had a total surface area of 4900 mm^2 and weighted 11.1 g. M1 comprised 3.11% of the total mass of the cortex and 2.57% of the total cortical surface area. Cell and neuron densities by weight are 91 million cells/g and 30 million neurons/g. Cell and neuron densities by surface area are 251,000 cells/mm^2 and 82,000 neurons/mm^2 of cortical surface area (**Table 1**). The overall cell density averaged across the entire cortex was 134 million cells/g or 279,862 cells per mm^2. With an overall neuron fraction of 55%, the overall cortical neuron density was 79.5 million neurons/g or 159,457 neurons per mm^2. V1 cell density was 202 million cells/g or 345,197 cells per mm^2. With a V1 neuron fraction of 75%, this resulted in a neuron density of 152 million neurons/g or 255,897 neurons per mm^2 of primary visual cortex. M1 neuron density is approximately five times lower than the neuron density in V1, and over two times lower than average cortical density.

In the chimpanzee, M1 weighted 7.25 g and had a surface area of 2700 mm^2. The cell and neuron densities for M1 are 73 million cells/g and 19 million neurons/g. The cell and neuron densities for M1 by surface area are 203,000

cells/mm^2 and 55,000 neurons/mm^2 (**Table 1**). M1 contains about 27% neurons overall. V1 data are not yet available for this species.

DISCUSSION

Here we demonstrate that tissue boundaries for cortical areal dissections are readily determined by electrophysiological mapping, and that estimates of areal boundaries based on cortical landmarks also result in reasonably accurate dissections. The average percentage of NeuN-immunoreactive cells in M1 was fairly consistent across all six species of primates reported here, ranging from approximately 27% neurons in the chimpanzee to 36% neurons in the baboon. From the present dataset, it appears that primary motor cortex is approximately 2–5 times less neuron-dense than primary visual cortex and 1.4–2.7 times less dense than cortex overall in the species examined here. Four of the five species examined here showed a 5-fold difference in M1:V1 neuron density, with the exception being the nocturnal owl monkey that had a two-fold difference. The owl monkey, however, is the only species examined here to have an overall neuron density in V1 that is less than 100 million neurons/g of cortical tissue, making it unusual in comparison to the other primates. In species where it was possible to dissect M1 according to motor representations, there appears to be a trend toward a higher density of neurons in more lateral regions of M1, representing hand and face, compared to more medial areas representing trunk and hindlimb. These data, however, are based on one case where representational boundaries were defined electrophsyiologically and four other cases in which the boundaries were approximated using cortical landmarks.

CELLS AND NEURON DENSITIES IN M1 IN PRIMATES

The locations and organizations of M1 are similar across the six species of primates we have examined, and between individuals within a species, which suggests that the primate pattern of primary motor cortex emerged early in primate evolution, and has been conserved in the prosimian and simian branches within the primate order. We have shown that the proportion of mass and surface area dedicated to M1 remains relatively constant across species, despite the roughly 15-fold variation in total cortical surface area across the species examined.

ARCHITECTURE AND NEURON DENSITY

In a previous study, we demonstrated that primate M1 has a distinctively lower neuron density relative to other areas and regions of cortex and that the primate cortex is not uniform in its distribution of neurons across areas and regions (Collins et al., 2010b). These results are consistent with those of other reports in which the lowest neuron densities in the cortex reported for cats and rats were also in the primary motor area (Beaulieu and Colonnier, 1989; Skoglund et al., 1996). Our data extend these findings to primates. In addition, our findings illustrating variations in neuron density by representational zone in M1 are analogous to the previous finding of the highest neuron density in V1 of cats, occurring in the binocular representational zone (Beaulieu and Colonnier, 1989). In contrast to these consistent findings for M1 across rats, cats and a range of primates, a recent report including several species reported similar neuron densities for all cortical areas, including M1, except for V1 of primates (Carlo and Stevens, 2013). This study basically repeated the earlier observations of Rockel et al. (1980). We do not know the reasons for such contradictory findings, except to note that both of the studies used extremely sparse sampling, and the methods for identifying cortical areas were unclear.

One reason for a real differences in neuron density appears to be layer 4. The neuron dense layer of tightly packed, small neurons is remarkably thin and nearly indistinguishable in primary motor cortex, M1. Beaulieu and Colonnier (1989) concluded that areas in cats with the highest neuron densities tended to be sensory areas with a wide, neuron-dense layer IV, whereas motor areas had lower neuron densities and a significantly reduced layer 4. Variations in neuron densities across areas and regions of the cortex have been attributed to differences in developmental programs, with primary sensory areas having higher neuron densities (Dehay and Kennedy, 2007) and rostral portions of the cerebral cortex generally having a lower overall neuron density relative to more caudal cortical areas (Cahalane et al., 2012).

In addition to having a thin or missing layer of small granule cells, M1 is characterized by some of the largest of pyramidal cells (e.g., Stepniewska et al., 1993; Preuss et al., 1996, 1997). The sizes of pyramidal cells also differ across cortical areas (e.g., see Elston and Rosa, 1997; Elston and Rockland, 2002; Elston et al., 2005a,b; Bianchi et al., 2012) in ways that likely account for different functional capabilities. For example, spine densities on the basal dendritic arbors of pyramidal neurons in layer III of granular prefrontal cortex (gPFC) are as much as 16 times greater than spine densities on layer III pyramidal cells in V1 (Elston et al., 2006). These large neurons are more densely interconnected and potentially sum more sources of inputs within their more complex dendritic arbors (Elston, 2007). In general, small cells are activated by few inputs and thereby preserve information, while large pyramidal neurons sum many inputs and have integrated functions (Kaas, 2000).

The agranular and dysgranular cortex of M1 is comprised mostly of large pyramidal neurons in prominent layers 3 and 5, with some pyramidal cells in layer 5 being Betz cells, the largest neurons in the cortex, with diameters as large as 100 microns. Given the relatively lower density of neurons in primary motor cortex in the primates examined here, particularly in relation to the extremely high neuron densities in V1 where the neurons are extremely small, it seems reasonable to surmise that neuron density and neuron size may co-vary. However, previous research has examined the relationship between soma size and dendritic arbor size, concluding that the largest cells do not necessarily have the largest dendritic arbors (Elston and Rockland, 2002). Moreover, the spine density of neurons in M1 is significantly higher than that in V1 layer III pyramidal cells, but is lower than in pyramidal cells in layer III of premotor area 6 (Elston and Rockland, 2002; Elston, 2007).

HETEROGENEITY WITHIN M1 IN PRIMATES

We have previously demonstrated that M1 in primates is a region that, as a whole, is neuron sparse relative to the rest of cortex (Collins et al., 2010b). Here we demonstrate that it is also a heterogeneous structure that varies in neuron density across different

representational zones, with lower neuron densities in medial M1 and higher neuron densities in lateral M1.

More medial M1 representing movements of the lower body is also more myelinated, possibly because corticospinal projections of the lower body movement representations in medial M1 are more heavily myelinated because they traverse longer distances to reach their more distant spinal cord targets (Glasser and Van Essen, 2011). Heavier myelination, in combination with a larger axon, would speed conductance to long-range targets. Hand and face body movement representations of lateral M1 would be less heavily myelinated due to closer proximity of their targets. In general, neurons with longer, thicker axons have larger cell bodies that reduce overall neuron densities.

Another possibility is that the higher neuron densities in lateral M1 reflect higher numbers of modulatory GABAergic interneurons. During the execution of voluntary movements, fast-spiking parvalbumin (PV)-expressing GABAergic interneurons are active in motor cortex, which suggests that they play a role in shaping ongoing movements (Isomura et al., 2009). The distribution and pattern of GABAergic immunoreacitve neurons in the visual areas processing areas (DeFelipe et al., 1999), and prefrontal cortex (Elston and Gonzalez-Albo, 2003) has been thought to vary with regional specializations related to information processing demands. The M1 face representation in hominids has a greater number of PV-immunoreactive neurons relative to Old World species, and this modification in face representation microcircuitry may be involved in supporting sophisticated coordination of facial muscles (Sherwood et al., 2004). A higher number of modulatory interneurons in face and hand representations may reflect an increased capacity for fine motor control, allowing the social advantage of better and increased skill in manipulating the external environment with the hands. The distribution of GABAergic subtypes have been characterized within specific movement representations and compared across species (Sherwood et al., 2003, 2004) or across other cortical areas outside M1 (Sherwood et al., 2010), but no study has yet examined the GABAergic neuron distribution within the mediolateral sequence of M1 movement representations.

ACKNOWLEDGMENTS

This work was supported by a grant from the G. Harold and Leila Y. Mathers Foundation to Jon H. Kaas and Christine E. Collins. Flow cytometry experiments were conducted in the Vanderbilt Medical Center (VMC) Flow Cytometry Shared Resource. The VMC Flow Cytometry Shared Resource is supported by the Vanderbilt Ingram Cancer Center (P30 CA68485) and the Vanderbilt Digestive Disease Research Center (DK058404). The authors would like to thank Dr. Iwona Stepniewska, Dr. Hui-Xin Qi, David Flaherty, Laura Trice, Feyi Aworunse, and Kallie Foust for assistance.

REFERENCES

Bailey, P., Von Bonin, G., and McCulloch, W. S. (1950). *The Isocortex of the Chimpanzee.* Urbana, IL: University of Illinois Press.

Beaulieu, C., and Colonnier, M. (1989). Number of neurons in individual laminae of areas 3B, 4 gamma, and 6a alpha of the cat cerebral cortex: a comparison with major visual areas. *J. Comp. Neurol.* 279, 228–234.

Bianchi, S., Stimpson, C. D., Bauernfeind, A. L., Schapiro, S. J., Baze, W. B., McArthur, M. J., et al. (2012). Dendritic morphology of pyramidal neurons in the chimpanzee neocortex: regional specializations and comparison to humans. *Cereb. Cortex.* doi: 10.1093/cercor/bhs239. [Epub ahead of print].

Cahalane, D. J., Charvet, C. J., and Finlay, B. L. (2012). Systematic, balancing gradients in neuron density and number across the primate isocortex. *Front. Neuroanat.* 6:28. doi: 10.3389/fnana.2012.00028

Campi, K. L., Collins, C. E., Todd, W. D., Kaas, J., and Krubitzer, L. (2011). Comparison of area 17 cellular composition in laboratory and wild-caught rats including diurnal and nocturnal species. *Brain Behav. Evol.* 77, 116–130.

Carlo, C. N., and Stevens, C. F. (2013). Structural uniformity of the neocortex, revisited. *Proc. Natl. Acad. Sci. U.S.A.* 110, 1488–1493.

Christensen, J. R., Larsen, K. B., Lisanby, S. H., Scalia, J., Arango, V., Dwork, A. J., et al. (2007). Neocortical and hippocampal neuron and glial cell numbers in the rhesus monkey. *Anat. Rec.* 290, 330–340.

Collins, C. E., Young, N. A., Flaherty, D. K., Airey, D. C., and Kaas, J. H. (2010a). A rapid and reliable method for counting neurons and other cells in brain tissue: a comparison of flow cytometry and manual counting methods. *Front. Neuroanat.* 4:5. doi: 10.3389/neuro.05.005.2010

Collins, C. E., Airey, D. C., Young, N. A., Leitch, D. B., and Kaas, J. H. (2010b). Neuron densities vary across and within cortical areas in primates. *Proc. Natl. Acad. Sci. U.S.A.* 107, 15927–15932.

DeFelipe, J., González-Albo, M. C., del Río, M. R., and Elston, G. N. (1999). Distribution and patterns of connectivity of interneurons containing calbindin, calretinin and parvalbumin in visual areas of the occipital and temporal lobes of the macaque monkey. *J. Comp. Neurol.* 412, 515–526.

Dehay, C., and Kennedy, H. (2007). Cell-cycle control and cortical development. *Nat. Rev. Neurosci.* 8, 438–450.

Donoghue, J. P., Liebociv, S. J., and Sanes, J. N. (1992). Organization of the forelimb area in squirrel monkey motor cortex: representation of individual digit, wrist, and elbow muscles. *Exp. Brain Res.* 89, 1–19.

Elston, G. N. (2007). "Specialization of the neocortical pyramidal cell during primate evolution," in *Evolution of the Nervous System: A Comprehensive System Reference,* ed J. H. Kaas (Oxford, UK: Elsevier Inc), 191–242.

Elston, G. N., Benavides-Piccione, R., Elston, A., DeFelipe, J., and Manger, P. (2005a). Specialization in pyramidal cell structure in the sensory-motor cortex of the vervet monkey (*Cercopithecus pygerythrus*). *Neuroscience* 134, 1057–1068.

Elston, G. N., Benavides-Piccione, R., Elston, A., Manger, P., and DeFelipe, J. (2005b). Specialization in pyramidal cell structure in the sensory-motor cortex of the Chacma baboon (*papio ursinus*) with comparative notes on the macaque monkey. *Anat. Rec. A Discov. Mol. Cell. Evol. Biol.* 286, 854–865.

Elston, G. N., Benavides-Piccione, R., Elston, A., Zietsch, B., Defelipe, J., Manger, P., et al. (2006). Specializations of the granular prefrontal cortex of primates: implications for cognitive processing. *Anat. Rec. A Discov. Mol. Cell. Evol. Biol.* 288, 26–35.

Elston, G. N., and Gonzalez-Albo, M. C. (2003). Parvalbumin-, calbindin-, and calretinin-immunoreactive neurons in the orefrontal cortex of the owl monkey (*Aotus trivirgatus*): a standardized quantitative comparsion with sensory and motor areas. *Brain Behav. Evol.* 62, 19–30.

Elston, G. N., and Rockland, K. (2002). The pyramidal cell of the sensorimotor cortex of the macaque monkey: phenotypic variation. *Cereb. Cortex* 12, 1071–1078.

Elston, G. N., and Rosa, M. G. P. (1997). The occipitoparietal pathway of the macaque monkey: comparison of pyramidal cell morphology in layer III of functionally related cortical visual areas. *Cereb. Cortex* 7, 432–452.

Fang, P. C., Stepniewska, I., and Kaas, J. H. (2008). Corpus callosum connections of subdivisions of motor and premotor cortex, and frontal eye field in a prosimian primate, *Otolemur garnetti*. *J. Comp. Neurol.* 508, 565–578.

Gaspar, P., Stepniewska, I., and Kaas, J. H. (1992). Topography and

collateralization of the dopaminergic projections to motor and lateral prefrontal cortex in owl monkeys. *J. Comp. Neurol.* 325, 1–21.

Gharbawie, O. A., Stepniewska, I., Qi, H. X., and Kaas, J. H. (2011). Multiple parietal-frontal pathways mediate grasping in macaque monkeys. *J. Neurosci.* 31, 11660–11677.

Glasser, M. F., and Van Essen, D. C. (2011). Mapping human cortical areas *in vivo* based on myelin content and revealed by T1- and T2-weighted MRI. *J. Neurosci.* 31, 11597–11616.

Gould, H. J., Cusick, C. G., Pons, T. P., and Kaas, J. H. (1986). The relationship of the corpus callosum connections to electrical stimulation maps of the motor, supplementary motor, and the frontal eye fields in owl monkeys. *J. Comp. Neurol.* 247, 297–325.

Herculano-Houzel, S., Collins, C. E., Wong, P., Kaas, J. H., and Lent, R. (2008). The basic non-uniformity of the cerebral cortex. *Proc. Natl. Acad. Sci. U.S.A.* 105, 12593–12598.

Herculano-Houzel, S., and Lent, R. (2005). Isotropic fractionator: a simple, rapid method for the quantification of total cell and neuron numbers in the brain. *J. Neurosci.* 25, 2518–2521.

Huang, C. S., Sirisko, M. A., Hiraba, H., and Murray, G. M. (1988). Organization of the primate face motor cortex as served by intracortical microstimulation and electrophysiological identification of afferent inputs and corticobulbar projections. *J. Neurophysiol.* 59, 796–818.

Huntley, G. W., and Jones, E. G. (1991). Relationship of intrinsic connections to forelimb movement representations in monkey motor cortex: a correlative anatomical and physiological study. *J. Neurophysiol.* 66, 390–413.

Isomura, Y., Harukuni, R., Takekawa, T., Aizawa, H., and Fukai, T. (2009). Microcircuitry coordination of cortical motor information in self-initiation of voluntary movements. *Nat. Neurosci.* 12, 1586–1593.

Jain, N., Qi, H. X., Catania, K. C., and Kaas, J. H. (2000). Anatomical correlates of the face and oral cavity representations in the somatosensory cortical area 3b on monkeys. *J. Comp. Neurol.* 429, 455–468.

Kaas, J. H. (2000). Why is brain size so important: design problems and solutions as neocortex gets bigger or smaller. *Brain Mind* 1, 7–23.

Kaas, J. H. (2012). Evoultion of columns, modules, and domains in the neocortex of primates. *Proc. Natl. Acad. Sci. U.S.A.* 109, 10655–10660.

Kaas, J. H., Gharbawie, O. A., and Stepniewska, I. (2012). Cortical networks for ethologically relevant behaviors in primates. *Am. J. Primatol.* doi: 10.1002/ajp.22065. [Epub ahead of print].

McGuinness, E., Sivertsen, D., and Allman, J. M. (1980). Organization of the face representation in macaque motor cortex. *J. Comp. Neurol.* 193, 591–608.

Nudo, R. J., Jenkins, W. M., Merzenich, M. M., Prejean, T., and Grenda, R. (1992). Neurophysiological correlates of the hand preference in primary motor cortex of adult squirrel monkeys. *J. Neurosci.* 12, 2918–2947.

Pakkenberg, B., and Gundersen, H. J. (1997). Neocortical neuron number in humans: effect of sex and age. *J. Comp. Neurol.* 384, 312–320.

Preuss, T. M., Stepniewska, I., Jain, N., and Kaas, J. H. (1997). Multiple divisions of macaque precentral motor cortex identified with neurofilament antibody SMI32. *Brain Res.* 767, 148–153.

Preuss, T. M., Stepniewska, I., and Kaas, J. H. (1992). Microstimulation studies of motor cortical organization in lorisid primates. *Eur. J. Neurosci. Suppl.* 5:174.

Preuss, T. M., Stepniewska, I., and Kaas, J. H. (1996). Movement representation in the dorsal and ventral premotor areas of owl monkeys: a microstimulation study. *J. Comp. Neurol.* 371, 649–676.

Qi, H.-X., Gharbawie, O. A., Wong, P., and Kaas, J. H. (2011). Cell-poor septa separate representations of digits in the ventroposterior nucleus of the thalamus in monkeys and prosimian galagos. *J. Comp. Neurol.* 519, 738–758.

Qi, H. X., Jain, N., Collins, C. E., Lyon, D. C., and Kaas, J. H. (2010). Functional organization of motor cortex of adult macaque monkeys is altered by sensory loss in infancy. *Proc. Natl. Acad. Sci. U.S.A.* 107, 3192–3197.

Qi, H. X., Stepniewska, I., and Kaas, J. H. (2000). Reorganization of primary motor cortex in adult macaque monkeys with long-standing amputations. *J. Neurophysiol.* 84, 2133–2147.

Rockel, A. J., Hiorns, R. W., Powel, T. P. (1980). The basic uniformity in the structure of the neocortex. *Brain* 103, 221–244.

Sessle, B. J., and Wiesendanger, M. (1982). Structural and functional definition of the motor cortex in the monkey (*Macaca fascicularis*). *J. Physiol.* 323, 245–265.

Sherwood, C. C., Holloway, R. L., Erwin, J. M., and Hof, P. R. (2004). Cortical orofacial motor representation in old world monkeys, great apes, and humans. II. Stereological analysis of chemoarchitecture. *Brain Behav. Evol.* 63, 82–106.

Sherwood, C. C., Holloway, R. L., Gannon, P. J., Semendeferi, K., Erwin, J. M., Zilles, K., et al. (2003). Neuroanatomical basis of facial expression in monkeys, apes, and humans. *Ann. N.Y. Acad. Sci.* 1000, 99–103.

Sherwood, C. C., Raghanti, M. A., Stimpson, C. D., Spocter, M. A., Uddin, M., Boddy, A. M., et al. (2010). Inhibitory interneurons of the uman prefrontal cortex display conserved evolution of the phenotype and related genes. *Proc. Biol. Sci.* 277, 1011–1120.

Skoglund, T. S., Pascher, R., and Berthold, C. H. (1996). Heterogeneity in the columnar number of neurons in different neocortical areas in the rat. *Neurosci. Lett.* 208, 97–100.

Stepniewska, I., Fang, P. C., and Kaas, J. H. (2005). Microstimulation reveals specialized subregions for different complex movements in posterior parietal cortex of prosimian galagos. *Proc. Natl. Acad. Sci. U.S.A.* 102, 4878–4883.

Stepniewska, I., Fang, P. Y., and Kaas, J. H. (2009). Organization of the posterior parietal cortex in galagos: 1. Functional zones identified by microstimulation. *J. Comp. Neurol.* 517, 765–782.

Stepniewska, I., Preuss, T. M., and Kaas, J. H. (1993). Architectonics, somatotopic organization, and ipsilateral cortical connections of the primary motor area (M1) of owl monkeys. *J. Comp. Neurol.* 330, 238–271.

Van Essen, D. C., Glasser, M. F., Dierker, D. L., and Harwell, J. (2011). Cortical parcellations of the macaque monkey analyzed on surface-based atlases. *Cereb. Cortex* 22, 2227–2240.

Waters, R. S., Samulack, D. D., Dykes, R. W., and McKinley, P. A. (1990). Topographic organization of the baboon primary motor cortex: face, hands, forelimb, and shoulder representations. *Somatosens. Mot. Res.* 7, 485–514.

Wise, S. P., and Tanji, J. (1981). Supplementary and precentral motor cortex: contrast in responsiveness to peripheral input in the hindlimb area of the unanesthetized monkey. *J. Comp. Neurol.* 195, 433–451.

Wong, P., and Kaas, J. H. (2010). Architectonic subdivisions of neocortex in the Galago (*Otolemur garnetti*). *Anat. Rec.* 293, 1033–1069.

Wu, C. W.-H., Bichot, N. P., and Kaas, J. H. (2000). Converging evidence from microstimulation, architecture, and connections for multiple motot areas in the frontal and cingulate cortex of prosimian primates. *J. Comp. Neurol.* 423, 140–177.

Wu, C. W.-H., and Kaas, J. H. (2003). Somatosensory cortex of prosimian Galagos: physiological recording, cytoarchitecture and corticocortical connections of anterior parietal cortex and cortex of the lateral sulcus. *J. Comp. Neurol.* 457, 263–292.

Young, N. A., Flaherty, D. K., Airey, D. C., Varlan, P., Aworunse, F., Kaas, J. H., et al. (2012). Use of flow cytometry for high-throughput cell population estimates in brain tissue. *Front. Neuroanat.* 6:27. doi: 10.3389/fnana.2012.00027

Young, N. A., Vuong, J., Flynn, C., and Teskey, G. C. (2011). Optimal parameters for microstimulation derived forelimb movement thresholds and motor maps in rats and mice. *J. Neurosci. Methods* 196, 60–69.

Conflict of Interest Statement: The authors declare that the research was conducted in the absence of any commercial or financial relationships that could be construed as a potential conflict of interest.

Received: 30 November 2012; accepted: 08 February 2013; published online: 27 February 2013.

Citation: Young NA, Collins CE and Kaas JH (2013) Cell and neuron densities in the primary motor cortex of primates. Front. Neural Circuits 7:30. doi: 10.3389/fncir.2013.00030

frontiers in
NEURAL CIRCUITS

MINI REVIEW ARTICLE
published: 21 February 2013
doi: 10.3389/fncir.2013.00021

The motor cortex: a network tuned to 7–14 Hz

Manuel A. Castro-Alamancos*

Department of Neurobiology and Anatomy, Drexel University College of Medicine, Philadelphia, PA, USA

Edited by:
Michael Brecht, Humboldt University Berlin, Germany

Reviewed by:
Daniel Huber, University of Geneva, Switzerland
Taro Kiritani, École Polytechnique Fédérale de Lausanne, Switzerland

***Correspondence:**
Manuel A. Castro-Alamancos, Department of Neurobiology and Anatomy, Drexel University College of Medicine, 2900 Queen Lane, Philadelphia, PA 19129, USA.

The neocortex or six layer cortex consists of at least 52 cytoarchitectonically distinct areas in humans, and similar areas can be distinguished in rodents. Each of these areas has a defining set of extrinsic connections, identifiable functional roles, a distinct laminar arrangement, etc. Thus, neocortex is extensively subdivided into areas of anatomical and functional specialization, but less is known about the specialization of cellular and network physiology across areas. The motor cortex appears to have a distinct propensity to oscillate in the 7–14 Hz frequency range. Augmenting responses, normal mu and beta oscillations, and abnormal oscillations or after discharges caused by enhancing excitation or suppressing inhibition are all expressed around this frequency range. The substrate for this activity may be an excitatory network that is unique to the motor cortex or that is more strongly suppressed in other areas, such as somatosensory cortex. Interestingly, augmenting responses are dependent on behavioral state. They are abolished during behavioral arousal. Here, I briefly review this evidence.

Keywords: oscillatory activity, motor cortex, behavioral state, potassium channels, voltage-gated, excitatory synapses

MOTOR CORTEX IS MORPHOLOGICALLY DISTINCT

The location, general organization, and cytoarchitectural correlates of the principal fields of the rat somatosensory and motor cortex have been established with anatomical and electrophysiological techniques. The primary motor cortex, identified as the region of cortex where intracortical stimulation produces movements at the lowest thresholds, occupies two cytoarchitectonic fields. The majority of motor cortex coincides with a distinct frontal agranular area called the *lateral agranular* field that represents the head including the whiskers, the trunk, and part of the forelimb (Hall and Lindholm, 1974; Donoghue and Wise, 1982). The remainder of motor cortex is contained in the rostral part of the granular parietal cortex. This part of the primary motor cortex overlaps with the somatosensory cortex and contains the representation of the hindlimb and part of the forelimb. The primary somatosensory cortex lies within the parietal cortex and has two subdivisions. One subdivision contains the representation of cutaneous receptors and coincides with cytoarchitectonically distinct areas that are marked by their densely *granular* layer IV. Each of these granule cell aggregates contains the representation of cutaneous inputs from a particular region of the body such as the forelimb, hindlimb, and whiskers (barrel cortex). Surrounding the granular fields is a second subdivision termed the *dysgranular* field, which has a thin layer IV and cells respond poorly to light tactile stimuli (Welker, 1971, 1976).

Despite the efforts to conceive a canonical cortical circuit (Douglas et al., 1995), the reality is that neocortical areas are morphologically, physiologically, and consequently functionally distinct (Brodmann, 1905; Zilles, 1985; Creutzfeldt and Creutzfeldt, 1993; Mountcastle, 1998). At the laminar, cellular, and synaptic level the motor (mostly agranular) and somatosensory (mostly granular) areas are quite different. In particular, the motor cortex contains a very large layer V and an almost inexistent layer IV, while the opposite is the case for the somatosensory cortex. Most if not all the excitatory cells in motor cortex are pyramidal cells, and the largest of these are encountered in layer V with apical dendrites that reach into layer I (DeFelipe and Farinas, 1992). The cortex also contains a variety of GABAergic non-pyramidal cells (Kawaguchi and Kubota, 1997; Somogyi et al., 1998). The large extension of layer V in motor cortex suggests that it may contain cell populations absent in somatosensory cortex. Indeed, the motor cortex contains a unique layer V cell population, called Betz cells or giant pyramidal cells (Betz, 1874). Interestingly, these cells become increasingly larger in more evolved species (Sherwood et al., 2003). They are generally encountered in layer Vb and can be up to 20 times larger than other pyramidal cells in the same layer. These obvious morphological differences, and many others in more subtle connectivity, are likely to contribute to the distinct specialization of cellular physiology across areas. Here I focus on one such physiological specialization of the motor cortex, its distinct tuning to the 7–14 Hz frequency band.

7–14 Hz AUGMENTING RESPONSES IN MOTOR CORTEX

Afferent activity between 7 and 14 Hz triggers augmenting responses in the motor cortex. Thus, progressively augmenting excitatory responses are generated in the motor cortex when the ventrolateral (VL) nucleus of the thalamus is stimulated electrically at 7–14 Hz, but only decrementing responses are observed in the primary sensory cortex when the ventroposterior medial (VPM) nucleus of the thalamus is stimulated (Castro-Alamancos and Connors, 1996b,c,d). The spatiotemporal response patterns can be revealed by measuring extracellular voltage at regular intervals through the cortical depth, and calculating a map of current source density (CSD). Electrical stimulation delivered in VL produces a response in motor cortex

consisting of a relatively small current sink in layer V and a corresponding current source in upper layers (Castro-Alamancos and Connors, 1996d), which is consistent with the anatomical projections of this thalamic nucleus (Herkenham, 1980; Castro-Alamancos and Connors, 1997). Repetitive electrical stimulation between 7 and 14 Hz generates a strong enhancement of the layer V current sink, and related excitatory postsynaptic potentials recorded intracellularly. These augmenting responses can be generated only within a narrow time interval following a conditioning stimulus; the second stimulus must occur between 50 and 200 ms. The intracellular correlate of the narrow time interval for generating the augmenting response is a prominent hyperpolarization of layer V cells generated by inhibitory postsynaptic potentials recruited through VL thalamocortical fibers stimulation of inhibitory interneurons (**Figure 1A**). The termination of the augmenting interval is marked by a long-latency event that peaks at around 200 ms, and is evident as a slow, negative field potential rebound component that corresponds to a current sink in layer V and a broad depolarizing event intracellularly; akin to a short Up state. Although several cellular mechanisms have been proposed to explain augmenting responses, the underlying mechanisms are not completely established.

Interestingly, the strength of augmenting is dependent on behavioral state (**Figure 1B**). During anesthesia, slow-wave sleep, and quiet periods of awake immobility augmenting is maximal, but as soon as the subject switches to a more activated state, such as exploration or skilled motor behavior (reaching and grasping), the augmenting response is abolished (Castro-Alamancos and Connors, 1996c). During the generation of augmenting responses, activity becomes synchronized over large regions of neocortex (Castro-Alamancos and Connors, 1996b,d). We found that a single VL stimulus, which does not elicit augmenting, activates a very limited region of motor cortex, but a second VL stimulus arriving within 50–200 ms, which elicits augmenting, synchronized the activity across an area several times larger in motor cortex. Thus, augmenting reflects a powerful mechanism that can dynamically change, depending on behavioral state, the level of synchronization of activity in large regions of neocortex. Highly synchronous activity throughout neocortex may impede normal information processing because cortical neurons will all respond in the same fashion at the same time, degrading spatial resolution.

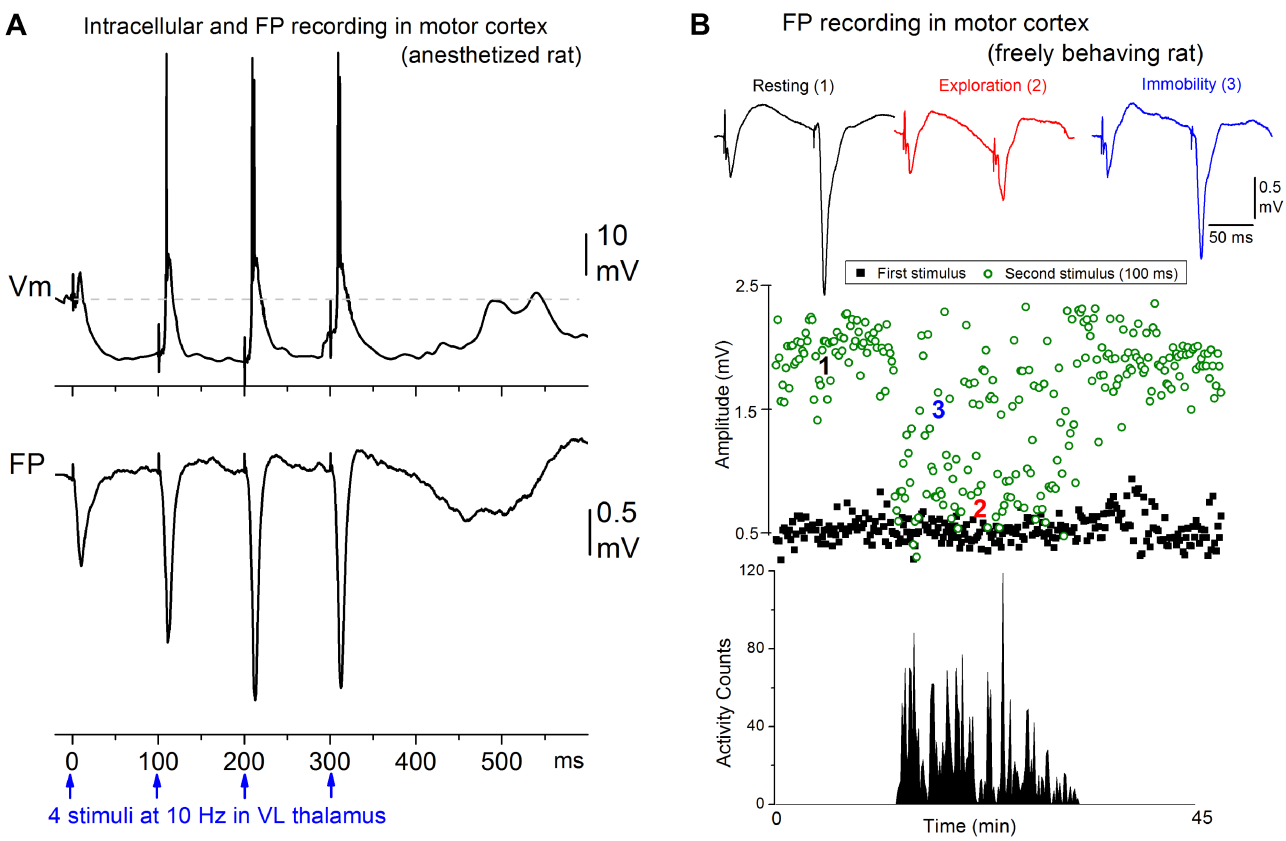

FIGURE 1 | Augmenting responses in motor cortex driven by ventrolateral (VL) thalamus activity at 7–14 Hz. (A) Intracellular (layer V) and field potential (FP) recordings showing an augmenting response evoked in motor cortex by electrical stimulation in VL at 10 Hz in a ketamine anesthetized rat (Castro-Alamancos and Connors, 1996b). **(B)** Behavioral state dependency of augmenting responses in a freely behaving rat (Castro-Alamancos and Connors, 1996c). The animal was allowed to freely explore the cage and locomotor activity was monitored with photobeam detectors. The amplitude of the responses to the first and second stimulus delivered at 10 Hz is plotted. The augmenting response is induced during periods of resting and awake immobility but is inactivated during periods of active exploration.

7–14 Hz NETWORK OSCILLATIONS IN MOTOR CORTEX

Enhancing excitation or dampening inhibition leads to 7–14 Hz network oscillations in motor cortex both in slices and *in vivo* (**Figures 2A–C**). Disinhibition (block of $GABA_A$ and $GABA_B$ receptors) in motor cortex, but not in somatosensory cortex, produces highly synchronous oscillations or afterdischarges at 7–14 Hz (Castro-Alamancos, 2000; Castro-Alamancos and Rigas, 2002). Low $[Mg^{2+}]_o$ buffers (~0.1 mM) that enhance network excitability, also produce 7–14 Hz oscillations in slices (Silva et al., 1991; Flint and Connors, 1996; Castro-Alamancos et al., 2007),

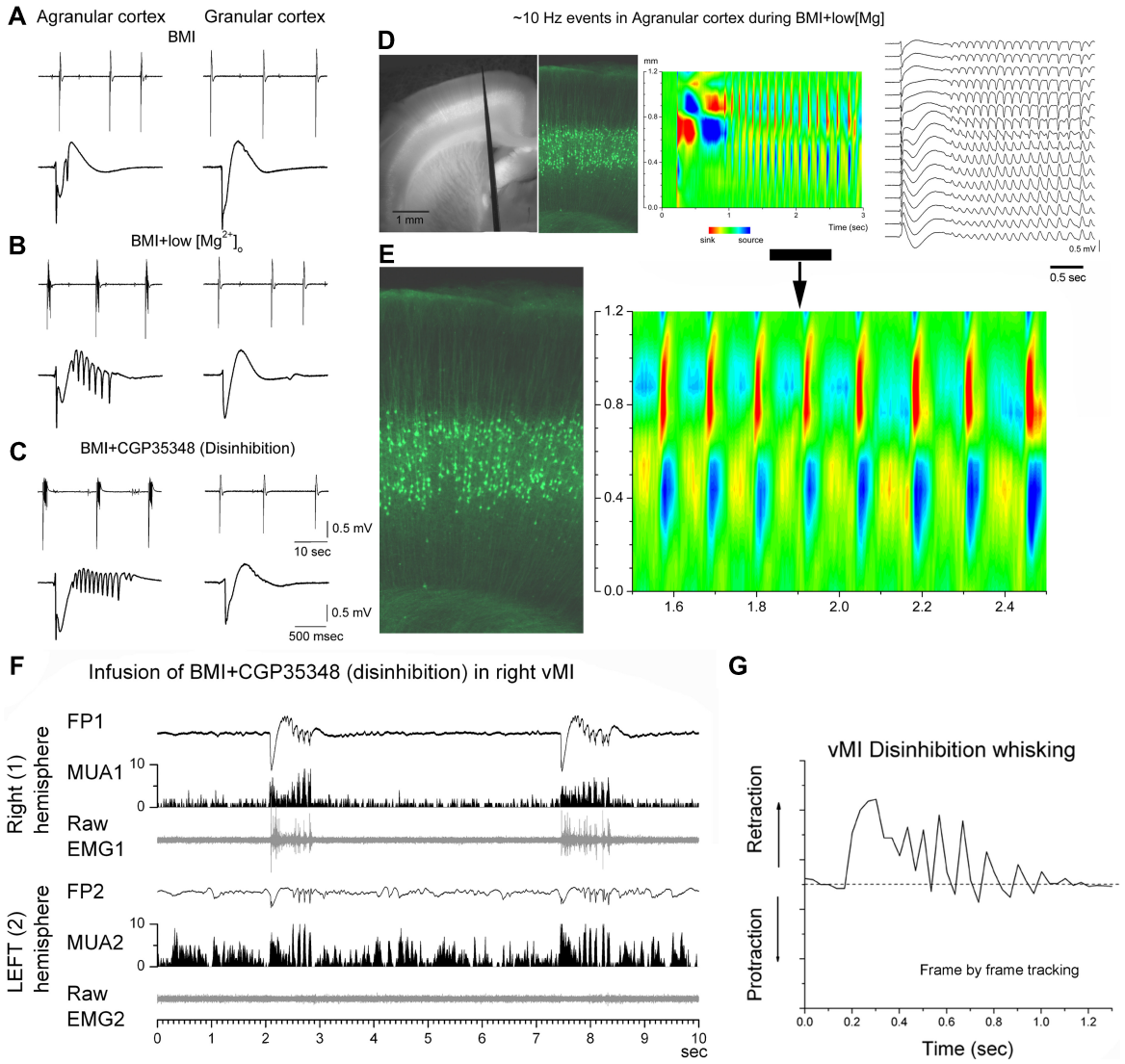

FIGURE 2 | 7–14 Hz oscillations are caused by low $[Mg^{2+}]_o$ buffer or disinhibition in the motor cortex but not in the somatosensory cortex. **(A–C)** Field potential (FP) recordings in neocortical slices showing typical spontaneous events recorded in motor (agranular) cortex (left panels) and in somatosensory (granular) cortex (right panels) during block of $GABA_A$ receptors with bicuculline (BMI) **(A)**, subsequent lowering of $[Mg^{2+}]_o$ **(B)**, or subsequent block of $GABA_B$ receptors **(C)**. Note the occurrence of 7–14 Hz oscillations only in agranular cortex. In each panel, the upper trace has a long time scale and the lower trace shows a close-up of a spontaneous discharge (Castro-Alamancos and Tawara-Hirata, 2007). **(D)** Recording from a fluorescent slice of an Thy1-eYFP mouse using a 16-channel silicon probe. The left panel shows a light/fluorescent image of the probe position in the motor cortex during the experiment. The middle left panel show a fluorescent image taken at the probe location revealing the layer V fluorescent cells. The current source density (CSD) and FP plots show a 7–14 Hz oscillation event. The CSD and fluorescent image are scaled to match the cortical layers location with the location of the current flow (Castro-Alamancos and Tawara-Hirata, 2007). **(E)** Close-up of the 7–14 Hz event shown in **(D)**. **(F)** 7–14 Hz oscillations caused by disinhibition in the whisker motor cortex (vMI) of a freely behaving rat. Bilateral field potential (FP) and multi-unit (MUA) activity recorded from the vMI during disinhibition caused by application of BMI + CGP (0.1 + 2 mM, 0.2 μl volume) into the right vMI. The corresponding raw electromyography (EMG) activity measured from the contralateral whisker pad is also displayed below the FP and MUA. 1 refers to the infused hemisphere and the related (contralateral) whisker pad, 2 refers to the non-infused hemisphere and the related whisker pad (Castro-Alamancos, 2006). **(G)** 7–14 Hz oscillations of vMI caused by disinhibition produce cycles of vibrissa retractions. Frame by frame tracking of a vibrissa movement caused by vMI disinhibition. Units in the *y*-axis are relative pixels (see Castro-Alamancos, 2006).

which occur more readily in motor cortex than in somatosensory cortex (Castro-Alamancos and Tawara-Hirata, 2007). However, 7–14 Hz oscillations can be unmasked in somatosensory cortex by suppressing specific outward currents, as described below (Castro-Alamancos and Tawara-Hirata, 2007). These results suggest that specific outward currents, such as the slowly inactivating K^+ current (I_D), may inhibit the ability of somatosensory cortex to generate 7–14 Hz oscillations.

WHAT IS THE SUBSTRATE OF 7–14 Hz RESONANCE IN MOTOR CORTEX?

When thinking about the mechanisms responsible for 7–14 Hz resonance in motor cortex it is important to consider the following. First, a pure excitatory network of interconnected pyramidal cells generates 7–14 Hz oscillations in motor cortex because these oscillations are present in the absence of GABAergic transmission (Castro-Alamancos and Borrell, 1995; Flint and Connors, 1996; Castro-Alamancos, 2000; Castro-Alamancos and Rigas, 2002). In fact, $GABA_B$ receptors normally suppress the generation of 7–14 Hz oscillations because when $GABA_B$ receptors are blocked these oscillations are readily expressed, as long as there is a robust excitatory drive caused by $GABA_A$ receptor block (Castro-Alamancos, 2000; Castro-Alamancos and Rigas, 2002). This implies that blocking $GABA_B$ receptors may unmask the mechanism(s) responsible for generating 7–14 Hz oscillations in the motor cortex.

Second, selective alpha-amino-3-hydroxy-5-methyl-4-isoxazolepropionic acid (AMPA) receptor antagonists completely abolish 7–14 Hz oscillations with little effects on the discharges that trigger them (Castro-Alamancos and Rigas, 2002; Castro-Alamancos et al., 2007). This indicates that fast synaptic excitation is critical for generating and/or synchronizing 7–14 Hz oscillations. In fact, slower *N*-methyl-D-aspartic acid (NMDA)-mediated synaptic currents cannot sustain 7–14 Hz oscillations without AMPA currents. NMDA receptor antagonists reduce the power and enhance the frequency of the oscillations but do not abolish them (Castro-Alamancos and Rigas, 2002; Castro-Alamancos et al., 2007). Therefore, slow NMDA-mediated synaptic currents modulate but are not required for generating 7–14 Hz oscillations.

Third, drugs that suppress the low-threshold calcium current (I_T) and the hyperpolarization-activated cation current (I_H) do not suppress 7–14 Hz oscillations in motor cortex (Castro-Alamancos et al., 2007). Thus, I_T and I_H are not required for 7–14 Hz oscillations.

Fourth, it has been known for some time that in addition to the transient Na^+ current, cortical pyramidal neurons express a persistent Na^+ current, I_{Nap}, which appears as a subthreshold inward rectification (Hotson et al., 1979; Connors et al., 1982; Stafstrom et al., 1982, 1984, 1985). Several drugs have been shown to somewhat selectively suppress the persistent component of the Na^+ current with less effect on the transient component, such as phenytoin (Quandt, 1988; Segal and Douglas, 1997) and riluzole (Urbani and Belluzzi, 2000; Kononenko et al., 2004; Niespodziany et al., 2004). These drugs, known to suppress I_{Nap}, abolish 7–14 Hz oscillations at doses that have little effects on synaptic transmission (Castro-Alamancos et al., 2007). Thus, I_{Nap} appears to be critical for 7–14 Hz oscillations.

Fifth, blockers of voltage-dependent K^+ channels have significant effects on 7–14 Hz oscillations of motor cortex. Pyramidal cells express a voltage-dependent K^+ current, the M-current (I_M), which activates positive to −60 mV and does not inactivate (Halliwell and Adams, 1982; Storm, 1990). I_M is blocked by XE991 and linopirdine in pyramidal cells (Aiken et al., 1995; Hu et al., 2002; Yue and Yaari, 2004). I_M blockers abolish 7–14 Hz oscillations in motor cortex (Castro-Alamancos et al., 2007). Thus, I_M appears to be critical for 7–14 Hz oscillations.

Sixth, CSD analysis shows that current flow in motor cortex during 7–14 Hz oscillations is strongest in layers V and II–III, and appears to propagate between the soma and apical dendrites of layer V cells (Castro-Alamancos and Rigas, 2002; see **Figures 2D,E**). This suggests a critical role for layer V cells in the generation of 7–14 Hz oscillations in motor cortex.

These results indicate that a network of pyramidal cells (interconnected by fast AMPA-mediated glutamatergic synapses) that intrinsically express I_{Nap} and I_M are involved in the generation of 7–14 Hz oscillations. Possibly, 7–14 Hz oscillations of motor cortex involve the interplay between synaptic (AMPA) and intrinsic inward (I_{Nap}) and outward currents (I_M and perhaps other non-inactivating voltage-dependent K^+ currents) in layer V pyramidal cells. Interestingly, such a scheme is supported by computational modeling (Golomb et al., 2006).

MOTOR CORTEX vs. SOMATOSENSORY CORTEX

An important question is, why are 7–14 Hz oscillations generated in motor but not in somatosensory cortex (i.e., during disinhibition or low $[Mg^{2+}]_o$)? There are at least two main possibilities to explain this result. The somatosensory cortex may be incapable of generating 7–14 Hz oscillations because it lacks the necessary intrinsic or synaptic mechanisms. Alternatively, some current(s) inhibits the ability of somatosensory cortex to generate 7–14 Hz oscillations. If the later is the case, blocking the "inhibiting current" should unmask 7–14 Hz oscillations. But what current may be responsible for keeping a pure excitatory network in somatosensory cortex from generating 7–14 Hz oscillations? In the absence of GABAergic inhibition, intrinsic K^+ currents are the counterbalance of excitation. Hence, it is possible that K^+ currents in somatosensory cortex impede the generation of 7–14 Hz oscillations (just like $GABA_B$ receptors suppress 7–14 Hz oscillations in motor cortex). CA1 and layer V pyramidal cells express three major types of voltage-dependent K^+ currents in the soma and dendrites (Storm, 1988, 1990; Hoffman et al., 1997; Bekkers, 2000a,b; Korngreen and Sakmann, 2000; Bekkers and Delaney, 2001); a transient current that rapidly activates and inactivates (I_A), a more slowly inactivating current (I_D), and a sustained delayed rectifier (I_K). Importantly, these three voltage-dependent K^+ current components have well-known sensitivities to K^+ channel blockers; low doses of 4-aminopyridine (4-AP; μM range) block the slowly inactivating K^+ current I_D, with little effect on I_K and I_A. Whereas, tetraethylammonium (TEA) at high doses (10–30 mM) blocks the sustained delayed rectifier I_K plus other K^+ currents (Storm, 1988, 1990; Hoffman et al., 1997; Bekkers and Delaney, 2001). Interestingly, 7–14 Hz oscillations are unmasked in somatosensory cortex by low doses of 4-AP, which blocks I_D (Castro-Alamancos and Tawara-Hirata, 2007). These results indicate that specific outward

currents, such as the slowly inactivating K^+ current (I_D), inhibit the ability of somatosensory cortex to generate 7–14 Hz oscillations because when this current is suppressed 7–14 Hz oscillations are expressed in somatosensory cortex. It is worth noting that the substrate unmasked in somatosensory cortex to produce 7–14 Hz oscillations may be different than the one normally engaged in motor cortex.

There are other known physiological differences between motor and somatosensory cortex that may contribute to their different susceptibility to 7–14 Hz oscillations. Pyramidal cells of the neocortex come in two major types: regular spiking and bursting (Connors and Gutnick, 1990). Regular spiking cells can be further differentiated according to the amount of spike-frequency adaptation. Bursting cells present different degrees; from single bursts to repetitive bursting. Studies *in vivo* have shown that the main electrophysiological types described in somatosensory cortex are also found in cat (Baranyi et al., 1993a,b) and rat motor cortex (Pockberger, 1991). Intriguingly, a unique "accelerating" firing type mediated by a Kv1 subunit is found in layer V pyramidal cells of rodent motor cortex but not in somatosensory cortex (Miller et al., 2008).

Few studies have directly compared the synaptic response properties of somatosensory and motor cortex. For example, theta-burst stimulation applied to layer V–IV produces long-term potentiation (LTP) in layer III of somatosensory (granular) cortex, while the same procedure in the adjacent motor (agranular) neocortex is less effective unless inhibition is suppressed (Castro-Alamancos et al., 1995). These differences appear to be related to the different response properties of synaptic pathways in these neocortical areas (Castro-Alamancos and Connors, 1996a). During tetanic stimuli the granular cortex, but not the agranular cortex, generated a strong short-term enhancement that correlated well with the subsequent expression of LTP (Castro-Alamancos and Connors, 1996a). The variation in short-term enhancement was due to pathway-specific differences in the short-term regulation of NMDA receptor-dependent responses, which in turn determine the differences in long-term NMDA receptor-dependent potentiation. Specifically, NMDA receptor-mediated responses are more strongly depressed in agranular than in granular cortex during high-frequency stimulation.

7–14 Hz MOTOR CORTEX OSCILLATIONS ARE FUNCTIONALLY RELEVANT

In humans and non-human primates, oscillatory activity in the beta frequency range (14–30 Hz) is commonly observed in sensorimotor cortex in relation to motor behavior (Donoghue et al., 1998; Saleh et al., 2010). Mu waves (12–18 Hz) occur in the sensorimotor cortex of awake cats during behavioral immobility and are blocked by active movement (Bouyer et al., 1983). In rodents, the intact motor cortex produces 7–14 Hz synchronized oscillations during specific types of whisker movements, such as twitching (Semba and Komisaruk, 1984), which may actually be an abnormal behavioral state that occurs in certain rodent strains (Shaw, 2004). Oscillations occur also during or in anticipation of active whisking (Ahrens and Kleinfeld, 2004; Friedman et al., 2006). These oscillations are usually much less widespread and less synchronous than those occurring during abnormal conditions, such as when inhibition is suppressed. Thus, 7–14 Hz oscillations induced in behaving rats by motor cortex disinhibition produce rhythmical jerks and tremor-like phase-locked movements of the contralateral body (Castro-Alamancos, 2006; **Figure 2F**). Whiskers produce abnormal retractions that contrast with the normal protractions during exploratory whisking (Castro-Alamancos, 2006; **Figure 2G**). This abnormal motor behavior resembles a cortical myoclonus in humans with *Epilepsia Partialis Continua*, which is also associated with large amplitude discharges at 7–14 Hz in the frontal lobes (Obeso et al., 1985; Chauvel et al., 1992).

CONCLUSION

Several lines of evidence presented here support the notion that the motor cortex contains a unique excitatory network that is tuned to the 7–14 Hz frequency band, and this network may be present but more strongly suppressed in somatosensory cortex. Under normal conditions, afferent activity from the VL thalamus at 7–14 Hz drives augmenting responses in the motor cortex. Augmenting responses are very dependent on behavioral state. They are abolished during sensorimotor processing, such as skilled movement or active exploration, but are fully expressed during sow-wave sleep, anesthesia, and awake quiescence. This activity may be linked to the ability of motor cortex to oscillate at mu and beta frequencies during certain states. Finally, the 7–14 Hz activity in motor cortex is fully expressed when inhibition is suppressed or excitation is enhanced, and it can drive abnormal movements that resemble those expressed during partial epilepsies.

ACKNOWLEDGMENT

This work was supported by the National Institutes of Health.

REFERENCES

Ahrens, K. F., and Kleinfeld, D. (2004). Current flow in vibrissa motor cortex can phase-lock with exploratory rhythmic whisking in rat. *J. Neurophysiol.* 92, 1700–1707.

Aiken, S. P., Lampe, B. J., Murphy, P. A., and Brown, B. S. (1995). Reduction of spike frequency adaptation and blockade of M-current in rat CA1 pyramidal neurones by linopirdine (DuP 996), a neurotransmitter release enhancer. *Br. J. Pharmacol.* 115, 1163–1168.

Baranyi, A., Szente, M. B., and Woody, C. D. (1993a). Electrophysiological characterization of different types of neurons recorded in vivo in the motor cortex of the cat. I. Patterns of firing activity and synaptic responses. *J. Neurophysiol.* 69, 1850–1864.

Baranyi, A., Szente, M. B., and Woody, C. D. (1993b). Electrophysiological characterization of different types of neurons recorded in vivo in the motor cortex of the cat. II. Membrane parameters, action potentials, current-induced voltage responses and electrotonic structures. *J. Neurophysiol.* 69, 1865–1879.

Bekkers, J. M. (2000a). Distribution and activation of voltage-gated potassium channels in cell-attached and outside-out patches from large layer 5 cortical pyramidal neurons of the rat. *J. Physiol.* 525(Pt 3), 611–620.

Bekkers, J. M. (2000b). Properties of voltage-gated potassium currents in nucleated patches from large layer 5 cortical pyramidal neurons of the rat. *J. Physiol.* 525(Pt 3), 593–609.

Bekkers, J. M., and Delaney, A. J. (2001). Modulation of excitability by alpha-dendrotoxin-sensitive potassium channels in neocortical pyramidal neurons. *J. Neurosci.* 21, 6553–6560.

Betz, K. (1874). Anatomischer Nachweis zweier Gehirnzentra. *Zentralbl. Med. Wiss.* 12, 578–580.

Bouyer, J. J., Tilquin, C., and Rougeul, A. (1983). Thalamic rhythms in cat during quiet wakefulness and immobility. *Electroencephalogr. Clin. Neurophysiol.* 55, 180–187.

Brodmann, K. (1905). Beiträge zur histologischen Lokalisation der Grosshirnrinde: Die Rindenfelder der niederen affen. *J. Psychol. Neurol.* 4, 177–226.

Castro-Alamancos, M. A. (2000). Origin of synchronized oscillations induced by neocortical disinhibition in vivo. *J. Neurosci.* 20, 9195–9206.

Castro-Alamancos, M. A. (2006). Vibrissa myoclonus (rhythmic retractions) driven by resonance of excitatory networks in motor cortex. *J. Neurophysiol.* 96, 1691–1698.

Castro-Alamancos, M. A., and Borrell, J. (1995). Contribution of NMDA and nonNMDA glutamate receptors to synchronized excitation and cortical output in the primary motor cortex of the rat. *Brain Res. Bull.* 37, 539–543.

Castro-Alamancos, M. A., and Connors, B. W. (1996a). Short-term synaptic enhancement and long-term potentiation in neocortex. *Proc. Natl. Acad. Sci. U.S.A.* 93, 1335–1339.

Castro-Alamancos, M. A., and Connors, B. W. (1996b). Cellular mechanisms of the augmenting response: short-term plasticity in a thalamocortical pathway. *J. Neurosci.* 16, 7742–7756.

Castro-Alamancos, M. A., and Connors, B. W. (1996c). Short-term plasticity of a thalamocortical pathway dynamically modulated by behavioral state. *Science* 272, 274–277.

Castro-Alamancos, M. A., and Connors, B. W. (1996d). Spatiotemporal properties of short-term plasticity sensorimotor thalamocortical pathways of the rat. *J. Neurosci.* 16, 2767–2779.

Castro-Alamancos, M. A., and Connors, B. W. (1997). Thalamocortical synapses. *Prog. Neurobiol.* 51, 581–606.

Castro-Alamancos, M. A., Donoghue, J. P., and Connors, B. W. (1995). Different forms of synaptic plasticity in somatosensory and motor areas of the neocortex. *J. Neurosci.* 15, 5324–5333.

Castro-Alamancos, M. A., and Rigas, P. (2002). Synchronized oscillations caused by disinhibition in rodent neocortex are generated by recurrent synaptic activity mediated by AMPA receptors. *J. Physiol.* 542, 567–581.

Castro-Alamancos, M. A., Rigas, P., and Tawara-Hirata, Y. (2007). Resonance (approximately 10 Hz) of excitatory networks in motor cortex: effects of voltage-dependent ion channel blockers. *J. Physiol.* 578, 173–191.

Castro-Alamancos, M. A., and Tawara-Hirata, Y. (2007). Area-specific resonance of excitatory networks in neocortex: control by outward currents. *Epilepsia* 48, 1572–1584.

Chauvel, P., Trottier, S., Vignal, J. P., and Bancaud, J. (1992). Somatomotor seizures of frontal lobe origin. *Adv. Neurol.* 57, 185–232.

Connors, B. W., and Gutnick, M. J. (1990). Intrinsic firing patterns of diverse neocortical neurons. *Trends Neurosci.* 13, 99–104.

Connors, B. W., Gutnick, M. J., and Prince, D. A. (1982). Electrophysiological properties of neocortical neurons in vitro. *J. Neurophysiol.* 48, 1302–1320.

Creutzfeldt, O. D., and Creutzfeldt, M. (1993). *Cortex Cerebri: Performance, Structural and Functional Organization of the Cortex.* Göttingen: Oxford University Press.

DeFelipe, J., and Farinas, I. (1992). The pyramidal neuron of the cerebral cortex: morphological and chemical characteristics of the synaptic inputs. *Prog. Neurobiol.* 39, 563–607.

Donoghue, J. P., Sanes, J. N., Hatsopoulos, N. G., and Gaal, G. (1998). Neural discharge and local field potential oscillations in primate motor cortex during voluntary movements. *J. Neurophysiol.* 79, 159–173.

Donoghue, J. P., and Wise, S. P. (1982). The motor cortex of the rat: cytoarchitecture and microstimulation mapping. *J. Comp. Neurol.* 212, 76–88.

Douglas, R. J., Koch, C., Mahowald, M., Martin, K. A., and Suarez, H. H. (1995). Recurrent excitation in neocortical circuits. *Science* 269, 981–985.

Flint, A. C., and Connors, B. W. (1996). Two types of network oscillations in neocortex mediated by distinct glutamate receptor subtypes and neuronal populations. *J. Neurophysiol.* 75, 951–957.

Friedman, W. A., Jones, L. M., Cramer, N. P., Kwegyir-Afful, E. E., Zeigler, H. P., and Keller, A. (2006). Anticipatory activity of motor cortex in relation to rhythmic whisking. *J. Neurophysiol.* 95, 1274–1277.

Golomb, D., Shedmi, A., Curtu, R., and Ermentrout, G. B. (2006). Persistent synchronized bursting activity in cortical tissues with low magnesium concentration: a modeling study. *J. Neurophysiol.* 95, 1049–1067.

Hall, R. D., and Lindholm, E. P. (1974). Organization of motor and somatosensory neocortex in the albino rat. *Brain Res.* 66, 23–38.

Halliwell, J. V., and Adams, P. R. (1982). Voltage-clamp analysis of muscarinic excitation in hippocampal neurons. *Brain Res.* 250, 71–92.

Herkenham, M. (1980). Laminar organization of thalamic projections to the rat neocortex. *Science* 207, 532–535.

Hoffman, D. A., Magee, J. C., Colbert, C. M., and Johnston, D. (1997). K+ channel regulation of signal propagation in dendrites of hippocampal pyramidal neurons. *Nature* 387, 869–875.

Hotson, J. R., Prince, D. A., and Schwartzkroin, P. A. (1979). Anomalous inward rectification in hippocampal neurons. *J. Neurophysiol.* 42, 889–895.

Hu, H., Vervaeke, K., and Storm, J. F. (2002). Two forms of electrical resonance at theta frequencies, generated by M-current, h-current and persistent Na+ current in rat hippocampal pyramidal cells. *J. Physiol.* 545, 783–805.

Kawaguchi, Y., and Kubota, Y. (1997). GABAergic cell subtypes and their synaptic connections in rat frontal cortex. *Cereb. Cortex* 7, 476–486.

Kononenko, N. I., Shao, L. R., and Dudek, F. E. (2004). Riluzole-sensitive slowly inactivating sodium current in rat suprachiasmatic nucleus neurons. *J. Neurophysiol.* 91, 710–718.

Korngreen, A., and Sakmann, B. (2000). Voltage-gated K+ channels in layer 5 neocortical pyramidal neurones from young rats: subtypes and gradients. *J. Physiol.* 525(Pt 3), 621–639.

Miller, M. N., Okaty, B. W., and Nelson, S. B. (2008). Region-specific spike-frequency acceleration in layer 5 pyramidal neurons mediated by Kv1 subunits. *J. Neurosci.* 28, 13716–13726.

Mountcastle, V. B. (1998). *Perceptual Neuroscience: The Cerebral Cortex.* Cambridge: Harvard University Press.

Niespodziany, I., Klitgaard, H., and Margineanu, D. G. (2004). Is the persistent sodium current a specific target of anti-absence drugs? *Neuroreport* 15, 1049–1052.

Obeso, J. A., Rothwell, J. C., and Marsden, C. D. (1985). The spectrum of cortical myoclonus. From focal reflex jerks to spontaneous motor epilepsy. *Brain* 108(Pt 1), 193–124.

Pockberger, H. (1991). Electrophysiological and morphological properties of rat motor cortex neurons in vivo. *Brain Res.* 539, 181–190.

Quandt, F. N. (1988). Modification of slow inactivation of single sodium channels by phenytoin in neuroblastoma cells. *Mol. Pharmacol.* 34, 557–565.

Saleh, M., Reimer, J., Penn, R., Ojakangas, C. L., and Hatsopoulos, N. G. (2010). Fast and slow oscillations in human primary motor cortex predict oncoming behaviorally relevant cues. *Neuron* 65, 461–471.

Segal, M. M., and Douglas, A. F. (1997). Late sodium channel openings underlying epileptiform activity are preferentially diminished by the anticonvulsant phenytoin. *J. Neurophysiol.* 77, 3021–3034.

Semba, K., and Komisaruk, B. R. (1984). Neural substrates of two different rhythmical vibrissal movements in the rat. *Neuroscience* 12, 761–774.

Shaw, F. Z. (2004). Is spontaneous high-voltage rhythmic spike discharge in Long Evans rats an absence-like seizure activity?. *J. Neurophysiol.* 91, 63–77.

Sherwood, C. C., Lee, P. W., Rivara, C. B., Holloway, R. L., Gilissen, E. P., Simmons, R. M., et al. (2003). Evolution of specialized pyramidal neurons in primate visual and motor cortex. *Brain Behav. Evol.* 61, 28–44.

Silva, L. R., Amitai, Y., and Connors, B. W. (1991). Intrinsic oscillations of neocortex generated by layer 5 pyramidal neurons. *Science* 251, 432–435.

Somogyi, P., Tamas, G., Lujan, R., and Buhl, E. H. (1998). Salient features of synaptic organisation in the cerebral cortex. *Brain Res. Brain Res. Rev.* 26, 113–135.

Stafstrom, C. E., Schwindt, P. C., Chubb, M. C., and Crill, W. E. (1985). Properties of persistent sodium conductance and calcium conductance of layer V neurons from cat sensorimotor cortex in vitro. *J. Neurophysiol.* 53, 153–170.

Stafstrom, C. E., Schwindt, P. C., and Crill, W. E. (1982). Negative slope conductance due to a persistent subthreshold sodium current in cat neocortical neurons in vitro. *Brain Res.* 236, 221–226.

Stafstrom, C. E., Schwindt, P. C., Flatman, J. A., and Crill, W. E. (1984). Properties of subthreshold response and action potential recorded in layer V neurons from cat sensorimotor cortex in vitro. *J. Neurophysiol.* 52, 244–263.

Storm, J. F. (1988). Temporal integration by a slowly inactivating K+ current in hippocampal neurons. *Nature* 336, 379–381.

Storm, J. F. (1990). Potassium currents in hippocampal pyramidal cells. *Prog. Brain Res.* 83, 161–187.

Urbani, A., and Belluzzi, O. (2000). Riluzole inhibits the persistent sodium current in mammalian CNS neurons. *Eur. J. Neurosci.* 12, 3567–3574.

Welker, C. (1971). Microelectrode delineation of fine grain somatotopic organization of (SmI) cerebral neocortex in albino rat. *Brain Res.* 26, 259–275.

Welker, C. (1976). Receptive fields of barrels in the somatosensory neocortex of the rat. *J. Comp. Neurol.* 166, 173–189.

Yue, C., and Yaari, Y. (2004). KCNQ/M channels control spike afterdepolarization and burst generation in hippocampal neurons. *J. Neurosci.* 24, 4614–4624.

Zilles, K. (1985). *The Cortex of the Rat.* Berlin: Springer-Verlag.

Conflict of Interest Statement: The author declares that the research was conducted in the absence of any commercial or financial relationships that could be construed as a potential conflict of interest.

Received: 22 November 2012; paper pending published: 07 December 2012; accepted: 31 January 2013; published online: 21 February 2013.

Citation: Castro-Alamancos MA (2013) The motor cortex: a network tuned to 7–14 Hz. Front. Neural Circuits ***7****:21. doi: 10.3389/fncir.2013.00021*

frontiers in
NEURAL CIRCUITS

REVIEW ARTICLE
published: 18 February 2013
doi: 10.3389/fncir.2013.00019

Role of cerebral cortex in the neuropathology of Huntington's disease

Ana M. Estrada-Sánchez and George V. Rebec*

Program in Neuroscience and Department of Psychological and Brain Sciences, Indiana University, Bloomington, IN, USA

Edited by:
Gordon M. G. Shepherd, Northwestern University, USA

Reviewed by:
Edward A. Stern, Bar-Ilan University, Israel
Jang-Ho J. Cha, Merck & Co., USA

****Correspondence:***
George V. Rebec, Program in Neuroscience and Department of Psychological and Brain Sciences, Indiana University, 1101 E. 10th St., Bloomington, IN 47405, USA.
e-mail: rebec@indiana.edu

An expansion of glutamine repeats in the N-terminal domain of the huntingtin protein leads to Huntington's disease (HD), a neurodegenerative condition characterized by the presence of involuntary movements, dementia, and psychiatric disturbances. Evaluation of postmortem HD tissue indicates that the most prominent cell loss occurs in cerebral cortex and striatum, forebrain regions in which cortical pyramidal neurons (CPNs) and striatal medium spiny neurons (MSNs) are the most affected. Subsequent evidence obtained from HD patients and especially from transgenic mouse models of HD indicates that long before neuronal death, patterns of communication between CPNs and MSNs become dysfunctional. In fact, electrophysiological signaling in transgenic HD mice is altered even before the appearance of the HD behavioral phenotype, suggesting that dysfunctional cortical input to the striatum sets the stage for the emergence of HD neurological signs. Striatal MSNs, moreover, project back to cortex via multi-synaptic connections, allowing for even further disruptions in cortical processing. An effective therapeutic strategy for HD, therefore, may lie in understanding the synaptic mechanisms by which it dysregulates the corticostriatal system. Here, we review literature evaluating the molecular, morphological, and physiological alterations in the cerebral cortex, a key component of brain circuitry controlling motor behavior, as they occur in both patients and transgenic HD models.

Keywords: basal ganglia, glutamate transmission, huntingtin, neuronal processing

INTRODUCTION

In 1872, George Huntington described a disease that affects certain families and is characterized by the presence of choreic movements that gradually increase in severity and variety; his description led to the name Huntington's disease (HD; Huntington, 1872, 2003). Although Huntington described the inherited feature of HD, it was not until 1983 that a DNA marker linked to HD was identified at the tip of chromosome 4 (Gusella et al., 1983). A decade later, in 1993, the same research group reported that the HD mutation consists of an unstable CAG repeat in exon 1 of the gene that codes for the protein called "huntingtin" (HTT; HD Collaborative Research Group, 1993). Normally, this exon contains between 3 and 30 CAGs, but if the number of CAGs exceeds 35, HD becomes increasingly likely with full penetrance occurring at ≥39 repeat (Harper, 2001). A rough inverse correlation between the number of CAGs and the age of HD onset occur (For review see, Langbehn et al., 2010). While individuals carrying 40 CAG repeats are likely to show the first signs of HD at 35–40 years of age; CAG repeats ranging from 50 to 200 (the highest number reported) may precipitate HD onset in childhood or teenage years. The last is characterized with psychiatric disturbances, accelerated mental and physical deterioration that culminates in death as soon as 5–10 years after onset (Rasmussen et al., 2000; Quarrell et al., 2012).

In adult-onset HD, patients show a progressive deterioration of motor and cognitive function that follows three well-defined stages spread over 15–20 years (Harper, 1991). At the initial stage and before the appearance of prominent motor alterations, HD patients are likely to show psychiatric symptoms that include apathy, irritability, depression, and other mood alterations (Harper, 1991; Reedeker et al., 2012; Thompson et al., 2012). Slight motor abnormalities, such as motor tics and jerky voluntary movements, also are likely (Beste et al., 2009). The second stage is characterized by a dramatic increase in involuntary movements, which become generalized, abrupt, and uncontrolled. As these choreic movements become more prominent, daily activities such as walking, eating, speaking, and swallowing deteriorate. In some cases, bradykinesia may coexist with the choreic movements that become prominent in the third stage (Thompson et al., 1988). Cognitive capacities progressively decline and finally culminate in dementia. Another hallmark of the second stage is the loss of body weight despite efforts to maintain a high caloric diet (Marder et al., 2009). Overall health progressively deteriorates and by the third stage, which typically occurs 10–15 years after diagnosis. In this stage, choreic movements are replaced by bradykinesia and rigidity. Death becomes imminent, and the most common causes are pneumonia and heart disease.

Soon after the HD gene was identified, different transgenic animal models were developed. The models, together with studies performed on HD patients and on postmortem HD brains, revealed that although mutant HTT is ubiquitously expressed, the most prominent pathology occurs in cerebral cortex and striatum. Cortical pyramidal neurons (CPNs) send massive and

widespread projections to the striatum, forming the corticostriatal pathway that among other functions shapes motor behavior. Because the development of involuntary movements is a prominent feature of the HD phenotype, dysfunctional cortical input to striatum is likely to constitute a key component of HD neuropathology. In fact, emerging evidence from transgenic HD models suggests that the expression of mutant HTT alters the pattern of communication between CPNs and medium spiny neurons (MSNs) in the striatum. Striatal MSNs, moreover, send information to downstream structures that project to thalamus, which in turn projects back to cortex, allowing for even further disruptions in cortical processing. Here, our aim is to review the functional alterations in cerebral cortex in both patients and transgenic models of HD and to assess how these alterations disrupt the corticostriatal system to drive the HD phenotype.

OVERVIEW OF CEREBRAL CORTEX ORGANIZATION

The cerebral cortex is the external sheet of neuronal tissue that covers the entire brain. In mammals, cerebral cortex folds together forming the "sulci" which compress a large portion of cortical tissue in a small area. In humans the thickness of the cerebral cortex is subject to regular local variations, but the average values range from 1.5 to 4.5 mm (Brodmann, 2010). The cortical mantle is divided into specialized regions that control language, decision-making, and motor activity, among other functions. Cortical neurons are organized into six main layers; the most superficial lamina (Layer I) contains apical dendritic tufts of CPNs and horizontal axons; it might also include the so-called Cajal-Retzius and spiny stellate cells (von Economo, 1927). Layer II is composed of numerous small granule cells. Layer III, contains large and robust CPNs, along with interneurons (von Economo, 1927; Ichinohe, 2012). Layer IV, consists of densely packed small polymorphous granule cells. Layer V, contains large CPNs. Layer VI, contains large CPNs and small spindle-like pyramidal and multiform neurons (von Economo, 1927). In addition to the different neuronal populations, astrocytes are homogeneously distributed throughout the six-layered cortical organization (von Economo, 1927).

Cortical neurons make local connections between cells of different layers, also send and receive projections from other brain regions (Szentágothai, 1975). For example, layer I in visual cortex receives axonal ramifications from apical dendrites of pyramidal neurons located in layers III and IV (Shipp, 2005, 2007). Layer I also receives input from thalamic (matrix) M-type neurons (Rubio-Garrido et al., 2009). Lateral connections occur between neurons in layers II and III, but these neurons also send projections to layer **V** (Shipp, 2007). Neurons located in layer IV project to layers II and III (Miller, 2003). In somatosensory cortex, pyramidal neurons in layer IV are the main target of thalamocortical afferents from type (core) C-neurons (Jones and Pons, 1998). CPNs from layer V are the principal source of input to the basal ganglia, brain stem, and spinal cord. CPNs in layer VI send projections to thalamus (Shipp, 2007). Although similar intrinsic and extrinsic connections are thought to occur along the length of the cortical mantle, significant deviations occur among some functionally distinct cortical areas. Detailed descriptions of cortical connections are available elsewhere (Sherman and Guillery, 2011; Espinosa and Stryker, 2012; Nieuwenhuys, 2012; Ray and Zald, 2012). In the next section, we focus on cortical motor areas and their projections to basal ganglia.

MOTOR CORTEX AND ITS PROJECTIONS TO BASAL GANGLIA

Motor cortex refers to the cortical areas associated with the planning, execution and control of voluntary movements. Motor cortex is subdivided into multiple motor areas: primary motor cortex (M1), premotor cortex dorsal caudal (PMdc), premotor cortex dorsal rostral (PMdr), cingulate motor area caudal (CGc), cingulate motor area rostral (CGr), premotor cortex ventral caudal (PMvc), premotor cortex ventral rostral (PMvr), pre-supplementary motor area (Pre-SMA), and supplementary motor area (SMA; Schieber and Baker, 2003). These areas were identified by evaluating motor responses elicited by electrical stimulation in different species, including humans (Foerster, 1936; Penfield and Boldrey, 1937; Bures and Bracha, 1990). Thus, motor areas are localized to Brodmann's cortical areas 4 (the giant pyramidal area) and 6 (agranular frontal area) (Brodmann, 2010). Brodmann's areas 23 and 24 are now known to contain at least two additional motor areas (Schieber and Baker, 2003). Motor cortical neurons follow the laminar organization, but motor cortex lacks granular layer IV and layer III is relatively thinner (Brodmann, 2010). Motor cortex also is characterized by the presence of giant pyramidal neurons known as Betz cells located in layer V; these cells are the largest neurons in the brain, reaching dimensions of 60–120/30–80 μm: height/width (von Economo, 1927; Rivara et al., 2003).

Motor cortical projections to the striatum, the first information processing stage of the basal ganglia (Jinnai and Matsuda, 1979; McGeorge and Faull, 1989), arise mainly from layer V, although retrograde labeling studies also identify pyramidal projections from layer III. Cortical projections are bilateral with an ipsilateral predominance and release glutamate, an excitatory amino acid transmitter (McGeorge and Faull, 1989). Besides motor cortical areas, the striatum receives projections form sensory and associative cortical areas (Kemp and Powell, 1970). Two types of striatal-projecting CPNs have been identified. They can be distinguished by the morphology of their projection: pyramidal tract (PT)-type neurons project to the striatum via collaterals arising from the main axon that extends to the PT and intra-telencephalically projecting (IT)-type neurons that project to striatum and cortex but not to areas outside telencephalon (Lévesque et al., 1996; Reiner et al., 2003). Anatomical and functional differences have been described between PT- and IT- type neurons (For review see, Reiner et al., 2010). While the PT type is mainly found in lower cortical layer V, the IT type is located in layer III and upper layer V (Reiner et al., 2003; Parent and Parent, 2006). Likewise, PT- and IT-type neurons differentially target striatal MSNs such that IT-type neurons preferentially target MSNs of the direct pathway and PT-type neurons preferentially innervate MSNs of the indirect pathway (Lei et al., 2004; Reiner et al., 2010). MSNs are GABAergic neurons that constitute 95% of the neuronal population of the striatum and comprise its main output system. Two MSN subtypes have been identified

according to the proteins they express and their synaptic targets. MSNs that preferentially express substance P, dynorphin, and the D1-like dopamine receptor make up the direct pathway, which projects to the internal segment of the globus pallidus (GPi) and substantia nigra pars reticulata (SNr). The indirect pathway is composed of MSNs that contain enkephalin and express the D2-like dopamine receptor; these neurons project to the external segment of the globus pallidus (GPe) and the subthalamic nucleus, while also sending collaterals to GPi and SNr (Smith et al., 1998).

Understanding the motor neuronal pathways involved in control, planning and execution of motor behavior is primary for understanding neurophatologic conditions such as HD, in which one of the main phenotypic alterations is the development of involuntary movements.

CEREBRAL CORTEX IN HD: POSTMORTEM STUDIES

Postmortem evaluation of the human HD brain indicates a 30% reduction of total brain weight (De la Monte et al., 1988). The most striking feature is neuronal loss in striatum (caudate-putamen) along with enlarged lateral ventricles (De la Monte et al., 1988). A scale of neuropathology based on the extent of striatal atrophy has been developed (Vonsattel et al., 1985). According to this scale, Grade 0 indicates that clinical symptoms are noticeable but with no observable neuropathological alterations. Grade 1 is characterized by no macroscopic evidence of damage but some neuronal loss and the presence of gliosis. Progressive striatal atrophy is observed in Grades 2 and 3, which includes substantial reductions in the neuronal population (>50%) and increased gliosis. Marked striatal atrophy (95% neuronal loss) and widespread gliosis define Grade 4. In addition to striatal damage, cortical changes also have been observed in postmortem studies of HD patients. Reduced cross-sectional area of gray and white matter has been reported for frontal, temporal, insular, and parietal cortical areas in HD Grades 2–4 (Mann et al., 1993; Halliday et al., 1998). Likewise, De la Monte et al. (1988) described a progressive reduction in overall cortical area and in cortical white matter during mild (Grades 1 and 2) and severe HD (Grades 3 and 4). There also is evidence of reduced thickness of the cortical ribbon (De la Monte et al., 1988; Heinsen et al., 1994). These findings are consistent with a 30% reduction in the number of CPNs in cortical layer III, V and VI (Cudkowicz and Kowall, 1990; Hedreen et al., 1991; Sotrel et al., 1991; Heinsen et al., 1994). Moreover, primary motor cortex (Brodmann's area 4) and the premotor area (Brodmann's area 6) of HD brains show a similar reduction in CPN numbers (Macdonald and Halliday, 2002; Thu et al., 2010). Interestingly, the extent of cortical atrophy in motor areas roughly correlates with the extent of the HD motor phenotype (Halliday et al., 1998; Thu et al., 2010). It is equally striking that in HD patients for whom mood alterations are the primary symptom, the loss of CPNs is most prominent in cingulate cortex, which processes emotion (Thu et al., 2010). On the other hand, despite progressive loss of CPNs, postmortem studies indicate that parvalbumin-, calretinin- and calbindin- positive interneurons appear to be normally distributed without evident morphological changes in motor cortical areas (Macdonald and Halliday, 2002).

Together, these postmortem assessments indicate that cortical atrophy and loss of CPNs is a neuropathological hallmark of HD. Most of these studies, however, were performed on tissue from neuropathological grades 2–4; little is known about cortical atrophy at early HD stages and even before symptoms develop. More importantly, a growing body of evidence from both HD patients and transgenic models suggests that alterations in neuronal communication precede neuronal loss and play a critical role in the development of HD symptoms. Early support for this view emerged from evaluation of proteins associated with synaptic transmission, including receptors, transporters, intra-cellular signaling pathways, and vesicular neurotransmitter release (Cross et al., 1986; Dunlop et al., 1992; Arzberger et al., 1997; Smith et al., 2007; Hassel et al., 2008; Faideau et al., 2010). Subsequent support has come from neuroimaging studies and recording of neuronal activity (Miller and Bezprozvanny, 2010; Estrada-Sánchez and Rebec, 2012; Hong et al., 2012c; Unschuld et al., 2012). The following sections focus on the cellular dysfunctions that are the likely drivers of the HD behavioral phenotype.

FUNCTIONAL ALTERATIONS IN CEREBRAL CORTEX: HD IMAGING STUDIES

Neuroimaging studies permit visualization of pathological changes *in vivo*, before clinical symptoms develop. Techniques such as magnetic resonance imaging (MRI), positron emission tomography (PET), and single-photon-emission computed tomography (SPECT) have been used to detect brain atrophy and functional changes in pre-symptomatic HD patients. These approaches have not only confirmed the thinning of cerebral cortex, but also showed that this effect occurs early, develops progressively, and extends through the cortical mantle, although distinct grades of cortical thinning may occur (Rosas et al., 2002, 2008, 2011). Interestingly, patterns of cortical thinning are associated with both the cognitive and motor phenotypes. For example, patients with more prominent bradykinesia and dystonia show more significant thinning in premotor and supplementary motor areas (Rosas et al., 2008). Moreover, longitudinal MRI evaluations indicate that the progression and topological distribution of cortical thinning is influenced by age of onset, suggesting an important role of cerebral cortex in HD neuropathology (Rosas et al., 2011).

Besides morphological changes, cerebral cortex also undergoes several changes that might compromise neuronal communication. SPECT, a technique based on alterations in blood flow, indicates reduced cerebral blood perfusion in presymptomatic HD patients (Hasselbalch et al., 1992; Sax et al., 1996). Reduced blood flow is widely observed along the cortical mantle and precedes the presence of cortical atrophy as evaluated by MRI (Jernigan et al., 1991; Hasselbalch et al., 1992; Sax et al., 1996). Given that blood provides oxygen and glucose essential for brain function, reduced blood perfusion in HD is likely to compromise neuronal signaling mechanisms. Accordingly, reduced glucose uptake and glucose metabolism have been identified in striatum and cerebral cortex of pre-symptomatic HD patients, as studied by 18F-fluorodeoxyglucose and PET (Kuhl et al., 1982; Kuwert et al., 1989, 1990; Jenkins et al., 1998). The rate of glucose uptake and its metabolism is an indicator of altered neuronal activity.

Thus, these studies suggest altered cortical function before HD symptoms become prominent, an effect that could alter communication between CPNs and deep brain structures. In fact, prodromal-HD patients show reduced corticostriatal functional connectivity (Unschuld et al., 2012). Consistent with this view, neuroimaging studies indicate white matter atrophy before the onset of clinical symptoms (Fennema-Notestine et al., 2004; Rosas et al., 2006, 2010). It appears, therefore, that compromised cortical circuitry occurs early in the course of HD (Rosas et al., 2006).

Collectively, these studies indicate that in HD the cerebral cortex undergoes morphological and functional changes that occur early in disease progression. Combined with evidence that the cortical changes parallel the manifestation of both cognitive and motor symptoms, these studies underscore the key role of cortical neuropathology in HD. Neuroimaging studies, moreover, suggest that cortical dysfunction rather than neuronal loss is a key factor in HD onset. This hypothesis gained considerable support from research on transgenic HD mice, which is reviewed in the next sections.

TRANSGENIC HD MODELS

Transgenic mouse models of HD are often separated into three broad categories based on the genetic manipulation: truncated, full-length, and knock-in models. The truncated model expresses only the first exon of the human mutant *htt* gene, while the full-length model expresses the entire human mutant *htt* gene. Thus, these two models express two normal alleles of the endogenous *Hdh* gene (the murine analog of *htt*) along with all or part of the exogenous human *htt* gene. In the knock-in model, CAG repeats are "knocked in" or directly inserted into the first exon of the endogenous *Hdh* gene.

Truncated models were developed first, and are represented by the R6 line of mice. Two variants are available: the R6/1 line, which contains ∼110 CAG repeats, and the R6/2 line, which contains ∼150 CAG repeats (Mangiarini et al., 1996). More recently, other truncated models have been created, including the N171-82Q mouse that expresses cDNA encoding 171 amino acids in the first exon of the *htt* gene with 82 CAG repeats (Schilling et al., 1999). A truncated transgenic HD rat model with 51 CAG repeats also has been created (von Hörsten et al., 2003). Like the truncated R6 line, the full-length HD model has two variants: the yeast artificial chromosome (YAC) and the bacterial artificial chromosome (BAC) models, the names of which refer to the genetic tool (yeast or bacteria) used to insert the human mutant *htt* gene. Three different YAC models are available based on CAG-repeat length, YAC46, YAC72, and YAC128; the latter is the most widely studied of this group (Hodgson et al., 1999). The BAC model expresses 97 CAG repeats (Gray et al., 2008). Finally, several knock-in variants have been developed, including: *Hdh*/Q72-80, *Hdh* Q111, CAG140, and CAG150 models, again with the numbers indicating CAG-repeat length (Menalled, 2005).

Despite the genetic difference that exists among HD transgenic models, they all develop a form of the behavioral phenotype and neuropathology seen in patients. HD transgenic models however, show varying degrees of behavior and neuropathological alterations. Truncated R6 models, for example, develop accelerated progressive motor alterations, reduced body weight, and shortened lifespan (∼10–14 and 3–5 months for R6/1 and R6/2, respectively) (Mangiarini et al., 1996). At the neuropathological level, these models show intracellular and intranuclear aggregates containing the mutant HTT fragment and other proteins; reduced striatal volume and neuronal atrophy also occur (Mangiarini et al., 1996; Davies et al., 1997; Stack et al., 2005). The N171-82Q model also has decreased body weight and motor alterations, but these are less severe than in the R6/2 model (Kim et al., 2011). The neuropathological changes, however, are similar to those described in the R6 models (Yu et al., 2003; McBride et al., 2006; Kim et al., 2011). In the case of the truncated HD transgenic rat, there are intracellular aggregates, but unlike the truncated mouse model, neurological deficits emerge in adulthood along with progressive motor alterations (von Hörsten et al., 2003). Full length models, on the other hand, show important differences relative to truncated models. For example, a notable increase in body weight occurs in the BACHD and YAC128 models (Van Raamsdonk et al., 2006; Pouladi et al., 2010, 2012). Both also show reduced striatal volume, although the presence of intracellular aggregates is more prominent in the striatum of YAC128 models (Gray et al., 2008; Spampanato et al., 2008; Miller et al., 2011b; Pouladi et al., 2012). Although full length models show impaired performance in motor tests, the motor changes are relatively mild compared with truncated models (Ferrante, 2009; Kim et al., 2011). Similar to full length models, knockin HD mice show slowly emerging motor changes along with intracellular aggregates and striatal atrophy (For review see, Menalled, 2005). Interestingly, the neuropathology in aged knockin mice (21 months of age) resembles that described for R6/2 mice, including widespread expression of aggregates and transcriptional alterations (Woodman et al., 2007).

These findings indicate important differences in the neural and behavioral phenotypes among the HD models. However, it is important to note that despite these differences, behavioral alterations appear prior to neuronal loss, suggesting that HD neurological signs are likely to be caused by impaired neuronal communication, particularly in the corticostriatal pathway.

DYSFUNCTIONAL CORTICOSTRIATAL NETWORK IN HD; EVIDENCE FROM TRANSGENIC MODELS

Electrophysiological recordings of CPNs in truncated and full length HD models indicate a change in electrical properties such as resting membrane potential, input resistance, and cell capacitance (Cummings et al., 2006, 2009). Similar membrane changes were observed *in vivo* during intracellular recordings of R6/2 CPNs (Stern, 2011). Likewise, there is consistent evidence of an imbalance between excitatory and inhibitory inputs to CPNs in HD, which may underlie hyperexcitable cortical neurons reported for HD models (Gu et al., 2005; Spampanato et al., 2008; Cummings et al., 2009).

Impaired CPN activity in HD also is likely to interfere with synaptic plasticity. Progressive alterations in long-term depression (LTD) occur in the perirhinal cortex of R6/1 mice (Cummings et al., 2006, 2007). Similarly, CPNs in medial prefrontal cortex show impaired long-term potentiation (LTP)

(Dallérac et al., 2011). Interestingly, in both cases, the loss of synaptic plasticity can be reversed by the activation of dopamine receptors (Cummings et al., 2006, 2007; Dallérac et al., 2011), suggesting an HD-induced change in dopamine modulation of cortical processing. This change may underlie the deficient cortical plasticity observed in R6/1 model performance in a somatosensory-discrimination learning task (Cybulska-Klosowicz et al., 2004; Mazarakis et al., 2005).

Dysfunctional interneurons also may contribute to impaired CPN activity in HD. For example, reduced GABAergic inhibitory input from interneurons occurs in HD models (Gu et al., 2005; Cummings et al., 2009). In BACHD mice at 3 months of age—when the motor phenotype is relatively mild—parvalbumin-containing interneurons in layers II and III show alterations in the kinetics of decay of spontaneously occurring inhibitory and excitatory postsynaptic currents (sIPSC and sEPSC, respectively; Spampanato et al., 2008). At 6 months, when motor alterations are more prominent, parvalbumin-containing interneurons show decreased excitation, while CPNs show decreased inhibition, indicating increased cortical excitability (Spampanato et al., 2008). Thus, cortical interneurons and CPNs show alterations that parallel the progressive motor phenotype seen in the BACHD model. Moreover, these results also suggest that interneurons might have an important role in the HD phenotype, given that their alterations may precede CPN dysfunction. In line with this view, it has been suggested that inhibitory interneurons are involved in shaping motor commands (For review see, Merchant et al., 2012).

Neurons communicate through the modulation of firing rate and by the generation of spike bursts, which are epochs of high firing frequency. Burst firing is relevant for the efficiency of neuronal transmission and also plays a role in neuronal plasticity (Lisman, 1997; Izhikevich et al., 2003). Cortical activity recorded in freely behaving R6/2 mice is characterized by decreased bursting activity and a decrease in the number of spikes that participate in a burst (Walker et al., 2008). Similarly, reduced bursting occurs in cultured cortical neurons expressing a fragment of mutant HTT (Gambazzi et al., 2010). Cortical neurons in both R6/2 and *Hdh* CAG140 mice are more likely to show a decrease in correlated activity between simultaneously recorded pairs of neurons than corresponding wild-type controls (Walker et al., 2008). Consistent with this evidence, *in vivo* intracellular recordings in HD mice indicate a decreased correlation between cortical spiking and simultaneously recorded electrocorticograms relative to wild-type (Stern, 2011). Importantly, correlated neuronal activity is a key factor in the operation of the neuronal circuits that shape behavior (Berke et al., 2004; Buzsáki and Chrobak, 2005; Burns et al., 2010), suggesting that deficient synchronous activity in cortical HD neurons is associated with the behavioral alterations in HD transgenic models (Walker et al., 2011). Interestingly, local field potentials (LFPs), which represent the activity of large populations of neurons in the vicinity of the recording electrode, also are altered in cortex of HD mice (Hong et al., 2012c). In this case, however, LFPs show the greatest deviation from wild-type during quiet rest and less so as behavior switches to grooming and exploring. It may be that the high frequency oscillations (~32 Hz) in resting HD mice prompt motor activation. In fact, HD mice spend less time resting than wild-type (Hong et al., 2012c).

Along with alterations in CPNs activity, striatal MSNs also show altered electrophysiological properties (reviewed by Cepeda et al., 2007). When studied *in vitro*, MSNs show increased excitability as indicated by a depolarized resting membrane potential and enhanced sensitivity to ionotropic glutamate receptor activation (Hodgson et al., 1999; Levine et al., 1999; Cepeda et al., 2001; Klapstein et al., 2001; Laforet et al., 2001; Milnerwood and Raymond, 2007). This evidence is consistent with increased firing in striatal MSNs recorded from behaving, symptomatic R6/2 mice (Rebec et al., 2006). As in cortex, decreased MSN bursting activity is the most common electrophysiological feature reported for HD models (Miller et al., 2008b, 2010, 2011a; Cayzac et al., 2011). As in CPNs, reductions in correlated firing and coincident bursting between simultaneously recorded pairs of MSNs occur in HD striatum (Miller et al., 2008b, 2010, 2011a; Höhn et al., 2011). In addition, striatal LFPs in behaving R6/2s parallel cortical LFPs in that high frequency gamma activity (focused around 32 Hz) predominates during quiet rest (Hong et al., 2012a,b). Interestingly, LFP oscillations recorded in the globus pallidus of HD patients show alterations in theta/alpha (4–12 Hz) and low gamma (35–45) activity (Groiss et al., 2011).

Collectively, these studies indicate that altered neuronal processing occurs in cerebral cortex of HD transgenic models, indicating that CPNs send aberrant information to MSNs. In fact, analysis of simultaneous recordings of LFPs from primary motor cortex and dorsal striatum, which receives major motor cortical input, indicates an overall reduction in the level of coherence or synchrony between these brain regions in R6/2 relative to wild-type mice across a range of behavioral episodes (Hong et al., 2012c). Given that dysfunctional corticostriatal processing occurs before HD signs are noticeable, these results provide further support for the hypothesis that altered neuronal communication is a prerequisite for the HD behavioral phenotype.

MECHANISM INVOLVED IN DISRUPTED CORTICOSTRIATAL COMMUNICATION IN HD

A critical question is how mutant HTT alters corticostriatal neuronal activity. Two mechanisms have been suggested: cell-autonomous toxicity and cell–cell interaction toxicity (Gu et al., 2005, 2007). The first proposes that the expression of mutant HTT itself is enough to alter the key neuronal mechanisms that lead to neuronal dysfunction. In support of this mechanism, *in vitro* and *in vivo* studies indicate that mutant HTT disrupts gene expression, calcium buffering, and mitochondrial function (Choo et al., 2004; Milakovic and Johnson, 2005; Tang et al., 2005; Thomas et al., 2011). The second mechanism proposes that the interaction between different cell populations is critical for the development of HD. Support for this hypothesis includes altered release of brain derived neurotrophic factor (BDNF) from corticostriatal synapses (reviewed by Zuccato and Cattaneo, 2009), impaired glutamate release from cortical projections (Cepeda et al., 2001; Klapstein et al., 2001; Laforet et al., 2001; Milnerwood and Raymond, 2007), and disrupted glutamate uptake by the astrocytes (Nicniocaill et al., 2001; Hassel et al., 2008). Collectively, these studies indicate that both cell-autonomous and cell–cell interaction toxicity are likely to occur in HD. Thus, a combination of both mechanisms may

disrupt neuronal communication and promote development of the HD phenotype.

Impaired energy production appears to be a key alteration in HD, as both HD transgenic models and HD patients show alteration in glycolytic and mitochondrial activity (Browne and Beal, 2004; Powers et al., 2007; Verwaest et al., 2011; Cepeda-Prado et al., 2012). Because neurons are highly dependent on ATP production, decreased glucose metabolism may compromise the activity of Na^+/K^+ ATPase, a key protein that helps to maintain the ionic gradient across the neuronal membrane (Bonvento et al., 2002). If the gradient is not maintained by this protein, neurons become depolarized and more excitable, which may explain evidence for increased neuronal excitability in transgenic HD models (see above). Deficient energy production and a loss of the ionic gradient, moreover, may compromise the function of glutamate transporters, transmembrane proteins located in neurons and astrocytes. These transporter proteins depend on the Na^+ gradient generated by the Na^+/K^+ ATPase to ensure glutamate clearance from the synapse and extracellular space. It is noteworthy that decreased glutamate uptake, a well-described feature of HD (Nicniocaill et al., 2001; Hassel et al., 2008; Miller et al., 2008a; for review see Estrada-Sánchez and Rebec, 2012), may result, at least in part, from decreased energy production. In this sense, glycolytic inhibition reduced glutamate transporters levels in the striatum of R6/2 model (Estrada-Sánchez et al., 2010). Moreover, compromised glutamate uptake coupled with impaired cellular metabolism may render neurons vulnerable to excitotoxic damage, a mechanism involved with neurodegeneration of MSNs in HD (Estrada-Sánchez et al., 2008, 2009, 2010). Besides, impaired function of glutamate transporters at corticostriatal synapses might compromise the dynamic of synaptic transmission, leading to aberrant neuronal processing (Beurrier et al., 2009). These mechanisms, of course, are likely to occur in conjunction with many other contributing factors, including altered expression and function of synaptic receptors, increased production of reactive oxidative species, diminished neuronal antioxidant capabilities (For reviews of these and other likely factors see: Browne et al., 1997; André et al., 2006; Chen, 2011; Kaplan and Stockwell, 2012).

CONCLUSION

An emerging picture of HD neuropathology includes aberrant cortical signaling that impacts striatal output systems and that then affects thalamic input back to cortex. In short, HD is characterized by dysregulated information flow through the cortico-striato-cortical pathway. This problem, moreover, emerges early in the course of HD, even before some neurological signs are present, suggesting a key role in the development and subsequent progression of the HD behavioral phenotype. Further research on alterations in cortical processing in HD, including the contribution of thalamic inputs and cortical interneurons, is emerging as fertile ground for further insight into the neuronal mechanisms underlying HD and for the development of effective therapeutic strategies.

ACKNOWLEDGMENTS

Research by the authors is supported by USPHS grant AG039818, the Indiana METACyt Initiative of Indiana University funded in part by a major grant from the Lilly Endowment, Inc., and a contract with the Cure Huntington's Disease Initiative (CHDI). We also gratefully acknowledge Faye Caylor for administrative support.

REFERENCES

André, V. M., Cepeda, C., Venegas, A., Gomez, Y., and Levine, M. S. (2006). Altered cortical glutamate receptor function in the R6/2 model of Huntington's disease. *J. Neurophysiol.* 95, 2108–2119.

Arzberger, T., Krampfl, K., Leimgruber, S., and Weindl, A. (1997). Changes of NMDA receptor subunit (NR1, NR2B) and glutamate transporter (GLT1) mRNA expression in Huntington's disease–an *in situ* hybridization study. *J. Neuropathol. Exp. Neurol.* 56, 440–454.

Berke, J. D., Okatan, M., Skurski, J., and Eichenbaum, H. B. (2004). Oscillatory entrainment of striatal neurons in freely moving rats. *Neuron* 43, 883–896.

Beste, C., Konrad, C., Saft, C., Ukas, T., Andrich, J., Pfleiderer, B., et al. (2009). Alterations in voluntary movement execution in Huntington's disease are related to the dominant motor system: evidence from event-related potentials. *Exp. Neurol.* 216, 148–157.

Beurrier, C., Bonvento, G., Kerkerian-Le Goff, L., and Gubellini, P. (2009). Role of glutamate transporters in corticostriatal synaptic transmission. *Neuroscience* 158, 1608–1615.

Bonvento, G., Sibson, N., and Pellerin, L. (2002). Does glutamate image your thoughts? *Trends Neurosci.* 25, 359–364.

Brodmann, K. (2010). *Brodmann's Localization in the Cerebral Cortex.* New York, NY: Springer.

Browne, S. E., and Beal, M. F. (2004). The energetics of Huntington's disease. *Neurochem. Res.* 29, 531–546.

Browne, S. E., Bowling, A. C., MacGarvey, U., Baik, M. J., Berger, S. C., Muqit, M. M., et al. (1997). Oxidative damage and metabolic dysfunction in Huntington's disease: selective vulnerability of the basal ganglia. *Ann. Neurol.* 41, 646–653.

Bures, J., and Bracha, V. (1990). "The control of movements by the motor cortex," in *The Cerebral Cortex of the Rat,* eds B. Kolb and R. Tees (Cambridge, MA; London, England: The MIT Press), 213–238.

Burns, S. P., Xing, D., and Shapley, R. M. (2010). Comparisons of the dynamics of local field potential and multiunit activity signals in macaque visual cortex. *J. Neurosci.* 30, 13739–13749.

Buzsáki, G., and Chrobak, J. J. (2005). Synaptic plasticity and self-organization in the hippocampus. *Nat. Neurosci.* 8, 1418–1420.

Cayzac, S., Delcasso, S., Paz, V., Jeantet, Y., and Cho, Y. H. (2011). Changes in striatal procedural memory coding correlate with learning deficits in a mouse model of Huntington disease. *Proc. Natl. Acad. Sci. U.S.A.* 108, 9280–9285.

Cepeda, C., Ariano, M. A., Calvert, C. R., Flores-Hernández, J., Chandler, S. H., Leavitt, B. R., et al. (2001). NMDA receptor function in mouse models of Huntington disease. *J. Neurosci. Res.* 66, 525–539.

Cepeda, C., Wu, N., André, V. M., Cummings, D. M., and Levine, M. S. (2007). The corticostriatal pathway in Huntington's disease. *Prog. Neurobiol.* 81, 253–271.

Cepeda-Prado, E., Popp, S., Khan, U., Stefanov, D., Rodríguez, J., Menalled, L. B., et al. (2012). R6/2 Huntington's disease mice develop early and progressive abnormal brain metabolism and seizures. *J. Neurosci.* 32, 6456–6467.

Chen, C. M. (2011). Mitochondrial dysfunction, metabolic deficits, and increased oxidative stress in Huntington's disease. *Chang. Gung. Med. J.* 34, 135–152.

Choo, Y. S., Johnson, G. V., MacDonald, M., Detloff, P. J., and Lesort, M. (2004). Mutant huntingtin directly increases susceptibility of mitochondria to the calcium-induced permeability transition and cytochrome C release. *Hum. Mol. Genet.* 13, 1407–1420.

Cross, A. J., Slater, P., and Reynolds, G. P. (1986). Reduced high-affinity glutamate uptake sites in the brains of patients with Huntington's disease. *Neurosci. Lett.* 67, 198–202.

Cudkowicz, M., and Kowall, N. W. (1990). Degeneration of pyramidal projection neurons in Huntington's disease cortex. *Ann. Neurol.* 27, 200–204.

Cummings, D. M., André, V. M., Uzgil, B. O., Gee, S. M., Fisher, Y. E., Cepeda, et al. (2009). Alterations

in cortical excitation and inhibition in genetic mouse models of Huntington's disease. *J. Neurosci.* 29, 10371–10386.

Cummings, D. M., Milnerwood, A. J., Dallérac, G. M., Vatsavayai, S. C., Hirst, M. C., and Murphy, K. P. (2007). Abnormal cortical synaptic plasticity in a mouse model of Huntington's disease. *Brain Res. Bull.* 72, 103–107.

Cummings, D. M., Milnerwood, A. J., Dallérac, G. M., Waights, V., Brown, J. Y., Vatsavayai, S. C., et al. (2006). Aberrant cortical synaptic plasticity and dopaminergic dysfunction in a mouse model of Huntington's disease. *Hum. Mol. Genet.* 15, 2856–2868.

Cybulska-Klosowicz, A., Mazarakis, N. K., Van Dellen, A., Blakemore, C., Hannan, A. J., and Kossut, M. (2004). Impaired learning-dependent cortical plasticity in Huntington's disease transgenic mice. *Neurobiol. Dis.* 17, 427–434.

Dallérac, G. M., Vatsavayai, S. C., Cummings, D. M., Milnerwood, A. J., Peddie, C. J., Evans, K. A., et al. (2011). Impaired long-term potentiation in the prefrontal cortex of Huntington's disease mouse models: rescue by D1 dopamine receptor activation. *Neurodegener. Dis.* 8, 230–239.

Davies, S. W., Turmaine, M., Cozens, B. A., DiFiglia, M., Sharp, A. H., Ross, C. A., et al. (1997). Formation of neuronal intranuclear inclusions underlies the neurological dysfunction in mice transgenic for the HD mutation. *Cell* 90, 537–548.

De la Monte, S. M., Vonsattel, J. P., and Richardson, E. P. Jr. (1988). Morphometric demonstration of atrophic changes in the cerebral cortex, white matter, and neostriatum in Huntington's disease. *J. Neuropathol. Exp. Neurol.* 47, 516–525.

Dunlop, D. S., Mc Hale, D. M., and Lajtha, A. (1992). Decreased brain N-acetylaspartate in Huntington's disease. *Brain Res.* 580, 44–48.

Espinosa, J. S., and Stryker, M. P. (2012). Development and plasticity of the primary visual cortex. *Neuron* 75, 230–249.

Estrada-Sánchez, A. M., Mejía-Toiber, J., and Massieu, L. (2008). Excitotoxic neuronal death and the pathogenesis of Huntington's disease. *Arch. Med. Res.* 39, 265–276.

Estrada-Sánchez, A. M., Montiel, T., and Massieu, L. (2010). Glycolysis inhibition decreases the levels of glutamate transporters and enhances glutamate neurotoxicity in the R6/2 Huntington's disease mice. *Neurochem. Res.* 35, 1156–1163.

Estrada-Sánchez, A. M., Montiel, T., Segovia, J., and Massieu, L. (2009). Glutamate toxicity in the striatum of the R6/2 Huntington's disease transgenic mice is age-dependent and correlates with d ecreased levels of glutamate transporters. *Neurobiol. Dis.* 34, 78–86.

Estrada-Sánchez, A. M., and Rebec, G. V. (2012). Corticostriatal dysfunction and glutamate transporter 1 (GLT1) in Huntington's disease: interactions between neurons and astrocytes. *Basal Ganglia* 2, 57–66.

Faideau, M., Kim, J., Cormier, K., Gilmore, R., Welch, M., Auregan, G., et al. (2010). *In vivo* expression of polyglutamine-expanded huntingtin by mouse striatal astrocytes impairs glutamate transport: a correlation with Huntington's disease subjects. *Hum. Mol. Genet.* 19, 3053–3067.

Fennema-Notestine, C., Archibald, S. L., Jacobson, M. W., Corey-Bloom, J., Paulsen, J. S., Peavy, G. M., et al. (2004). *In vivo* evidence of cerebellar atrophy and cerebral white matter loss in Huntington disease. *Neurology* 63, 989–995.

Ferrante, R. J. (2009). Mouse models of Huntington's disease and methodological considerations for therapeutic trials. *Biochim. Biophys. Acta* 1792, 506–520.

Foerster, O. (1936). The motor cortex of man in the light of Hughlings Jackson's doctrines. *Brain* 59, 135–159.

Gambazzi, L., Gokce, O., Seredenina, T., Katsyuba, E., Runne, H., Markram, H., et al. (2010). Diminished activity-dependent brain-derived neurotrophic factor expression underlies cortical neuron microcircuit hypoconnectivity resulting from exposure to mutant huntingtin fragments. *J. Pharmacol. Exp. Ther.* 335, 13–22.

Gray, M., Shirasaki, D. I., Cepeda, C., André, V. M., Wilburn, B., Lu, X. H., et al. (2008). Full-length human mutant huntingtin with a stable polyglutamine repeat can elicit progressive and selective neuropathogenesis in BACHD mice. *J. Neurosci.* 28, 6182–6195.

Groiss, S. J., Elben, S., Reck, C., Voges, J., Wojtecki, L., and Schnitzler, A. (2011). Local field potential oscillations of the globus pallidus in Huntington's disease. *Mov. Disord.* 26, 2577–2578.

Gu, X., André, V. M., Cepeda, C., Li, S. H., Li, X. J., Levine, M. S., et al. (2007). Pathological cell-cell interactions are necessary for striatal pathogenesis in a conditional mouse model of Huntington's disease. *Mol. Neurodegener.* 2:8. doi: 10.1186/1750-1326-2-8

Gu, X., Li, C., Wei, W., Lo, V., Gong, S., Li, S. H., et al. (2005). Pathological cell-cell interactions elicited by a neuropathogenic form of mutant Huntingtin contribute to cortical pathogenesis in HD mice. *Neuron* 46, 433–444.

Gusella, J. F., Wexler, N. S., Conneally, P. M., Naylor, S. L., Anderson, M. A., Tanzi, R. E., et al. (1983). A polymorphic DNA marker genetically linked to Huntington's disease. *Nature* 306, 234–238.

Halliday, G. M., McRitchie, D. A., Macdonald, V., Double, K. L., Trent, R. J., and McCusker, E. (1998). Regional specificity of brain atrophy in Huntington's disease. *Exp. Neurol.* 154, 663–672.

Harper, P. S. (1991). *Huntington's Disease*. Philadelphia, PA: W. B. Saunders.

Harper, P. S. (2001). "The epidemiology of Huntington's disease," in *Huntington's Disease*, eds G. Bates, P. S. Harper, and L. Jones (New York, NY: Oxford University Press), 159–197.

Hassel, B., Tessler, S., Faull, R. L., and Emson, P. C. (2008). Glutamate uptake is reduced in prefrontal cortex in Huntington's disease. *Neurochem. Res.* 33, 232–237.

Hasselbalch, S. G., Oberg, G., Sørensen, S. A., Andersen, A. R., Waldemar, G., Schmidt, J. F., et al. (1992). Reduced regional cerebral blood flow in Huntington's disease studied by SPECT. *J. Neurol. Neurosurg. Psychiatry* 55, 1018–1023.

Hedreen, J. C., Peyser, C. E., Folstein, S. E., and Ross, C. A. (1991). Neuronal loss in layers V and VI of cerebral cortex in Huntington's disease. *Neurosci. Lett.* 133, 257–261.

Heinsen, H., Strik, M., Bauer, M., Luther, K., Ulmar, G., Gangnus, D., et al. (1994). Cortical and striatal neurone number in Huntington's disease. *Acta Neuropathol.* 88, 320–333.

Hodgson, J. G., Apopyan, N., Gutekunts, C. A., Leavitt, B. R., LePiane, F., and Singaraja, R. (1999). A YAC mouse model for Huntington's disease with full-length mutant huntingtin, cytoplasmic toxicity, and selective striatal neurodegeneration. *Neuron* 23, 181–192.

Höhn, S., Dallérac, G., Faure, A., Urbach, Y. K., Nguyen, H. P., Riess, O., et al. (2011). Behavioral and *in vivo* electrophysiological evidence for presymptomatic alteration of prefrontostriatal processing in the transgenic rat model for huntington disease. *J. Neurosci.* 31, 8986–8997.

Hong, S. L., Barton, S. J., and Rebec, G. V. (2012a). Altered neural and behavioral dynamics in Huntington's disease: an entropy conservation approach. *PLoS ONE* 7:e30879. doi: 10.1371/journal.pone.0030879

Hong, S. L., Barton, S. J., and Rebec, G. V. (2012b). Neural correlates of unpredictability in behavioral patterns of wild-type and R6/2 mice. *Commun. Integr. Biol.* 5, 259–261.

Hong, S. L., Cossyleon, D., Hussain, W. A., Walker, L. J., Barton, S. J., and Rebec, G. V. (2012c). Dysfunctional behavioral modulation of corticostriatal communication in the R6/2 mouse model of Huntington's disease. *PLoS ONE* 7:e47026. doi: 10.1371/journal.pone.0047026

Huntington, G. (1872). On chorea. *Med. Sur. Rep.* 26, 317–321. Re-edited: Huntington, G. (2003). On chorea. *J. Neuropsychiatry Clin. Neurosci.* 15, 109–112.

Huntington's Disease Collaborative Research Group. (1993). A novel gene containing a trinucleotide repeat that is expanded and unstable on Huntington's disease chromosomes. *Cell* 72, 971–983.

Ichinohe, N. (2012). Small-scale module of the rat granular retrosplenial cortex: an example of the minicolumn-like structure of the cerebral cortex. *Front. Neuroanat.* 5:69. doi: 10.3389/fnana.2011.00069

Izhikevich, E. M., Desai, N. S., Walcott, E. C., and Hoppensteadt, F. C. (2003). Bursts as a unit of neural information: selective communication via resonance. *Trends Neurosci.* 26, 161–167.

Jenkins, B. G., Rosas, H. D., Chen, Y. C., Makabe, T., Myers, R., MacDonald, M., et al. (1998). 1H NMR spectroscopy studies of Huntington's disease: correlations with CAG repeat numbers. *Neurology* 50, 1357–1365.

Jernigan, T. L., Salmon, D. P., Butters, N., and Hesselink, J. R. (1991). Cerebral structure on MRI, Part II: specific changes in Alzheimer's and Huntington's diseases. *Biol. Psychiatry* 29, 68–81.

Jinnai, K., and Matsuda, Y. (1979). Neurons of the motor cortex projecting commonly on the caudate nucleus and the lower brain stem in the cat. *Neurosci. Lett.* 13, 121–126.

Jones, E. G., and Pons, T. P. (1998). Thalamic and brainstem contributions to large-scale

plasticity of primate somatosensory cortex. *Science* 282, 1121–1125.

Kaplan, A., and Stockwell, B. R. (2012). Therapeutic approaches to preventing cell death in Huntington disease. *Prog. Neurobiol.* 99, 262–280.

Kemp, J. M., and Powell, T. P. (1970). The cortico-striate projection in the monkey. *Brain* 93, 525–546.

Kim, J., Bordiuk, O. L., and Ferrante, R. J. (2011). Experimental models of HD and reflection on therapeutic strategies. *Int. Rev. Neurobiol.* 98, 419–481.

Klapstein, G. J., Fisher, R. S., Zanjani, H., Cepeda, C., Jokel, E. S., Chesselet, M. F., et al. (2001). Electrophysiological and morphological changes in striatal spiny neurons in R6/2 Huntington's disease transgenic mice. *J. Neurophysiol.* 86, 2667–2677.

Kuhl, D. E., Phelps, M. E., Markham, C. H., Metter, E. J., Riege, W. H., and Winter, J. (1982). Cerebral metabolism and atrophy in Huntington's disease determined by 18FDG and computed tomographic scan. *Ann. Neurol.* 12, 425–434.

Kuwert, T., Lange, H. W., Langen, K. J., Herzog, H., Aulich, A., and Feinendegen, L. E. (1989). Cerebral glucose consumption measured by PET in patients with and without psychiatric symptoms of Huntington's disease. *Psychiatry Res.* 29, 361–362.

Kuwert, T., Lange, H. W., Langen, K. J., Herzog, H., Aulich, A., and Feinendegen, L. E. (1990). Cortical and subcortical glucose consumption measured by PET in patients with Huntington's disease. *Brain* 113, 1405–1423.

Laforet, G. A., Sapp, E., Chase, K., McIntyre, C., Boyce, F. M., Campbell, M., et al. (2001). Changes in cortical and striatal neurons predict behavioral and electrophysiological abnormalities in a transgenic murine model of Huntington's disease. *J. Neurosci.* 21, 9112–9123.

Langbehn, D. R., Hayden, M. R., Paulsen, J. S., and PREDICT-HD Investigators of the Huntington Study Group. (2010). CAG-repeat length and the age of onset in Huntington disease (HD): a review and validation study of statistical approaches. *Am. J. Med. Genet. B. Neuropsychiatr. Genet.* 153, 397–408.

Lei, W., Jiao, Y., Del Mar, N., and Reiner, A. (2004). Evidence for differential cortical input to direct pathway versus indirect pathway striatal projection neurons in rats. *J. Neurosci.* 24, 8289–8299.

Lévesque, M., Charara, A., Gagnon, S., Parent, A., and Deschenes, M. (1996). Corticostriatal projections from layer V cells in rat are collaterals of long-range corticofugal axons. *Brain Res.* 709, 311–315.

Levine, M. S., Klapstein, G. J., Koppel, A., Gruen, E., Cepeda, C., Vargas, M. E., et al. (1999). Enhanced sensitivity to N-methyl-D-aspartate receptor activation in transgenic and knockin mouse models of Huntington's disease. *J. Neurosci. Res.* 58, 515–532.

Lisman, J. E. (1997). Bursts as a unit of neural information: making unreliable synapses reliable. *Trends Neurosci.* 20, 38–43.

Macdonald, V., and Halliday, G. (2002). Pyramidal cell loss in motor cortices in Huntington's disease. *Neurobiol. Dis.* 10, 378–386.

Mangiarini, L., Sathasivam, K., Seller, M., Cozens, B., Harper, A., Hetherington, C., et al. (1996). Exon 1 of the HD gene with an expanded CAG repeat is sufficient to cause a progressive neurological phenotype in transgenic mice. *Cell* 87, 493–406.

Mann, D. M., Oliver, R., and Snowden, J. S. (1993). The topographic distribution of brain atrophy in Huntington's disease and progressive supranuclear palsy. *Acta Neuropathol.* 85, 553–559.

Marder, K., Zhao, H., Eberly, S., Tanner, C. M., Oakes, D., Shoulson, I., et al. (2009). Dietary intake in adults at risk for Huntington disease: analysis of PHAROS research participants. *Neurology* 73, 385–392.

Mazarakis, N. K., Cybulska-Klosowicz, A., Grote, H., Pang, T., Van Dellen, A., Kossut, M., et al. (2005). Deficits in experience-dependent cortical plasticity and sensory-discrimination learning in presymptomatic Huntington's disease mice. *J. Neurosci.* 25, 3059–3066.

McBride, J. L., Ramaswamy, S., Gasmi, M., Bartus, R. T., Herzog, C. D., Brandon, E. P., et al. (2006). Viral delivery of glial cell line-derived neurotrophic factor improves behavior and protects striatal neurons in a mouse model of Huntington's disease. *Proc. Natl. Acad. Sci. U.S.A.* 103, 9345–9350.

McGeorge, A. J., and Faull, R. L. (1989). The organization of the projection from the cerebral cortex to the striatum in the rat. *Neuroscience* 29, 503–537.

Menalled, L. B. (2005). Knock-in mouse models of Huntington's disease. *NeuroRx* 2, 465–470.

Merchant, H., de Lafuente, V., Peña-Ortega, F., and Larriva-Sahd, J. (2012). Functional impact of interneuronal inhibition in the cerebral cortex of behaving animals. *Prog. Neurobiol.* 99, 163–178.

Milakovic, T., and Johnson, G. V. (2005). Mitochondrial respiration and ATP production are significantly impaired in striatal cells expressing mutant huntingtin. *J. Biol. Chem.* 280, 30773–30782.

Miller, B. R., and Bezprozvanny, I. (2010). Corticostriatal circuit dysfunction in Huntington's disease: intersection of glutamate, dopamine and calcium. *Future Neurol.* 5, 735–756.

Miller, B. R., Dorner, J. L., Shou, M., Sari, Y., Barton, S. J., Sengelaub, D. R., et al. (2008a). Up-regulation of GLT1 expression increases glutamate uptake and attenuates the Huntington's disease phenotype in the R6/2 mouse. *Neuroscience* 153, 329–337.

Miller, B. R., Walker, A. G., Shah, A. S., Barton, S. J., and Rebec, V. G. (2008b). Dysregulated information processing by medium spiny neurons in striatum of freely behaving mouse models of Huntington's disease. *J. Neurophysiol.* 100, 2205–2216.

Miller, B. R., Walker, A. G., Barton, S. J., and Rebec, G. V. (2011a). Dysregulated neuronal activity patterns implicate corticostriatal circuit dysfunction in multiple rodent models of Huntington's Disease. *Front. Syst. Neurosci.* 5:26. doi: 10.3389/fnsys.2011.00026

Miller, J., Arrasate, M., Brooks, E., Libeu, C. P., Legleiter, J., Hatters, D., et al. (2011b). Identifying polyglutamine protein species *in situ* that best predict neurodegeneration. *Nat. Chem. Biol.* 7, 925–934.

Miller, B. R., Walker, A. G., Fowler, S. C., von Hörsten, S., Riess, O., Johnson, M. A., et al. (2010). Dysregulation of coordinated neuronal firing patterns in striatum of freely behaving transgenic rats that model Huntington's disease. *Neurobiol. Dis.* 37, 106–113.

Miller, K. D. (2003). Understanding layer 4 of the cortical circuit: a model based on cat V1. *Cereb. Cortex.* 13, 73–82.

Milnerwood, A. J., and Raymond, L. A. (2007). Corticostriatal synaptic function in mouse models of Huntington's disease: early effects of huntingtin repeat length and protein load. *J. Physiol.* 585, 817–831.

Nicniocaill, B., Haraldsson, B., Hansson, O., O'Connor, W. T., and Brundin, P. (2001). Altered striatal amino acid neurotransmitter release monitored using microdialysis in R6/1 Huntington transgenic mice. *Eur. J. Neurosci.* 13, 206–210.

Nieuwenhuys, R. (2012). The insular cortex: a review. *Prog. Brain. Res.* 195, 123–163.

Parent, M., and Parent, A. (2006). Single-axon tracing study of corticostriatal projections arising from primary motor cortex in primates. *J. Comp. Neurol.* 496, 202–213.

Penfield, W., and Boldrey, E. (1937). Somatic motor and sensory representation in the cerebral cortex of man as studied by electrical stimulation. *Brain* 60, 389–443.

Pouladi, M. A., Stanek, L. M., Xie, Y., Franciosi, S., Southwell, A. L., Deng, Y., et al. (2012). Marked differences in neurochemistry and aggregates despite similar behavioural and neuropathological features of Huntington disease in the full-length BACHD and YAC128 mice. *Hum. Mol. Genet.* 21, 2219–2232.

Pouladi, M. A., Xie, Y., Skotte, N. H., Ehrnhoefer, D. E., Graham, R. K., Kim, J. E., et al. (2010). Full-length huntingtin levels modulate body weight by influencing insulin-like growth factor 1 expression. *Hum. Mol. Genet.* 19, 1528–1538.

Powers, W. J., Videen, T. O., Markham, J., McGee-Minnich, L., Antenor-Dorsey, J. V., Hershey, T., et al. (2007). Selective defect of *in vivo* glycolysis in early Huntington's disease striatum. *Proc. Natl. Acad. Sci. U.S.A.* 104, 2945–2949.

Quarrell, O., O'Donovan, K. L., Bandmann, O., and Strong, M. (2012). The prevalence of juvenile Huntington's disease: a review of the literature and meta-analysis. *PLoS Curr.* 4:e4f8606b742ef3. doi: 10.1371/4f8606b742ef3

Rasmussen, A., Macias, R., Yescas, P., Ochoa, A., Davila, G., and Alonso, E. (2000). Huntington disease in children: Genotype–phenotype correlation. *Neuropediatrics* 31, 190–194.

Ray, R. D., and Zald, D. H. (2012). Anatomical insights into the interaction of emotion and cognition in the prefrontal cortex. *Neurosci. Biobehav. Rev.* 36, 479–501.

Rebec, G. V., Conroy, S. K., and Barton, S. J. (2006). Hyperactive striatal neurons in symptomatic Huntington R6/2 mice: variations with behavioral state and repeated ascorbate treatment. *Neuroscience* 137, 327–336.

Reedeker, W., van der Mast, R. C., Giltay, E. J., Kooistra, T. A., Roos, R. A., and van Duijn, E.

(2012). Psychiatric disorders in Huntington's disease: a 2-year follow-up study. *Psychosomatics* 53, 220–229.

Reiner, A., Hart, N. M., Lei, W., and Deng, Y. (2010). Corticostriatal projection neurons- dichotomous types and dichotomous functions. *Front. Neuroanat.* 4:142. doi: 10.3389/fnana.2010.00142

Reiner, A., Jiao, Y., Del Mar, N., Laverghetta, A. V., and Lei, W. L. (2003). Differential morphology of pyramidal tract-type and intratelencephalically projecting-type corticostriatal neurons and their intrastriatal terminals in rats. *J. Comp. Neurol.* 457, 420–440.

Rivara, C. B., Sherwood, C. C., Bouras, C., and Hof, P. R. (2003). Stereologic characterization and spatial distribution patterns of Betz cells in the human primary motor cortex. *Anat. Rec. A. Discov. Mol. Cell. Evol. Biol.* 270, 137–151.

Rosas, H. D., Lee, S. Y., Bender, A. C., Zaleta, A. K., Vangel, M., Yu, P., et al. (2010). Altered white matter microstructure in the corpus callosum in Huntington's disease: implications for cortical "disconnection." *Neuroimage* 49, 2995–3004.

Rosas, H. D., Liu, A. K., Hersch, S., Glessner, M., Ferrante, R. J., Salat, D. H., et al. (2002). Regional and progressive thinning of the cortical ribbon in Huntington's disease. *Neurology* 58, 695–701.

Rosas, H. D., Reuter, M., Doros, G., Lee, S. Y., Triggs, T., Malarick, K., et al. (2011). A tale of two factors: what determines the rate of progression in Huntington's disease? A longitudinal MRI study. *Mov. Disord.* 26, 1691–1697.

Rosas, H. D., Salat, D. H., Lee, S. Y., Zaleta, A. K., Pappu, V., Fischl, B., et al. (2008). Cerebral cortex and the clinical expression of Huntington's disease: complexity and heterogeneity. *Brain* 131, 1057–1068.

Rosas, H. D., Tuch, D. S., Hevelone, N. D., Zaleta, A. K., Vangel, M., Hersch, S. M., et al. (2006). Diffusion tensor imaging in presymptomatic and early Huntington's disease: selective white matter pathology and its relationship to clinical measures. *Mov. Disord.* 21, 1317–1325.

Rubio-Garrido, P., Pérez-de-Manzo, F., Porrero, C., Galazo, M. J., and Clascá, F. (2009). Thalamic input to distal apical dendrites in neocortical layer 1 is massive and highly convergent. *Cereb. Cortex* 19, 2380–2395.

Sax, D. S., Powsner, R., Kim, A., Tilak, S., Bhatia, R., Cupples, L. A., et al. (1996). Evidence of cortical metabolic dysfunction in early Huntington's disease by single-photon-emission computed tomography. *Mov. Disord.* 11, 671–677.

Schieber, M. H., and Baker, J. F. (2003). "Descending control of movement," in *The Fundamental Neurosciences*, eds L. R. Squiere, F. E. Bloom, S. K. McConnell, J. L. Roberts, N. C. Spitzer, and M. J. Zigmond (San Diego, CA; Academic press), 802–805.

Schilling, G., Becher, M. W., Sharp, A. H., Jinnah, H. A., Duan, K., Kotzuk, J. A., et al. (1999). Intranuclear inclusions and neuritic aggregates in transgenic mice expressing a mutant N-terminal fragment of huntingtin. *Hum. Mol. Genet.* 8, 397–407.

Sherman, S. M., and Guillery, R. W. (2011). Distinct functions for direct and transthalamic corticocortical connections. *J. Neurophysiol.* 106, 1068–1077.

Shipp, S. (2005). The importance of being agranular: a comparative account of visual and motor cortex. *Philos. Trans. R. Soc. Lond. B Biol. Sci.* 360, 797–814.

Shipp, S. (2007). Structure and function of the cerebral cortex. *Curr. Biol.* 17, R443–R449.

Smith, R., Klein, P., Koc-Schmitz, Y., Waldvogel, H. J., Faull, R. L., Brundin, P., et al. (2007). Loss of SNAP-25 and rabphilin 3a in sensory-motor cortex in Huntington's disease. *J. Neurochem.* 103, 115–123.

Smith, Y., Bevan, M. D., Shink, E., and Bolam, J. P. (1998). Microcircuitry of the direct and indirecty pathways of the basal ganglia. *Neuroscience* 86, 353–387.

Sotrel, A., Paskevich, P. A., Kiely, D. K., Bird, E. D., Williams, R. S., and Myers, R. H. (1991). Morphometric analysis of the prefrontal cortex in Huntington's disease. *Neurology* 41, 1117–1123.

Spampanato, J., Gu, X., Yang, X. W., and Mody, I. (2008). Progressive synaptic pathology of motor cortical neurons in a BAC transgenic mouse model of Huntington's disease. *Neuroscience* 157, 606–620.

Stack, E. C., Kubilus, J. K., Smith, K., Cormier, K., Del Signore, S. J., Guelin, E., et al. (2005). Chronology of behavioral symptoms and neuropathological sequela in R6/2 Huntington's disease transgenic mice. *J. Comp. Neurol.* 490, 354–370.

Stern, E. A. (2011). Functional changes in neocortical activity in Huntington's disease model mice: an *in vivo* intracellular study. *Front. Syst. Neurosci.* 5:47. doi: 10.3389/fnsys.2011.00047

Szentágothai, J. (1975). The "module-concept" in cerebral cortex architecture. *Brain Res.* 95, 475–496.

Tang, T. S., Slow, E., Lupu, V., Stavrovskaya, I. G., Sugimori, M., Llinás, R., et al. (2005). Disturbed Ca^{2+} signaling and apoptosis of medium spiny neurons in Huntington's disease. *Proc. Natl. Acad. Sci. U.S.A.* 102, 2602–2627.

Thomas, E. A., Coppola, G., Tang, B., Kuhn, A., Kim, S., Geschwind, D. H., et al. (2011). *In vivo* cell-autonomous transcriptional abnormalities revealed in mice expressing mutant huntingtin in striatal but not cortical neurons. *Hum. Mol. Genet.* 20, 1049–1060.

Thompson, J. C., Harris, J., Sollom, A. C., Stopford, C. L., Howard, E., Snowden, J. S., et al. (2012). Longitudinal evaluation of neuropsychiatric symptoms in Huntington's disease. *J. Neuropsychiatry Clin. Neurosci.* 24, 53–60.

Thompson, P. D., Berardelli, A., Rothwell, J. C., Day, B. L., Dick, J. P., Benecke, R., et al. (1988). The coexistence of bradykinesia and chorea in Huntington's disease and its implications for theories of basal ganglia control of movement. *Brain* 111, 223–244.

Thu, D. C., Oorschot, D. E., Tippett, L. J., Nana, A. L., Hogg, V. M., Synek, B. J., et al. (2010). Cell loss in the motor and cingulate cortex correlates with symptomatology in Huntington's disease. *Brain* 133, 1094–1110.

Unschuld, P. G., Joel, S. E., Liu, X., Shanahan, M., Margolis, R. L., Biglan, K. M., et al. (2012). Impaired corticostriatal functional connectivity in prodromal Huntington's disease. *Neurosci. Lett.* 514, 204–209.

Van Raamsdonk, J. M., Gibson, W. T., Pearson, J., Murphy, Z., Lu, G., Leavitt, B. R., et al. (2006). Body weight is modulated by levels of full-length huntingtin. *Hum. Mol. Genet.* 15, 1513–1523.

Verwaest, K. A., Vu, T. N., Laukens, K., Clemens, L. E., Nguyen, H. P., Van Gasse, B., et al. (2011). (1)H NMR based metabolomics of CSF and blood serum: a metabolic profile for a transgenic rat model of Huntington disease. *Biochim. Biophys. Acta* 1812, 1371–1379.

von Economo, C. (1927). *Cellular Structure of the Human Cerebral Cortex*. Trans. and ed L. C. Triarhou (2009). Basel: Karger.

von Hörsten, S., Schmitt, I., Nguyen, H. P., Holzmann, C., Schmidt, T., Walther, T., et al. (2003). Transgenic rat model of Huntington's disease. *Hum. Mol. Genet.* 12, 617–624.

Vonsattel, J. P., Myers, R. H., Stevens, T. J., Ferrante, R. J., Bird, E. D., and Richardson, E. P. Jr. (1985). Neuropathological classification of Huntington's disease. *J. Neuropathol. Exp. Neurol.* 44, 559–577.

Walker, A. G., Miller, B. R., Fritsh, J. N., Barton, S. J., and Rebec, G. V. (2008). Altered information processing in the proforntal cortex of Huntington's disease mouse models. *J. Neurosci.* 28, 8973–8982.

Walker, A. G., Ummel, J. R., and Rebec, G. V. (2011). Reduced expression of conditioned fear in the R6/2 mouse model of Huntington's disease is related to abnormal activity in prelimbic cortex. *Neurobiol. Dis.* 43, 379–387.

Woodman, B., Butler, R., Landles, C., Lupton, M. K., Tse, J., Hockly, E., et al. (2007). The Hdh(Q150/Q150) knock-in mouse model of HD and the R6/2 exon 1 model develop comparable and widespread molecular phenotypes. *Brain Res. Bull.* 72, 83–97.

Yu, Z. X., Li, S. H., Evans, J., Pillarisetti, A., Li, H., and Li, X. J. (2003). Mutant huntingtin causes context-dependent neurodegeneration in mice with Huntington's disease. *J. Neurosci.* 23, 2193–2202.

Zuccato, C., and Cattaneo, E. (2009). Brain-derived neurotrophic factor in neurodegenerative diseases. *Nat. Rev. Neurol.* 5, 311–322.

Conflict of Interest Statement: The authors declare that the research was conducted in the absence of any commercial or financial relationships that could be construed as a potential conflict of interest.

Received: 14 November 2012; accepted: 28 January 2013; published online: 18 February 2013.

Citation: Estrada-Sánchez AM and Rebec GV (2013) Role of cerebral cortex in the neuropathology of Huntington's disease. Front. Neural Circuits 7:19. doi: 10.3389/fncir.2013.00019